Mars Precision Entry Guidance Using Internal Moving Mass Actuators

Brad M. Atkins

Dissertation submitted to the Faculty of the
Virginia Polytechnic Institute and State University
in partial fulfillment of the requirements for the degree of

Doctor of Philosophy
in
Aerospace Engineering

Craig A. Woolsey, Chair
Eric M. Queen
Cornel Sultan
Andrew Kurdila

September 26, 2014
Blacksburg, Virginia

Keywords: Mars, Precision Entry Guidance, Capsules, Hypersonic Inflatable Aerodynamic Decelerators, Attitude Control, Center of Mass Control, Internal Moving Mass Actuators

Mars Precision Entry Guidance Using Internal Moving Mass Actuators

Brad M. Atkins

(ABSTRACT)

Many landing sites of scientific interest on Mars including most of the Southern Hemisphere at elevations above 2km Mars Orbiter Laser Altimeter reference are inaccessible due to current limitations in precision entry guidance and payload deceleration. Precision guidance and large payload deceleration is challenging due to the thin Martian atmosphere, large changes in free stream conditions during entry, and aerothermal and aerodynamic instability concerns associated with control systems with direct external flow field interaction. Such risks have descoped past Mars missions to unguided entry with the exception of Mars Science Laboratory's (MSL) bank angle guidance. Consequently, prior to MSL landing ellipses were on the order of 100's of km. MSL has approached the upper limit of payload deceleration capability for rigid, blunt body sphere cone aeroshells used on all successful Mars entry missions. Hypersonic Inflatable Aerodynamic Decelerators (HIADS) are in development for larger payload deceleration capability through inflated aeroshell diameters greater than rigid aeroshells constrained by the launch rocket diameter, but to date there has been limited dynamics, control, and guidance development for their use on future missions.

This dissertation develops internal moving mass actuator (IMMA) control systems for improving Mars precision entry guidance of rigid capsules and demonstrating precision guidance capability for HIADs. IMMAs provide vehicle control moments without direct interaction with the external flow field and can increase payload mass delivered through reducing propellant mass for control and using portions of the payload for the IMMAs. Dynamics models for entry vehicles with rotation and translation IMMAs are developed. IMMA control systems using the models are developed for two NASA vehicle types: a 2.65 m, 602 kg Mars Phoenix-sized entry capsule and an 8.3 m, 5.9 metric ton HIAD approaching payload requirements for robotic precursor missions for future human missions. Linear Quadratic controllers with integral action for guidance command tracking are developed for translation and rotation IMMA configurations. Angle of attack and sideslip guidance laws are developed as an alternative to bank angle guidance for decoupling range and cross-range control for improved precision entry guidance. A new variant of the Apollo Earth return terminal guidance algorithm is implemented to provide the closed-loop angle of attack range control commands.

Nonlinear simulations of the entire 8 degree of freedom closed-loop systems demonstrate precision guidance to nominal trajectories and final targets for off-nominal initial entry conditions for flight path angle, range, cross-range, speed and attitude. Mechanical power studies for IMMA motion show rotation IMMA require less total mechanical power than translation actuators, but both systems have low nominal mechanical power requirements (below 100 Watts). Precision guidance for both systems to terminal targets greater than 37 km down-range from an open-loop ballistic entry is shown for low mechanical power, low CM displacement, (< 4.5 in) and at low internal velocities (< 2 in/s) over significant dynamic pressure changes. The collective precision guidance results and low mechanical power requirements show IMMA based entry guidance control systems constitute a promising alternative to thruster-based control systems for future Mars landers.

This work was financially supported by the National Defense Science and Engineering Graduate Fellowship Program.

Dedication

This Dissertation is dedicated to my parents, Paul and Robin Atkins, and my sister, Anna Claire Atkins.

Acknowledgments

I would like to express my sincere gratitude to each of my committee members for their personal investment in my graduate education, from Dissertation research guidance to academic instruction in the classroom. I am especially grateful to Dr. Eric Queen for his mentorship throughout my graduate program and his significant guidance with my graduate research. I am also very thankful to my committee chair Dr. Craig Woolsey for serving me as a graduate advisor and for his help and patience throughout the program. I am thankful for the incredible opportunity to have attended Virginia Polytechnic Institute and State University's graduate Aerospace and Ocean Engineering Program.

I have many people to thank that have helped me along my path towards graduate school. I am most grateful to my parents, Paul and Robin Atkins, for the tremendous financial sacrifices they have made on behalf of my sister and I for our education. I am thankful for the love, encouragement, and patience they have shown me along the way. This Dissertation is dedicated to them. I am also very grateful for the undergraduate academic training by the Rhodes College Physics Department faculty. I am especially grateful for the encouragement and guidance given to me by Dr. Brent Hoffmeister. I am also very thankful to have had excellent research mentors including Dr. Christopher Wohl. A very special thanks is owed to Dr. Wohl for his kindness, patience, and research skills he taught me during multiple summers at the NASA Langley Research Center. I am also thankful to Dr. Troy Henderson for his research guidance and for bringing me in as graduate student at Virginia Tech. I also sincerely thank the National Defense Science and Engineering Graduate Fellowship Program for their financial support of this research.

Contents

List of Figures

List of Tables

Chapter 1

Introduction

1.1 Mars Precision Guidance and Payload Deceleration Challenges

Many landing sites of scientific interest on Mars including most of the Southern Hemisphere are at elevations above 2km Mars Orbiter Laser Altimeter reference. Landing sites at these elevations are currently inaccessible due to limitations in precision entry guidance and payload deceleration [1,4]. Improving precision guidance and payload deceleration is challenging due to the thin Martian atmosphere, seasonal atmospheric variability, large dynamic pressure changes during entry, and low lift per drag ratios of the 70 degree blunt body sphere cone entry capsule used on all successful US lander missions. The Martian atmosphere is thin, approximately 1/40 the density at the surface of Mars compared with Earth, leading to low altitude hypersonic deceleration. However, the atmosphere is still thick enough so that thruster based control for guidance such as Reaction Control Systems (RCS) can pose aeorothermal and aerodynamic insatiability hazards for control jet interaction with the free-stream flow. Aerothermal risks include ablation and increased aeroheating caused by RCS jets impacting thermal protection systems. Aerodynamic instability risks include aerodynamic control torque interference where in extreme cases RCS control authority can be negated and even cause control torque reversals [3,7,8]. These aerothermal and aerodynamic risks combined with difficulties in computational methods for wake instability prediction for jet flow interaction led to the descoping of past Mars missions to ballistic, unguided entry with the exception of the Mars Science Laboratory (MSL) misison [7]. Consequently, prior to MSL landing ellipses were on the order of hundreds of kms.

MSL used bank angle modulation to steer the vehicle lift vector for range control. A nonzero lift vector was produced due to a negative trim angle of attack from a static center of mass (CM) offset with RCS jets used for roll control of the lift vector [9]. To date no mission has employed dynamic CM variation for controlling angle of attack for range guidance. Bank

angle guidance for range control induces cross-range error through lateral diversion of the lift vector which must later be corrected through bank reversals. Late bank angle reversals can lead to range misses [10]. A late bank angle reversal is proposed to have been one of the largest contributors to final miss distance for MSL [9]. Future human and robotic Mars exploration missions call for precision guidance to with tens of meters of prepositioned assets to landing sites of scientific interest at elevation + 2km or greater for payloads on the order of 5 - 60 metric tons. Current rigid entry capsule control systems have not achieved such precision and cannot adequately decelerate such large payloads due to heat shield diameter constraints. For rigid aeroshells, the launch rocket's fairing diameter constrains the maximum entry capsule aeorshell diameter size which in turn limits total drag capability. MSL had a heat shield diameter of 4.5 meters, almost maximum rocket fairing diameter of the Atlas 5 Launch vehicle. Accordingly, MSL's total payload delivery of 1.6 tons is near maximum capability for rigid blunt body vehicles.

A new class of entry aeroshells, Hypersonic Inflatable Aerodynamic Decelerators (HIADS), is under development for increasing payload deceleration capability. HIADS are compact aeroshells which can be inflated to diameters greater than is practical for rigid aeroshells, but to date there has been limited dynamics, control, and guidance development for their application to future missions. This Dissertation develops internal moving mass actuator (IMMA) control systems for hypersonic angle of attack and angle of sideslip control of a Mars Phoenix sized entry vehicle and for a HIAD inspired by NASA's High Energy Atmospheric Re-entry Vehicle Experiment. IMMA based angle of attack and sideslip control decouples range and cross-range control, eliminates bank induced cross-range errors, is integratable into proven aeroshell technology, and provides control moments independent of aerodynamic flap or thruster systems. IMMA control systems are developed for two NASA vehicle types: a 2.65 meter 602 kg Mars Phoenix sized entry capsule and an 8.3 meter 5.9 metric ton HIAD approaching payload requirements for robotic precursor missions for future human missions. The next sections overview rigid and HIAD aeroshell vehicles followed by specif sections describing the Dissertation IMMA control work in context of past IMMA research. This chapter ends with an overview of each Chapter and a summary of the significant research contributions of the Dissertation.

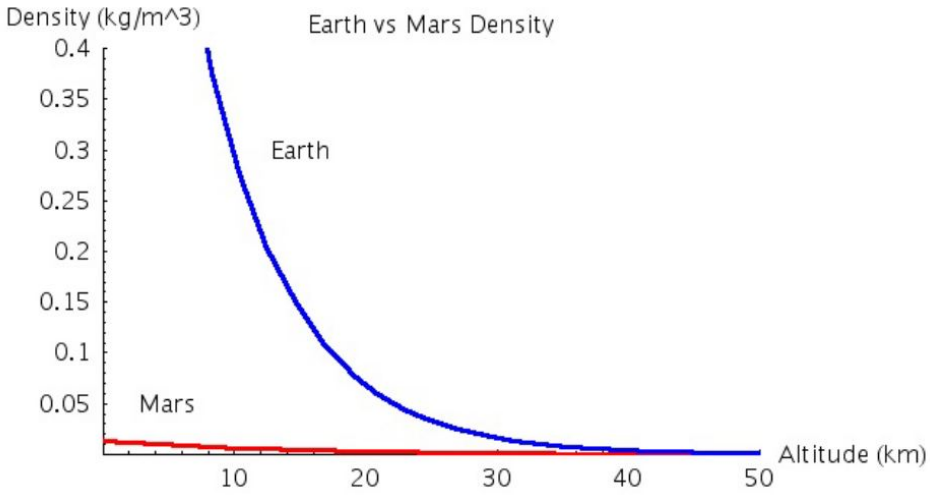

Figure 1.1: Comparison of atmospheric density between Earth and Mars from Reference [1]

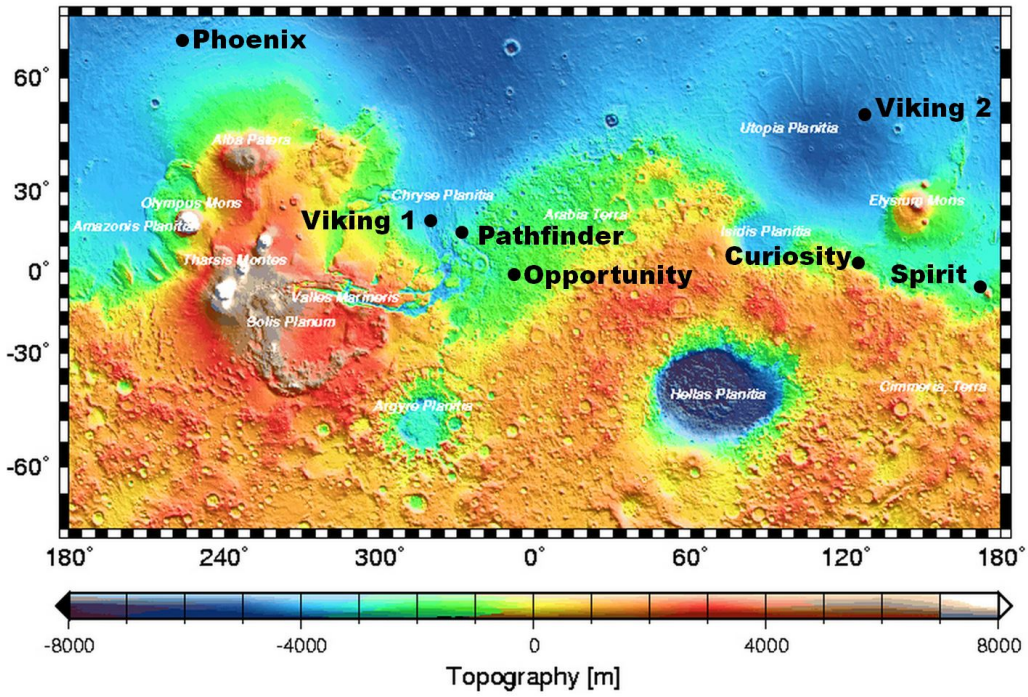

Figure 1.2: All past Mars landing sites have been at low elevations in the Northern Hemisphere. Lander data shown on MOLA elevation map from Reference [2].

1.1.1 Blunt Body Sphere Cone Entry Capsules

All of the successful 7 Mars lander missions have used scaled variations of the Viking Missions' 70 degree, blunt-body aeroshell. The aeroshell shape provides favorable payload packing, aeothermal characteristics, and large hypersonic drag coefficient for deceleration – approximately 1.7 at zero angle of attack. Substantial modeling, wind tunnel testing, and in situ data measurement and flight reconstruction has led to comprehensive aerodynamics data validation for the aeroshell shape. Figure 1.3 from Reference [3] summarizes the successful missions using this aeroshell shape. Substantial improvements in terminal landing accuracy have been made, with the recent MSL having the most precise, largest delivered payload, and highest landing elevation of any mission. However, future missions call for higher altitude landing for payloads on the order of 5 - 60 metric tons, to landing sites of scientific to landing ellipses within tens of meters of pre-positioned assets. [1, 4].

An IMMA control system is developed in this Dissertation for a Mars Phoenix sized vehicle to demonstrate improved precision guidance of rigid entry capsules through angle of attack and sidelsip control for guidance. This strategy is developed as an alternative to RCS bank angle guidance for decoupled down-range and cross-range guidance. IMMA control systems are also developed for a new class of entry vehicle, Hypersonic Aerodynamic Inflatable Decelerators (HIADS). HIADs are aeroshells which stow compactly prior to entry and are then inflated to diameters greater than their launch rocket diameter. Ballistic coefficient governs un-powered entry vehicle's deceleration profile where lowering a vehicle's ballistic coefficient enable higher altitude deceleration. Ballistic coefficient is defined as:

$$\beta = \frac{M_T}{C_D A} \tag{1.1}$$

where M_T is the total vehicle mass, C_D is the vehicle's drag coefficient, and A is the aeroshell surface area.

A HIAD's inflated diameter lowers its ballistic coefficient beyond a comparably sized rigid entry capsule. This is due to the inflated aeroshell's drag surface area per mass ratio is smaller than a comparably sized rigid entry capsule. In addition, HIADS drag surface area can exceed rigid entry capsules through inflation to greater diameters than current rigid aeroshells where maximum diameter is limited by the launch vehicle's rocket diameter.The next subsection overviews current HIAD vehicles and shows deceleration profiles for a 5900 kg entry vehicle mass, the lower limit for robotic precursor missions to human missions, for varying ballistic coefficients. The varying ballistic coefficients correspond to rigid aeroshell diameters for the Mars Phoenix Mission, MSL Mission, and for a 8.3 meter HIAD inspired by NASA's High Energy Atmospheric Re-entry Test Vehicle. The deceleration profiles demonstrate the improved payload delivery capability of HIADs.

	Viking 1/2	Pathfinder	MER A/B	Phoenix	MSL
					
Diameter, m	3.5	2.65	2.65	2.65	4.5
Entry Mass, kg	930	585	840	602	2919
Landed Mass, kg	603	360	539	364	1541
Landing Altitude, km	-3.5	-1.5	-1.3	-3.5	+1.0
Landing Ellipse, km	420 x 200	100 x 50	80 x 20	75 x 20	< 10 x 10
Relative Entry Vel., km/s	4.5/4.42	7.6	5.5	5.9	> 5.5
Relative Entry FPA, deg	-17.6	-13.8	-11.5	-13	-15.2
$m/(C_DA)$, kg/m^2	63.7	62.3	89.8	65	126
Turbulent at Peak Heating?	No	No	No	No	Yes
Peak Heat Flux, W/cm^2	24	115	54	56	243
Hypersonic α, deg	-11.2	0	0	0	-15.5
Hypersonic L/D	0.18	0	0	0	0.24
Control	3-axis	Spinning	Spinning	3-axis	3-axis
Guidance	No	No	No	No	Yes

Figure 1.3: Summary of successful Mars landing missions using scaled variants of Viking Missions' 70 degree sphere cone aeroshells [3]

1.1.2 Hypersonic Inflatable Aerodynamic Decelerators

Figure 1.4 shows comparison of the larger HEART HIAD inflated diameter to the MSL rigid aeroshell diameter which was constrained by its rocket payload fairing size. The HEART HIADs' larger aeroshell diameter enables higher altitude deceleration than MSL for the same sized payload. Higher altitude payload deceleration will enable access to new Southern highland regions of Mars, can increase Entry Descent and Landing (EDL) time-line for pre-parachute deployment and landing safety checks, and can reduce parachute deceleration demands. HEART's predecessor, the Inflatable Reentry Vehicle Experiment (IRVE), were blunt, 3 m diameter inflated HIADs with 70 degree cone angles. The actual HEART vehicle is being designed to have cone angle between 55-65 degrees. For the HIAD vehicles studied in this Dissertation, the Mars Phoenix aerodynamics database from Reference [5] is implemented in guidance simulation. Appropriate scaling for the vehicle reference area, null (zero IMMA displacement) center of mass location, and cone angle is made for the HIAD reference vehicle in order to accurately apply the aerodynamic database. Specific design details are provided in Chapter 4.

Figure 1.5 shows altitude versus speed comparisons for ballistic entry, entry at zero angle of attack, for 5900 kg vehicles with varying heat shield diameters. The entry profiles were produced assuming planar motion as described in Chapter 7 and the aerodynamic database and atmospheric model of Chapter 8. The deceleration profiles show that the MSL and Phoenix aeroshell diameters are insufficient for parachute safe deceleration, defined as speed below approximately 370 m/s at altitudes above 12.9 km from reference speed and altitude from the Mars Phoenix Mission [5]. The HIAD vehicle with the same aeroshell diameter as HEART, 8.3 m, has ballistic coefficient of 64 kg/m^2. This is the same value as the Phoenix

vehicle with its actual entry mass of 602 kg. The HIAD achieves deceleration to 370 m/s at sufficient altitude for effective parachute deployment. Flight tests are underway for HEART, but to date no HIAD has demonstrated active closed-loop guidance. Planned Earth flight tests for HEART and IRVE may include open loop center of mass actuation for maneuverability studies and aerodynamic damping characterization. This Dissertation develops IMMA control systems to demonstrate precision guidance capability and low mechanical power requirements for HIADS.

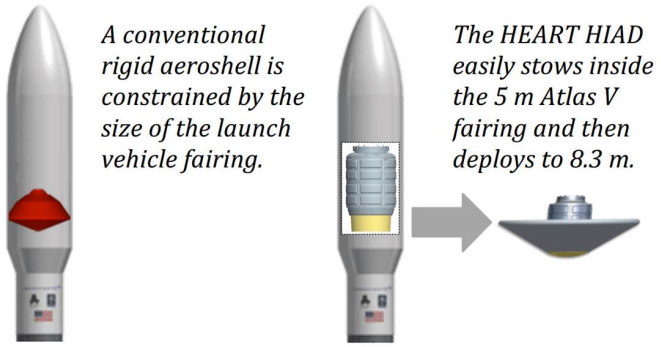

Figure 1.4: HIADs vs rigid aeroshell payload faring diameter limits [4]

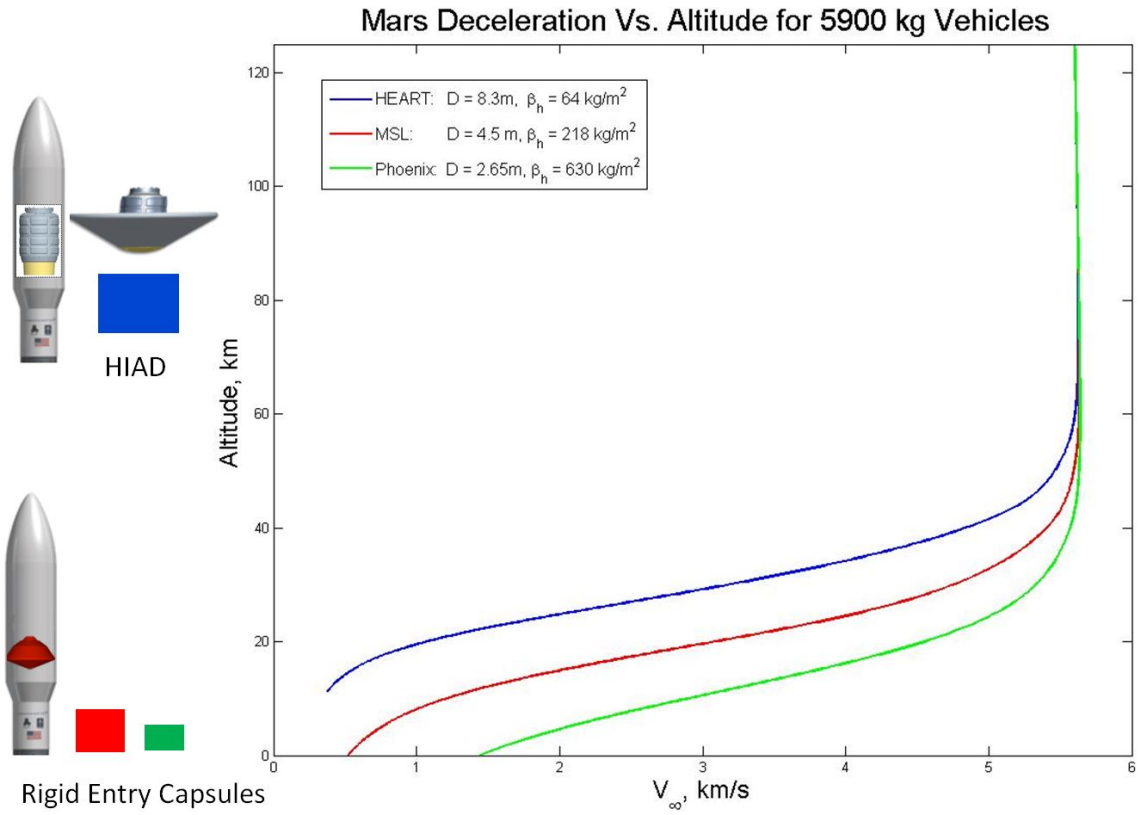

Figure 1.5: Deceleration profiles for 5900 kg entry vehicles with rigid and HIAD diameters. The colored squares show relative aeroshell surface area size.

1.2 Motivation for IMMA for Precision Mars Entry Guidance of Capsules and HIADS

The principal control strategy for non-spinning entry vehicles with IMMA is to control a moment arm from the vehicle center of pressure to the current CM location, with the external aerodynamic force acting at the center of pressure for aerodynamic control moments. There are additional dynamic effects for IMMA motion, shown clearly in the attitude and force dynamics derivations of Chapter 2 and included in nonlinear guidance simulations. However, IMMA configurations designed using this principal control moment strategy are effective for guidance command tracking through control tuning to mitigate destabilizing effects for high IMMA acceleration. Chapter 3 explains how the IMMA control strategy is well suited for blunt body entry capsules and HIADs due to axial aerodynamic force dominance. Expansion of the control moment arm is shown where axial aerodynamic force dominance enables largely decoupled pitch and yaw control moments for angle of attack and sideslip decouple control. Guidance command tracking for low IMMA velocity is shown in IMMA precision guidance simulation results in Chapters 9-10.

The IMMA aerodynamic control moments do not directly modify the external pressure distribution of the vehicle and therefore avoid ablation and destabilization concerns associated with RCS thruster systems. This reduces the Computational Fluid Dynamic analysis required for control system design. In addition the control moment arms manipulated by IMMA can be varied smoothly for high fidelity control torques. This is in contrast to RCS systems. RCS systems have restrictions in their locations due to aerodynamic instability concerns and involve bang-bang thrust pulses which ultimately impacts their control torque fidelity. [3, 8]. An additional benefit of IMMA control is that portions of the payload can be used for the IMM for increasing usable landed mass through eliminating propellant mass used only for attitude control. The HIAD concepts of this dissertation use portions of the vehicle as the IMMA; see Chapter 4 for design details.

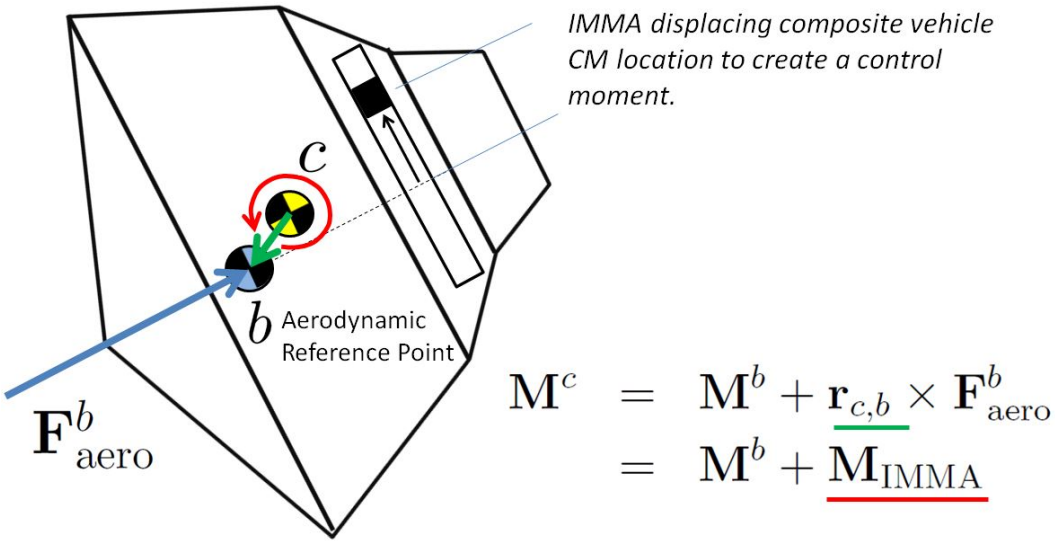

Figure 1.6: Example of IMMA attitude control moment strategy

1.3 Literature Review: Survey of Past IMMA Research

IMMA based control has previously been studied for earth application to projectile and entry vehicle trajectory control [11–17]. The authors of Reference [11] developed a 1 degree of freedom (DOF) translation IMMA system for dynamic control of stability and maneuverability of smart munitions. The IMMA was aligned with the longitudinal axis for static margin control. IMMA configurations in this Dissertation were developed to produce vehicle control torques for IMMA orthogonal to the vehicle longitudinal axis. This was done in order to avoid large mechanical power requirements associated with IMMA motion parallel to the longitudinal axis which for small angles of attack and sideslip experiences the brunt of axial deceleration force. This deceleration force can exceed 9 earth g's for Mars atmospheric

entry [5]. Control IMMA motion along the longitudinal axis will require significantly more mechanical power than motion along orthogonal axes, see the mechanical power model for translational IMMA in Chapter 11.

References [13, 14, 16–18] have investigated control authority and stability for roll axis spin stabilized projectiles, spinning projectiles with moving internal parts, and IMMAs for correcting spin axis misalignments. Reference [14] investigated swerve authority for spinning earth projectiles through high frequency vibration control of an IMMA aft of the vehicle CM and orthogonal to the body roll spin axis. The high frequency vibration control system for swerve control had large mechanical power requirements which could exceed a kW. The control systems of this study require nominal mechanical power less than 100 W shown in Chapter 11.

Equations of motion in Reference [14] are developed in the projectile body frame, whereas the current work extends the work of Reference [12] through developing the equations of motion IMMA with translational and rotational DOF from the composite system CM frame. Composite system center of mass (CM) frame attitude dynamics are desirable for implementation into validated trajectory simulation codes such as NASA's Program to Optimize Simulated Trajectory 2 (POST2), used in design for multiple Mars entry missions. In contrast to the strategy of References [11, 13, 14, 16, 17], IMMA systems are designed for a non-spinning vehicle with 2 DOF IMMA for controlling aerodynamic attitude. The authors of References [16, 17] propose orthogonal moving mass configurations similar to the translation IMMA configuration in this Dissertation for spinning vehicles. In Reference [16] trim angle of attack and sideslip controllers are developed for rapidly or slowly spinning slender rockets and re-entry vehicles for divert capability where closed-loop guidance was not shown. In Reference [17] the IMMAs are used for spin nutation damping of a ballistic earth vehicle. Four of the seven successful Mars landings have used a non-spinning entry. The others have used spin stabilization to obviate the need for an active control system. A non-spinning entry enables CM control based lift vector guidance strategies, avoids loss of swerve and angle of attack control authority due to atmospheric spin degradation, and is preferred for future human Mars entry missions.

Non-spinning earth projectile and entry vehicle control using IMMA has been explored in References [12, 15]. Reference [15] used a two moving mass configuration similar to the mass configuration of this paper for proportional navigation guidance of a 70 pound, right circular conic projectile with 5 pound moving masses and thrust capability. Equations of motion were developed for a three mass system, but the axial mass was not used for control. The dynamic equations of motion were developed from the vehicle body frame using Kane's method and did not include aerodynamic damping and unsteady aerodynamic effects. Numeric feedback linearization of the dynamic equations of motion in conjunction with pole-placement design technique were used to develop line of sight angle controllers for Earth endoatmospheric and exoatmospheric missile intercept engagements. The work of this Dissertation uses Linear Quadratic Control methodology for control development for tracking angle of attack and sideslip guidance commands for Mars hypersonic entry guidance

to terminal parachute targets over larger dynamic pressure changes and larger atmospheric density changes than in Reference [15]. Closed-loop guidance simulations in Reference [15] were for a 2.5 km altitude change through Earth's atmosphere compared to the 36 km altitude guidance range of the current work through Mars' atmosphere, see guidance results in Chapters 9-10. Exoatmospheric closed-loop guidance was also shown in Reference [15] where the vehicle had a constant thrust which provided increased control authority of the primary aerodynamic control moment through controlling both the external aerodynamic force and the internal CM location.

Internal CM control for an un-powered earth entry vehicle was employed in Reference [12] for a single IMMA for a roll controlled system. A cross-product guidance strategy was developed which is schematically similar to bank angle guidance. The objective of this work is for decoupling range and cross-range guidance through IMMA configurations for angle of attack and sideslip control. In Reference [12], the slender shape and base cut asymmetry of the vehicle considered provided increased normal force coefficient enabling greater roll control authority than a larger, more blunted vehicle. For a 70 degree blunt body Mars entry capsule, the dominant aerodynamic force is the axial force [5]. Axial force dominance motivates a pitch and yaw control strategy for angle of attack and angle of sideslip control; see Chapter 3.

The authors of Reference [12] make a flat-Earth gravitation assumption in their guidance simulations. A flat-Mars gravity model assumption leads to inaccurate peak dynamic pressure, peak axial deceleration, shorter times of flight, and shorter entry range. Terminal range differences can be on the order of hundreds of km for a flat Mars gravitation model. This was discovered through analysis of the in-plane equations of motion for flight over a spherical Mars used in the design of the guidance law of Chapter 7. These equations include latitude variation of the local horizontal frame where the gravity vector is aligned along the altitude direction. In guidance law design, a flat Mars treatment led to peak dynamic pressure of 12.5 kPa versus 6 kPa using the Mars Phoenix reference aerodynamic characteristics, entry initial conditions, and atmospheric model [5]. The IMMA aerodynamic control moments are proportional to dynamic pressure, so accurate modeling is fundamental to control authority prediction and in assessment of mechanical power required for IMMA motion. A latitude rotation model for the local horizontal orientation to an inertial planet surface fixed frame was incorporated into entry simulations. Using this model with reference entry initial conditions and aerodynamics for the Mars Phoenix entry vehicle led to simulation output in close agreement with published Phoenix Mission design simulation work of References [5, 7]. This output included time of flight, peak dynamic, pressure, axial deceleration, and Mach number at parachute altitude.

The goal of this work is also to demonstrate precision landing at Mars for future HIAD aeroshell technology. To date, limited dynamics, control, and guidance work has been performed for development of IMMA systems for HIADS. IMMA control systems have been proposed for open-loop CM maneuvers for future flight tests for the IRVE class of HIADS [19]. However, to date no comprehensive dynamics and control models have been developed. Ref-

erence [20] is a preliminary investigation of IMMA for angle of attack and sideslip control for application to HIADS using prescribed aerodynamic trim moment changes corresponding to dynamic CM offsets. The CM offset rates in simulation were set at or below 0.5 in/sec. No specific actuator configurations were developed nor explicit IMMA parameters for power studies in contrast to the translation and rotation configurations developed in this Dissertation. The authors of Reference [20] explain POST 2 has high fidelity 6 DOF simulation capability, but they did not clarify if the IMMA DOF were accounted for in the dynamics models. Further, no explicit equations of motion were shown. Vehicles with IMMA have 6 DOF plus their respective IMMA , which can exert both an aerodynamic torque to change the composite vehicle CM location and for the masses "wagging" the vehicle as characterized by the authors of References [12, 14] and shown clearly in the attitude dynamics models of Chapter 2.

It was found in tuning of the 8 DOF HIAD with Translation IMMA system of Chapter 6, that guidance commands could not be tracked for composite vehicle CM motion greater than 1 in/sec. This was due to the 2 DOF IMMA acceleration creating counter-active torques on the HIAD to the principal aerodynamic control moment term, CM control of a moment arm to the vehicle center of pressure. This is the trim condition control term which the authors of Reference [20] are using for their IMMA guidance studies. In Chapters 9-10, extensive guidance results are shown for HIAD IMMA using nonlinear attitude dynamics models accounting for their internal degrees of freedom. Guidance is shown for control to targets for off-nominal entry conditions and terminal targets downrange by more 37 km from an unguided ballistic entry. Chapter 9 shows extensive guidance results for a rigid entry capsule based off of the Mars Phoenix entry capsule. In summary, the Dissertation work is for comprehensive IMMA control system development and a new guidance strategy applied to a class of vehicles not previously considered; namely, large, blunt-body, non-spinning entry vehicles subject to large changes in free stream conditions.

1.4 Dissertation Focus and Overview of Significant Research Contributions

The focus of this Dissertation is to demonstrate viability of IMMA control systems for improving precision guidance of Mars blunt-body, axisymmetric entry capsules and for steering HIADS for precision guidance of large payloads to Mars. Improving precision guidance and payload delivery is critical to accessing landing sites at high elevation on Mars and paving the way for future human exploration missions. IMMA control systems are desirable because they provide attitude control moments without ablation and aerodynamic instability risks associated with traditional RCS thruster and aerodynamic-flap control systems. In addition, IMMA can be used to meet direct angle of attack and sideslip steering commands for decoupling range and cross-range guidance.

General, multi-body attitude dynamics models for rotation and translation IMMA are developed with respect to the instantaneous CM for implementation into space certified simulation programs such as NASA′s POST2. IMMA controllers using the dynamics models are developed for angle of attack and angle of sideslip guidance command tracking for two reference vehicles. The reference vehicles are a 2.65 m diameter, Mars Phoenix sized entry capsule and an 8.3 m diameter HIAD inspired by NASAs HEART HIAD. Translation and rotation IMMA configurations are developed for the HIAD reference vehicle for guidance performance and mechanical power comparison. A new variant of the Apollo Earth return terminal guidance algorithm is implemented for the angle of attack guidance commands for improved range control over bank angle guidance. A Cross-range sidelsip guidance law is also developed and shown effective for correcting initial cross-range errors and for guidance to terminal parachute targets with cross-range offsets as large as 10 km.

Nonlinear closed-loop precision guidance is shown demonstrating the ability to correct off-nominal range, flight path angle, attitude, and entry speed. This guidance is over large dynamic pressure changes to terminal targets located greater than 37 km downrange from the ballistic impact point. Mechanical power studies for the translation and rotation IMMA actuator configurations demonstrate low mechanical power requirements for IMMA based guidance. Based on guidance performance and mechanical power requirements, the rotation IMMA system is recommended over the translation IMMA system. The dynamics models, guidance development, and control development for the Phoenix-sized entry capsule with translation IMMA studied in this Dissertation have been submitted for publication in Reference [21]. The collective research of this Dissertation shows IMMA control systems constitute a promising control system for application to future Mars lander missions.

1.5 Organization of Dissertation

Chapter 1 identifies current major challenges to precision landing at Mars which provides motivation for improvement. Chapter 1 describes unique contributions of the Dissertation in context of previous IMMA research. Chapter 2 develops the vehicle attitude and force dynamics models for vehicles with translation IMMA and for vehicles with rotation IMMA. Chapter 3 provides overview of the control strategy, and discussion of the feasibility of angle of attack and sideslip based entry vehicle guidance. Chapter 4 overviews IMMA configurations for the entry capsule and HIAD vehicles studied in the Dissertation. Chapter 5 summarizes nonlinear equations of motion and linearization for control system development. Chapter 6 describes linear quadratic tracking controller development. Chapter 7 describes closed-loop guidance command generation including development of a new variant of the Apollo Earth return terminal guidance law. Chapter 8 describes implementation of the Phoenix aerodynamic database and atmospheric model. Chapter 9 presents precision guidance results for a rigid entry capsule with two 1 DOF translation IMMA. Chapter 10 presents closed-loop guidance results for two HIAD systems which have either a 2 DOF translation

IMMA or a 2 DOF rotation IMMA configuration. Terminal targets in Chapter 10 include cross-range offsets not shown in Chapter 9 and side-by-side comparison between the IMMA translation and rotation configurations. Chapter 11 describes mechanical power models and presents power study results for the HIAD guidance results of Chapter 10. Chapter 12 summarizes major research contributions and recommends areas for future study.

IMMA	=	abbreviation for internal moving mass actuator
HIAD	=	abbreviation for hypersonic inflatable aerodynamic decelerator
CM	=	abbreviation for center of mass
m_b, m_i, M_T	=	mass of base body, mass of ith actuator, total mass: vehicle + IMMAs, kg
$\mu_i = \frac{m_i m_b}{M_T}$	=	reduced mass of ith actuator, kg
$\mathrm{g}_{\mathrm{mars}}$	=	gravitational acceleration of Mars, $\frac{m}{s^2}$
subscripts: i, l, b, c, mi, t	=	inertial frame, local horizontal frame, vehicle body frame, vehicle CM frame, ith actuator CM frame, target frame
$\underline{\mathrm{x}}_i, \underline{\mathrm{y}}_i, \underline{\mathrm{z}}_i$	=	inertial frame unit vectors
$\underline{\mathrm{x}}_l, \underline{\mathrm{y}}_l, \underline{\mathrm{z}}_l$	=	local frame unit vectors
$\underline{\mathrm{x}}_b, \underline{\mathrm{y}}_b, \underline{\mathrm{z}}_b$	=	fixed vehicle body frame unit vectors
$\underline{\mathrm{x}}_c, \underline{\mathrm{y}}_c, \underline{\mathrm{z}}_c$	=	composite vehicle CM frame unit vectors
$\underline{\mathrm{x}}_{mi}, \underline{\mathrm{y}}_{mi}, \underline{\mathrm{z}}_{mi}$	=	ith actuator CM frame unit vectors
$\underline{\mathrm{x}}_t, \underline{\mathrm{y}}_t, \underline{\mathrm{z}}_t$	=	ith target frame unit vectors
$\mathbf{R}_c^i, \mathbf{R}_b^c, \mathbf{R}_{mi}^b$	=	rotation matrices mapping from: c to i, b to c, mi to b
$\mathbb{I}$	=	3 by 3 Identity Matrix
$\mathbf{k}_{ri,mi}^{mi}$	=	vector convention: $\mathbf{k}$ from ri to mi in the mi basis, no superscript implies b basis which has identity orientation to c basis
$\tilde{\mathbf{a}}\mathbf{b}$	=	$\mathbf{a} \times \mathbf{b}$
$\dot{\mathbf{k}}$	=	convention: "overdot" denotes time derivative of vector $\mathbf{k}$
$\mathbf{r}_{i,c}$, $\mathbf{v}_{i,c}$, $\mathbf{a}_{i,c}$	=	position, velocity, and acceleration of c relative to i, m, $\frac{m}{s}$, $\frac{m}{s^2}$
$\mathbf{r}_{c,b}$, $\mathbf{v}_{c,b}$, $\mathbf{a}_{c,b}$	=	position, velocity, and acceleration of b relative to c, m, $\frac{m}{s}$, $\frac{m}{s^2}$
$\mathbf{r}_{c,mi}$, $\mathbf{v}_{c,mi}$, $\mathbf{a}_{c,mi}$	=	position, velocity, and acceleration of ith IMMA CM relative to c, m, $\frac{m}{s}$, $\frac{m}{s^2}$
$\mathbf{r}_{b,mi}$, $\mathbf{v}_{b,mi}$, $\mathbf{a}_{b,mi}$	=	position, velocity, and acceleration of ith IMMA center of mass relative to b, m, $\frac{m}{s}$, $\frac{m}{s^2}$
$\mathbf{r}_{b,ri}$, $\mathbf{v}_{b,ri}$, $\mathbf{a}_{b,ri}$	=	position, velocity, and acceleration of ith rotation IMMA rotation point relative to b, m, $\frac{m}{s}$, $\frac{m}{s^2}$
$\mathbf{r}_{ri,mi}$, $\mathbf{v}_{ri,mi}$, $\mathbf{a}_{ri,mi}$	=	position, velocity, and acceleration of ith rotation IMMA center of mass from its respective rotation point, m, $\frac{m}{s}$, $\frac{m}{s^2}$
$c_{mi}, k_{mi}, \mathrm{F}_{b,mi}$	=	damping constant $\frac{\mathrm{N}\cdot\mathrm{s}}{m}$, spring constant $\frac{\mathrm{N}}{m}$, control force of ith actuator rel. to b, N
τ_{ai}	=	control torque of ith actuator rel. to b, $\mathrm{N}\cdot\mathrm{m}$
$\boldsymbol{\omega}_{i,c}$	=	angular velocity of c relative to i, $\frac{\mathrm{rad}}{s}$
$\boldsymbol{\omega}_{b,mi}$	=	angular velocity of mi relative to b, $\frac{\mathrm{rad}}{s}$
$\mathbf{I}_c$	=	composite vehicle inertia matrix $kg \cdot m^2$
$\mathbf{M}^c$, $\mathbf{F}^c$	=	external vehicle moments and forces in c frame, $\mathrm{N}\cdot m$, N
$\boldsymbol{p}_{i,c}$, $d\boldsymbol{p}_{i,dm}$	=	inertial momentum: composite vehicle CM and differential mass dm, $kg \cdot m/s$
u_c, v_c, w_c	=	CM frame inertial velocity components in b basis, $\frac{m}{s}$
V_∞	=	entry vehicle speed, $\frac{m}{s}$

ρ	=	atmospheric density $\frac{\text{kg}}{m^3}$
θ_l, γ	=	latitude angle, flight path angle, deg
α, β	=	angle of attack, angle of sideslip, deg
p, q, r	=	CM frame rotation rate components, $\frac{\text{rad}}{s}$
ψ, θ, ϕ	=	yaw, pitch, and roll Euler angles of l frame to c frame, deg
D, $S = \pi \frac{D}{2}^2$	=	reference length and area for entry vehicle aerodynamic coefficients, m , m^2
C_l, C_m, C_n	=	static aerodynamic moment coefficients
C_{lp}, $C_{m_{(q+\dot{\alpha})}}$, $C_{n_{(r-\dot{\beta})}}$	=	dynamic aerodynamic moment coefficients
C_A, C_Y, C_N	=	axial, normal, and side force coefficients
C_D, C_S, C_L	=	drag, side, and lift force coefficients
$\mathbf{A}, \mathbf{B}, \mathbf{C}$	=	Plant, Control Influence, and Output Matrices
$\mathbf{x}$, $\mathbf{u}$, $\mathbf{y}$	=	state, control, and output vectors
$\mathbf{r} = (\alpha_c \ \beta_c)^T$	=	reference vector for command angles of attack and sideslip
$\mathbf{J}$, $\mathbf{R}_{xx}$, $\mathbf{R}_{uu}$	=	Performance Index, state weighting matrix, control weighting matrix
$\bar{\mathbf{P}}, \mathbf{K}$, $\mathbf{K}_I$	=	solution to Algebraic Riccati Equation, feedback proportionate gains, feedback integral gains
$\mathbf{R} = -\sigma \mathbf{C}^T$	=	feed-forward control term where: $0 \leq \sigma < 1$
$(L/D)_{\text{ipc}}$, α_c, β_c	=	In plane lift-per-drag command, angle of attack command, sideslip command
K_0, $K_1(h)$, $K_2(h)$, $K_3(h)$	=	over-control, speed, flight path angle, and lift-per-drag ratio sensitivity gains
s^*	=	nominal final range
$v^*(h)$, $\gamma^*(h)$, $L/D^*(h)$	=	altitude indexed: nominal speed, flight path angle, and lift-per-drag ratio
δ_v, δ_γ, $\delta_{L/D}$	=	perturbations for speed, flight path angle, and lift-per-drag ratio
s_{vp}, $s_{\gamma p}$, $s_{(L/D)p}$	=	range due to perturbations for: speed, flight-path angle, and lift-per-drag ratio

Chapter 2

Entry Vehicle Dynamics for Translation and Rotation IMMA

The following dynamics models for entry vehicles with translation and rotation IMMAs are developed with respect to the instantaneous center of mass (CM) frame. By expressing the system dynamics in a frame that is fixed in the center of mass, one can more easily incorporate the models into proven, certified entry guidance simulation software such as NASA's Program to Optimize Simulated Trajectories 2. The dynamics models involve multiple coordinate frames: an inertial frame, an internal fixed vehicle body frame, an internal moving CM frame, internal moving mass frames at their respective center of mass positions, and intermediary rotation point frames if the IMMAs have rotational degrees of freedom. Figure 2 illustrates the general coordinate frames used for attitude dynamics derivation. An inertial frame relative to the local horizontal frame and terminal target frames are described in Section 2.3 and Chapter 7 respectively.

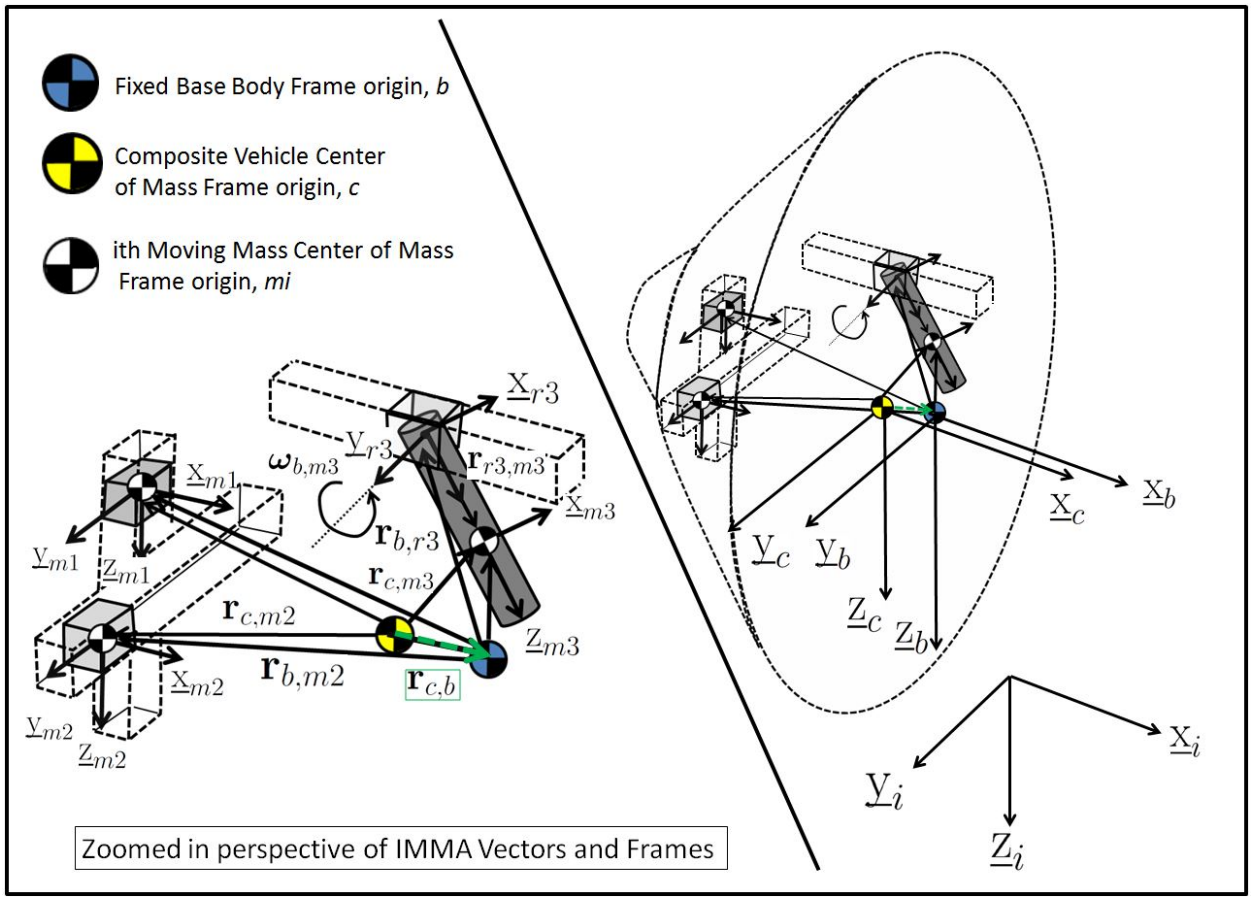

Figure 2.1: Example entry vehicle with translation and rotation IMMA

2.1 CM Frame Attitude Equation for Translation and Rotation IMMA

The Newton-Euler attitude and force dynamic formulations below extend the two-body attitude dynamics formulation developed in Reference [22]. This formulation was for a single lateral moving mass for roll control of a re-entry vehicle where the internal mass was restricted to translational motion relative to the fixed vehicle body frame b. The following formulation is for n IMMAs that can translate and rotate within the vehicle. A base body frame b located at the vehicle center of mass corresponds to the vehicle independent of the moving internal masses and is fixed to the re-entry vehicle. Unless explicitly noted with a superscript to indicate a different basis, all quantities are expressed in the base body frame basis, b. The composite system instantaneous CM frame c is assigned to always have an identity orientation relative to the base body frame, but its origin location will translate within the vehicle upon actuation of the IMMAs. IMMAs that can only translate relative to

the fixed vehicle body frame b, have their coordinate frame origins at their respective CM. The notation $\mathbf{R}^b_{mi}$ corresponds to the rotation matrix mapping from the ith moving mass CM frame, mi, to the vehicle body fixed frame, b. For IMMAs with rotational degrees of freedom relative to b, an additional coordinate frame $\mathbf{R}^{ri}_b$ is assigned at the IMMA rotation point. This coordinate frame is parallel to the IMMA CM coordinate frame $\mathbf{R}^{mi}_b$ and its origin is located relative to b at $\mathbf{r}_{b,ri}$. Note that the following derivation uses the skew symmetric matrix to represent vector cross products using the standard representation:

$$\mathbf{a} \times \mathbf{b} = \tilde{\mathbf{a}}\mathbf{b} \tag{2.1}$$

where:

$$\tilde{\mathbf{a}} = \begin{bmatrix} 0 & -a_3 & a_2 \\ a_3 & 0 & -a_1 \\ -a_2 & a_1 & 0 \end{bmatrix} \tag{2.2}$$

for $\mathbf{a} = \begin{pmatrix} a_1 & a_2 & a_3 \end{pmatrix}^T$.

The total system mass for an entry vehicle with n IMMA is:

$$M_T = m_b + \sum_{i=1}^{n} m_i \tag{2.3}$$

where m_b is the entry vehicle mass independent of the IMMA and m_i is the mass of ith IMMA. The base body position, velocity, and acceleration vectors relative to c in the b basis are:

$$\begin{aligned}
\mathbf{r}_{c,b} &= -\frac{1}{M_T}\sum_{i=1}^{n} m_i \left[\mathbf{r}_{b,ri} + \mathbf{r}^{mi}_{ri,mi}\right] && (2.4)\\
&= -\frac{1}{M_T}\sum_{i=1}^{n} m_i \left[\mathbf{r}_{b,ri} + \mathbf{R}^b_{ri}\,\mathbf{r}^{mi}_{ri,mi}\right] \\
&= -\frac{1}{M_T}\sum_{i=1}^{n} m_i \mathbf{r}_{b,mi} && (2.5)\\
\mathbf{v}_{c,b} &= -\frac{1}{M_T}\sum_{i=1}^{n} m_i \left[\mathbf{v}_{b,ri} + \mathbf{R}^b_{ri}\left(\mathbf{v}^{mi}_{ri,mi} + \tilde{\boldsymbol{\omega}}^{mi}_{b,mi}\mathbf{r}^{mi}_{ri,mi}\right)\right] && (2.6)\\
&= -\frac{1}{M_T}\sum_{i=1}^{n} m_i \mathbf{v}_{b,mi} && (2.7)\\
\mathbf{a}_{c,b} &= -\frac{1}{M_T}\sum_{i=1}^{n} m_i \left[\mathbf{a}_{b,ri} + \mathbf{R}^b_{ri}\left(\tilde{\boldsymbol{\omega}}^{mi}_{b,mi}\tilde{\boldsymbol{\omega}}^{mi}_{b,mi}\mathbf{r}^{mi}_{ri,mi} + \mathbf{a}^{mi}_{ri,mi} + \dot{\tilde{\boldsymbol{\omega}}}^{mi}_{b,mi}\mathbf{r}^{mi}_{ri,mi} + 2\tilde{\boldsymbol{\omega}}^{mi}_{b,mi}\mathbf{v}^{mi}_{ri,mi}\right)\right] \\
&= -\frac{1}{M_T}\sum_{i=1}^{n} m_i \mathbf{a}_{b,mi}\,. && (2.8)
\end{aligned}$$

The quantities $\mathbf{r}_{b,ri}$ and $\mathbf{r}^{mi}_{ri,mi}$ correspond respectively to the location of the rotation point of the ith internal mass relative to the fixed body frame b and the center of mass of the ith internal mass relative to its rotation point origin expressed in the mi center of mass frame. For the following general form, $\mathrm{r}^{mi}_{ri,mi}$ is allowed to translate such as a telescoping rod or a prismatic actuator that can also be rotated. For IMMA with rotational degrees of freedom, $\mathbf{R}^{b}_{ri}$ is the rotation matrix mapping from the mi rotation point frame to the b frame.

The negative sign in Eq. (2.4) is because it is the antiparallel vector of the composite vehicle CM location, c relative to the base body frame b origin. Eq. (2.6) follows from application of the kinematic differential equation for the derivative of the ith rotation matrix to the body frame and the application of the Transport Theorem in the differentiation of Eq. (2.4) relative to the b frame [6,23]. Eq. (2.8) follows from a second differentiation relative to b and collecting common terms. Equations (2.5), Eq. (2.7), and Eq. (2.8) denote the respective position, velocity, and acceleration of the ith IMMA cm relative to b. The constraint equations relative to c in the b basis for the ith IMMA are:

$$\mathbf{r}_{c,mi} = \mathbf{r}_{c,b} + \mathbf{r}_{b,mi} \tag{2.9}$$

$$\mathbf{v}_{c,mi} = \mathbf{v}_{c,b} + \mathbf{v}_{b,mi} \tag{2.10}$$

$$\mathbf{a}_{c,mi} = \mathbf{a}_{c,b} + \mathbf{a}_{b,mi}\,. \tag{2.11}$$

The velocity of a differential mass element dm relative to the inertial frame i is:

$$\mathbf{v}_{i,dm} = \mathbf{v}_{i,c} + \mathbf{v}_{c,dm} + \boldsymbol{\omega}_{i,c} \times \mathbf{r}_{c,dm}\,. \tag{2.12}$$

The linear momentum of dm is:

$$d\boldsymbol{p}_{i,dm} = \mathbf{v}_{i,dm} dm\,. \tag{2.13}$$

The angular momentum of the composite system about the instantaneous CM is:

$$\begin{aligned}
\mathbf{h}_c &= \int\int\int_{M_T} \mathbf{r}_{c,dm} \times d\boldsymbol{p}_{i,dm} && (2.14)\\
&= \int\int\int_{M_T} \mathbf{r}_{c,dm} \times (\mathbf{v}_{i,c} + \mathbf{v}_{c,dm} + \boldsymbol{\omega}_{i,c} \times \mathbf{r}_{c,dm})\, dm && (2.15)\\
&= -\mathbf{v}_{i,c} \times \int\int\int_{M_T} \mathbf{r}_{c,dm} dm \\
&\quad + \int\int\int_{M_T} (\mathbf{r}_{c,dm} \times \mathbf{v}_{c,dm} + \mathbf{r}_{c,dm} \times \boldsymbol{\omega}_{i,c} \times \mathbf{r}_{c,dm})\, dm && (2.16)\\
&= \mathbf{0} + \int\int\int_{M_T} \mathbf{r}_{c,dm} \times \mathbf{v}_{c,dm} dm + \int\int\int_{M_T} \mathbf{r}_{c,dm} \times \boldsymbol{\omega}_{i,c} \times \mathbf{r}_{c,dm} dm && (2.17)\\
&= \mathbf{r}_{c,b} \times m_b \mathbf{v}_{c,b} + \sum_{i=1}^{n} \mathbf{r}_{c,mi} \times m_i \mathbf{v}_{c,mi} + \mathbf{I}_c \boldsymbol{\omega}_{i,c} && (2.18)\\
&= m_b \tilde{\mathbf{r}}_{c,b} \mathbf{v}_{c,b} + \sum_{i=1}^{n} m_i \tilde{\mathbf{r}}_{c,mi} \mathbf{v}_{c,mi} + \mathbf{I}_c \boldsymbol{\omega}_{i,c} && (2.19)
\end{aligned}$$

Eq. (2.15) follows from substituting Eq. (2.12) into Eq. (2.14). In Eq. (2.16) the cross product has been reversed with appropriate sign change and the velocity of the composite CM relative to the inertial frame has been factored out of the integral because it is constant over the composite body. Eq. (2.17) follows as noted in Reference [22], because the resultant integral is the distance of the composite CM to c. This is zero from construction that c is the location of composite CM. The first two terms of Eq. (2.18) is the first nonzero triple integral of Eq. (2.17) summed over the composite vehicle which are the base body and n actuator velocity constraints, Eq. (2.6) and Eq. (2.10). The final term of Eq. (2.18) follows from standard definition of the Inertia matrix [23]. Eq. (2.19) uses the skew-symmetric matrix form for cross product terms. For the composite vehicle inertia matrix, $\mathbf{I}_c$, from construction that $\mathbf{R}_{\mathbf{b}}^{\mathbf{c}} = \mathbb{I}$, the identity matrix is:

$$\mathbf{I}_c = \mathbf{I}_b + \left[m_b \left(\mathbf{r}_{c,b}^T \mathbf{r}_{c,b} \mathbb{I} - \mathbf{r}_{c,b} \mathbf{r}_{c,b}^T\right)\right] + \sum_{i=1}^{n} \left[\mathbf{R}_{mi}^{b} \mathbf{I}_{mi}^{mi} \mathbf{R}_{b}^{mi} + m_i \left(\mathbf{r}_{c,mi}^T \mathbf{r}_{c,mi} \mathbb{I} - \mathbf{r}_{c,mi} \mathbf{r}_{c,mi}^T\right)\right]. \quad (2.20)$$

In Eq. (2.20), $\mathbf{I}_b$ and $\mathbf{I}_{mi}^{mi}$ correspond to the base body inertia matrix and inertia matrices of the IMMA respectively. The remaining terms arise from application of the Parallel Axis Theorem [23] to track the base body and IMMA's inertia matrices relative to the instantaneous CM at c. Note that in the summation of the final term of Eq. (2.20), the change of basis

formula [23] has been applied due to the inertia matrices of the internal masses expressed in their coordinate bases. Recall that the constraint equations $\mathbf{r}_{c,mi}$ were expressed in the b basis thereby eliminating need for application of Change of Basis Theorem to to the final term of Eq. (2.20). Recall from construction:

$$\mathbf{R}^b_{mi} = \mathbf{R}^c_{mi} \ . \tag{2.21}$$

The attitude equation governing the rotational dynamics of the composite system CM is obtained from application of Euler's 2nd Law:

$$\begin{aligned}
\mathbf{M}^c &= \dot{\mathbf{h}}\Big|_c + \boldsymbol{\omega}_{i,c} \times \mathbf{h}_c && (2.22)\\
&= \frac{d}{dt}\Big|_c \left(m_b \tilde{\mathbf{r}}_{c,b}\mathbf{v}_{c,b} + \sum_{i=1}^{n} m_i \tilde{\mathbf{r}}_{c,mi}\mathbf{v}_{c,mi} + \mathbf{I}_c\boldsymbol{\omega}_{i,c} \right) \\
&\quad + \tilde{\boldsymbol{\omega}}_{i,c} \left(m_b \tilde{\mathbf{r}}_{c,b}\mathbf{v}_{c,b} + \sum_{i=1}^{n} m_i \tilde{\mathbf{r}}_{c,mi}\mathbf{v}_{c,mi} + \mathbf{I}_c\boldsymbol{\omega}_{i,c} \right) && (2.23)\\
&= m_b \tilde{\mathbf{r}}_{c,b}\mathbf{a}_{c,b} + \sum_{i=1}^{n} m_i \tilde{\mathbf{r}}_{c,mi}\mathbf{a}_{c,mi} + \dot{\mathbf{I}}_c\boldsymbol{\omega}_{i,c} + \mathbf{I}_c\dot{\boldsymbol{\omega}}_{i,c} + \\
&\quad \tilde{\boldsymbol{\omega}}_{i,c} \left(m_b \tilde{\mathbf{r}}_{c,b}\mathbf{v}_{c,b} + \sum_{i=1}^{n} m_i \tilde{\mathbf{r}}_{c,mi}\mathbf{v}_{c,mi} + \mathbf{I}_c\boldsymbol{\omega}_{i,c} \right) && (2.24)
\end{aligned}$$

where terms involving cross-products of like vectors have been eliminated. Note that Eq. (2.24) requires the base body and IMMA constraint equations, Eq. (2.4) - Eq. (2.8) and Eq. (2.31) - Eq. (2.11). Also required is the composite inertia matrix and its derivative which involves these constraint equations and using the kinematic differential equation [6] for the rotation matrix derivative terms:

$$\begin{aligned}
\dot{\mathbf{I}}_c &= m_b \left[2\mathbf{r}^T_{c,b}\mathbf{v}_{c,b}\mathbb{I} - \mathbf{r}_{c,b}\mathbf{v}^T_{c,b} - \mathbf{v}_{c,b}\mathbf{r}^T_{c,b} \right] + \sum_{i=1}^{n} m_i \left[2\mathbf{r}^T_{c,mi}\mathbf{v}_{c,mi}\mathbb{I} - \mathbf{r}_{c,mi}\mathbf{v}^T_{c,mi} - \mathbf{v}_{c,mi}\mathbf{r}^T_{c,mi} \right] \\
&\quad + \sum_{i=1}^{n} \left[\tilde{\boldsymbol{\omega}}_{b,mi}\mathbf{R}^b_{mi}\mathbf{I}^{mi}_{mi}\mathbf{R}^{mi}_b - \mathbf{R}^b_{mi}\mathbf{I}^{mi}_{mi}\mathbf{R}^{mi}_b\tilde{\boldsymbol{\omega}}_{b,mi} \right] \ . && (2.25)
\end{aligned}$$

The following additional steps are needed to arrive at a final, more compact form of Eq. (2.24). First, the general vector for the composite CM:

$$\mathbf{r}_c = \frac{1}{M_T} \left(\sum_{i=1}^{n} m_i \mathbf{r}_{mi} + m_b \mathbf{r}_b \right) \tag{2.26}$$

is written with respect to the composite vehicle CM frame, which by definition is zero:

$$\mathbf{r}_{c,c} = \frac{1}{M_T}\left(\sum_{i=1}^{n} m_i \mathbf{r}_{c,mi} + m_b \mathbf{r}_{c,b}\right) \tag{2.27}$$

$$= \mathbf{0}\,. \tag{2.28}$$

This relationship implies:

$$\mathbf{r}_{c,b} = -\frac{1}{m_b}\sum_{i=1}^{n} m_i \mathbf{r}_{c,mi} \tag{2.29}$$

$$= -\frac{1}{M_T}\sum_{i=1}^{n} m_i \mathbf{r}_{b,mi} \tag{2.30}$$

where Eq. (2.30) is Eq. (2.5). Together Eq. (2.29) and Eq. (2.30) imply:

$$\sum_{i=1}^{n} \mathbf{r}_{c,mi} = \frac{m_b}{M_T}\sum_{i=1}^{n} \mathbf{r}_{b,mi}\,. \tag{2.31}$$

Eq. (2.29) and Eq. (2.31) imply the following similar coefficients for their first and second derivatives:

$$\mathbf{v}_{c,b} = -\frac{1}{M_T}\sum_{i=1}^{n} m_i \mathbf{v}_{b,mi} \tag{2.32}$$

$$\sum_{i=1}^{n} \mathbf{v}_{c,mi} = \frac{m_b}{M_T}\sum_{i=1}^{n} \mathbf{v}_{b,mi} \tag{2.33}$$

$$\mathbf{a}_{c,b} = -\frac{1}{M_T}\sum_{i=1}^{n} m_i \mathbf{a}_{b,mi} \tag{2.34}$$

$$\sum_{i=1}^{n} \mathbf{a}_{c,mi} = \frac{m_b}{M_T}\sum_{i=1}^{n} \mathbf{a}_{b,mi}\,. \tag{2.35}$$

Note that the shorthand form of the IMMA constraint equations, Eq. (2.5), Eq. (2.7), and Eq. (2.8) are used here. Substituting Eq. (2.32) - Eq. (2.35) into Eq. (2.24) and rearranging terms leads to:

$$\begin{aligned}\mathbf{M}^c = {} & \mathbf{I}_c\dot{\boldsymbol{\omega}}_{i,c} + \dot{\mathbf{I}}_c\boldsymbol{\omega}_{i,c} + \tilde{\boldsymbol{\omega}}_{i,c}\mathbf{I}_c\boldsymbol{\omega}_{i,c} \\ & -\frac{m_b}{M_T}\tilde{\mathbf{r}}_{c,b}\sum_{i=1}^{n} m_i \mathbf{a}_{b,mi} + \frac{m_b}{M_T}\sum_{i=1}^{n} m_i \tilde{\mathbf{r}}_{c,mi}\mathbf{a}_{b,mi} \\ & -\frac{m_b}{M_T}\tilde{\boldsymbol{\omega}}_{i,c}\tilde{\mathbf{r}}_{c,b}\sum_{i=1}^{n} m_i \mathbf{v}_{b,mi} + \frac{m_b}{M_T}\tilde{\boldsymbol{\omega}}_{i,c}\sum_{i=1}^{n} m_i \tilde{\mathbf{r}}_{c,mi}\mathbf{v}_{b,mi}\,.\end{aligned} \tag{2.36}$$

Substituting in the following general reduced mass definition:

$$\mu = \frac{m_b m_i}{M_T} \tag{2.37}$$

then reversing the cross products in the last four terms and factoring out common terms leads to:

$$\begin{aligned}\mathbf{M}^c &= \mathbf{I}_c\dot{\boldsymbol{\omega}}_{i,c} + \dot{\mathbf{I}}_c\boldsymbol{\omega}_{i,c} + \tilde{\boldsymbol{\omega}}_{i,c}\mathbf{I}_c\boldsymbol{\omega}_{i,c} \\ &\quad + \sum_{i=1}^{n}\mu_i\tilde{\mathbf{a}}_{b,mi}\left(\mathbf{r}_{c,b} - \sum_{i=1}^{n}m_i\mathbf{r}_{c,mi}\right) + \tilde{\boldsymbol{\omega}}_{i,c}\sum_{i=1}^{n}\mu_i\tilde{\mathbf{v}}_{b,mi}\left(\mathbf{r}_{c,b} - \sum_{i=1}^{n}m_i\mathbf{r}_{c,mi}\right) .\end{aligned} \tag{2.38}$$

Subtracting Eq. (2.31) from Eq. (2.30), using the definition for total mass in Eq. (2.3), rearranging, and simplifying leads to the relationship:

$$\mathbf{r}_{c,b} - \sum_{i=1}^{n}\mathbf{r}_{c,mi} = -\sum_{i=1}^{n}\mathbf{r}_{b,mi} . \tag{2.39}$$

Substituting in this relationship and reversing the cross products in the last two terms we arrive at the final form of the attitude dynamic equation:

$$\mathbf{M}^c = \mathbf{I}_c\dot{\boldsymbol{\omega}}_{i,c} + \dot{\mathbf{I}}_c\boldsymbol{\omega}_{i,c} + \tilde{\boldsymbol{\omega}}_{i,c}\mathbf{I}_c\boldsymbol{\omega}_{i,c} + \sum_{i=1}^{n}\mu_i\tilde{\mathbf{r}}_{b,mi}\mathbf{a}_{b,mi} + \tilde{\boldsymbol{\omega}}_{i,c}\sum_{i=1}^{n}\mu_i\tilde{\mathbf{r}}_{b,mi}\mathbf{v}_{b,mi} . \tag{2.40}$$

This equation exactly agrees with Reference [22] for the case of one translation IMMA with one degree of freedom. For multiple IMMA with and without rotational degrees of freedom, extra terms arise as listed above in the constraint equations for the base body and IMMA.

2.2 Composite Vehicle CM Force Equation

The inertial position of a differential mass element dm within the entry vehicle is:

$$\mathbf{r}^i_{c,dm} = \mathbf{r}^i_{i,c} + \mathbf{R}^i_b\mathbf{r}^b_{c,dm} \tag{2.41}$$

where c is the location of the vehicle instantaneous center of mass to the inertial frame and $\mathbf{R}^i_b$ is rotation matrix mapping the center of mass frame to the inertial frame. Recall from construction in the previous section that the CM frame at c always maintains parallel orientation to the vehicle frame at b:

$$\mathbf{R}^b_c = \mathbb{I} . \tag{2.42}$$

Unless a different basis is explicitly stated with a superscript, all vectors are with respect to the b frame just as they were in the attitude dynamics equation development.

Applying the Transport Theorem for the derivative of Equation (2.41) leads to the inertial velocity of the differential mass element:

$$\mathbf{v}^i_{i,dm} = \mathbf{v}^i_{i,c} + \mathbf{R}^i_b \left(\mathbf{v}_{c,dm} + \boldsymbol{\omega}_{i,c} \times \mathbf{r}_{c,dm} \right) . \tag{2.43}$$

This vector can be expressed in the b frame by premultiplying both sides by the rotation matrix $\mathbf{R}^b_i$ and re-arranging to arrive at:

$$\begin{aligned} \mathbf{R}^b_i \mathbf{v}^i_{i,dm} &= \mathbf{R}^b_i \left(\mathbf{v}^i_{i,c} + \mathbf{R}^i_b \left(\mathbf{v}_{c,dm} + \boldsymbol{\omega}_{i,c} \times \mathbf{r}_{c,dm} \right) \right) & (2.44) \\ \mathbf{v}_{i,dm} &= \mathbf{v}_{i,c} + \mathbf{v}_{c,dm} + \boldsymbol{\omega}_{i,c} \times \mathbf{r}_{c,dm} . & (2.45) \end{aligned}$$

The linear momentum of dm is:

$$\begin{aligned} d\boldsymbol{p}_{i,dm} &= \mathbf{v}_{i,dm} dm & (2.46) \\ &= \left(\mathbf{v}_{i,c} + \mathbf{v}_{c,dm} + \boldsymbol{\omega}_{i,c} \times \mathbf{r}_{c,dm} \right) dm & (2.47) \end{aligned}$$

The composite vehicle linear momentum of the system is the sum of all differential momentums of the mass elements over the entry vehicle:

$$\begin{aligned} \boldsymbol{p}_{i,c} &= \int\int\int_{M_T} d\boldsymbol{p}_{i,dm} & (2.48) \\ &= \int\int\int_{M_T} \left(\mathbf{v}_{i,c} + \mathbf{v}_{c,dm} + \boldsymbol{\omega}_{i,c} \times \mathbf{r}_{c,dm} \right) dm & (2.49) \\ &= \mathbf{v}_{i,c} \int\int\int_{M_T} dm + \int\int\int_{M_T} \mathbf{v}_{c,dm} dm - \boldsymbol{\omega}_{i,c} \times \int\int\int_{M_T} \left(\mathbf{r}_{c,dm} \right) dm & (2.50) \\ &= \left(\sum_{i=1}^{n} m_i + m_b \right) \mathbf{v}_{i,c} & (2.51) \\ &= M_T \mathbf{v}_{i,c} & (2.52) \end{aligned}$$

Eq. (2.49) follows from substituting Eq. (2.47) into Eq. (2.48). In Eq. (2.49) the cross product has been reversed with appropriate sign change and both the CM frame inertial angular and linear velocity vectors have been factored out of the integral because they are constant over the composite body. The third integral term of Eq. (2.50) is the distance of the composite CM divided by the total mass to c which is zero from construction. The second integral term of Eq. (2.50) is also because it is the composite vehicle CM velocity relative to the CM frame origin which is zero by construction. The remaining nonzero integral of Eq. (2.50) is the product the total system mass with the CM frame inertial velocity. The composite vehicle force equation follows from applying the Transport Theorem [23] for the inertial derivative of Eq. (2.52):

$$\begin{aligned} \mathbf{F}^c &= \frac{d}{dt}|_c \, \boldsymbol{p}_{i,c} + \boldsymbol{\omega}_{i,c} \times \boldsymbol{p}_{i,c} & (2.53) \\ &= M_T \mathbf{a}_{i,c} + \boldsymbol{\omega}_{i,c} \times M_T \mathbf{v}_{i,c} . & (2.54) \end{aligned}$$

2.3 External Moments and Forces

The external moments $\mathbf{M}^c$, acting on the vehicle are:

$$\mathbf{M}^c = \mathbf{M}^b_{\text{static aero}} + \mathbf{M}^b_{\text{dynamic aero}} + \mathbf{r}_{c,b} \times \mathbf{F}^b_{\text{aero}} \,. \tag{2.55}$$

No rotation matrix is required to map the moments in the vehicle body frame b to the composite system CM frame c, because the b and c frames are parallel by definition. The aerodynamic reference point is located at the vehicle frame origin at b, for the rigid entry capsule of this Dissertation. In Eq. (2.55), the term $\mathbf{r}_{c,b} \times \mathbf{F}^b_{\text{aero}}$ corresponds to a moment arising from a moment arm from the CM location at c and aerodynamic reference point at b, and the aerodynamic force acting at b. For the HIAD vehicles of this Dissertation, the aerodynamic reference point, r_{arp} is not at b, but is located along the vehicle axis of symmetry at -0.253/D from the aeroshell nose. This distance corresponds to the Phoenix aerodynamic reference point ratio of Reference [5]. Accordingly, for HIADs the final term of Eq. 2.55 is

$$\mathbf{r}_{c,arp} \times \mathbf{F}^b_{\text{aero}} \,. \tag{2.56}$$

From Reference [24] the aerodynamic moments at aerodynamic reference point, b are:

$$\mathbf{M}^b_{\text{static aero}} = \begin{pmatrix} q_\infty S D C_l \\ q_\infty S D C_m \\ q_\infty S D C_n \end{pmatrix} \tag{2.57}$$

$$\mathbf{M}^b_{\text{dynamic aero}} = \begin{pmatrix} q_\infty S D C_{lp} \left[p \left(\frac{D}{2V_\infty} \right) \right] \\ q_\infty S D C_{m_{(q+\dot{\alpha})}} \left[\left(\frac{q+\dot{\alpha}}{2} \right) \left(\frac{D}{2V_\infty} \right) \right] \\ q_\infty S D C_{n_{(r-\dot{\beta})}} \left[\left(\frac{r-\dot{\beta}}{2} \right) \left(\frac{D}{2V_\infty} \right) \right] \end{pmatrix} . \tag{2.58}$$

In Eq. (2.57) , Eq. (2.58), and Eq. (2.63), q_∞ corresponds to the dynamic pressure:

$$q_\infty = \frac{1}{2} \rho V_\infty^2 \tag{2.59}$$

where ρ is the atmospheric density and V_∞ is the vehicle CM velocity magnitude. D and S are the respective reference length and reference area of the entry vehicle. C_l, C_m, and C_n are the static roll, pitch, and yaw aerodynamic moment coefficients. The final term of Eq. 2.55 accounts for shifting the static aerodynamic moments from the null CM to the current CM location. C_{lp}, $C_{m_{(q+\dot{\alpha})}}$, and $C_{n_{(r-\dot{\beta})}}$ are the dynamic roll, pitch, and yaw aerodynamic moments coefficients. The dynamic moment coefficients correspond to damping terms. For axisymmetric blunt body vehicles flying at angle of attack, accurate analytical models have not been developed to transfer dynamic moment coefficients at displaced CM locations away from b. Analysis from Reference [25] has found that better measurements or predictions of blunt body damping derivatives are required before a correct implementation

of the damping terms in simulation will have any significant influence on capsule damping predictions. Accordingly, the dynamic moment coefficients implemented in simulation are taken from the aerodynamic reference point from the Phoenix aerodynamic database.

In Eq. 2.58, p, q, r correspond respectively to the vehicle CM rotation rate components, relative to the inertial frame, in the c basis. α, $\dot{\alpha}$, β, and $\dot{\beta}$ correspond respectively to angle of attack, time derivative of angle of attack, sideslip angle, and time derivative of sideslip angle. Their respective equations are developed in Chapter 3. In the full nonlinear guidance simulations, aerodynamic coefficients for the Mars Phoenix capsule [5] were implemented with value lookup tables indexed by the total angle attack and clock angle which are functions of angle of attack and sideslip:

$$\alpha_T = \arccos\left(\cos\alpha\cos\beta\right) \tag{2.60}$$

$$\phi_{\alpha_T} = \arctan\left(\frac{\sin\beta}{\sin\alpha\cos\beta}\right). \tag{2.61}$$

The aerodynamic force acting at aerodynamic reference point from Reference [24] is:

$$\mathbf{F}^b_{aero} = \begin{pmatrix} -F^b_A & F^b_Y & -F^b_N \end{pmatrix}^T \tag{2.62}$$

$$= \begin{pmatrix} -q_\infty S C_A \\ q_\infty S C_Y \\ -q_\infty S C_N \end{pmatrix} \tag{2.63}$$

where C_A, C_Y, C_N correspond to the axial, normal, and side force coefficients. The Mars Phoenix aerodynamics database is described in detail in Chapter 8.

The external vehicle forces consist of the gravitational force and the aerodynamic force acting on the vehicle :

$$\begin{pmatrix} F^c_x & F^c_y & F^c_z \end{pmatrix}^T = \mathbf{F}_{\text{aero}} + \mathbf{R}^c_l \mathbf{F}^i_{\text{grav}}\,. \tag{2.64}$$

A 3-2-1 yaw, pitch, roll, sequence:

$$\mathbf{R}^c_l = \begin{bmatrix} c\theta c\psi & c\theta s\psi & -s\theta \\ s\phi s\theta c\psi - c\phi s\psi & s\phi s\theta s\psi + c\phi c\psi & s\phi c\theta \\ c\phi s\theta c\psi + s\phi s\psi & c\phi s\theta s\psi - s\phi c\psi & c\phi c\theta \end{bmatrix} \tag{2.65}$$

is used to map gravitational force defined along the z axis of the local horizontal frame to the CM frame:

$$\mathbf{F}^l_{grav} = \begin{pmatrix} 0 & 0 & M_T\, g_{\text{mars}} \end{pmatrix}^T. \tag{2.66}$$

Figure 2.2 illustrates the local horizontal frame relative to the inertial frame and vehicle CM frame. This Dissertation treats the local frame as having latitude variation only, no longitudinal variation. Entry trajectories studied are treated as initially aligned with the Martian Prime Meridian. Down-range motion is treated as latitude varying motion and

cross-range motion is treated as longitude varying motion. Cross-range motion is studied for terminal targets and initial off nominal entry positions. However, the relative cross-range to down-range motion is less than 2 percent, see Chapters 9 and 10, and oblate planet effects are neglected. For the latitude local horizontal restriction, the rotation of the local horizontal frame to the inertial frame is modeled as rotation by the latitude angle, θ_L. The relative angular velocity between the inertial frame and the CM frame is the sum of the angular velocity from the inertial to the local frame and the angular velocity from the local frame to the CM frame:

$$\boldsymbol{\omega}_{i,c} = \boldsymbol{\omega}_{i,l} + \boldsymbol{\omega}_{l,c} \,. \tag{2.67}$$

The angular velocity from the inertial to local frame:

$$\boldsymbol{\omega}_{i,l} = \dot{\theta}_L \underline{\mathrm{y}}_l \tag{2.68}$$

corresponds to latitude rotation rate:

$$\dot{\theta}_L = \frac{V_\infty}{R_{\mathrm{Mars}} + h} \,. \tag{2.69}$$

The rotation matrix from the local horizontal to the inertial frame for latitude angle rotation angle is:

$$R_i^l = \begin{bmatrix} c\theta_L & 0 & s\theta_L \\ 0 & 1 & 0 \\ -s\theta_L & 0 & c\theta_L \end{bmatrix} . \tag{2.70}$$

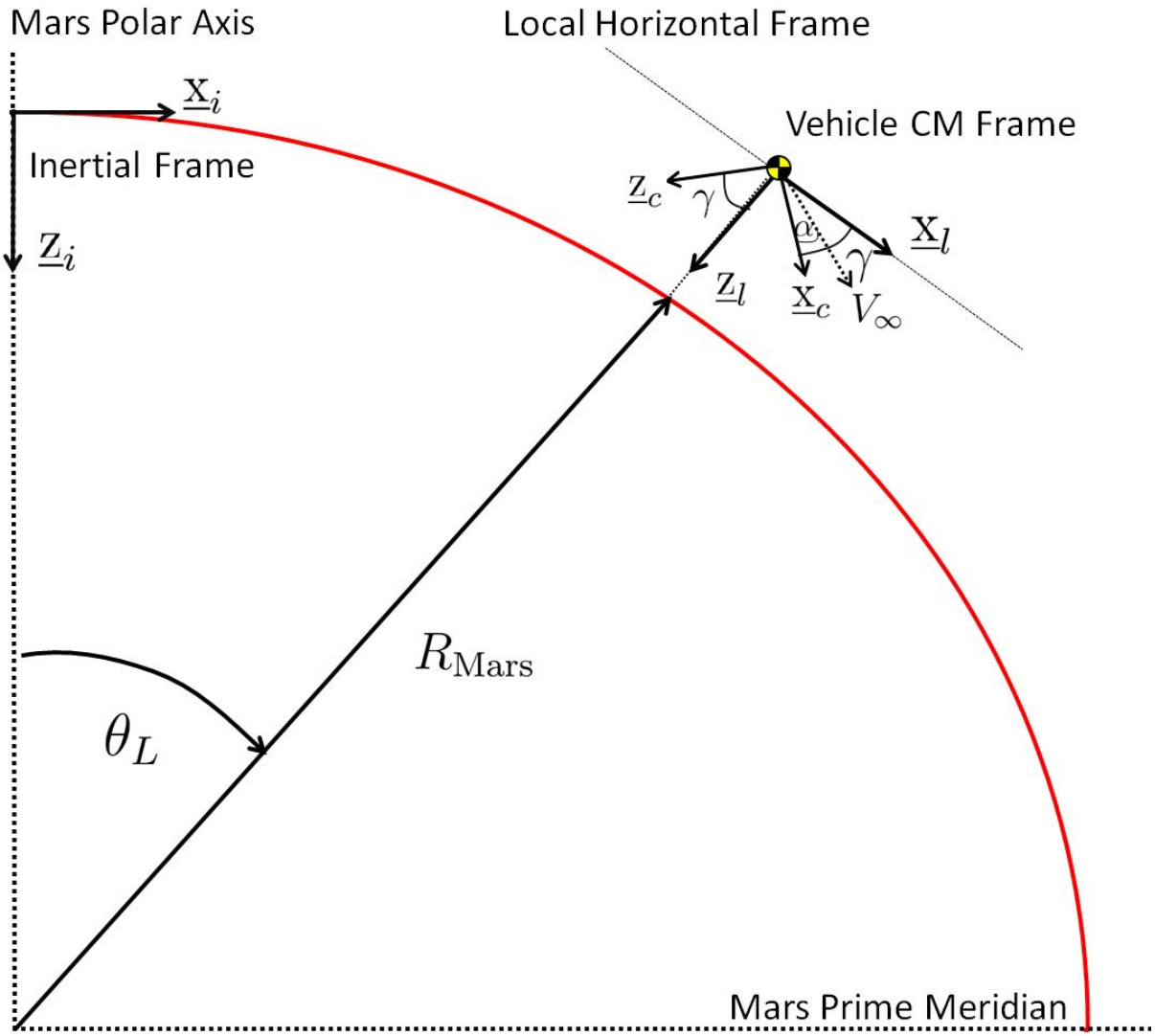

Figure 2.2: Inertial and local frame relationships

Chapter 3

IMMA Angle of Attack and Sideslip Control

This Chapter describes an angle of attack and sideslip control strategy for decoupled down-range and cross-range guidance. Lift, drag, and side Force coefficients are shown with their respective angle of attack and angle of sideslip dependence. Angle of attack and angle of sideslip rate equations are developed along with analysis of the principal aerodynamic pitch and yaw control moments created by CM displacement. IMMA configurations are shown for largely decoupled pitch and yaw control for blunt body vehicles to meet command angles of attack and sideslip. The Chapter concludes with discussion of feasibility of real-time angle of attack and angle of sideslip measurement for feedback control in actual missions.

3.1 Angle of Attack and Sideslip Equations

In this Dissertation, angle of attack and sideslip equations are computed from the composite CM frame velocity components, not the fixed vehicle body frame velocity components. There are slight differences between the internal vehicle body frame velocity and the CM frame velocity, but the differences are small because of the small internal CM displacement velocity relative to the vehicle frame. In guidance simulations these velocity differences were typically less than 1.25 cm/s (0.5 in/s).

Using the CM frame velocity components, u_c, v_c, w_c, the angle of attack and sideslip equations are:

$$\alpha = \arctan\left(\frac{w_c}{u_c}\right) \tag{3.1}$$

$$\beta = \arcsin\left(\frac{v_c}{V_\infty}\right) . \tag{3.2}$$

The angle of attack and sideslip rate equations are:

$$\dot{\alpha} = \frac{u_c\dot{w}_c - \dot{u}_c w_c}{u_c^2 + w_c^2} \tag{3.3}$$

$$\dot{\beta} = \frac{\dot{v}_c V_\infty^2 - v_c\left(u_c\dot{u}_c + v\dot{v}_c + w_c\dot{w}_c\right)}{V_\infty^2\sqrt{u_c^2 + w_c^2}}\,. \tag{3.4}$$

The CM frame inertial acceleration components, $\dot{u}_c, \dot{v}_c, \dot{w}_c$, follow from the composite vehicle force equation developed in the previous chapter:

$$\mathbf{F}^c = \left.\frac{d}{dt}\right|_c \boldsymbol{p}_{i,c} + \tilde{\boldsymbol{\omega}}_{i,c}\boldsymbol{p}_{i,c} \tag{3.5}$$

$$= M_T\dot{\mathbf{v}}_{i,c}^c + M_T\tilde{\boldsymbol{\omega}}_{i,c}\mathbf{v}_{i,c}^c \tag{3.6}$$

which is rearranged to solve for the CM acceleration components:

$$\dot{u}_c = -qw_c + rv_c + F_x^c/M_T \tag{3.7}$$

$$\dot{v}_c = -ru_c + pw_c + F_y^c/M_T \tag{3.8}$$

$$\dot{w}_c = -pv_c + qu_c + F_z^c/M_T. \tag{3.9}$$

where the F^c force components are provided in Chapter 2. For the linear tracking controllers developed in Chapters 5-6 , the vehicle CM frame inertial velocity vector components are re-expressed in terms of angle of attack and sideslip through the geometric relations:

$$u_c = V_\infty \cos\alpha\cos\beta \tag{3.10}$$

$$v_c = V_\infty \sin\beta \tag{3.11}$$

$$w_c = V_\infty \sin\alpha\cos\beta\,. \tag{3.12}$$

3.2 Angle of Attack and Sideslip Control for Decoupled Down-range and Cross-range Guidance

The ultimate objective of controlling vehicle angle of attack and sideslip angle is for decoupling down-range and cross-range guidance. Angle of attack control provides lift and drag force control for down-range guidance. Sideslip angle control provides cross-range guidance through control of the side force acting on the vehicle. Angle of attack range control and sideslip cross-range control guidance command laws are developed in Chapter 7. Eqs. (3.13)-(3.15) show the angle of attack and sideslip dependence of drag, side, and lift force coefficients.

$$C_D = (C_A\cos\alpha + C_N\sin\alpha)\cos\beta - C_Y\sin\beta \tag{3.13}$$

$$C_S = -(C_A\cos\alpha + C_N\sin\alpha)\sin\beta - C_Y\cos\beta \tag{3.14}$$

$$C_L = -C_A\sin\alpha + C_N\cos\alpha \tag{3.15}$$

Figure 3.1 illustrates pitch and yaw control moments and the lift, side, and drag forces acting on the vehicle.

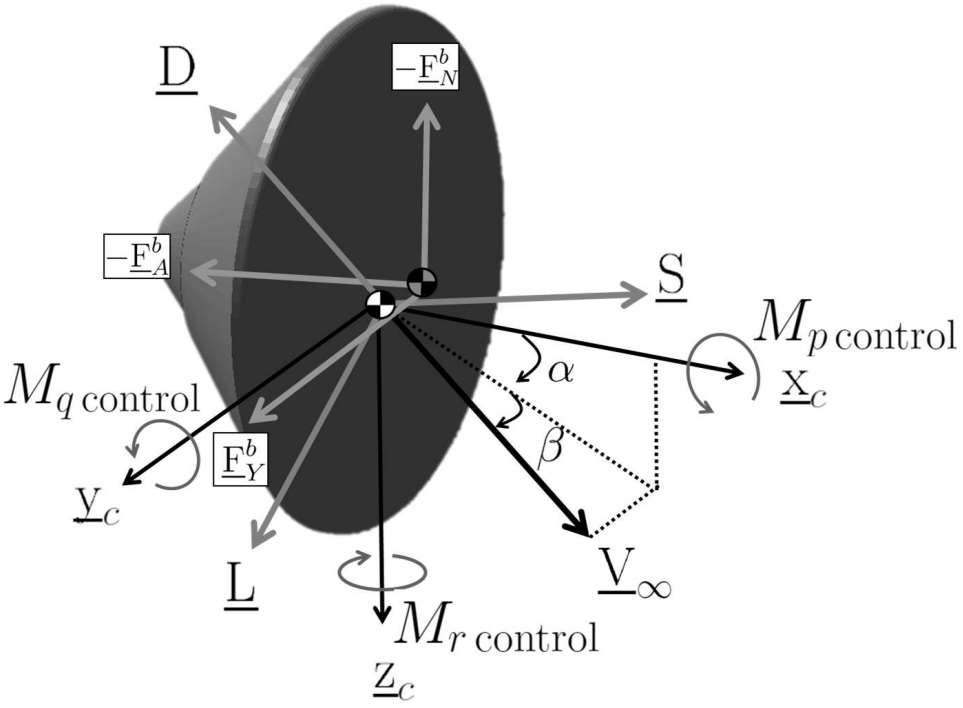

Figure 3.1: Entry vehicle control moments and aerodynamic forces

3.2.1 Pitch and Yaw Control Strategy for Angle of Attack and and Sideslip Control

The axial force for blunt body vehicles dominates the normal and side force [5]. From inspection of the cross product in Eq. (2.55):

$$\mathbf{r}_{c,b} \times \mathbf{F}^b_{\text{aero}} = \begin{pmatrix} -F^b_N\, y_{c,b} - F^b_Y\, z_{c,b} \\ F^b_N\, x_{c,b} - F^b_A\, z_{c,b} \\ -F^b_Y\, x_{c,b} + F^b_A\, y_{c,b} \end{pmatrix} \tag{3.16}$$

$$= \begin{pmatrix} M_{p\,\text{control}} & M_{q\,\text{control}} & M_{r\,\text{control}} \end{pmatrix}^T \tag{3.17}$$

pitch and yaw aerodynamic control moments, $M_{q\,\text{control}}$ and $M_{r\,\text{control}}$, are produced from the dominant axial aerodynamic force for respective CM displacement relative to the b frame of

$z_{c,b}$ and $y_{c,b}$. The IMMA translation and rotation configurations of Chapter 4 are designed to displace $z_{c,b}$ and $y_{c,b}$ to use the axial aerodynamic force to largely decouple pitch and yaw control moments. Pitch moments are designed to control the vehicle angle of attack and yaw moments the sideslip angle.

3.2.2 Feasibility of Real-Time Angle of Attack and Sideslip Measurement for Control

The advanced, real-time aerothermal and aerodynamic sensor suite employed for the recent MSL mission and existing data reconstruction techniques for inertial measurement unit (IMU) and accelerometer data suggest real-time angle of attack and sideslip estimation for flight control is implementable for future entry missions. The MSL Entry, Decent, and Landing Instrumentation (MEDLI) suite flown during the mission included the Mars Entry Atmospheric Data System (MEADS). MEADS consisted of a pressure transducer system that measured real-time pressure at 7 locations on the aeroshell for real-time estimation of dynamic pressure, Mach number, and angle of attack and sideslip [26]. Reconstructed data analysis with and without MEADS has shown good agreement between angle of attack and sideslip measurement from three separate reconstruction techniques: descent inertial measurement unit (DIMU) accelerometer and gyro rate data, MSL aerodynamic reference data base plus DIMU accelerometer data, and hybrid MEADS and DIMU combined data [27].

Reference [28] describes an extended Kalman filter technique used to blend the MEADS and IMU measurements for computing winds and atmospheric state variables directly from the MEADS measured surface pressures and integrated DIMU data. The authors of Reference [28] note that their solution is conceptually similar to the philosophy proposed for real-time air data processing for flight control in Reference [29]. The authors of Reference [30] also propose a real-time angle of attack and sideslip measurement technique, even if airflow measurements such as MEADS are unavailable. Their technique estimates angle of attack and sideslip using only IMU accelerometer and angular rate data. The time scale of hypersonic guided entry is less than four minutes, compared to longer duration aircraft flight, so errors associated with time integration of sensor bias drift should be relatively small. Collectively, MEADS and DIMU instrumentation , combined with techniques such as References [28–30] suggest that obtaining angle of attack and sideslip measurements in real-time is feasible for implementation in future IMMA angle of attack and sideslip guidance and control systems.

Chapter 4

Capsule and HIAD Vehicles with IMMA

This Chapter describes IMMA control systems developed for two separate reference vehicles, a rigid blunt body entry capsule inspired by the Mars Phoenix entry capsule from Reference 5 and a HIAD inspired by NASA's High Energy Atmospheric Re-entry Test (HEART) HIAD from Reference [4]. A 2, 1 DOF translation IMMA control system is developed for the entry capsule reference vehicle. For the HIAD reference vehicle, two separate IMMA configurations are developed, a 2 DOF translation system and a 2 DOF rotation system. All IMMA configurations were developed to meet the CM $z_{c,b}$ and $y_{c,b}$ control strategy of Chapter 3.

The Mars Phoenix entry capsule was a 70 degree sphere cone, 602 kg vehicle with a 2.65 aeroshell diameter. The Mars Phoenix-sized entry capsule IMMA system is shown in Figure 4.1. The actual HEART HIAD has a nominal inflated diameter of 8.3 m to form a 55-65 degree sphere cone. The Mars Phoenix aerodynamics database was implemented for aerodynamic coefficients of both reference vehicles studied in this Dissertation. For the HIAD reference vehicle, the aerodynamic reference point is scaled to the Phoenix axial location of (-0.253·D) m from the aeroshell nose along the vehicle axis of symmetry. In addition, the inflated cone angle is modeled as 70 degrees. The inflated aeroshell for the HIADS are approximated as comprising 11 inflated toroids with a total mass 175 kg inspired by the HEART vehicle of Reference [4]. The base payload structure of the vehicle was approximated as a 3.4 m tall by 4.15 m diameter cylinder with total mass including the inflation system of 5150 kg. A top structure is attached to the base payload structure and treated as an IMMA. The top structure was modeled as a 1.5 m tall 3.32 m diameter cylinder with total mass of 750 kg. The top structure is treated as a 2 DOF IMMA with either translation only or rotation only controlled motion.

The total HIAD vehicle mass for both the translation and rotation systems is 5900 kg. A HIAD vehicle mass > 5 metric tons is consistent with next generation payload delivery requirements [1, 4]. In addition, this vehicle mass for an 8.3 m inflated aeroshell diameter

corresponds to the same ballistic coefficient of 64 kg/m^2 as the Mars Phoenix-sized reference entry capsule with 602 kg mass. It is also close to the ballistic coefficients for the Viking 1, Viking 2, and Pathfinder Missions. Hence, choosing the 5900 kg payload for the HIAD vehicles leads to a ballistic coefficient with significant space flight heritage. Chapter 7 develops a range control law involving sensitivity gains that premultiply range, speed, and attitude error to produce angle of attack guidance commands. Because the same reference aerodynamics are used for both the capsule and HIADs, and because both vehicles have the same ballistic coefficients, the same sensitivity gains are used in range control laws implemented in simulation.

For the HIAD reference vehicle, two separate IMMA configurations are developed for the angle of attack and sideslip pitch and yaw control moment strategy described in Chapter 3. These configurations are respective 2 DOF translation and rotation IMMA systems illustrated in Figure 4.2 and Figure 4.3. The only difference between the two HIAD systems is the path the IMMA could take. All vehicle parameters except the IMMA motion paths were kept the same in order to compare guidance and mechanical power IMMA performance studied in Chapter 10 and 11. It is shown that both systems are quite capable of precision guidance and low mechanical power requirements. However, the rotation IMMA HIAD system has better guidance precision and lower mechanical power requirements. The respective IMMA to vehicle mass ratios for the entry capsule and the HIADs are 15.2 percent and 12 percent respectively. For the proposed HIAD vehicles, the top structure IMMA mass could be composed of scientific equipment, stowed parachute, or other functional payload which would increased landed usable payload.

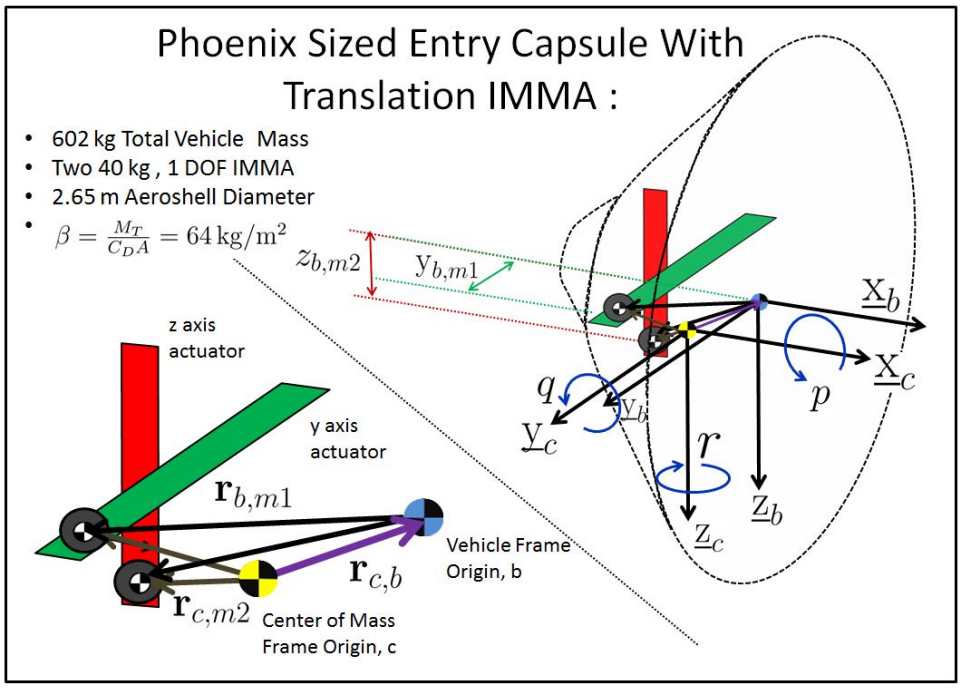

Figure 4.1: Entry capsule with 2, 1 DOF translation IMMA

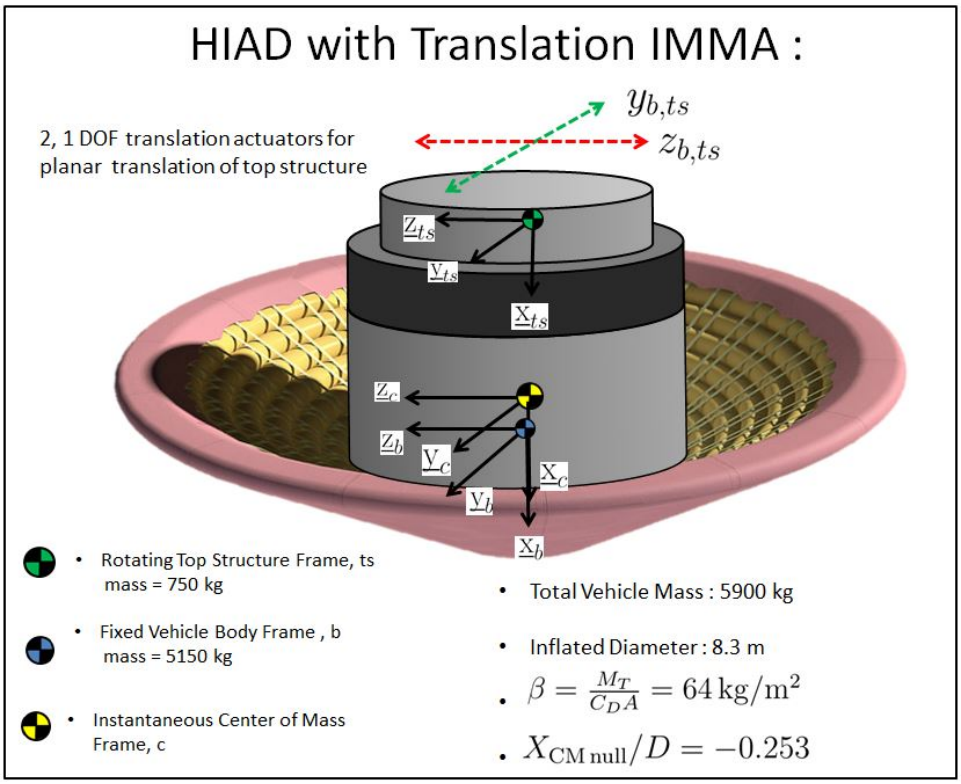

Figure 4.2: HIAD with top structure 2 DOF translation IMMA

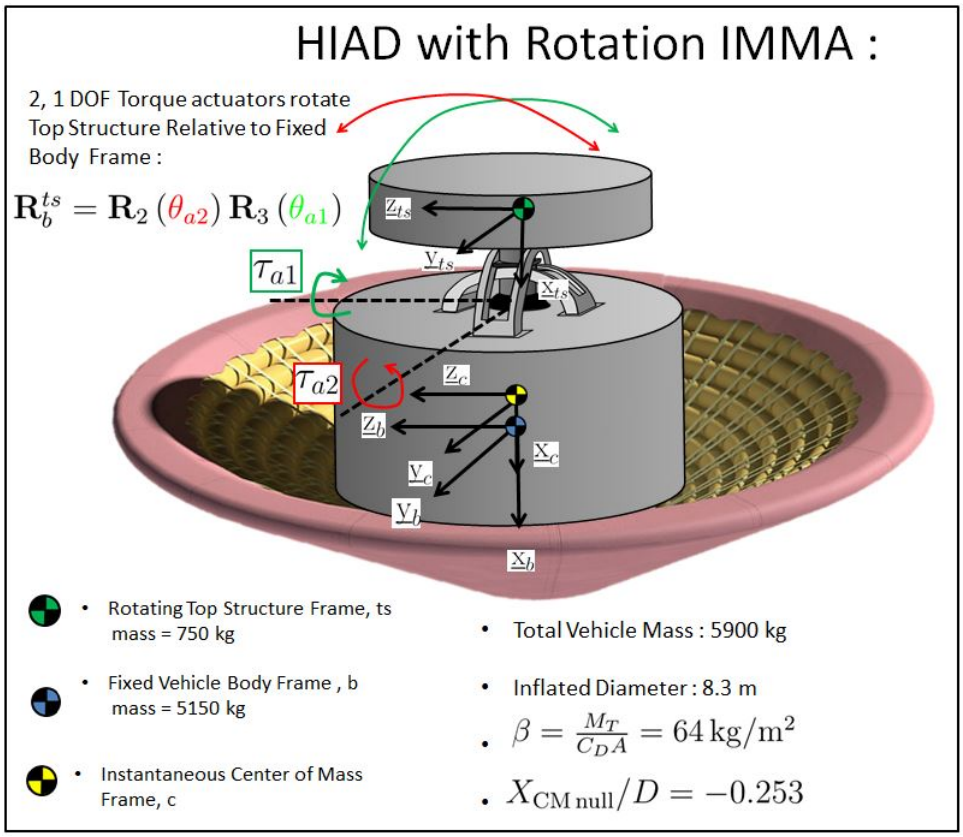

Figure 4.3: HIAD with top structure 2 DOF rotation IMMA

Chapter 5

Nonlinear Equations of Motion and Linearization

The system of equations that forms the basis for the capsule and HIAD control systems includes: the CM frame inertial angular yaw and pitch angular acceleration, the Euler yaw and pitch angle rates relative to the local horizontal frame, and the angle of attack and sideslip angle rates. Their general form is summarized below. Additional equations used to develop each controller also include specific actuator equations for their respective IMMA configurations relative to the base frame b. The actuator models are listed in the respective sections for each system along with specific nonlinear system vector, linear state vectors, control vectors, and linearized plant and control influence matrices.

The CM frame yaw and pitch angular accelerations, $\dot{r}$ and $\dot{q}$, are computed from solving for $\dot{\boldsymbol{\omega}}_{i,c}$ in the attitude equation[1], Eq. 2.40 developed in Chapter 2:

$$\dot{\boldsymbol{\omega}}_{i,c} = \begin{pmatrix} \dot{p} & \dot{q} & \dot{r} \end{pmatrix}^T \tag{5.1}$$

$$= -\mathbf{I}_c^{-1}[\dot{\mathbf{I}}\boldsymbol{\omega}_{i,c} + \tilde{\boldsymbol{\omega}}_{i,c}\mathbf{I}_c\boldsymbol{\omega}_{i,c} + \sum_{i=1}^{n}\mu_i\tilde{\mathbf{r}}_{b,m_i}\mathbf{a}_{b,mi} + \tilde{\boldsymbol{\omega}}_{i,c}\sum_{i=1}^{n}\mu_i\tilde{\mathbf{r}}_{b,m_i}\mathbf{v}_{b,mi} \tag{5.2}$$

$$-\mathbf{M}^b_{\text{stat. aero}} - \mathbf{M}^b_{\text{dyn. aero}} - \tilde{\mathbf{r}}_{c,arp}\mathbf{F}^b_{\text{aero}}]\,. \tag{5.3}$$

where Eq. 2.55 has been substituted in for the vehicle external moments, $\mathbf{M}_c$.

The roll angular acceleration, $\dot{p}$, and roll rate, $\dot{\phi}$, are not part of the feedback linear controllers, but are included in full nonlinear simulations of the systems in Chapters 9-10. The static rolling moment coefficient is assumed zero for the axisymmetric entry capsules and

[1]Discussed in Chapter 2, the aerodynamic reference point is located at the vehicle frame origin at b, for the rigid entry capsule of this Dissertation. For the HIAD vehicles of this Dissertation, the aerodynamic reference point, r_{arp} is not at b , but is located along the vehicle frame, b, axis of symmetry at -0.253/D from the aeroshell nose.

HIADs of this Dissertation. This assumption is consistent with blunt body axially symmetric aeroshells. The aerodynamics database implemented in simulation was developed for the Phoenix entry capsule in Reference [5] which does not include roll static or dynamic coefficients. Roll moments can be induced for lateral CM displacement from the vehicle axis of symmetry in the $\underline{y}_b$ direction for a nonzero aerodynamic normal force. Such roll moments are expected to be small because the normal force is small, much smaller than the dominant axial force which leads to principally yaw and pitch moments for respective CM displacement in the $\underline{y}_b$ and $\underline{z}_b$ directions. Chapter 3 provides clear discussion of CM displacement and aerodynamic force relationships to control moments.

Roll dynamics are omitted in the feedback controllers because the IMMA configuration of are designed designed to produce yaw and pitch control moments. Yaw and pitch moments are able to provide sideslip and angle of attack control of lift, drag, and side forces for guidance independent of roll control moments. Additionally, roll dynamics are neglected from the nonlinear equations of motion linearized for each of the controllers so that the controllers minimally satisfy conditions for stabilizability for computation of optimal Linear Quadratic feedback control gains in Chapter 6. In the full 8 degree of freedom nonlinear guidance simulations, roll dynamics are included. The uncontrolled Euler roll angle was small, $<$ $\pm$ 5 degrees, even for simultaneous vehicle angle of attack and sideslip angle attitudes see Chapters 9-10.

Euler yaw and pitch angle rates relative to the local horizontal frame are computed from a 3-2-1 sequence [23]:

$$\dot{\psi} = \frac{1}{\cos\theta}\left(r_l\cos\phi + q_l\sin\phi\right) \tag{5.4}$$

$$\dot{\theta} = q_l\cos\phi - r_l\sin\phi. \tag{5.5}$$

with:

$$\boldsymbol{\omega}_{l,c} = \boldsymbol{\omega}_{i,c} - \boldsymbol{\omega}_{i,l} \tag{5.6}$$

$$= \begin{pmatrix} p_l & q_l & r_l \end{pmatrix}^T \tag{5.7}$$

where:

$$\boldsymbol{\omega}_{i,l} = \dot{\theta}_L \underline{y}_l \tag{5.8}$$

$$= \frac{V_\infty}{R_{\text{Mars}} + h}\,\underline{y}_l \tag{5.9}$$

from the Latitude local horizontal variation restriction described at the end of Chapter 2. In design point simulations used for linear control tuning in Chapter 6, latitude variation is ignored, giving the approximation:

$$\boldsymbol{\omega}_{l,c} = \boldsymbol{\omega}_{i,c}\,. \tag{5.10}$$

The angle of attack and sideslip rate equations from Chapter 3 are:

$$\dot{\alpha} = \frac{u_c \dot{w}_c - \dot{u}_c w_c}{u_c^2 + w_c^2} \tag{5.11}$$

$$\dot{\beta} = \frac{\dot{v}_c V_\infty^2 - v_c \left(u_c \dot{u}_c + v \dot{v}_c + w_c \dot{w}_c \right)}{V_\infty^2 \sqrt{u_c^2 + w_c^2}} \tag{5.12}$$

where CM acceleration components:

$$\dot{u}_c = -q w_c + r v_c + F_x^c / M_T \tag{5.13}$$

$$\dot{v}_c = -r u_c + p w_c + F_y^c / M_T \tag{5.14}$$

$$\dot{w}_c = -p v_c + q u_c + F_z^c / M_T \tag{5.15}$$

along with the external vehicle CM force, F^c, components are developed in Chapter 2.

5.1 Nonlinear Structure of Equations of Motion

The nonlinear equations of motion can be cast in general form for application of nonlinear control synthesis techniques such as block backstepping for angle of attack and sideslip angle tracking. Treating control inputs as acceleration inputs of n IMMA actuators and excluding Euler pitch and yaw angle rates:

$$\dot{\mathbf{x}} = \mathbf{f}(\mathbf{x}) + \mathbf{g}(\mathbf{x}) \mathbf{y} \tag{5.16}$$

$$\dot{\mathbf{y}} = \mathbf{h}(\mathbf{x}, \mathbf{y}) + \mathbf{k}(\mathbf{x}, \mathbf{y}) \mathbf{u} \,. \tag{5.17}$$

This structure requires the following vectors and matrices:

$$\mathbf{x} = \begin{bmatrix} \alpha \\ \beta \end{bmatrix}, \quad \mathbf{y} = \begin{bmatrix} \boldsymbol{\omega}_{i,c} \\ \mathbf{r}_{b,m_1} \\ \vdots \\ \mathbf{r}_{b,m_n} \\ \mathbf{v}_{b,m_1} \\ \vdots \\ \mathbf{v}_{b,m_n} \end{bmatrix}, \quad \mathbf{u} = \begin{bmatrix} \mathbf{a}_{b,m_1} \\ \vdots \\ \mathbf{a}_{b,m_n} \end{bmatrix} \tag{5.18}$$

$$\mathbf{f}(\mathbf{x}) = \begin{bmatrix} f_a \\ f_b \end{bmatrix}, \quad \mathbf{g}(\mathbf{x}) = \begin{bmatrix} g_a & g_b \end{bmatrix} \tag{5.19}$$

$$\mathbf{h}\left(\mathbf{x},\mathbf{y}\right)=\left[\begin{array}{c} h_a \\ \mathbf{v}_{b,m_1} \\ \vdots \\ \mathbf{v}_{b,m_n} \\ \mathbf{0} \\ \vdots \\ \mathbf{0} \end{array}\right], \quad \mathbf{k}=\left[\begin{array}{c} \mu_1\tilde{\mathbf{r}}_{b,m_1} \\ \vdots \\ \mu_n\tilde{\mathbf{r}}_{b,m_n} \\ \mathbf{0} \\ \vdots \\ \mathbf{0} \\ \mathbb{I} \\ \vdots \\ \mathbb{I} \end{array}\right] \tag{5.20}$$

$$u = V_\infty \cos\left(\alpha\right)\cos\left(\beta\right) \tag{5.21}$$

$$v = V_\infty \sin\left(\beta\right) \tag{5.22}$$

$$w = V_\infty \sin\left(\alpha\right)\sin\left(\beta\right) \tag{5.23}$$

$$\boldsymbol{\omega}_{i,c}=\left(\begin{array}{ccc} p & q & r \end{array}\right)^T \tag{5.24}$$

$$\left[\begin{array}{c} \dot{\alpha} \\ \dot{\beta} \end{array}\right]=\left[\begin{array}{c} f_a \\ f_b \end{array}\right]+\left[\begin{array}{ccc} -\cos\left(\alpha\right)\tan\left(\beta\right) & 1 & -sin\left(\alpha\right)\tan\left(\beta\right) \\ \sin\left(\alpha\right) & 0 & -\cos\left(\alpha\right) \end{array}\right]\left[\begin{array}{c} p \\ q \\ r \end{array}\right] \tag{5.25}$$

$$f_a = \frac{f_z\cos\left(\alpha\right)-f_x\sin\left(\alpha\right)}{M_T V_\infty \cos\left(\beta\right)} \tag{5.26}$$

$$f_b = \frac{1}{M_T V_\infty}\left(f_y\cos\left(\beta\right)-f_x\cos\left(\alpha\right)\sin\left(\beta\right)-f_z\sin\left(\alpha\right)\sin\left(\beta\right)\right) \tag{5.27}$$

$$\left[\begin{array}{c} f_x \\ f_y \\ f_z \end{array}\right]=\mathbf{F}^b_{\text{aero}}+\mathbf{R}^c_l\mathbf{F}^l_{\text{gravity}} \tag{5.28}$$

$$g_a = \left[\begin{array}{ccc} -\cos\left(\alpha\right)\tan\left(\beta\right) & 1 & -sin\left(\alpha\right)\tan\left(\beta\right) \\ \sin\left(\alpha\right) & 0 & -\cos\left(\alpha\right) \end{array}\right] \tag{5.29}$$

$$g_b = \left[\mathbf{0}\right] \tag{5.30}$$

$$h_a=\mathbf{I}_c^{-1}[\mathbf{M}^b_{\text{stat}}+\mathbf{M}^b_{\text{dyn}}-\frac{1}{m_b}\tilde{\mathbf{F}}_{\text{aero}}\sum_{i=1}^{n}\mu_i\mathbf{r}_{b,m_i}-\dot{\mathbf{I}}_c\boldsymbol{\omega}_{i,c}-\tilde{\boldsymbol{\omega}}_{i,c}\mathbf{I}_c\boldsymbol{\omega}_{i,c}-\tilde{\boldsymbol{\omega}}_{i,c}\sum_{i=1}^{n}\mu_i\tilde{\mathbf{r}}_{b,m_i}\mathbf{v}_{b,mi}]\,. \tag{5.31}$$

5.2 Motivation for Linear Quadratic Controllers with Integral Action

Linear Quadratic (LQ) controllers with integral action are a desirable first approach to control design because Linear Control Theory is well understood, has extensive space-flight heritage, and linear controllers are generally much more tractable to develop and implement than nonlinear controllers. A significant additional benefit of LQ control is that controllers can be tuned at specif design altitudes with interpolation used for control gains between the design altitudes. This enables approximating time-varying parameters at specific design point altitudes leading to better tracking performance than if one set of feedback control gains were used throughout the entire trajectory. Time-varying parameters include entry vehicle speed and atmospheric density. Although neither parameter has explicit time-variation, both have large changes leading to large changes in dynamic pressure which directly impacts IMMA control authority.

LQ controllers with integral action are proportional-integral controllers. The benefit of the LQ method with integral error state feedback is that it eliminates static error offsets associated with proportional controllers. In addition, the LQ method is desirable because it permits straightforward performance tuning where states of interest other than the command angles can be penalized for performance tuning. For example, vehicle pitch rate and actuator velocity, can be penalized to reduce high frequency pitch oscillation and rapid IMMA velocity tracking guidance commands. Avoiding high vehicle pitch oscillation is important for protecting the vehicle structure and payload. Avoiding large IMMA velocities is important for keeping mechanical power requirements low.

The specific form of the the LQ controllers with integral action and tuning at operation altitudes are provided in the next Chapter. The controllers are shown to provide excellent command tracking performance in Chapters 9-10. The following subsections of this chapter overview linearization for each system required for control development in Chapter 6.

5.3 Linearization of Entry Capsule EOM With Translation IMMA

5.3.1 IMMA Actuator Equations

Eq. (5.32) and Eq. (5.33) describe single degree of freedom actuator accelerations of the IMMA relative to the vehicle body frame. The IMMA are modeled as 8 in diameter, 40 kg iron spheres, see Table 5.1. Their accelerations are treated as damped, driven, harmonic oscillators with damping constants (c_{m1}, c_{m2}), spring constants (k_{m1}, k_{m2}), and driving forces $(\mathrm{F}_{y,m1}, \mathrm{F}_{z,m2})$. These notional actuator models, Eq. (5.32) and Eq. (5.33), are used to gener-

ate prescribed relative IMMA acceleration to the vehicle frame, b for the attitude dynamics equation, Eq. 5.1. The action-reaction effects of the prescribed motion are accurately captured in the vehicle attitude dynamics. The actual driving forces for the notional models do not represent the actual force requirements to meet the prescribed motion because they do not include constraint forces and torques applied to the IMMA by acceleration of the vehicle. In Chapter 11, for the translation and rotation IMMA HIAD control systems, actual constraint forces and torques are computed for the prescribed IMMA motion for the guidance simulations of Chapter 10. These respective forces and torques are used in computing the requisite mechanical power for the prescribed IMMA motion.

$$\ddot{y}_{b,m1} = (1/m_1)\left(F_{ym1} - k_{m1}y_{b,m1} - c_{m1}\dot{y}_{b,m1}\right) \tag{5.32}$$
$$\ddot{z}_{b,m2} = (1/m_2)\left(F_{zm2} - k_{m2}z_{b,m2} - c_{m2}\dot{y}_{b,m2}\right) \tag{5.33}$$

5.3.2 Linearization With Translation IMMA

The state and control input vectors for the entry capsule system with translation IMMA are:

$$\mathbf{x} = \begin{pmatrix} r & q & \psi & \theta & \alpha & \beta & y_{b,m1} & \dot{y}_{b,m1} & z_{b,m2} & \dot{z}_{b,m2} \end{pmatrix}^T \tag{5.34}$$
$$\mathbf{u} = \begin{pmatrix} F_{ym1} & F_{zm2} \end{pmatrix}^T . \tag{5.35}$$

The nonlinear system:

$$\dot{\mathbf{x}} = \mathbf{f}\left(\mathbf{x}, \mathbf{u}\right) \tag{5.36}$$

is linearized about the equilibrium:

$$\mathbf{x}_{\text{eq}} = \begin{pmatrix} 0 & 0 & 0 & \gamma & 0 & 0 & 0 & 0 & 0 & 0 \end{pmatrix}^T \tag{5.37}$$
$$\mathbf{u}_{\text{eq}} = \begin{pmatrix} 0 & 0 \end{pmatrix}^T \tag{5.38}$$

to form the linear system:

$$\dot{\mathbf{x}} = \mathbf{A}\mathbf{x} + \mathbf{B}\mathbf{u} . \tag{5.39}$$

The plant and control influence matrices:

$$\mathbf{A} = \frac{\partial \mathbf{f}}{\partial \mathbf{x}}\Big|_{(\mathbf{x}_{\text{eq}}, \mathbf{u}_{\text{eq}})} \quad \mathbf{B} = \frac{\partial \mathbf{f}}{\partial \mathbf{u}}\Big|_{(\mathbf{x}_{\text{eq}}, \mathbf{u}_{\text{eq}})} \tag{5.40}$$

are:

$$\mathbf{A} = \begin{bmatrix} A_{11} & 0 & 0 & 0 & 0 & 0 & A_{17} & 0 & 0 & 0 \\ 0 & A_{22} & 0 & 0 & 0 & 0 & 0 & 0 & A_{29} & 0 \\ \frac{1}{\cos\gamma} & 0 & 0 & 0 & 0 & 0 & 0 & 0 & 0 & 0 \\ 0 & 1 & 0 & 0 & 0 & 0 & 0 & 0 & 0 & 0 \\ 0 & 1 & 0 & \frac{-g_{\text{mars}}\sin\gamma}{V_\infty} & A_{55} & 0 & 0 & 0 & 0 & 0 \\ -1 & 0 & 0 & 0 & 0 & A_{66} & 0 & 0 & 0 & 0 \\ 0 & 0 & 0 & 0 & 0 & 0 & 0 & 1 & 0 & 0 \\ 0 & 0 & 0 & 0 & 0 & 0 & \frac{-k_{m1}}{m_{a1}} & \frac{c_{m1}}{m_{a1}} & 0 & 0 \\ 0 & 0 & 0 & 0 & 0 & 0 & 0 & 0 & 0 & 1 \\ 0 & 0 & 0 & 0 & 0 & 0 & 0 & 0 & \frac{-k_{m2}}{m_{a2}} & \frac{c_{ma2}}{m_{a2}} \end{bmatrix} \tag{5.41}$$

$$\mathbf{B} = \begin{bmatrix} 0 & 0 \\ 0 & 0 \\ 0 & 0 \\ 0 & 0 \\ 0 & 0 \\ 0 & 0 \\ 0 & 0 \\ 1/m_{a1} & 0 \\ 0 & 0 \\ 0 & 1/m_{a2} \end{bmatrix} \tag{5.42}$$

where:

$$A_{11} = \frac{C_{n_{(r-\dot{\beta})}} D^2 S q_\infty}{4V_\infty \left(M_T \left(\mathrm{I_{bzz}} + 2\mathrm{I_{mzz}}\right) + m_\mathrm{a}^2\epsilon^2 + 2m_b m_\mathrm{a}\,\mathrm{x_{off}^2} + m_b m_\mathrm{a}\epsilon^2 + 2m_b m_\mathrm{a}\mathrm{x_{off}}\epsilon\right)} \tag{5.43}$$

$$A_{22} = \frac{C_{m_{(q+\dot{\alpha})}} D^2 S q_\infty}{4V_\infty \left(M_T \left(\mathrm{I_{byy}} + 2\mathrm{I_{myy}}\right) + m_\mathrm{a}^2\epsilon^2 + 2m_b m_\mathrm{a}\,\mathrm{x_{off}^2} + m_b m_\mathrm{a}\epsilon^2 + 2m_b m_\mathrm{a}\mathrm{x_{off}}\epsilon\right)} \tag{5.44}$$

$$A_{55} = \frac{M_T g_{\text{mars}}\sin(\gamma) + C_A S q_\infty}{M_T V_\infty} \tag{5.45}$$

$$A_{66} = \frac{M_T g_{\text{mars}}\sin(\gamma) + C_A S q_\infty}{M_T V_\infty} \tag{5.46}$$

$$A_{17} = \frac{-m_\mathrm{a} C_A S\, q_\infty}{\left(2m_\mathrm{a}(\mathrm{I_{bzz}} + 2\mathrm{I_{mzz}}) + \mathrm{m_b}\left(m_\mathrm{a}\epsilon^2 + 2m_\mathrm{a}\epsilon\mathrm{x_{off}} + 2m_\mathrm{a}\mathrm{x_{off}^2} + \mathrm{I_{bzz}} + 2\mathrm{I_{mzz}}\right) + m_\mathrm{a}^2\epsilon^2\right)} \tag{5.47}$$

$$A_{29} = \frac{m_\mathrm{a} C_A S q_\infty}{\left(2m_\mathrm{a}(\mathrm{I_{byy}} + 2\mathrm{I_{myy}}) + \mathrm{m_b}\left(m_\mathrm{a}\epsilon^2 + 2m_\mathrm{a}\epsilon\mathrm{x_{off}} + 2m_\mathrm{a}\mathrm{x_{off}^2} + \mathrm{I_{byy}} + 2\mathrm{I_{myy}}\right) + m_\mathrm{a}^2\epsilon^2\right)}\,. \tag{5.48}$$

The above system is for IMMAs with equal mass, m_a, at respective static vehicle b frame x axis offsets of x_off and $x_\text{off}+\epsilon$. MATLAB routines using the Symbolic Toolbox were developed

for linearization. Numerical **A** and **B** matrices were computed for estimates of γ, ρ, V_∞, $C_{m_{(q+\dot{\alpha})}}$, and $C_{n_{(r-\dot{\beta})}}$ at 4 design point altitudes of 53, 44, 33, and 22.5 km. Table 5.1 lists linearization parameter values based on design consideration of References [5] and [31] and a planar entry simulation for computing the numeric plant and control influence matrices.

The planar entry simulation was for a zero angle of attack trajectory for a vehicle with ballistic coefficient of 64 $\frac{\text{kg}}{\text{m}^2}$ using in-plane equations of motion of Chapter 7. The ballistic coefficient corresponds to both the reference entry capsule and HIAD vehicle. Accordingly, the flight path angle, density, entry speed estimates, and static moment coefficients at the design point altitudes are used in linearization of both the entry capsule and the HIADs. This simulation output is shown in Figure 5.1. The design point altitude distribution of 53km, 44km, 33km, and 22.5 km were chosen because the dynamic pressure change from one altitude to the next is approximately linear. Aerodynamic control moments using IMMA are proportionate to dynamic pressure. The strategy of tuning controllers at design altitudes at approximately linear and symmetric changes in dynamic pressure from the previous altitude was to help improve tracking performance versus tuning at altitudes with large nonlinear dynamic pressure changes. The specif focus was to improve tracking performance at altitudes between the design point altitudes where the feedback control gains are linearly interpolated between the feedback gains developed at design points above and below the current altitude. Data markers for design point altitudes and dynamic pressure values are shown in Figure 5.1.

Table 5.1: Linearization parameters for entry capsule with translation IMMA

Parameter	Value
p, q, r	$(0, 0, 0)$ rad/s
α, β	$(0, 0)$, rad
$\dot{\alpha}, \dot{\beta}$	$(0, 0)$ rad/s
ψ, ϕ	$(0, 0)$ $\frac{\pi}{180}$
g_{mars}	3.7 m/s^2
C_A, C_Y, C_N	$(1.7, 0.01, 0.03)$
D, S	2.65 m, 5.15 m^2
C_l, C_m, C_n, C_{lp}	$(0, 0, 0, 0)$
x_{off} , $x_{\text{off}} + \epsilon$.	-0.5,-0.627 m
$m_1 = m_2 = m_a, m_b$	40, 40, 552 kg
$mB = 522$kg	
Vehicle Moments of Inertia: $I_{bxx}, I_{byy}, I_{bzz}$	$(348.39, 226.14, 226.14)$ kg $\cdot$ m^2
IMMA Moments of Inertia: $I_{mxx}, I_{myy}, I_{mzz}$	$(0.182, 0.182, 0.182)$ kg $\cdot$ m^2
k_{m1}, k_{m2}, c_{m1}, c_{m2}	2000, 2000 $\frac{\text{N}}{\text{m}}$, 455, 455 $\frac{\text{N}}{\text{m/s}}$
Parameters at Specific Altitudes:	
ρ_{53}, ρ_{44}, ρ_{33}, $\rho_{22.5}$	(6.27e$-$5, 2.29e$-$4, 8.1e$-$4, 2.7e$-$3) kg/m^3
$\gamma_{53} = \theta_{53}$, $\gamma_{44} = \theta_{44}$, $\gamma_{33} = \theta_{33}$, $\gamma_{22.5} = \theta_{22.5}$	$(8.438, 7.84, 7.31, 8.86)$ deg
$V_{\infty\,53}, V_{\infty\,44}, V_{\infty\,33}, V_{\infty\,22.5}$	$(5.52, 5.2, 3.77, 1.49)$ km/s
$C_{m_{(q+\dot{\alpha})}\,53}, C_{m_{(q+\dot{\alpha})}\,44}, C_{m_{(q+\dot{\alpha})}\,33}, C_{m_{(q+\dot{\alpha})}\,22.5}$	$(-0.338, -0.338, -0.338, -0.1)$
$C_{n_{(r-\dot{\beta})}\,53}, C_{n_{(r-\dot{\beta})}\,44}, C_{n_{(r-\dot{\beta})}\,33}, C_{n_{(r-\dot{\beta})}\,22.5}$	$(-0.338, -0.338, -0.338, -0.1)$

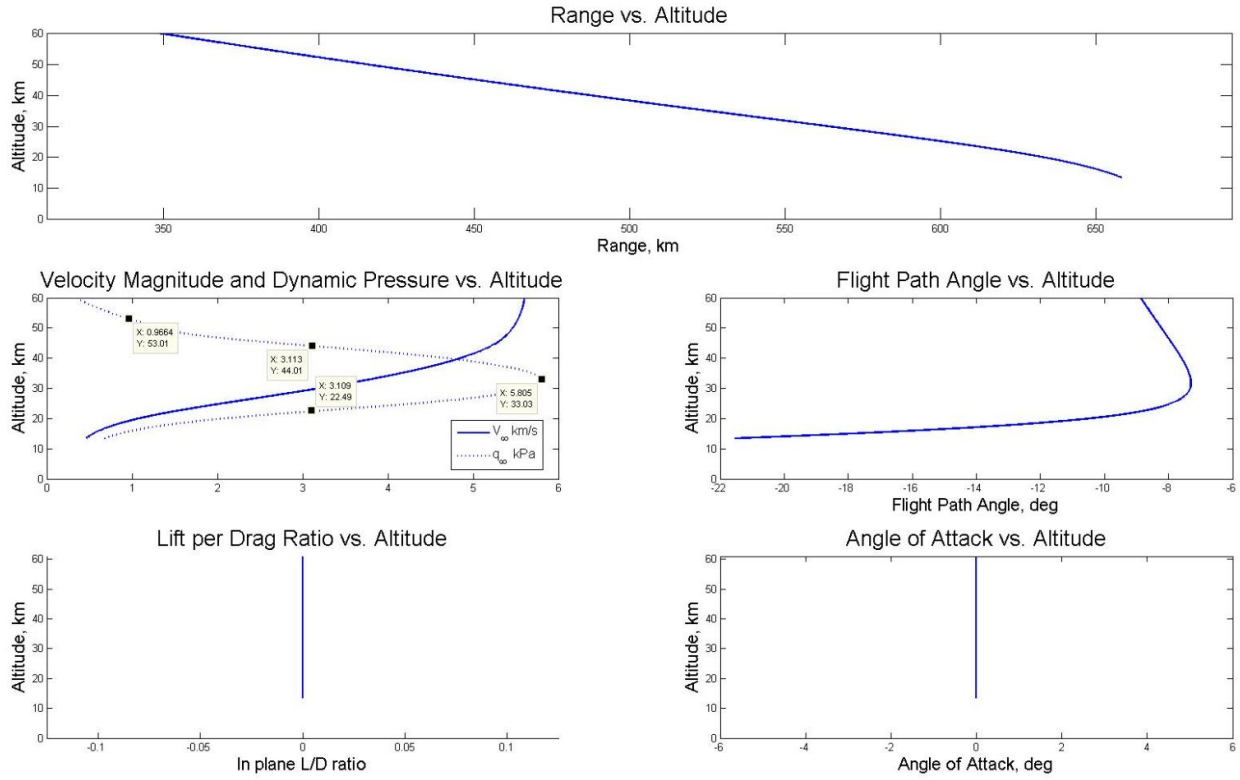

Figure 5.1: Planar entry simulation: speed, density, and flight path angle, versus altitude for numeric plant and control influence matrices for vehicles with $\beta = \frac{64\,\mathrm{kg}}{\mathrm{m}^2}$

5.4 Linearization of HIAD With Translation IMMA

5.4.1 Actuator Equations

For the HIAD with translation IMMA, notional actuator models similar to the IMMA entry capsule system were used for prescribed IMMA acceleration:

$$\ddot{y}_{b,ts} = \frac{1}{\mu}\left(\mathrm{F}_{y\,ts} - c_1\dot{y}_{b,ts}\right) \tag{5.49}$$

$$\ddot{z}_{b,ts} = \frac{1}{\mu}\left(\mathrm{F}_{z\,ts} - c_2\dot{z}_{b,ts}\right) \tag{5.50}$$

where:

$$\mu = \frac{m_{ts}m_b}{m_{ts}+m_b}\,. \tag{5.51}$$

Control inputs are actuator force inputs, $F_{y\,ts}$ and $F_{z\,ts}$, relative to the fixed vehicle frame. No spring stiffness was modeled. The IMMA actuator geometric constraint equations and composite vehicle attitude equations developed in Chapter 2 Section 1 were implemented

in the nonlinear simulations to fully account for the dynamics of the IMMA for the entry vehicle attitude using the prescribed IMMA acceleration. In Chapter 11, mechanical power models are developed for computation of the actual constraint forces acting on the IMMA and the required mechanical power to meet the prescribed IMMA motion.

5.4.2 Linearization With Translation IMMA

The state and control input vectors for the translation IMMA HIAD system are:

$$\mathbf{x} = \begin{pmatrix} r & q & \psi & \theta & \alpha & \beta & y_{ts} & \dot{y}_{ts} & z_{ts} & \dot{z}_{ts} \end{pmatrix}^T \tag{5.52}$$

$$\mathbf{u} = \begin{pmatrix} \mathrm{F}_{y\,ts} & \mathrm{F}_{z\,ts} \end{pmatrix}^T . \tag{5.53}$$

The nonlinear system:

$$\dot{\mathbf{x}} = \mathbf{f}\left(\mathbf{x}, \mathbf{u}\right) \tag{5.54}$$

is linearized about the equilibrium:

$$\mathbf{x}_{\mathrm{eq}} = \begin{pmatrix} 0 & 0 & 0 & \gamma & 0 & 0 & 0 & 0 & 0 & 0 \end{pmatrix}^T \tag{5.55}$$

$$\mathbf{u}_{\mathrm{eq}} = \begin{pmatrix} 0 & 0 \end{pmatrix}^T \tag{5.56}$$

to form the linear system:

$$\dot{\mathbf{x}} = \mathbf{A}\mathbf{x} + \mathbf{B}\mathbf{u}\,. \tag{5.57}$$

The plant and control influence matrices:

$$\mathbf{A} = \frac{\partial \mathbf{f}}{\partial \mathbf{x}}_{|_{(\mathbf{x}_{\mathrm{eq}}, \mathbf{u}_{\mathrm{eq}})}} \quad \mathbf{B} = \frac{\partial \mathbf{f}}{\partial \mathbf{u}}_{|_{(\mathbf{x}_{\mathrm{eq}}, \mathbf{u}_{\mathrm{eq}})}} \tag{5.58}$$

are:

$$\mathbf{A} = \begin{bmatrix} A_{11} & 0 & 0 & 0 & 0 & 0 & A_{17} & 0 & 0 & 0 \\ 0 & A_{22} & 0 & 0 & 0 & 0 & 0 & 0 & A_{29} & 0 \\ \frac{1}{\cos\gamma} & 0 & 0 & 0 & 0 & 0 & 0 & 0 & 0 & 0 \\ 0 & 1 & 0 & 0 & 0 & 0 & 0 & 0 & 0 & 0 \\ 0 & 1 & 0 & \frac{-g_{\mathrm{mars}}\sin\gamma}{V_\infty} & A_{55} & 0 & 0 & 0 & 0 & 0 \\ -1 & 0 & 0 & 0 & 0 & A_{66} & 0 & 0 & 0 & 0 \\ 0 & 0 & 0 & 0 & 0 & 0 & 0 & 1 & 0 & 0 \\ 0 & 0 & 0 & 0 & 0 & 0 & 0 & \frac{c_1}{\mu} & 0 & 0 \\ 0 & 0 & 0 & 0 & 0 & 0 & 0 & 0 & 0 & 1 \\ 0 & 0 & 0 & 0 & 0 & 0 & 0 & 0 & 0 & \frac{c_2}{\mu} \end{bmatrix} \tag{5.59}$$

$$\mathbf{B} = \begin{bmatrix} 0 & 0 \\ 0 & 0 \\ 0 & 0 \\ 0 & 0 \\ 0 & 0 \\ 0 & 0 \\ 0 & 0 \\ \frac{1}{\mu} & 0 \\ 0 & 0 \\ 0 & \frac{1}{\mu} \end{bmatrix} \tag{5.60}$$

where:

$$A_{11} = \frac{C_{n(r-\dot{\beta})} D^2 S q_\infty M_T}{4V_\infty \left(m_b m_{ts}\, \mathrm{x}_{\mathrm{off}}^2 + M_T \left(\mathrm{I}_{\mathrm{bzz}} + \mathrm{I}_{\mathrm{ts\,zz}}\right)\right)} \tag{5.61}$$

$$A_{22} = \frac{C_{m(q+\dot{\alpha})} D^2 S q_\infty}{4V_\infty \left(m_b m_{ts}\, \mathrm{x}_{\mathrm{off}}^2 + M_T \left(\mathrm{I}_{\mathrm{byy}} + \mathrm{I}_{\mathrm{ts\,yy}}\right)\right)} \tag{5.62}$$

$$A_{55} = \frac{M_T g_{\mathrm{mars}} \sin(\gamma) + C_A S q_\infty}{M_T V_\infty} \tag{5.63}$$

$$A_{66} = \frac{M_T g_{\mathrm{mars}} \sin(\gamma) + C_A S q_\infty}{M_T V_\infty} \tag{5.64}$$

$$A_{17} = \frac{-m_{\mathrm{ts}} C_A S\, q_\infty}{\left(M_T(\mathrm{I}_{\mathrm{bzz}} + 2\mathrm{I}_{\mathrm{ts\,zz}}) + m_{ts} m_b \mathrm{x}_{\mathrm{off}}^2\right)} \tag{5.65}$$

$$A_{29} = \frac{m_{\mathrm{a}} C_A S q_\infty}{\left(M_T(\mathrm{I}_{\mathrm{byy}} + 2\mathrm{I}_{\mathrm{ts\,yy}}) + m_{ts} m_b \mathrm{x}_{\mathrm{off}}^2\right)}\,. \tag{5.66}$$

MATLAB routines using the Symbolic Toolbox were developed for linearization. Numerical **A** and **B** matrices were computed for estimates of ρ, γ, V_∞, $C_{m_{(q+\dot{\alpha})}}$, and $C_{n_{(r-\dot{\beta})}}$ at 4 design point altitudes of 53, 44, 33, and 22.5 km. Table 5.3 list values based on design consideration of References 5 and 31 and from reference velocity, flight path angle, and density values from the ballistic, zero angle of attack simulation of Figure 5.1.

Table 5.2: Linearization parameters for HIAD with translation IMMA

Parameter	Value
p, q, r	$(0, 0, 0)$ rad/s
α, β	$(0, 0)$, rad
$\dot{\alpha}, \dot{\beta}$	$(0, 0)$ rad/s
ψ, ϕ	$(0, 0)$ $\frac{\pi}{180}$
g_{mars}	3.7 m/s^2
C_A, C_Y, C_N	$(1.7, 0.01, 0.03)$
C_l, C_m, C_n, C_{lp}	$(0, 0, 0, 0)$
Static $\underline{x}_b$ axis offset of top structure center of mass from vehicle frame: x_{off}	-3.4919 m
m_{ts}	750 kg
m_b	5150 kg
μ	654 kg
Axial, aerodynamic reference point from aeroshell nose: r_{arp}	-0.253·D, m
Null offset of vehicle frame, b, from CM frame, c : $r_{c,b}$	0.441, m
D, S	8.3 m, 54.1 m^2
Vehicle Frame Moments of Inertia: $I_{bxx}, I_{byy}, I_{bzz}$	$(1.116, 1.062, 1.062)$e4 kg $\cdot$ m^2
IMMA Moments of Inertia: $I_{tsxx}, I_{tsyy}, I_{tszz}$	$(1.033, 657.3, 657.3)$e3 kg $\cdot$ m^2
c_1, c_2	5.8919e3, 5.8919e3 $\frac{\text{N}}{m/s}$
Parameters at Specific Altitudes:	
ρ_{53}, ρ_{44}, ρ_{33}, $\rho_{22.5}$	(6.27e−5, 2.29e−4, 8.1e−4, 2.7e−3) kg/m^3
$\gamma_{53} = \theta_{53}$, $\gamma_{44} = \theta_{44}$, $\gamma_{33} = \theta_{33}$, $\gamma_{22.5} = \theta_{22.5}$	$(8.438, 7.84, 7.31, 8.86)$ $\frac{\pi}{180}$
$V_{\infty\,53}, V_{\infty\,44}, V_{\infty\,33}, V_{\infty\,22.5}$	$(5.52, 5.2, 3.77, 1.49)$ km/s
$C_{m_{(q+\dot{\alpha})\,53}}, C_{m_{(q+\dot{\alpha})\,44}}, C_{m_{(q+\dot{\alpha})\,33}}, C_{m_{(q+\dot{\alpha})\,22.5}}$	$(-0.338, -0.338, -0.338, -0.1)$
$C_{n_{(r-\dot{\beta})\,53}}, C_{n_{(r-\dot{\beta})\,44}}, C_{n_{(r-\dot{\beta})\,33}}, C_{n_{(r-\dot{\beta})\,22.5}}$	$(-0.338, -0.338, -0.338, -0.1)$

5.5 Linearization of HIAD With Rotation IMMA

5.5.1 Actuator Equations

For the HIAD with rotation IMMA, notional actuator models were used for prescribed IMMA angular acceleration:

$$\dot{\boldsymbol{\omega}}_{b,ts}^{m_{ts}} = \mathbf{I}_{ts}^{-1}\mathbf{R}_{b}^{m_{ts}}\tau_{b,ts} \tag{5.67}$$

for control torque inputs :

$$\tau_{b,ts} = \begin{pmatrix} 0 & \tau_{b,a1} & \tau_{b,a2} \end{pmatrix}^{T} . \tag{5.68}$$

No actuator damping or stiffness was modeled for the notional equations. The IMMA actuator geometric constraint equations and composite vehicle attitude equations developed in Chapter 2 were implemented in the nonlinear simulations to fully account for the dynamics of the IMMA for the entry vehicle attitude using the prescribed IMMA angular acceleration. In Chapter 11 mechanical power models are presented and used for computation of the actual constraint torques acting on the IMMA and the required mechanical power to meet the prescribed IMMA motion.

Equation 5.67 implements a 3-2 yaw pitch rotation sequence to map control torques from the fixed vehicle frame at b to the top structure IMMA center of mass frame:

$$\mathbf{R}_{b}^{m_{ts}} = \begin{bmatrix} c\theta_{a2}c\theta_{a1} & c\theta_{a2}s\theta_{a1} & -s\theta_{a2} \\ -s\theta_{a1} & c\theta_{a1} & 0 \\ s\theta_{a2}c\theta_{a1} & s\theta_{a2}s\theta_{a1} & c\theta_{a2} \end{bmatrix} . \tag{5.69}$$

This is for the two degree of freedom ring actuator rotation mechanism presented in Chapter 4. Roll of the top structure relative to the vehicle frame is treated as zero. The spherical joint is modeled as having 2 degrees of freedom only, pitch and yaw relative to the vehicle frame.

5.5.2 Linearization With Rotation IMMA

The state and control input vectors for the rotation IMMA HIAD system are:

$$\mathbf{x} = \begin{pmatrix} r & q & \psi & \theta & \alpha & \beta & r_{b,ts} & q_{b,ts} & \theta_{a1\,ts} & \theta_{a2\,ts} \end{pmatrix}^{T} \tag{5.70}$$

$$\mathbf{u} = \begin{pmatrix} \tau_{b,a1} & \tau_{b,a2} \end{pmatrix}^{T} . \tag{5.71}$$

The nonlinear system:

$$\dot{\mathbf{x}} = \mathbf{f}\left(\mathbf{x}, \mathbf{u}\right) \tag{5.72}$$

is linearized about the equilibrium:

$$\mathbf{x}_{\text{eq}} = \begin{pmatrix} 0 & 0 & 0 & \gamma & 0 & 0 & 0 & 0 & 0 & 0 \end{pmatrix}^{T} \tag{5.73}$$

$$\mathbf{u}_{\text{eq}} = \begin{pmatrix} 0 & 0 \end{pmatrix}^{T} \tag{5.74}$$

to form the linear system:

$$\dot{\mathbf{x}} = \mathbf{A}\mathbf{x} + \mathbf{B}\mathbf{u}\,. \tag{5.75}$$

The plant and control influence matrices:

$$\mathbf{A} = \frac{\partial \mathbf{f}}{\partial \mathbf{x}}_{|_{(\mathbf{x}_{\rm eq},\mathbf{u}_{\rm eq})}} \quad \mathbf{B} = \frac{\partial \mathbf{f}}{\partial \mathbf{u}}_{|_{(\mathbf{x}_{\rm eq},\mathbf{u}_{\rm eq})}} \tag{5.76}$$

are:

$$\mathbf{A} = \begin{bmatrix} A_{11} & 0 & 0 & 0 & 0 & 0 & 0 & 0 & A_{19} & 0 \\ 0 & A_{22} & 0 & 0 & 0 & 0 & 0 & 0 & 0 & A_{2\,10} \\ \frac{1}{\cos\gamma} & 0 & 0 & 0 & 0 & 0 & 0 & 0 & 0 & 0 \\ 0 & 1 & 0 & 0 & 0 & 0 & 0 & 0 & 0 & 0 \\ 0 & 1 & 0 & \frac{-g_{\rm mars}\sin\gamma}{V_\infty} & A_{55} & 0 & 0 & 0 & 0 & 0 \\ -1 & 0 & 0 & 0 & 0 & A_{66} & 0 & 0 & 0 & 0 \\ 0 & 0 & 0 & 0 & 0 & 0 & 0 & 0 & 0 & 0 \\ 0 & 0 & 0 & 0 & 0 & 0 & 0 & 0 & 0 & 0 \\ 0 & 0 & 0 & 0 & 0 & 0 & 1 & 0 & 0 & 0 \\ 0 & 0 & 0 & 0 & 0 & 0 & 0 & 1 & 0 & 0 \end{bmatrix} \tag{5.77}$$

$$\mathbf{B} = \begin{bmatrix} 0 & 0 \\ 0 & 0 \\ 0 & 0 \\ 0 & 0 \\ 0 & 0 \\ 0 & 0 \\ \frac{1}{m_{ts}l_{cm}^2 + I_{ts\,zz}} & 0 \\ 0 & \frac{1}{m_{ts}l_{cm}^2 + I_{ts\,yy}} \\ 0 & 0 \\ 0 & 0 \end{bmatrix} \tag{5.78}$$

where:

$$A_{11} = \frac{C_{n(r-\dot{\beta})} D^2 S q_\infty M_T}{4V_\infty \left(m_b m_{ts}\left(l_{cm}^2 + 2\mathrm{l_{cm}x_{off}} + \mathrm{x_{off}^2}\right) + M_T\left(\mathrm{I_{bzz}} + \mathrm{I_{ts\,zz}}\right)\right)} \tag{5.79}$$

$$A_{22} = \frac{C_{m(q+\dot{\alpha})} D^2 S q_\infty}{4V_\infty \left(m_b m_{ts}\left(l_{cm}^2 + 2\mathrm{l_{cm}x_{off}} + \mathrm{x_{off}^2}\right) + M_T\left(\mathrm{I_{bzz}} + \mathrm{I_{ts\,zz}}\right)\right)} \tag{5.80}$$

$$A_{55} = \frac{M_T g_{\rm mars}\sin(\gamma) + C_A S q_\infty}{M_T V_\infty} \tag{5.81}$$

$$A_{66} = \frac{M_T g_{\rm mars}\sin(\gamma) + C_A S q_\infty}{M_T V_\infty} \tag{5.82}$$

$$A_{19} = \frac{m_{\rm ts} C_A l_{cm} q_\infty}{\left(m_b m_{ts}\left(l_{cm}^2 + 2\mathrm{l_{cm}x_{off}} + \mathrm{x_{off}^2}\right) + M_T\left(\mathrm{I_{bzz}} + \mathrm{I_{ts\,zz}}\right)\right)} \tag{5.83}$$

$$A_{2\,10} = \frac{m_{\rm ts} C_A l_{cm} q_\infty}{\left(m_b m_{ts}\left(l_{cm}^2 + 2\mathrm{l_{cm}x_{off}} + \mathrm{x_{off}^2}\right) + M_T\left(\mathrm{I_{bzz}} + \mathrm{I_{ts\,zz}}\right)\right)}\,. \tag{5.84}$$

MATLAB routines using the Symbolic Toolbox were developed for linearization. Numerical **A** and **B** matrices were computed for estimates of ρ, γ, V_∞, $C_{m_{(q+\dot{\alpha})}}$, and $C_{n_{(r-\dot{\beta})}}$ at 4 design point altitudes of 53, 44, 33, and 22.5 km. Table 5.3 list values based on design consideration of References 5 and 31 and from the ballistic, zero angle of attack simulation.

Table 5.3: Linearization parameters for HIAD with rotation IMMA

Parameter	Value
p, q, r	$(0, 0, 0)$ rad/s
α, β	$(0, 0)$, rad
$\dot{\alpha}, \dot{\beta}$	$(0, 0)$ rad/s
ψ, ϕ	$(0, 0)$ $\frac{\pi}{180}$
g_{mars}	3.7 m/s^2
C_A, C_Y, C_N	$(1.7, 0.01, 0.03)$
C_l, C_m, C_n, C_{lp}	$(0, 0, 0, 0)$
Static $\underline{x}_b$ axis offset of top structure actuator rotation point from vehicle frame: x_{off}	-1.7417 m
Distance from Top Structure $\underline{x}_{ts}$ CM location to its actuator rotation point	1.75 m
m_{ts}	750 kg
m_b	5150 kg
Axial, aerodynamic reference point from aeroshell nose: r_{arp}	-0.253·D, m
Null offset of vehicle frame, b, from CM frame, c : $r_{c,b}$	0.441, m
D, S	8.3 m, 54.1 m^2
Vehicle Frame Moments of Inertia : $I_{bxx}, I_{byy}, I_{bzz}$	$(1.116, 1.062, 1.062)$e4 kg $\cdot$ m^2
IMMA Moments of Inertia : $I_{tsxx}, I_{tsyy}, I_{tszz}$	$(1.033, 657.3, 657.3)$e3 kg $\cdot$ m^2
Parameters at Specific Altitudes :	
ρ_{53}, ρ_{44}, ρ_{33}, $\rho_{22.5}$	(6.27e−5, 2.29e−4, 8.1e−4, 2.7e−3) kg/m^3
$\gamma_{53} = \theta_{53}$, $\gamma_{44} = \theta_{44}$, $\gamma_{33} = \theta_{33}$, $\gamma_{22.5} = \theta_{22.5}$	$(8.438, 7.84, 7.31, 8.86)$ $\frac{\pi}{180}$
$V_{\infty\,53}, V_{\infty\,44}, V_{\infty\,33}, V_{\infty\,22.5}$	$(5.52, 5.2, 3.77, 1.49)$km/s
$C_{m_{(q+\dot{\alpha})}\,53}, C_{m_{(q+\dot{\alpha})}\,44}, C_{m_{(q+\dot{\alpha})}\,33}, C_{m_{(q+\dot{\alpha})}\,22.5}$	$(-0.338, -0.338, -0.338, -0.1)$
$C_{n_{(r-\dot{\beta})}\,53}, C_{n_{(r-\dot{\beta})}\,44}, C_{n_{(r-\dot{\beta})}\,33}, C_{n_{(r-\dot{\beta})}\,22.5}$	$(-0.338, -0.338, -0.338, -0.1)$

Chapter 6

Linear Quadratic Integral Controllers For Angle of Attack and Sideslip Command Tracking

6.1 Structure of Linear Quadratic Integral Controllers for Capsules and HIADs

Linear Time Invariant (LTI), Linear Quadratic (LQ) controllers were developed to track desired angle of attack and sideslip reference commands:

$$\mathbf{r} = \begin{pmatrix} \alpha_d & \beta_d \end{pmatrix}^T \tag{6.1}$$

with integral error and proportional error feedback. Differences between the final feedback control law form for the entry capsule and HIAD vehicles primarily consist in the IMMA actuator states and static vehicle mass and inertia parameters,see Chapter 5. However, all vehicles share the same general common structure and objective for angle of attack and sideslip command tracking, described below.

First, each linear system is appended with the integral error vector $\mathbf{x}_I$:

$$\begin{aligned} \dot{\mathbf{x}}_I &= \mathbf{e} && (6.2)\\ &= \mathbf{r} - \mathbf{y}. && (6.3) \end{aligned}$$

with corresponding output equation :

$$\begin{aligned} \mathbf{y} &= \mathbf{C}\mathbf{x} && (6.4)\\ &= (\alpha\ \beta)^T && (6.5) \end{aligned}$$

to form new closed-loop systems with form:

$$\begin{bmatrix} \dot{\mathbf{x}} \\ \dot{\mathbf{x}}_\mathbf{I} \end{bmatrix} = \begin{bmatrix} \mathbf{A} & \mathbf{0} \\ -\mathbf{C} & \mathbf{0} \end{bmatrix} \begin{bmatrix} \mathbf{x} \\ \mathbf{x}_I \end{bmatrix} + \begin{bmatrix} \mathbf{B} \\ \mathbf{0} \end{bmatrix} \mathbf{u} + \begin{bmatrix} \mathbf{0} \\ \mathbf{I} \end{bmatrix} \mathbf{r}\,. \tag{6.6}$$

Next, the stabilizing feedback and integral error gains $\mathbf{K}$ and $\mathbf{K}_I$ are found for the optimal feedback control law [32]:

$$\begin{aligned} \mathbf{u} &= -\mathbf{R}_{\mathbf{uu}}^{-1}\mathbf{B}^T\bar{\mathbf{P}}\hat{\mathbf{x}} && (6.7)\\ &= -\begin{bmatrix} \mathbf{K} & \mathbf{K}_I \end{bmatrix} \begin{bmatrix} \mathbf{x} \\ \mathbf{x}_I \end{bmatrix} && (6.8) \end{aligned}$$

for Performance Index:

$$J = \int_0^\infty \left[\hat{\mathbf{x}}\mathbf{R}_{xx}\hat{\mathbf{x}} + \mathbf{u}^T\mathbf{R}_{uu}\mathbf{u}\right] dt \tag{6.9}$$

and $\mathbf{r} = \mathbf{0}$. $\bar{\mathbf{P}}$ in Eq. (6.7) is the unique positive definite solution to the Algebraic Riccati equation [32] :

$$\mathbf{P}\hat{\mathbf{A}} + \hat{\mathbf{A}}^T\mathbf{P} - \mathbf{P}\hat{\mathbf{B}}\mathbf{R}_{uu}^{-1}\hat{\mathbf{B}}^T\mathbf{P} + \mathbf{R}_{xx} = \mathbf{0}\,. \tag{6.10}$$

Note, $\hat{\mathbf{A}}$ and $\hat{\mathbf{B}}$ from Eq. (6.6) are :

$$\hat{\mathbf{A}} = \begin{bmatrix} \mathbf{A} & \mathbf{0} \\ -\mathbf{C} & \mathbf{0} \end{bmatrix} \quad \hat{\mathbf{B}} = \begin{bmatrix} \mathbf{B} \\ \mathbf{0} \end{bmatrix}\,. \tag{6.11}$$

$\mathbf{R}_{xx}$ and $\mathbf{R}_{uu}$ are the respective state and control weighting matrices. For each LTI controller, $\left(\hat{\mathbf{A}}, \hat{\mathbf{B}}\right)$ was stabilizable and $\left(\hat{\mathbf{A}}, \hat{\mathbf{C}}\right)$ for $\mathbf{R}_{xx} = \hat{\mathbf{C}}^T\hat{\mathbf{C}}$ was observable ensuring detectability and together that $\bar{\mathbf{P}}$ was the unique positive definite solution to the respective Algebraic Riccati equation. Stabilizability was checked by applying the Popov-Belevitch-Hautus eigenvector test and verifying unstable modes were controllable. Observability was checked by verifying all observability matrices were full rank.

To improve tracking performance through error feedback, feedforward term:

$$\mathbf{R} = -\sigma\mathbf{C}^T\mathbf{r} \tag{6.12}$$

with $\sigma < 1$ is added to the control law:

$$\mathbf{u} = -\mathbf{K}\left(\mathbf{x} + \mathbf{R}\mathbf{r}\right) - \mathbf{K}_I\mathbf{x}_I\,. \tag{6.13}$$

The final form of the closed loop system is:

$$\begin{bmatrix} \dot{\mathbf{x}} \\ \dot{\mathbf{x}}_\mathbf{I} \end{bmatrix} = \begin{bmatrix} \mathbf{A} & -\mathbf{B}\mathbf{K}_I \\ -\mathbf{C} & \mathbf{0} \end{bmatrix} \begin{bmatrix} \mathbf{x} \\ \mathbf{x}_I \end{bmatrix} + \begin{bmatrix} -\mathbf{B}\mathbf{K}\mathbf{R} \\ \mathbf{I} \end{bmatrix} \mathbf{r}\,. \tag{6.14}$$

6.2 Capsule With Translation IMMA: Linear Quadratic Integral Control Tuning

The state and control weighting matrices used in computation of $\bar{\mathbf{P}}$ for the capsule translation IMMA system at the design altitudes have structure:

$$\begin{aligned}\mathbf{R}_{xx} &= \text{diag}\left[\frac{15}{r^2_{\max}}, \frac{15}{q^2_{\max}}, \frac{1}{\psi^2_{\max}}, \frac{1}{\theta^2_{\max}}, \frac{1}{\alpha^2_{\max}}, \frac{1}{\beta^2_{\max}} \ldots\right. \\ &\quad \left.\frac{1}{y^2_{b,m1\,\max}}, \frac{1}{\dot{y}^2_{b,m1\,\max}}, \frac{1}{z^2_{b,m2\,\max}}, \frac{1}{\dot{z}^2_{b,m2\,\max}}, \frac{r_{x11}}{(\int \alpha_{\max})^2}, \frac{r_{x12}}{(\int \beta_{\max})^2}\right] \qquad (6.15)\\ \mathbf{R}_{uu} &= \text{diag}\left[\frac{r_{u1}}{y^2_{b,m1\,\max}}, \frac{r_{u2}}{z^2_{b,m2\,\max}}\right]. \qquad (6.16)\end{aligned}$$

Table 6.1 lists the specific gain normalization parameters for $\mathbf{R}_{xx}$ and $\mathbf{R}_{uu}$. The gains r_{x11}, r_{x12}, r_{u11}, and r_{u12} were tuned through step response analysis and design point simulations. Step reference commands for the linear closed-loop system for each design altitude were generated to determine reference command following response time, overshoot, and amount of coupling of the system. Figure 6.1 provides step response for selection of gains at 44 km altitude. It is clear that that the linear system is decoupled and angle of attack and sideslip commands are followable for the linear system.

Design point simulations consisted of simulation of the capsule with translation IMMA nonlinear system including roll dynamics with the feedback controller tracking reference commands. In design point simulations dynamic pressure, q_∞, was kept constant and the initial attitude and entry conditions were chosen from a reference ballistic entry simulation. In design point simulations the local horizontal was treated as fixed, no latitude rotation rate between the inertial frame and local horizontal frame. Gains were adjusted until tracking occurred without large overshoots, without large CM angular velocity rates, and without actuator displacements beyond track limits of 20 inches. This displacement restriction was chosen from consideration of the diameter of the Mars Phoenix aeroshell. Figure 6.2 shows tracking performance, Euler angles, and CM location for gains chosen at the 44 km design point altitude.

IMMA velocity oscillation occurred at times corresponding to peak error in guidance command tracking in the design point simulation for 44 km altitude. This can be partially explained due to the vehicle pitch and yaw angular velocity and Euler angle feedback control gains having approximate magnitude as the integral error angle of attack and sideslip gains. The comparable magnitude sized gains follow from the linearized angle of attack and sideslip rate equations being proportional to vehicle pitch and yaw angular velocity. In order to produce command tracking the integral error states were heavily penalized leading to gains of nearly the same magnitude. The comparable magnitude gains can lead to counteractive feedback control forces applied to the IMMA. At peak guidance command tracking error, the integral and proportional error portions of the feedback controller call for increasing IMMA

force to lower tracking error which increases pitch and yaw rates. This leads to the feedback controller also attempting to quell large pitch and yaw angular velocity leading to counter-active IMMA control force reversals, thereby driving error back up. After a few cycles the IMMA velocity oscillations tend to dampen out as command tracking error dampens out.

As guidance command tracking errors increase due to changing reference commands, the integral and proportional error portions of the feedback controller tend to dominate the pitch and yaw angular velocity counter-active quelling control forces. In general the design point simulations were designed to be more taxing than the expected guidance commands to track the nominal reference trajectory. The nominal reference trajectory is described in Chapter 7 and corresponds to constant angle of attack at -3 degrees and constant sideslip angle at 0 degrees. In Chapter 9, full nonlinear guidance simulations with the feedback linear controllers at nominal entry conditions except angle of attack attitude, Guided trajectory G1, there is negligible IMMA oscillation. In the full nonlinear guidance simulations the feedback gains are linearly interpolated by altitude between the design point altitude gains. Figure 6.3 shows gains versus altitude at the design points with linear interpolation between the design point altitudes.

Table 6.1: $\mathbf{R}_{xx}$ and $\mathbf{R}_{uu}$ gain normalization parameters for capsule with translation IMMA

Parameter	Value
$r_{\max}$	$\frac{5\pi}{180}$ $\frac{\text{rad}}{s}$
$q_{\max}$	$\frac{5\pi}{180}$ $\frac{\text{rad}}{s}$
$\psi_{\max}$	$\frac{25\pi}{180}$ rad
$\theta_{\max}$	$\frac{25\pi}{180}$ rad
$\alpha_{\max}$	$\frac{15\pi}{180}$ rad
$\beta_{\max}$	$\frac{15\pi}{180}$ rad
$y_{b,m1\,\max}$	$\frac{10}{39}$ m
$\dot{y}_{b,m1\,\max}$	$\frac{2}{39}$ $\frac{\text{m}}{s}$
$z_{b,m2\,\max}$	$\frac{10}{39}$ m
$\dot{z}_{b,m2\,\max}$	$\frac{2}{39}$ $\frac{\text{m}}{s}$
$\int \alpha_{\max}$	$\frac{\pi}{180}$ rad $\cdot$ s
$\int \beta_{\max}$	$\frac{\pi}{180}$ rad $\cdot$ s

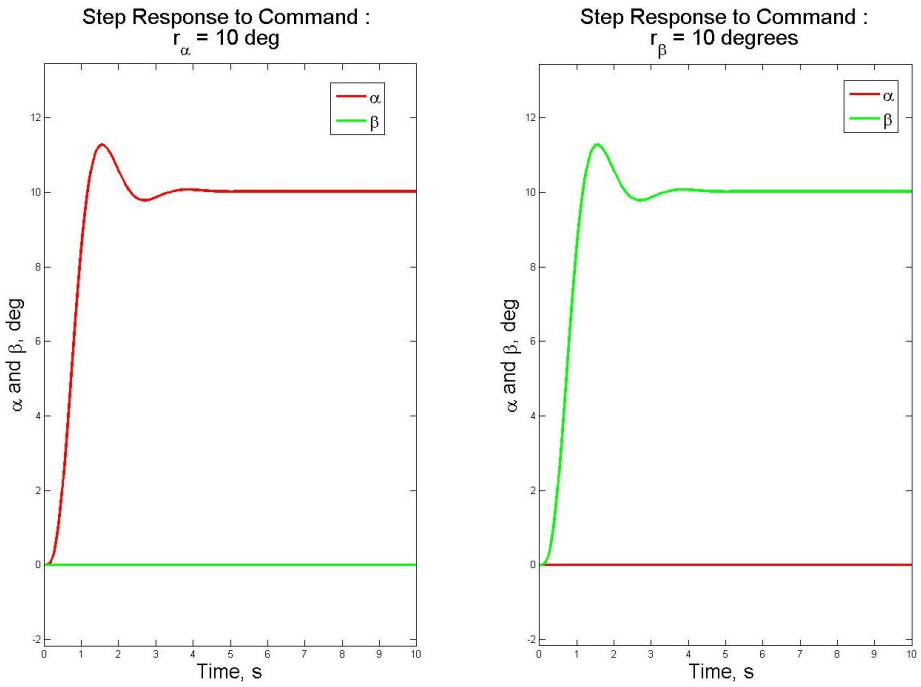

Figure 6.1: Step responses at 44 km altitude

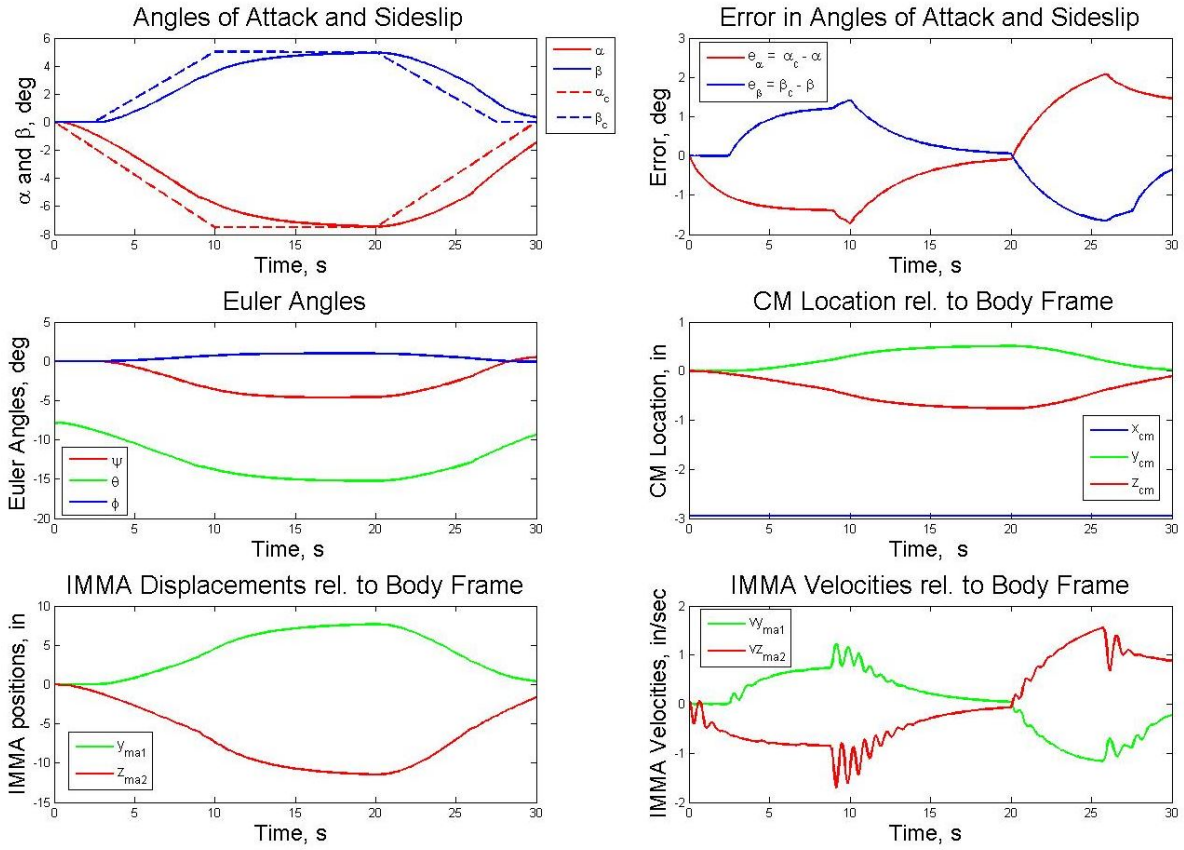

Figure 6.2: Design point simulation: tracking performance at 44 km altitude

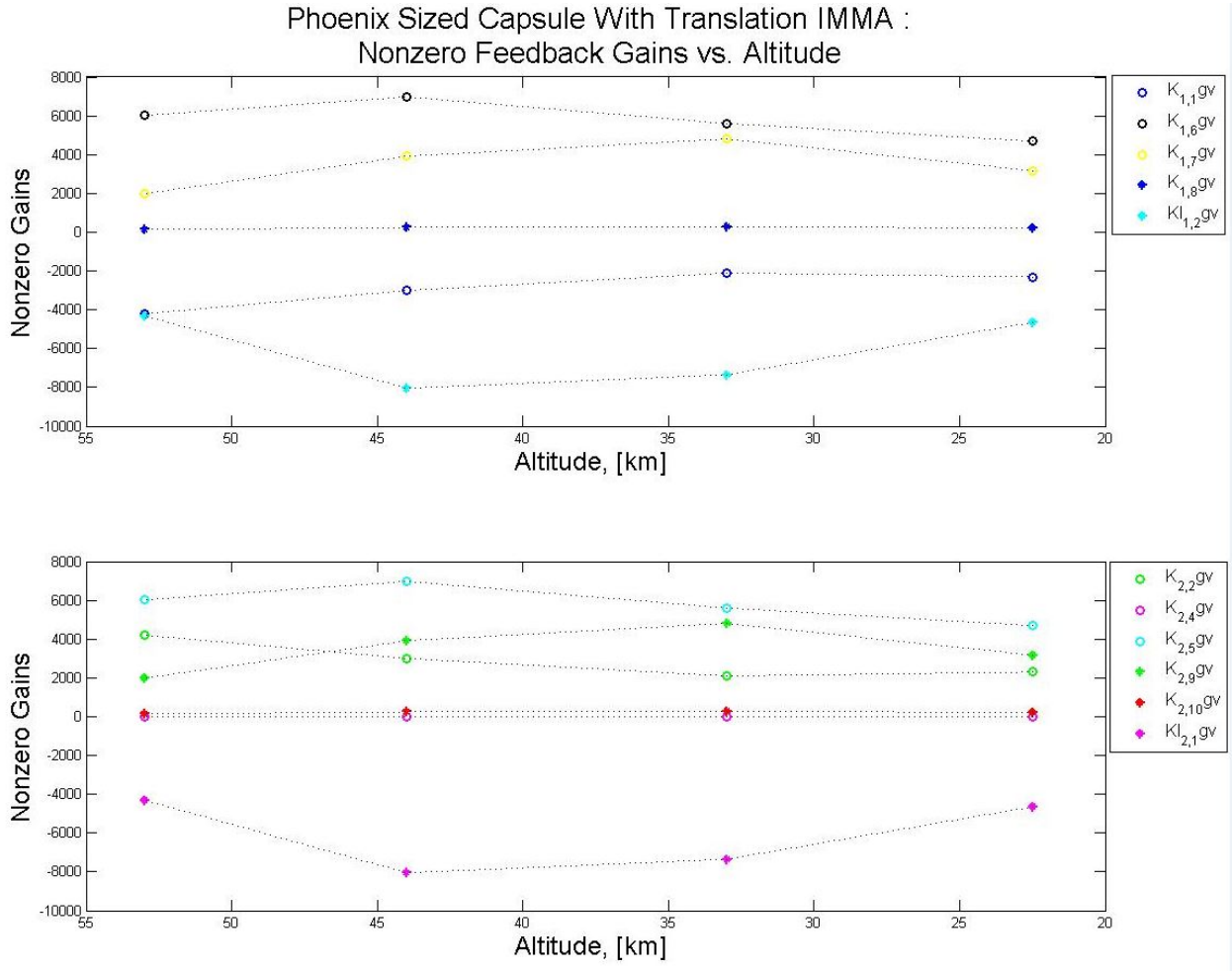

Figure 6.3: Feedback gains vs. altitude with linear interpolation between design points

6.3 HIAD with Translation IMMA: Linear Quadratic Integral Control Tuning

The state and control weighting matrices used in computing $\bar{\mathbf{P}}$ for the translation IMMA HIAD system at the design altitudes have structure:

$$\begin{aligned}\mathbf{R}_{xx} &= \text{diag}\Big[\frac{15}{r^2_{\max}}, \frac{15}{q^2_{\max}}, \frac{1}{\psi^2_{\max}}, \frac{1}{\theta^2_{\max}}, \frac{1}{\alpha^2_{\max}}, \frac{1}{\beta^2_{\max}} \ \ldots \\ &\qquad \frac{1}{y^2_{ts,m1\,\max}}, \frac{1}{\dot{y}^2_{ts,m1\,\max}}, \frac{1}{z^2_{ts,m2\,\max}}, \frac{1}{\dot{z}^2_{ts,m2\,\max}}, \frac{r_{x11}}{(\int \alpha_{\max})^2}, \frac{r_{x12}}{(\int \beta_{\max})^2}\Big] \qquad (6.17)\\ \mathbf{R}_{uu} &= \text{diag}\Big[\frac{r_{u1}}{y^2_{ts,m1\,\max}}, \frac{r_{u2}}{z^2_{ts,m2\,\max}}\Big]. \qquad (6.18)\end{aligned}$$

Table 6.2 lists the specific gain normalization parameters for $\mathbf{R}_{xx}$ and $\mathbf{R}_{uu}$. Following the same tuning process as the capsule vehicle, gains were tuned through step response analysis and nonlinear design point simulations. Step reference command response plots for the linear closed-loop system for the HIAD with translation IMMA with respective plant and control influence matrices at each design altitude were generated to determine reference command following response time, overshoot, and amount of coupling of the system. Figure 6.4 shows step response for selection of gains at 44 km altitude. Like the capsule IMMA translation system, the HIAD with translation IMMA configuration was chosen for a similar CM displacement strategy for angle of attack and angle of sideslip tracking. As expected, the linear system is also decoupled and angle of attack and sideslip commands are followable for the linear system.

Design point simulations consisted of simulating of the HIAD with translation IMMA nonlinear system including roll dynamics with the feedback controller tracking reference commands. In design point simulations dynamic pressure, q_∞, was kept constant and the initial attitude and entry conditions were chosen from a reference ballistic entry simulation. In design point simulations the local horizontal was treated as fixed, no latitude rotation rate between the inertial frame and local horizontal frame. Gains were adjusted until tracking occurred without large overshoots, without large CM angular velocity rates, and without actuator displacements in excess of geometric limits. It was very difficult to obtain comparable step response time with the entry capsule and rotation IMMA HIAD systems and still have effective guidance command tracking. Gains were adjusted to penalize actuator velocity leading to the comparably sluggish tracking performance. However, it is shown in the full nonlinear guidance simulations of Chapter 10 that the translation IMMA HIAD system is still quite capable of precision guidance. The relatively slow IMMA track velocities help keep mechanical power requirements low as shown in Chapter 11.

Figure 6.5 shows tracking performance, Euler angles, and CM location for gains chosen at the 44 km design point altitude. Ringing in the IMMAs near the end of the 44 km design point simulation is due to the proportional error and integral error feedback control states being counteract-acted by feedback vehicle Euler pitch and yaw angle states away from their equilibria at zero degrees. These equilibria correspond to ballistic reference trajectory chosen for linearization. The respective integral and proportional error gains have the same magnitude as the vehicle pitch and yaw angular velocities and Euler Angles. Similar to the rigid entry capsule translation IMMA system, this follows from the linearized angle of attack and sideslip rate equations being proportional to vehicle pitch and yaw angular velocity and Euler angles. In order to produce command tracking the integral error states were heavily penalized leading to gains of nearly the same magnitude. The comparable magnitude can produce counteractive feedback control forces applied to the IMMA when tracking integral and proportionate error was low and the vehicle was away from its equilibrium pitch and yaw Euler angles. Increasing guidance command tracking error can then lead to control reversal. As guidance command tracking errors increase due to changing reference commands, the integral and proportional error portions of the feedback controller tend to quell angular

velocity and Euler angle counter-active control forces. Figure 6.6 show feedback gains versus altitudes at the design point with linear interpolation between the design point altitudes. These gains were implemented in full nonlinear guidance simulation of the translation IMMA HIAD system in Chapter 10.

Table 6.2: $\mathbf{R}_{xx}$ and $\mathbf{R}_{uu}$ gain normalization parameters for HIAD with translation IMMA

Parameter	Value
$r_{\max}$	$\frac{5\pi}{180}$ $\frac{\text{rad}}{s}$
$q_{\max}$	$\frac{5\pi}{180}$ $\frac{\text{rad}}{s}$
$\psi_{\max}$	$\frac{25\pi}{180}$ rad
$\theta_{\max}$	$\frac{25\pi}{180}$ rad
$\alpha_{\max}$	$\frac{10\pi}{180}$ rad
$\beta_{\max}$	$\frac{10\pi}{180}$ rad
$y_{ts,m1\,\max}$	0.5 m
$\dot{y}_{ts,m1\,\max}$	0.05 $\frac{\text{m}}{s}$
$z_{ts,m2\,\max}$	0.5 m
$\dot{z}_{ts,m2\,\max}$	0.05 $\frac{\text{m}}{s}$
$\int \alpha_{\max}$	$\frac{0.1\pi}{180}$ rad $\cdot$ s
$\int \beta_{\max}$	$\frac{0.1\pi}{180}$ rad $\cdot$ s

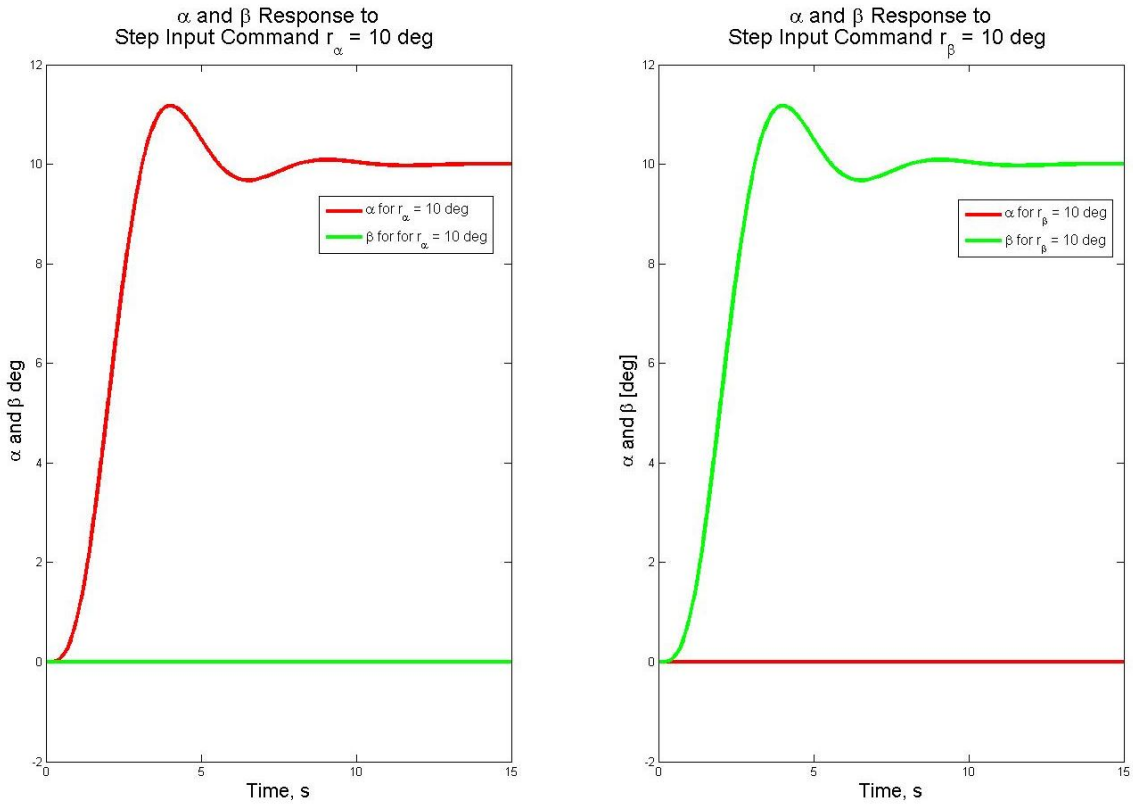

Figure 6.4: Step responses at 44 km altitude

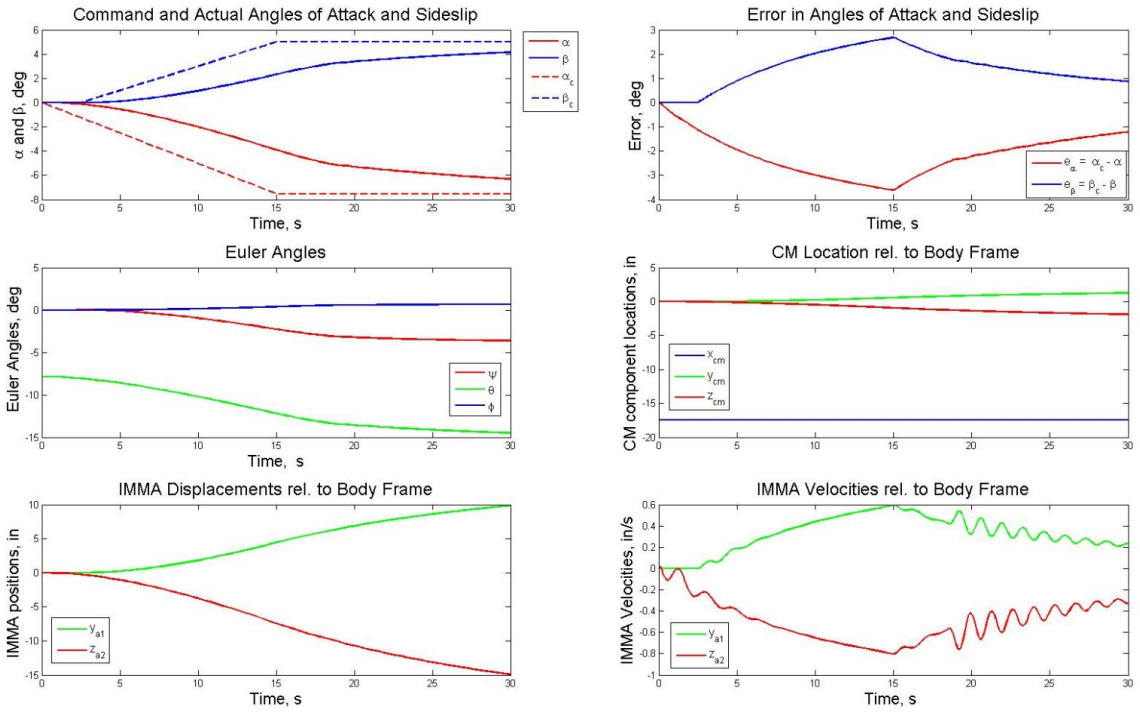

Figure 6.5: Design point simulation: tracking performance at 44 km altitude

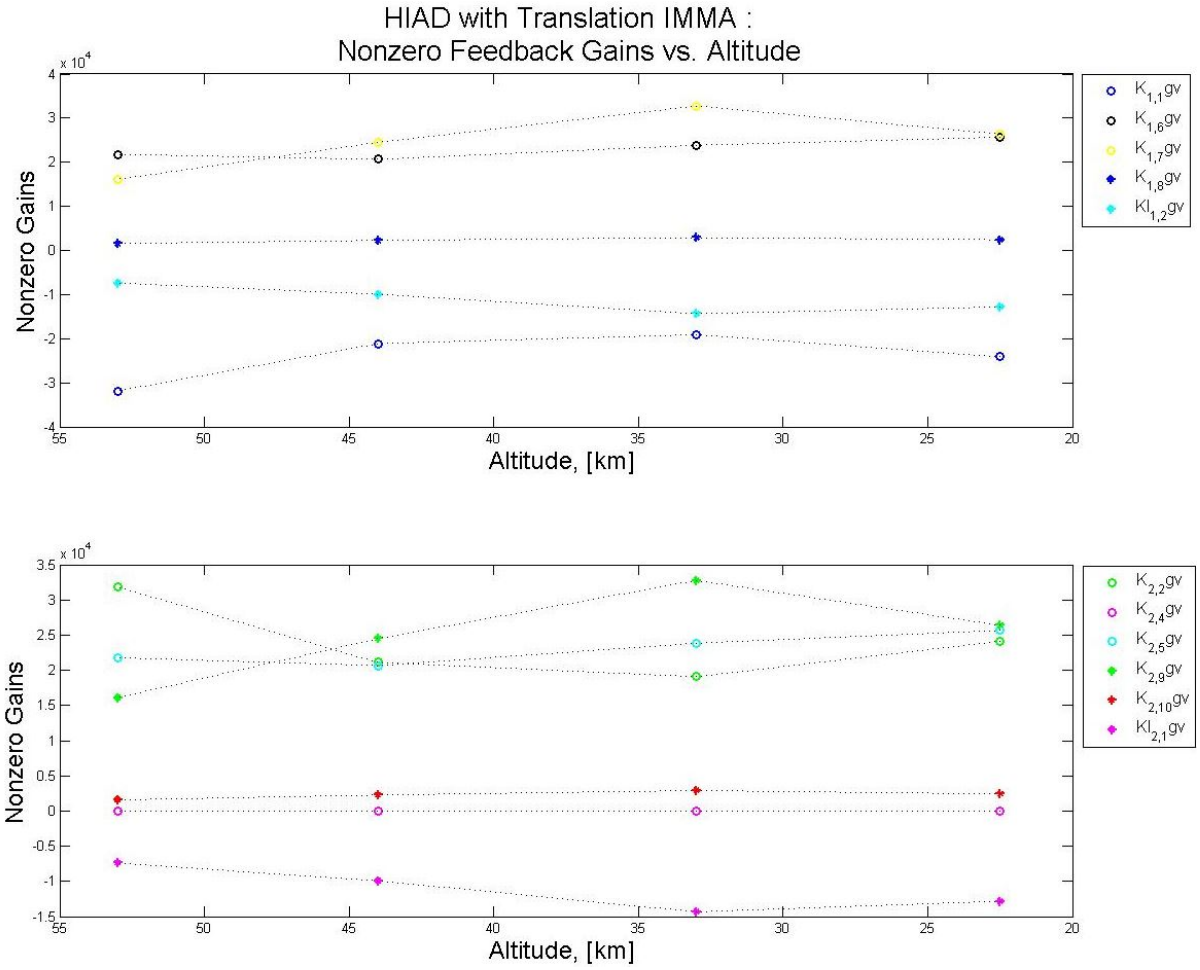

Figure 6.6: Feedback gains vs. altitude with linear interpolation between design points

6.4 HIAD With Rotation IMMA: Linear Quadratic Integral Control Tuning

The state and control weighting matrices used in computing $\bar{\mathbf{P}}$ for the rotation IMMA HIAD system at the design altitudes have structure:

$$\begin{aligned}\mathbf{R}_{xx} &= \operatorname{diag}\Big[\frac{10}{r^2_{\max}}, \frac{10}{q^2_{\max}}, \frac{1}{\psi^2_{\max}}, \frac{1}{\theta^2_{\max}}, \frac{1}{\alpha^2_{\max}}, \frac{1}{\beta^2_{\max}} \ \ldots \\ &\qquad \frac{1}{r^2_{b,ts\,\max}}, \frac{1}{q^2_{b,ts\,\max}}, \frac{1}{\theta^2_{a1\,ts\,\max}}, \frac{1}{\theta^2_{a1\,ts\,\max}}, \frac{r_{x11}}{(\int \alpha^2_{\max})}, \frac{r_{x12}}{(\int \beta^2_{\max})}\Big] \qquad (6.19)\\ \mathbf{R}_{uu} &= \operatorname{diag}\Big[\frac{r_{u1}}{\theta^2_{a1\,ts\,\max}}, \frac{r_{u2}}{\theta^2_{a2\,ts\,\max}}\Big]. \qquad (6.20)\end{aligned}$$

Table 6.3 lists the specific gain normalization parameters for $\mathbf{R}_{xx}$ and $\mathbf{R}_{uu}$. Following the same tuning process for the capsule and HIAD translation IMMA systems, gains were tuned through step response analysis and nonlinear design point simulations. Step response plots for the linear closed-loop system with respective plant and control influence matrices at each design altitude was performed to determine reference command following response time, overshoot, and amount of coupling of the system. The rotation IMMA configuration was developed to meet the CM displacement strategy used by both the capsule and HIAD translation IMMA systems. Accordingly, it is expected that step responses to reference command tracking inputs should also show the linear system is decoupled and reference commands can be tracked. Figure 6.7 confirms this expectation.

Design point simulations consisted of simulation of the HIAD with rotation IMMA nonlinear system including roll dynamics with the feedback controller tracking reference commands. In design point simulations dynamic pressure, q_∞, was kept constant and the initial attitude and entry conditions were chosen from a reference ballistic entry simulation. In design point simulations the local horizontal was treated as fixed, no latitude rotation rate between the inertial frame and local horizontal frame. Following the same tuning process as the capsule and HIAD translation systems, gains were adjusted until tracking occurred without large overshoots, without large CM angular velocity rates, and with actuator displacements within geometric limits. Figure 6.8 shows tracking performance, Euler angles, and CM location for gains chosen at the 44 km design point altitude. Figure 6.9 show feedback gains versus altitudes at the design point with linear interpolation between the design point altitudes. These gains were implemented in full nonlinear guidance simulation of the rotation IMMA HIAD system in Chapter 10.

Table 6.3: $\mathbf{R}_{xx}$ and $\mathbf{R}_{uu}$ gain normalization parameters for HIAD with rotation IMMA

Parameter	Value
$r_{\max}$	$\frac{5\pi}{180}\ \frac{\text{rad}}{s}$
$q_{\max}$	$\frac{5\pi}{180}\ \frac{\text{rad}}{s}$
$\psi_{\max}$	$\frac{25\pi}{180}$ rad
$\theta_{\max}$	$\frac{25\pi}{180}$ rad
$\alpha_{\max}$	$\frac{10\pi}{180}$ rad
$\beta_{\max}$	$\frac{10\pi}{180}$ rad
$r_{b,ts\,\max}$	$0.05\ \frac{2\pi}{180}\ \frac{\text{rad}}{s}$
$q_{b,ts\,\max}$	$0.05\ \frac{2\pi}{180}\ \frac{\text{rad}}{s}$
$\theta_{a1\,ts\,\max}$	$\frac{25\pi}{180}$ rad
$\theta_{a2\,ts\,\max}$	$\frac{25\pi}{180}$ rad
$\int \alpha_{\max}$	$\frac{\pi}{180}$ rad $\cdot$ s
$\int \beta_{\max}$	$\frac{\pi}{180}$ rad $\cdot$ s

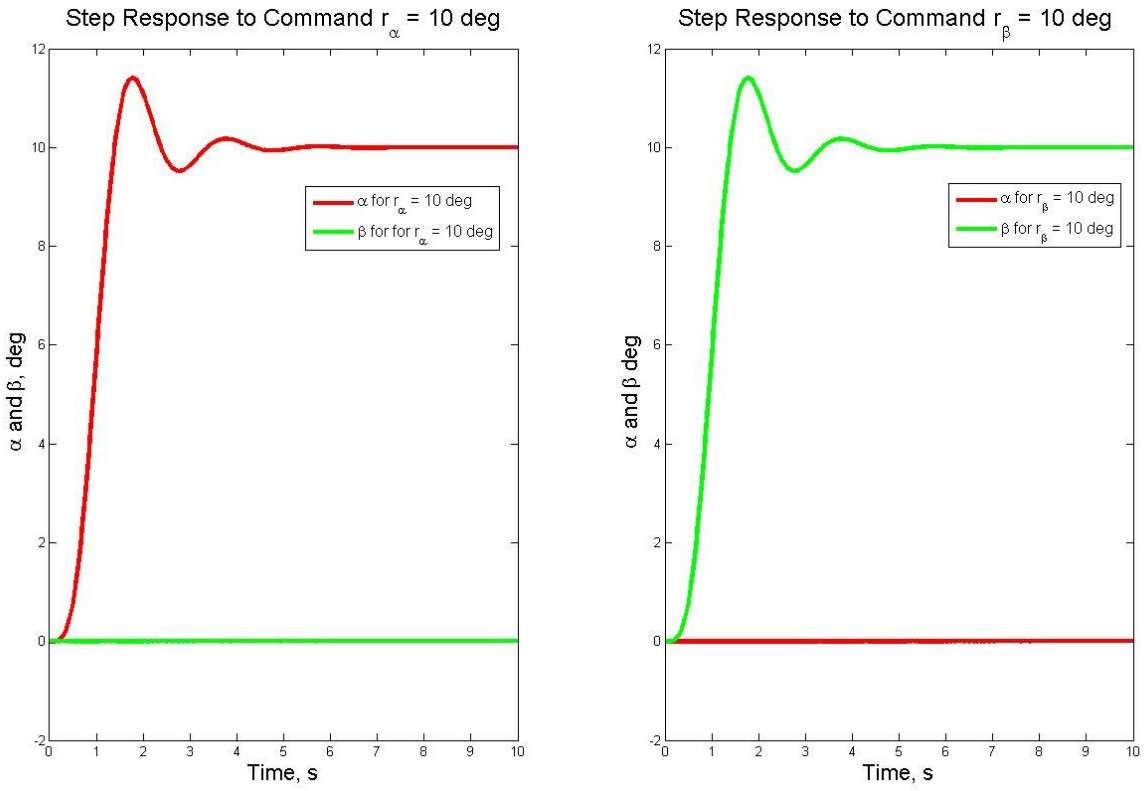

Figure 6.7: Step responses at 44 km altitude

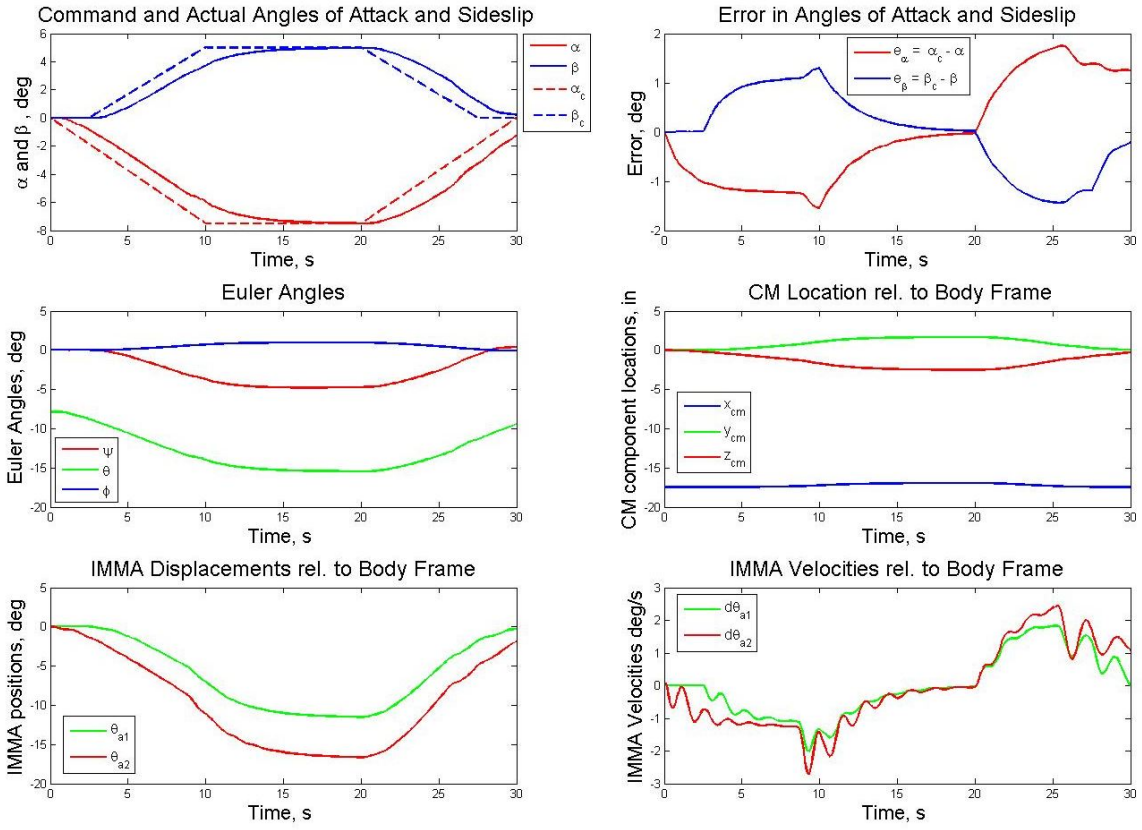

Figure 6.8: Design point simulation: tracking performance at 44 km altitude

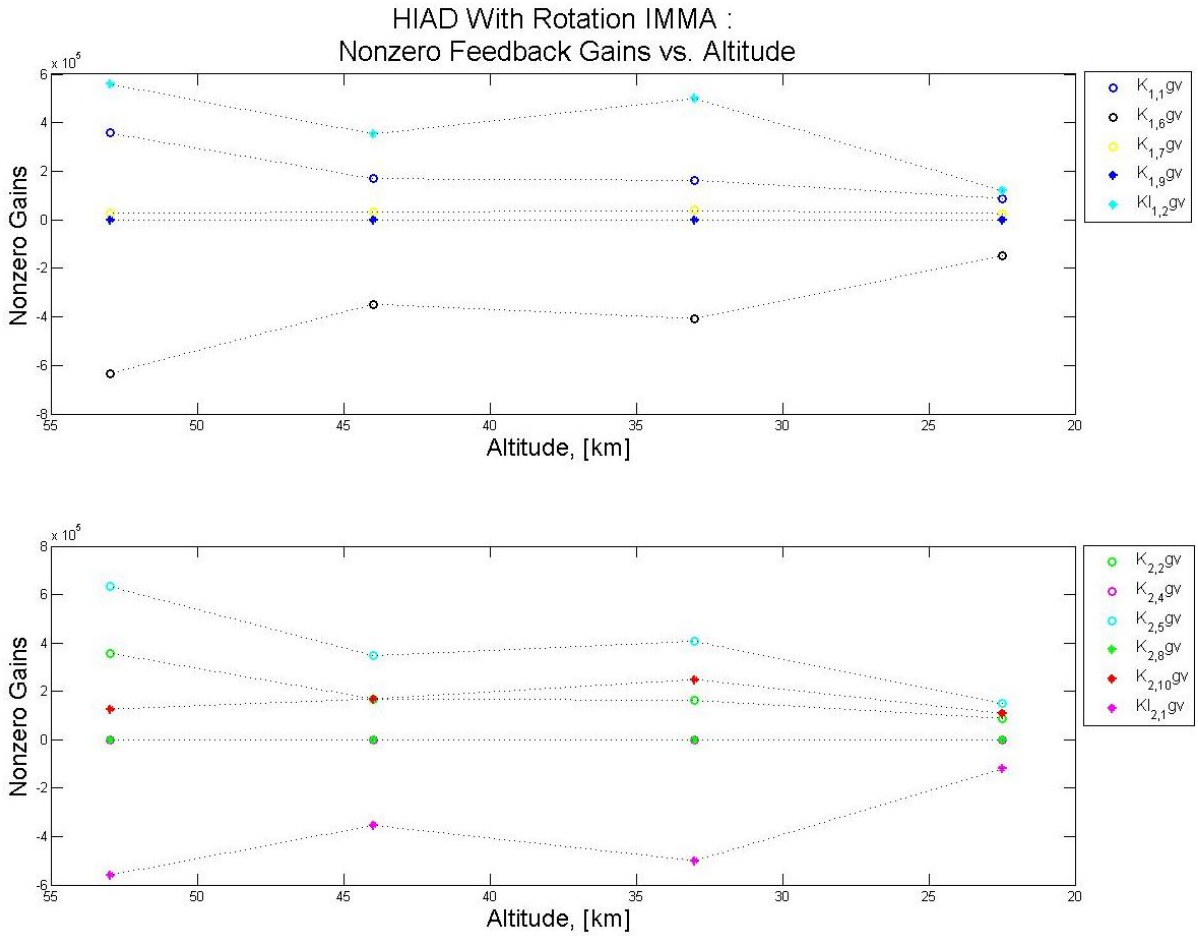

Figure 6.9: Feedback gains vs. altitude with linear interpolation between design points

Chapter 7

Closed-loop Guidance Command Generation

7.1 Angle of Attack Commands for Range Control

The original Apollo Earth entry terminal descent guidance algorithm used gains calculated by numerical integration of adjoint (costate) equations backwards in time along a nominal reference trajectory [10]. These gains represent sensitivity of the final landing location to perturbations away from the nominal trajectory. A new variation of this guidance algorithm was developed with Dr. Eric Queen in Reference [21]. The new guidance variation calculates the sensitivities by propagation of trajectories forward in time from states perturbed away from the reference trajectory. Also, the command equation has been recast in terms of velocity, v, and flight path angle, γ instead of altitude rate and drag acceleration. A planar lifting trajectory for a constant $L/D = 0.05$ corresponding to $(\alpha = -3^\circ, \beta = 0^\circ)$ was selected as the nominal reference trajectory.

In-plane lift commands are computed by multiplying the deviations from the nominal trajectory by the previously computed sensitivities:

$$(L/D)_{\text{ipc}} = (L/D)^* - \frac{K_0}{K_{3(h)}} \left[(s - s(h)^*) + K_{1(h)} (v - v(h)^*) + K_{2(h)} (\gamma - \gamma(h)^*) \right] . \quad (7.1)$$

The proposed IMMA systems are capable of generating a maximum $L/D = 0.16$ at maximum command angle of attack, $\alpha = -10^\circ$.

The sensitivity gains :

$$K_1(h) = (s_{vp} - s*) / \delta v \quad (7.2)$$

$$K_2(h) = (s_{\gamma p} - s*) / \delta \gamma \quad (7.3)$$

$$K_3(h) = \left(s_{(L/D)p} - s*\right) / \delta (L/D) \quad (7.4)$$

were computed numerically and indexed by altitude. Figure 7.1 provides the 24 nonlinear simulations, used to compute the gains at 8 separate altitudes. At each altitude a nominal initial condition simulation and 3 single perturbed initial conditions simulations for $\delta\gamma$, $\delta\, v$, or $\delta\,(L/D)$ were run to numerically compute the sensitivity gains. Figure 7.2 provides the altitude dependent sensitivity gains linearly interpolated between the 8 design altitudes. K_0 is a constant over-control gain. K_0 has the affect of increasing the in-plane lift commands to null range errors early in the trajectory. The numerical sensitivity gains show that flight path angle and L/D ratio have significant effect on final landing range, much larger than initial velocity for the perturbations studied, but their effect decreases as altitude decreases.

In Reference [10], the in-plane lift command was translated to bank angle guidance commands. Banking the vehicle to modify the in-plane lift induces cross-range motion which must be corrected with later bank reversals. The IMMA control system developed in this Dissertation decouples range and cross-range control by controlling angle of attack and angle of sideslip independently. The in-plane L/D command is generated from equation 7.1 and is then converted to an angle of attack command by:

$$\alpha_{\mathrm{c}} = \frac{\mathrm{C_N} - (\mathrm{L/D})_{\mathrm{ipc}}\,\mathrm{C_A}}{(\mathrm{L/D})_{\mathrm{ipc}}\,\mathrm{C_N} + \mathrm{C_A}}\,. \tag{7.5}$$

The in-plane equations of motion for atmospheric flight over a spherical planet from References [6, 10] were implemented in simulation for the perturbed and nominal simulations:

$$\frac{ds}{dt} = v\cos\gamma \tag{7.6}$$

$$\frac{dv}{dt} = -\left(\frac{D}{m} + g_{\mathrm{Mars}}\sin\gamma\right) \tag{7.7}$$

$$\frac{d\gamma}{dt} = \frac{L}{mv} + \left(\frac{v}{R_{\mathrm{Mars}} + h} - \frac{g_{\mathrm{Mars}}}{v}\right)\cos\gamma \tag{7.8}$$

$$\frac{dh}{dt} = v\sin\gamma \tag{7.9}$$

where Lift and Drag Force are defined as:

$$L = q_\infty C_L S \tag{7.10}$$

$$D = q_\infty C_D S \tag{7.11}$$

where dynamic pressure, lift force coefficient, drag force coefficient are:

$$q_\infty = \frac{1}{2}\rho v^2 \tag{7.12}$$

$$C_L = -C_A\sin\alpha + C_N\cos\alpha \tag{7.13}$$

$$C_D = C_A\cos\alpha + C_N\sin\alpha\,. \tag{7.14}$$

The aerodynamics database and atmosphere model used for the in-plane simulations are described in Chapter 8.

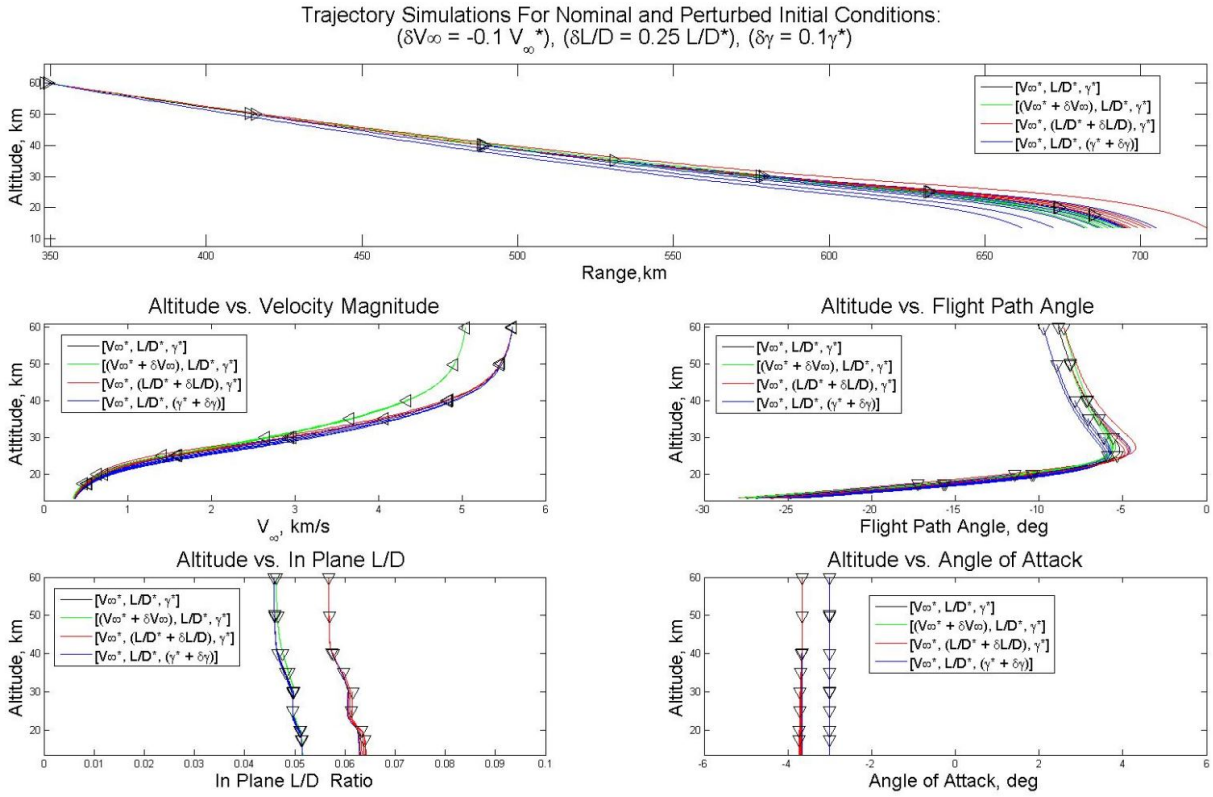

Figure 7.1: Trajectory simulations for nominal and perturbed initial conditions at 8 altitudes

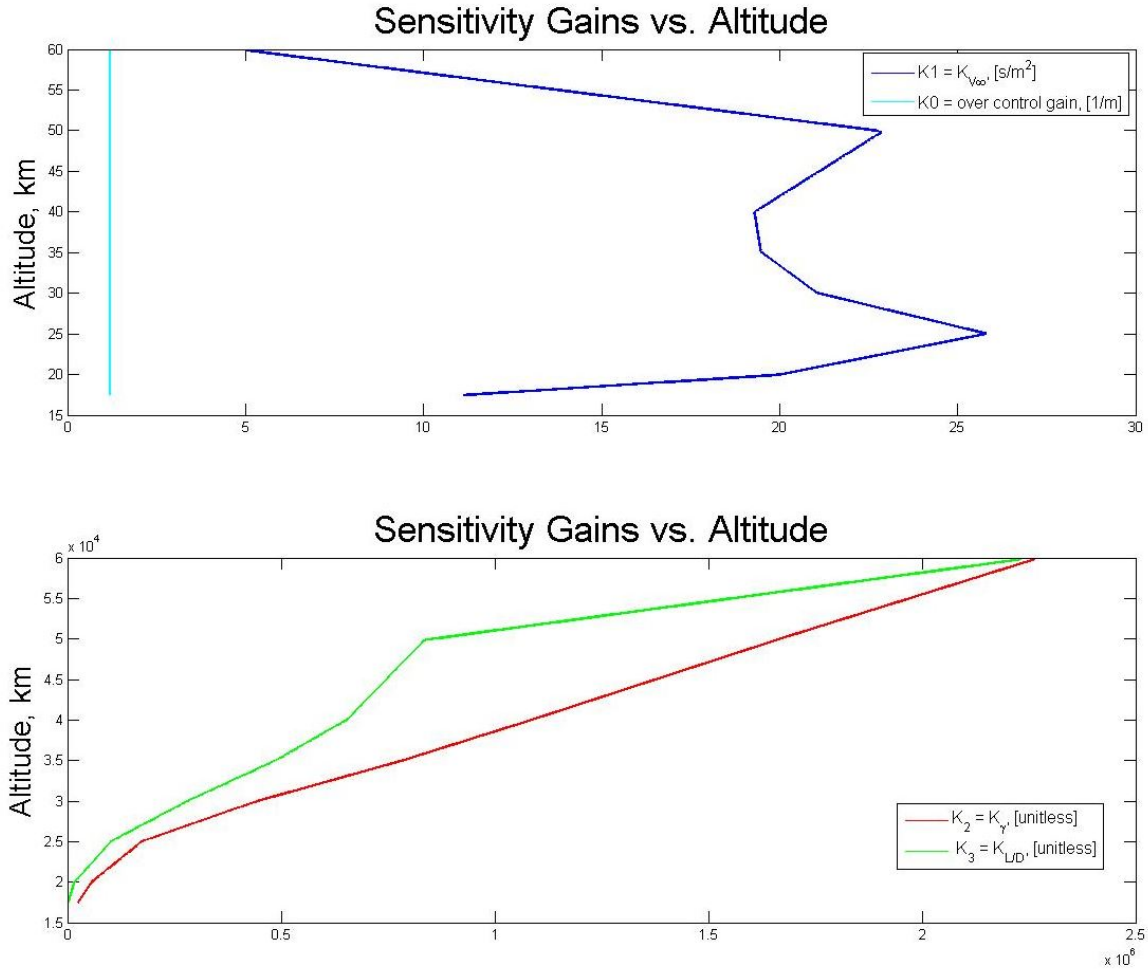

Figure 7.2: Sensitivity gains versus altitude

7.2 Sideslip Commands for Cross-range Control

For cross-range guidance, sideslip commands are generated from a straight-line flight strategy to direct the y CM inertial velocity vector component at the desired target:

$$\mathbf{r}^i_{c,t} = \mathbf{r}^i_{i,t} - \mathbf{r}^i_{i,c} \,. \tag{7.15}$$

$\mathbf{r}^i_{i,t}$ is the inertial position of the fixed target and $\mathbf{r}^i_{i,c}$ s the current inertial position of the vehicle. The cross-range guidance command is computed from determining the desired velocity vector components to direct the vehicle lateral velocity at the target:

$$\mathbf{V}_{\text{desired}} = \mathrm{V}_\infty \mathbf{R}^c_i \frac{\mathbf{r}_{c,t}}{\sqrt{\mathbf{r}_{c,t} \cdot \mathbf{r}_{c,t}}} \tag{7.16}$$

$$= \begin{pmatrix} u_{\text{desired}} & v_{\text{desired}} & w_{\text{desired}} \end{pmatrix}^T \tag{7.17}$$

from which the sideslip command is:

$$\beta_c = \arcsin\left(\frac{v_{\text{desired}}}{\mathrm{V}_{\text{desired}}}\right) . \tag{7.18}$$

$\mathrm{V}_{\text{desired}}$ is the desired velocity vector magnitude:

$$\mathrm{V}_{\text{desired}} = \sqrt{\mathbf{V}_{\text{desired}} \cdot \mathbf{V}_{\text{desired}}} \,. \tag{7.19}$$

Note that no sensitivity nor over-control gains were added to the sideslip command. The sideslip angle guidance command strategy is shown in Figure 7.3.

Note that angle of attack commands can be generated from this strategy:

$$\alpha_c = \arctan\left(\frac{w_{\text{desired}}}{u_{\text{desired}}}\right) . \tag{7.20}$$

However, using this strategy for angle of attack commands is very imprecise compared with Apollo-like guidance angle of attack command strategy. Large range misses are expected due to the angle of attack command not accounting for the entry vehicle's altitude varying lift-per-drag control authority. The Apollo-like angle of attack command law is implemented instead in the full nonlinear guidance simulations of Chapters 9-10. This command law is shown effective for correcting off-nominal entry conditions for speed, attitude, range, cross-range, and flight path angle.

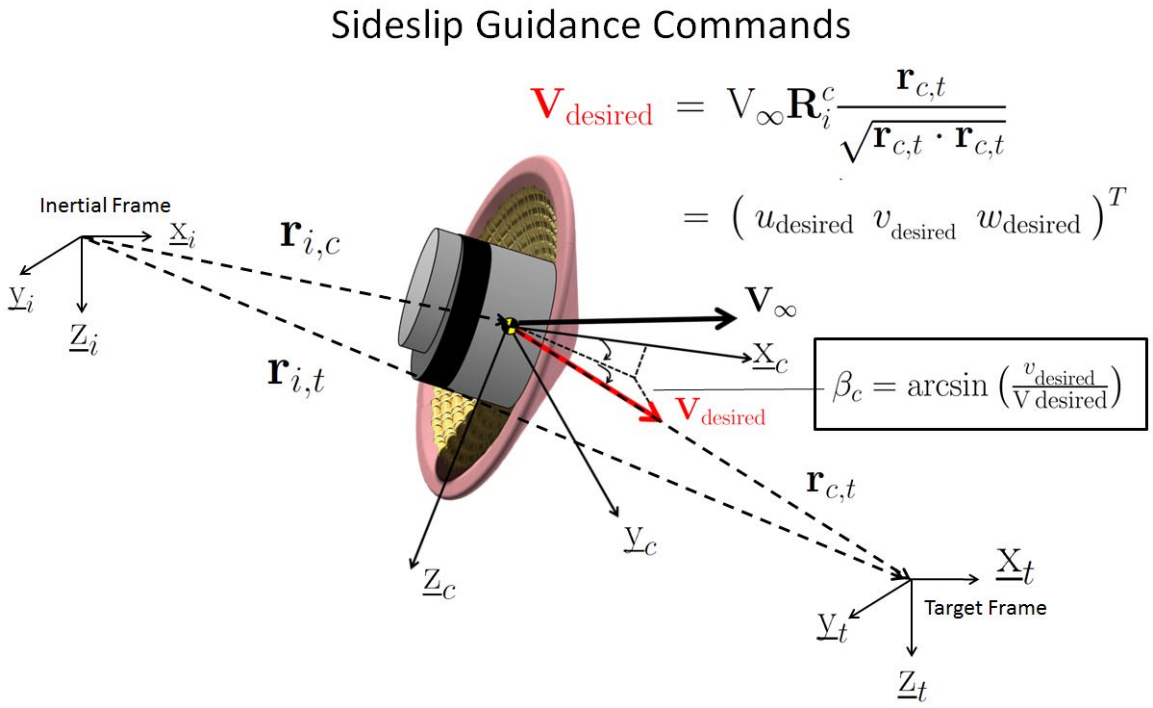

Figure 7.3: Sideslip commands for cross-range control

Chapter 8

Aerodynamics Database and Atmosphere Model

8.1 Mars Phoenix Entry Capsule Aerodynamics Database

The aerodynamic axial force, normal force, and static pitch moment coefficients $(C_{A_T}, C_{N_T}, C_{m_T})$ at the aerodynamic reference point for the Mars Phoenix entry capsule are indexed by total angle of attack:

$$\alpha_T = \arccos\left(\cos\alpha\cos\beta\right) \tag{8.1}$$

where α and β are the angle of attack and sideslip. The total angle of attack and total angle of attack clock angle:

$$\phi_{\alpha_T} = \arctan\left(\frac{\sin\beta}{\sin\alpha\cos\beta}\right) \tag{8.2}$$

are used in computation of the static aerodynamic force coefficients:

$$\begin{aligned} C_A &= C_{A_T} && (8.3)\\ C_Y &= -C_{N_T}\sin\left(\phi_{\alpha_T}\right) && (8.4)\\ C_N &= C_{N_T}\cos\left(\phi_{\alpha_T}\right). && (8.5) \end{aligned}$$

The pitch and yaw static moment coefficients at the null CM location from Reference [24] are:

$$\begin{aligned} C_m &= C_{m_T}\cos\phi_{\alpha_T} && (8.6)\\ C_n &= -C_{m_T}\sin\phi_{\alpha_T}. && (8.7) \end{aligned}$$

From Reference [5], the dynamic pitch and yaw moment coefficients are treated as equivalent:

$$C_{m_{(q+\dot{\alpha})}} = C_{n_{(r-\dot{\beta})}}. \tag{8.8}$$

This follows from the axial symmetry of the Phoenix entry capsule. Output from the aerodynamics routine used in simulation, developed from Reference [5] are listed in Figures 8.1-8.2. Linear interpolation was used at total angle attack values between the reference values.

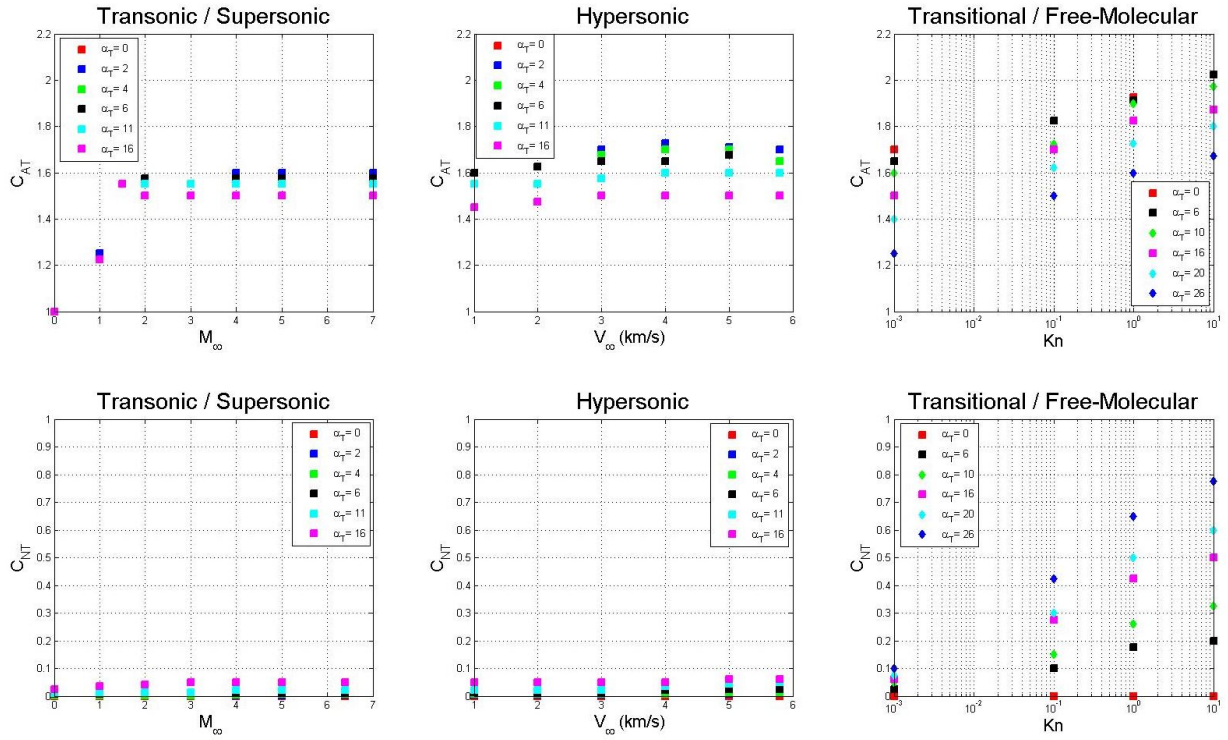

Figure 8.1: Axisymmetric axial and normal force coefficients from the aerodynamics routine developed from Reference [5]

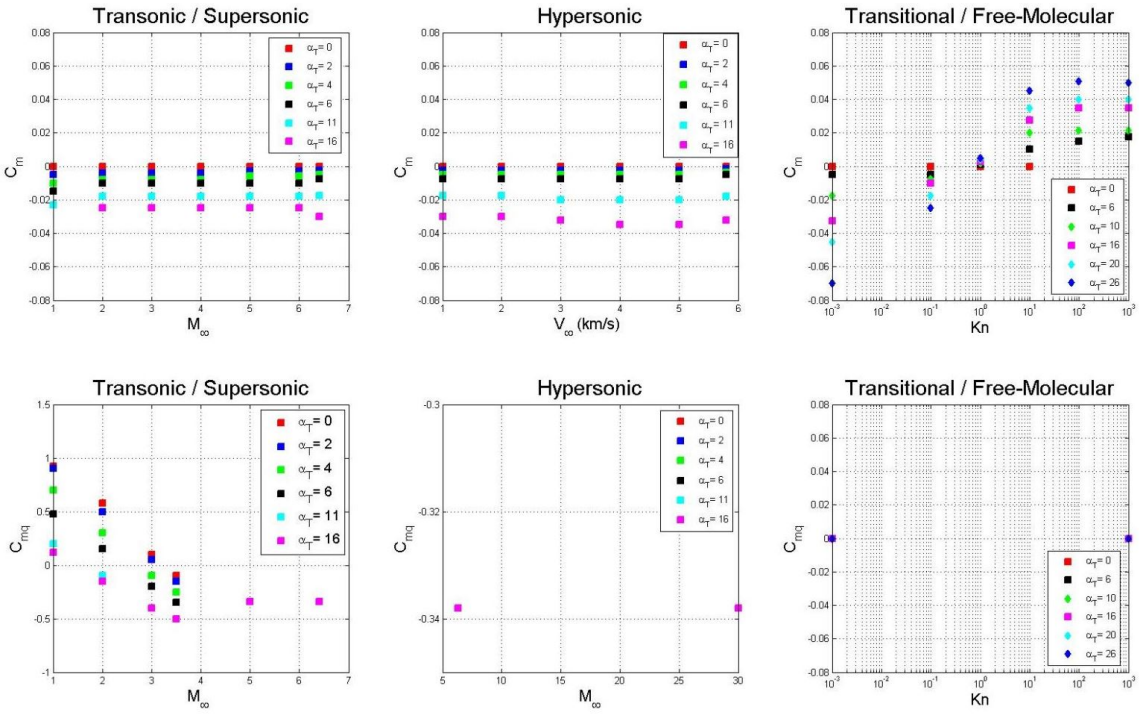

Figure 8.2: Static and dynamic pitch moment coefficients from the aerodynamics routine developed from Reference [5]

8.2 Mars Atmosphere Model

An atmospheric density model was developed from atmospheric flight data from the Mars Pathfinder Mission reported in Reference [31]. Figure 8.3 shows the atmospheric density profile used in guidance simulations. Knudsen number versus altitude profile was used in simulation at altitudes above 60 km using data from the Mars Phoenix mission in Reference [5]. Aerodynamic coefficients for the Transonic/Supersonic flight regime (Mach number at or below 6.4) were indexed by total angle of attack using standard Mach definition:

$$M_\infty = \frac{V_\infty}{v_{\text{sound}}} \,. \tag{8.9}$$

Figure 8.4 lists speed of sound for C02, the primary atmospheric constituent using the temperature versus altitude profile of Figure 8.5 developed from data from the Viking 2 Mission listed in Reference [6]. The terminal parachute altitude used to end the guidance simulations, 13.53 km, was chosen for Mach number 1.65 for a ballistic entry with similar entry conditions to the Mars Phoenix mission. Both the entry capsule and HIAD reference vehicle were designed to have the same ballistic coefficient as the actual Mars Phoenix mission vehicle. At Mach 1.65 in the guidance simulations the vehicle entry speed was 370 m/s which is close to the predicted and reconstructed pre-parachute speed of 372 m/s [5, 33].

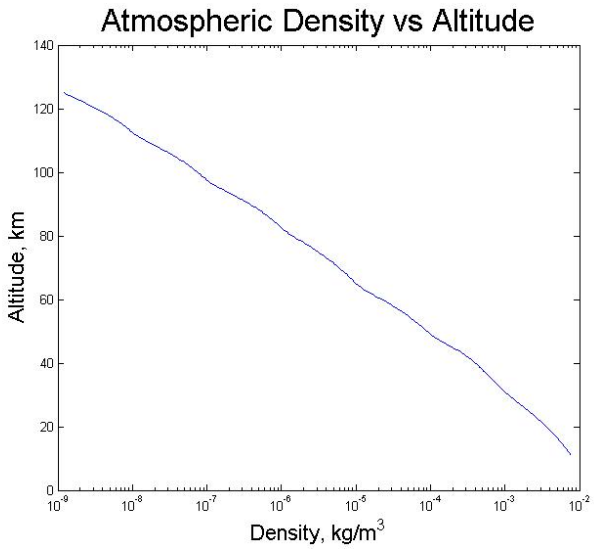

Figure 8.3: Atmospheric density versus altitude from Pathfinder Mission data reported in Reference [6]

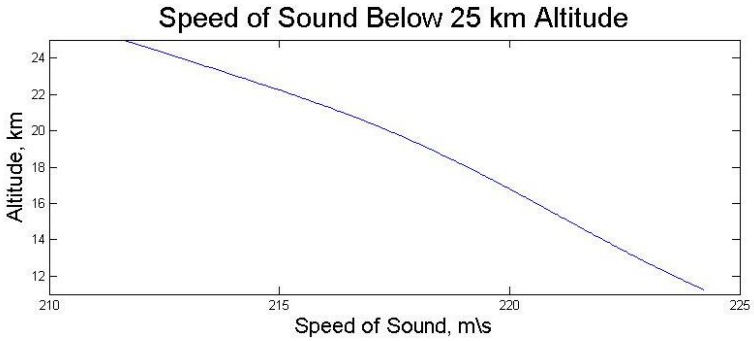

Figure 8.4: Sound speed versus altitude

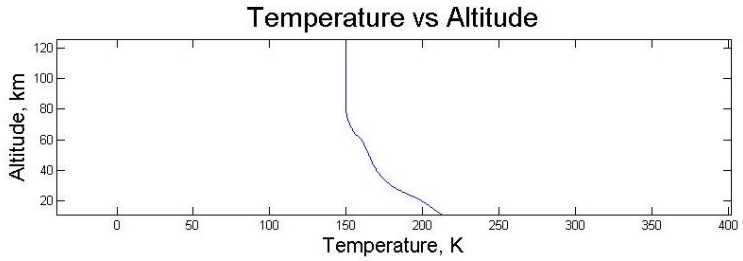

Figure 8.5: Temperature versus altitude from Viking 2 Mission data reported in Reference [6]

Chapter 9

Entry Capsule Closed-loop Guidance Simulations

Nonlinear entry guidance simulations of the 8 DOF capsule translation IMMA system of Chapter 5 for feedback LQ integral control guidance command tracking were implemented with MATLAB and Simulink. Roll dynamics were included. The simulations use an ode45 solver with a relative tolerance of $1e-6$ to integrate the nonlinear equations of motion. No atmospheric winds were modeled. The feedback controller operates between 53 km and a predefined parachute altitude of 13.53 km. The initial control altitude was set to 53 km, the approximate beginning of the hypersonic flight regime where there is sufficient dynamic pressure ($\approx$ 1kPa) for the CM based control moment strategy to be effective. The terminal parachute altitude of 13.53 km was chosen from consideration of the Mars Phoenix mission [5]. The feedback gains of Chapter 6 were implemented using linear interpolation between the design point altitudes. For altitudes below 22.5 km, the feedback gains were set to their 22.5 km design point values. Track limits were not directly imposed nor collision forces modeled, however, force saturation limits were imposed and guidance commands were limited to maximum angle of attack and sideslip angle of $\pm$ 10° to prevent IMMA displacements past 63.5 cm (25 in). All simulations had IMMA track displacements within their travel limits.

The desired nominal parachute target location is at 13.53 km altitude at 695.5 km down-range from the nominal initial entry position. This nominal trajectory to reach the terminal target was developed in Chapter 7 for a constant angle of attack at -3 degrees and sideslip angle at zero degrees. The objective of 10 guidance simulations, G1$-$G10, was to steer out initial condition errors and correct for errors in tracking commanded angles of attack and sideslip to reach the desired target. The initial roll attitude for all 10 of the guided trajectories was zero degrees. Guided trajectories G1$-$G4 and G9$-$G10 involved range guidance only requiring only IMMA pitch control moments to meet guidance angle of attack commands. The pitch control moments do not induce a rolling moment nor a yaw moment when the vehicle is at

zero angle of sideslip. Yaw control moments for sideslip guidance was required for correcting initial cross-range errors to reach the desired target for G5−G8 trajectories. Accordingly, only G5−G8 required simultaneous pitch and yaw attitude changes which induced small roll attitude changes. These small roll angle attitude changes never exceeded more than ±5 degrees, shown in Figures 9.10, 9.12, 9.14, and 9.16.

Table 9.1 lists simulation initial conditions for a ballistic open-loop trajectory, the nominal trajectory, and the 10 guided trajectories. G1 and G2 correspond to correcting off nominal initial entry conditions for respective angle of attack and angle of attack and flight path angle. G3 and G4 correspond to entry with off nominal angle of attack attitude and respective range offsets at 10 km in front of and 10 km behind the nominal trajectory range position. G5−G8 have off nominal initial angle of attack attitude and cross-range positions. G9-G10 correspond to off nominal initial entry speed of respective 200 m/s slower and faster than the nominal trajectory initial entry speed. The last column of Table 9.1 provides the final target miss distance for each of the trajectories. Figure 9.1 shows the ballistic, nominal, and 10 guided trajectories respective range vs. altitude and cross-range vs. altitude positions. Figure 9.22 shows the entry trajectories with respect to the inertial frame and over the surface of Mars. Recall from Chapter 2, that the inertial frame is fixed to the planet surface aligned with the Mars Polar axis. The guided trajectories start at 125 km altitude above the planet. At the terminal parachute targets at 13.53 km altitude, the surface of Mars is 60 km below the inertial frame origin. A flat Mars approximation would not have captured this extra flight distance and would have produced inaccurate range guidance, time of flight prediction, peak dynamic pressure, and peak axial deceleration.

Guidance command tracking and IMMA internal dynamics versus altitude are shown in figure pairs for each of the 10 guided trajectories. The altitude range shown is from the initial control altitude, 53 km, to the terminal parachute altitude, 13.53 km. The first figure of each pair shows commanded and achieved angle of attack and sideslip, error in command tracking, and Euler angles relative to the local horizontal. The second figure of each of the 10 figure pairs shows the IMMA internal positions, velocities, and accelerations along with the composite vehicle CM location. An initial spike in the angle of attack command tracking error at the initial control altitude for each of the guided trajectories is due to the guidance angle of attack command switching from a predefined value of zero degrees above the control altitude to a commanded value close to the nominal trajectory angle of attack, -3 degrees. The entry vehicle angle of attack above the control altitude is small, oscillating with amplitude less than 1 degree around zero degrees angle of attack. A spike in the vehicle angle of attack also occurred around 25 km. The changing dynamic pitch moment coefficient from the hypersonic to supersonic-transonic flight domain is most likely the primary source for the spike at the 25 km altitude. A transition from a stable, constant dynamic pitch moment coefficient in the hypersonic flight domain occurs around 25 km. As the vehicle desecrates in the supersonic-transonic flight regime the dynamic pitch moment coefficient drops to zero then switches sign for nonzero angles of attack. This causes attitude oscillation growth rather than decay. The dynamic pitch moment coefficient database for

each flight domain is shown in Figure 8.2. The authors of the Mars Phoenix aerodynamics database characterize the dynamic pitch moment coefficient as destabilizing when it is ≥ 0.

The z_c IMMA internal velocity for guided trajectory G2 in Figure 9.5 shows oscillation between altitudes 45 km to 30 km. This oscillation has small amplitude (0.5 inches per second) and dampens out close to the 33 km design point altitude. G2 corresponded to correcting initial flight path angle and angle of attack which involved correcting an initial range error of 40 km behind the nominal trajectory at the initial control altitude. This required angle of attack commands near maximum limit to generate maximum lift to catch up in range and then after catching up necessitated a counteractive pitch attitude change to correct for range overshoot. The oscillation in IMMA velocity is partially due to the LQ integral controller resisting large vehicle pitch rate changes which counteracts nulling the angle of attack tracking error. The feedback vehicle pitch rate, pitch gain,angle of attack gain, and integral error angle of attack gain have approximately the same magnitude. This is because the linearized angle of attack is proportional to it and for tracking the angle of attack gain and integral angle of attack error gain are heavily penalized. The equilibrium pitch angle was set to pitch angle at the design point altitudes corresponding to a ballistic, zero angle of attack entry. Discussed in Chapter 12 recommended areas of future study is the suggestion to linearize the controller about the nominal reference trajectory. The oscillations could be due to the feedback pitch angle gain counteracting the integral error gain which could be reduced for linearizing about the nominal trajectory. The decision was made to linearize around a ballistic trajectory with future missions in mind, where in the event of IMMA failure to move, the vehicle will remain close to a stable zero angle of attack stable attitude configuration leading to big terminal range misses, but avoiding catastrophic instability. Changing the pitch angle parameter used in linearization, better tuning of the 44 km gain, or tuning the controller at additional design points could reduce such IMMA oscillation.

For guided trajectory G3, IMMA displacement and command angle of attack had large changes near 17.5 km altitude, seen in Figure 9.7 and Figure 9.6 respectively. The large IMMA displacement changes corresponded directly to meeting the command changes in angle of attack. Reasons for the large change in command angle of attack around 17.5 km include: sensitivity gain altitude limit, G3′s 10 km range initial off nominal offset, over-control gain choice, reduced lift capability at low altitudes, and dynamic pitch moment coefficient in transonic-supersonic flight regime. The sensitivity gains used in computing the command angle of attack were developed from 60 km to 17.5 km altitude. For altitudes below 17.5 km the sensitivity gains were set to their 17.5 km values. Computing gains for altitudes below 17.5 km should decrease the sharp changes in command angle of attack. For G3 the vehicle initially had to increase drag due to range offset overshoot, but then due to the large downrange target distance, had to increase lift in order to reach the target. Increasing the over-control gain could help null range errors at higher altitudes where lift capability is greater than lower altitudes. This would mitigate large IMMA displacements late in the trajectory. An additional contributing factor to the large angle of attack changes

is due to the dynamic pitch moment coefficient value at 17.5 km which is in the supersonic-transonic flight regime where its value becomes increasingly positive leading to pitch moment excitation rather than damping.

Despite instances of guided with IMMA oscillation and late changes in angle of attack commands, the 10 guided trajectories were all able to correct substantial off-nominal entry conditions and for close landing to the terminal parachute target. Note that the unguided, ballistic open-loop simulation had a target down-range miss of 38 km. G1 had the same initial entry conditions as the ballistic open-loop simulation. For G1 with IMMA guidance the terminal down-range miss was 60 m. G4 had a the second largest terminal range miss 340 m (60 m smaller than G3). However, the initial range of G4 was 10 km behind the nominal trajectory's range. The ballistic open-loop entry at this same initial range would have a down-range miss of 48 km. The entry vehicles do not have thrust capability for increased lift and have low lift-per-drag ratios, yet the IMMAs can produce significant down-range and cross-range guidance. The significant guidance of G1-G10 was for small, less than 5 cm (2 in), movement of the vehicle composite CM location. This was for track displacements less than 63.5 cm (25 in) within geometric constraints for the Phoenix aeroshell. The IMMA have track displacements and low relative speed to the vehicle frame for all of the guided trajectories. Note that the uncontrolled roll Euler angle was small , even for simultaneous yawing and pitching of the entry vehicle. Increasing either the IMMA masses or track lengths for greater CM displacement would increase control authority for range and cross-range control. However, the IMMA system developed for the capsule vehicle shows substantial guidance performance. Collectively, the 10 guided trajectories are illustrative of the significant closed-loop guidance performance of the linear controller and precision guidance capability of the decoupled range and cross-range IMMA guidance strategy.

Table 9.1: Simulation runs for entry capsule with translation IMMA

Simulation Run:	Initial Conditions:				Range Miss, km	Cross-range Miss, km
	γ, deg	NED Position, km	V_∞, km/s	(α, β), deg		
Open-loop	-12.25	(0, 0, -125)	5.6	$(0, 0)$	-38	0
Nominal Trajectory	-12.25	(0, 0, -125)	5.6	$(-3, 0)$	0	0
G1	-12.25	(0, 0, -125)	5.6	$(0, 0)$	0.06	0
G2	-13.00	(0, 0, -125)	5.6	$(0, 0)$	0.03	0
G3	-12.25	(10, 0, -125)	5.6	$(0, 0)$	-0.4	0
G4	-12.25	(-10,0, -125)	5.6	$(0, 0)$	0.34	0
G5	-12.25	(0, 5, -125)	5.6	$(0, 0)$	0.02	0.012
G6	-12.25	(0, -5, -125)	5.6	$(0, 0)$	0.02	-0.012
G7	-12.25	(0, 10, -125)	5.6	$(0, 0)$	-0.02	0.07
G8	-12.25	(0, -10, -125)	5.6	$(0, 0)$	-0.02	-0.07
G9	-12.25	(0, 0, -125)	5.4	$(0, 0)$	0.4	0
G10	-12.25	(0, 0, -125)	5.8	$(0, 0)$	- 0.4	0

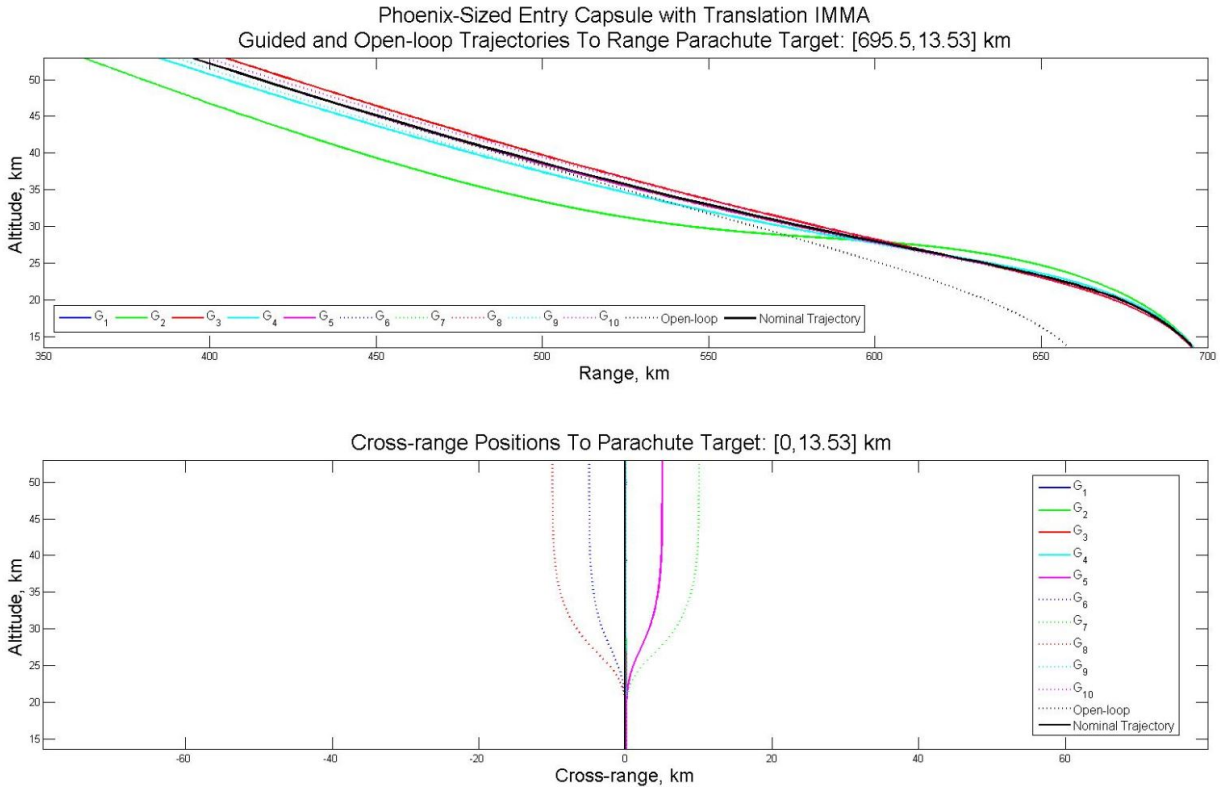

Figure 9.1: Phoenix-sized entry capsule with translation IMMA: range and cross range for guided trajectories

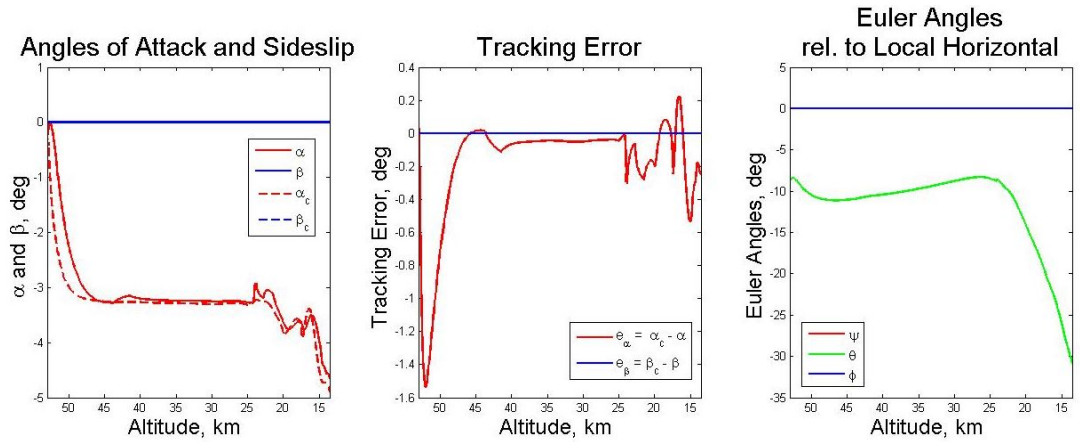

Figure 9.2: Guided trajectory G1, guidance commands and tracking performance

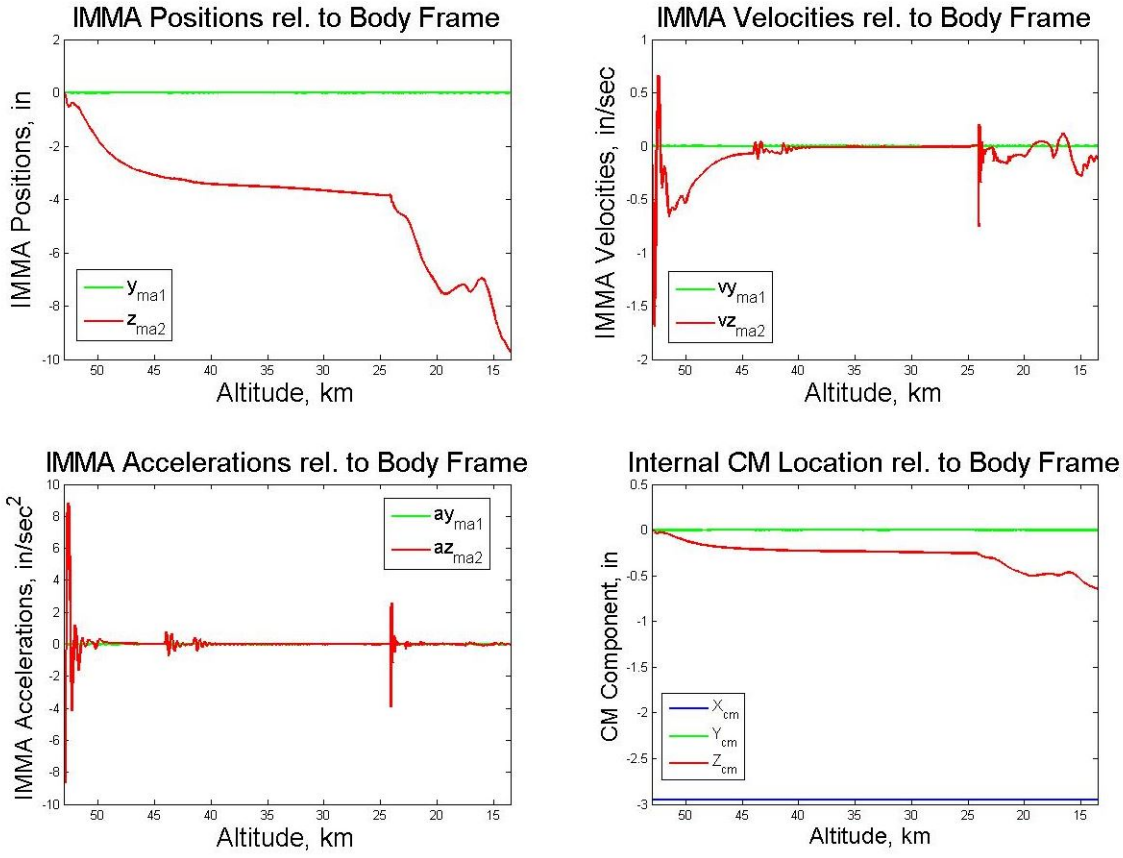

Figure 9.3: Guided trajectory G1, IMMA kinematics and CM internal location

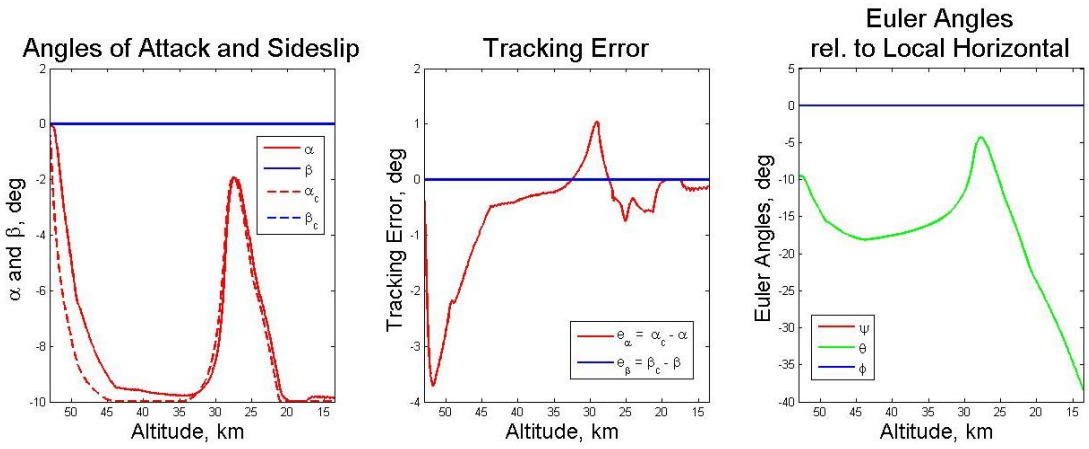

Figure 9.4: Guided trajectory G2, guidance commands and tracking performance

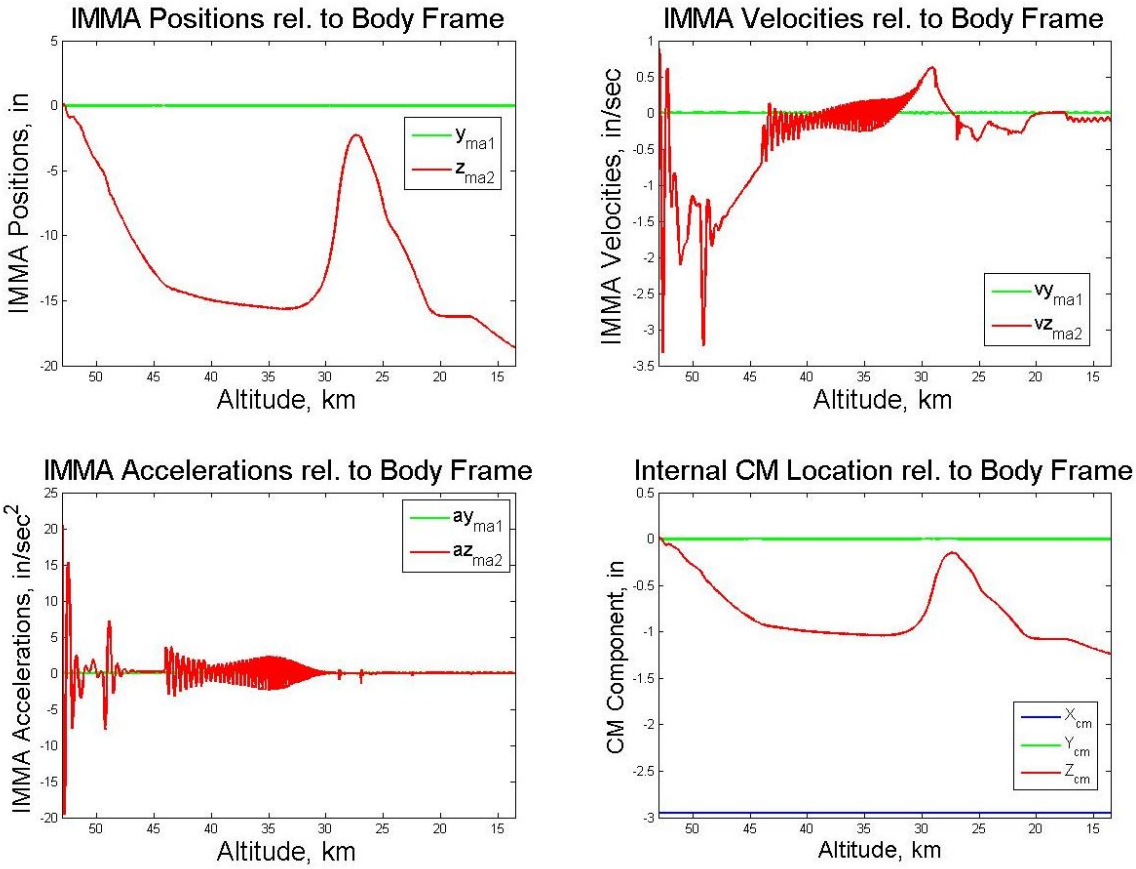

Figure 9.5: Guided trajectory G2, IMMA kinematics and CM internal location

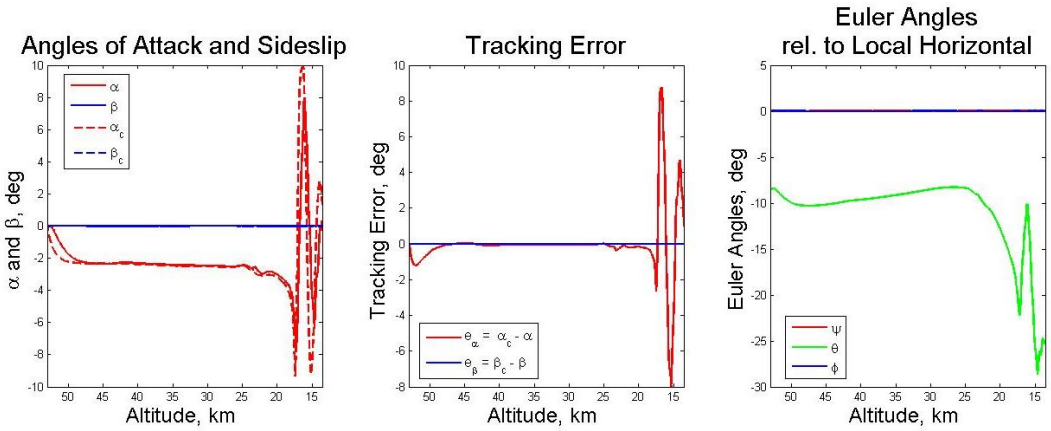

Figure 9.6: Guided trajectory G3, guidance commands and tracking performance

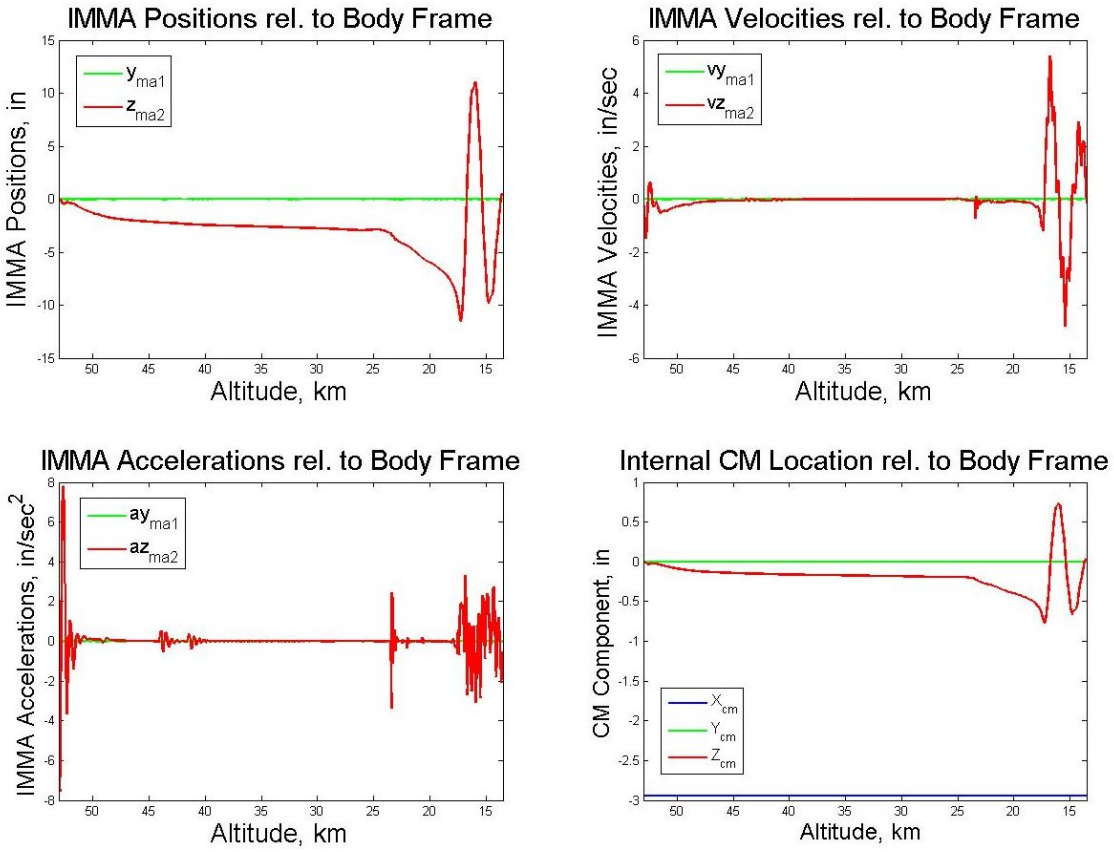

Figure 9.7: Guided trajectory G3, IMMA kinematics and CM internal location

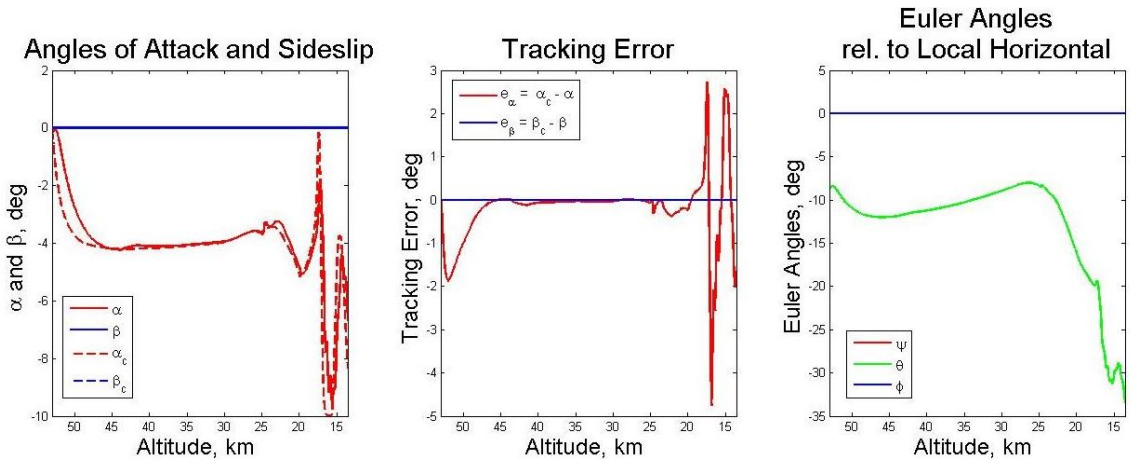

Figure 9.8: Guided trajectory G4, guidance commands and tracking performance

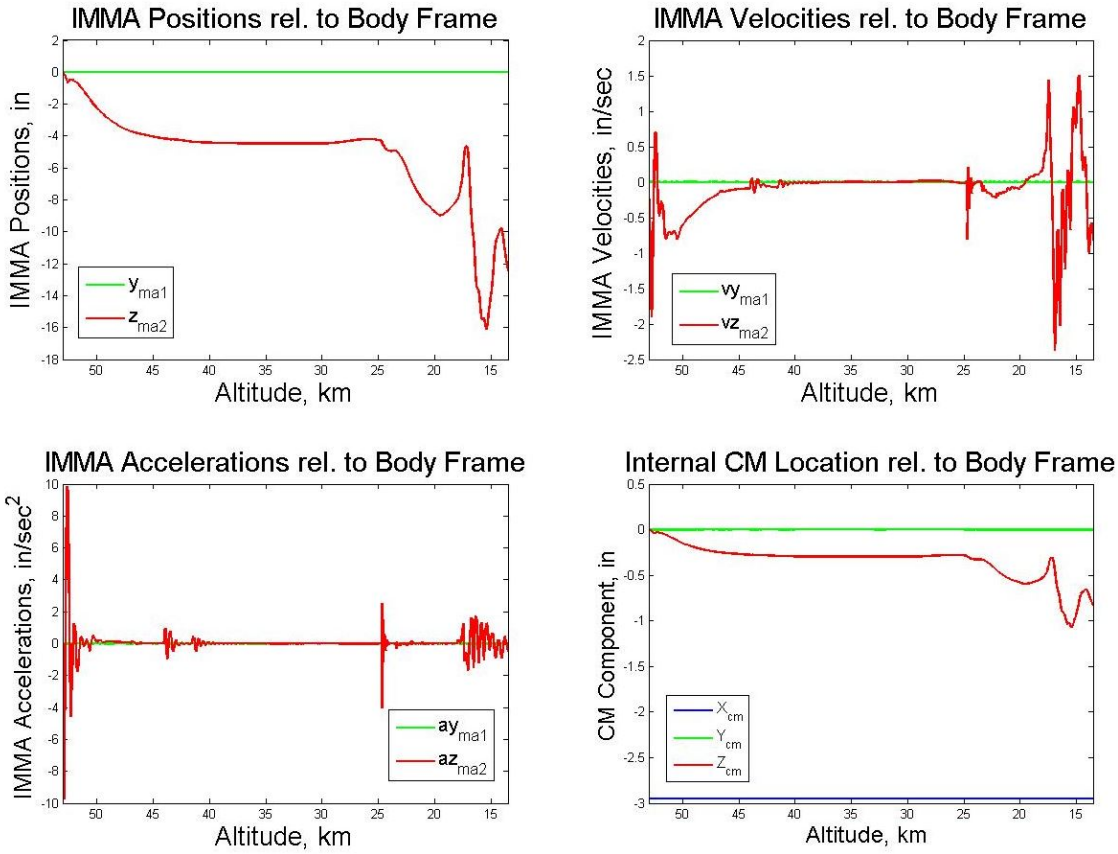

Figure 9.9: Guided trajectory G4, IMMA kinematics and CM internal location

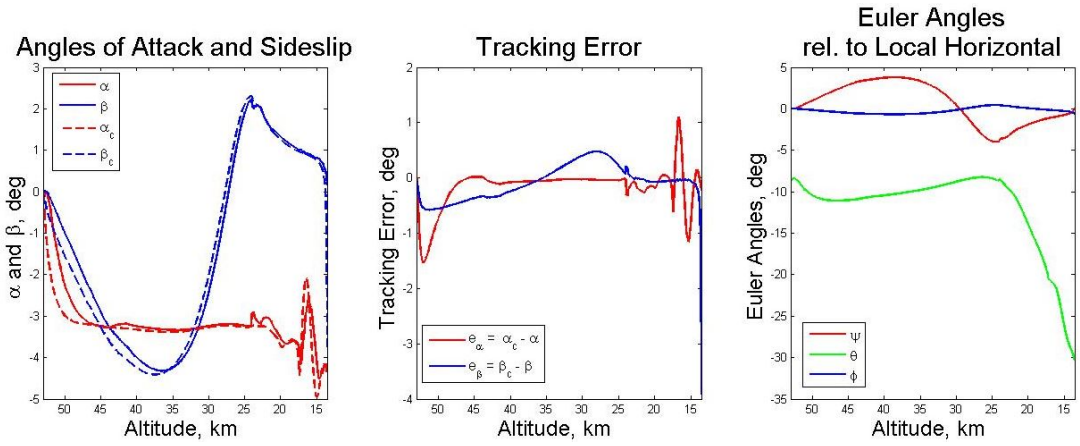

Figure 9.10: Guided trajectory G5, guidance commands and tracking performance

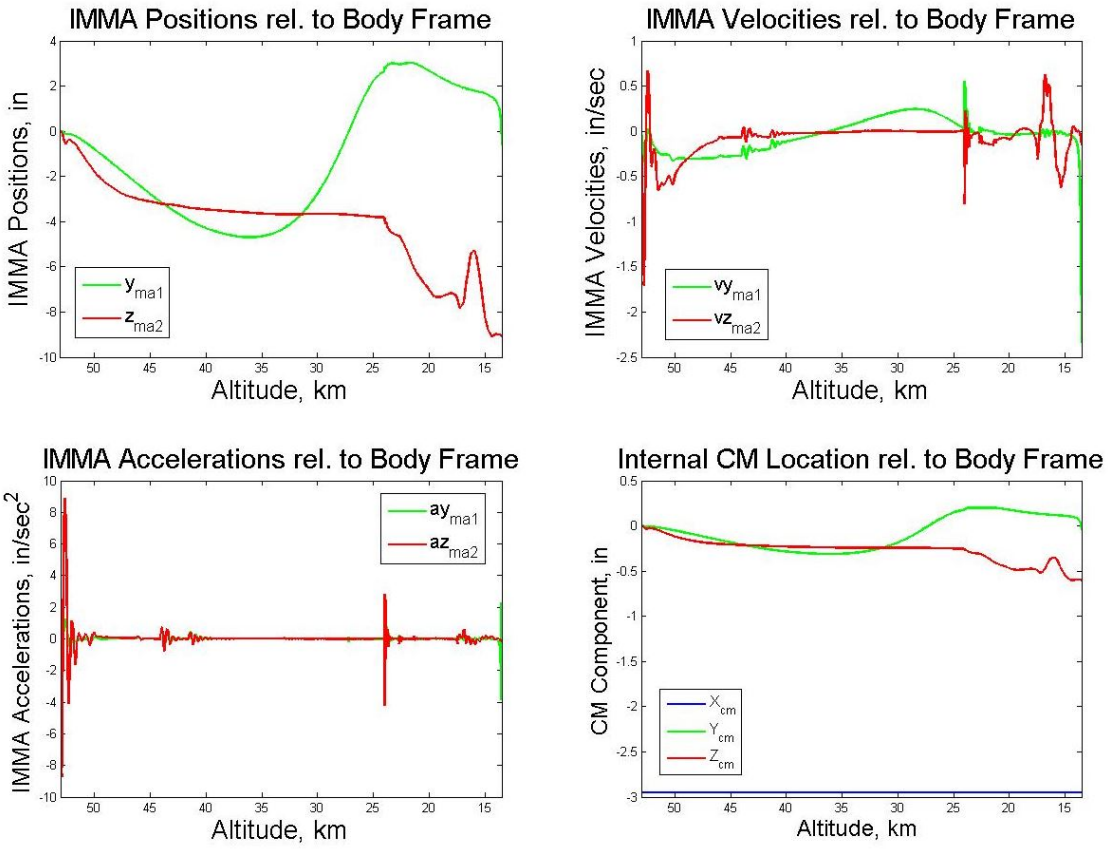

Figure 9.11: Guided trajectory G5, IMMA kinematics and CM internal location

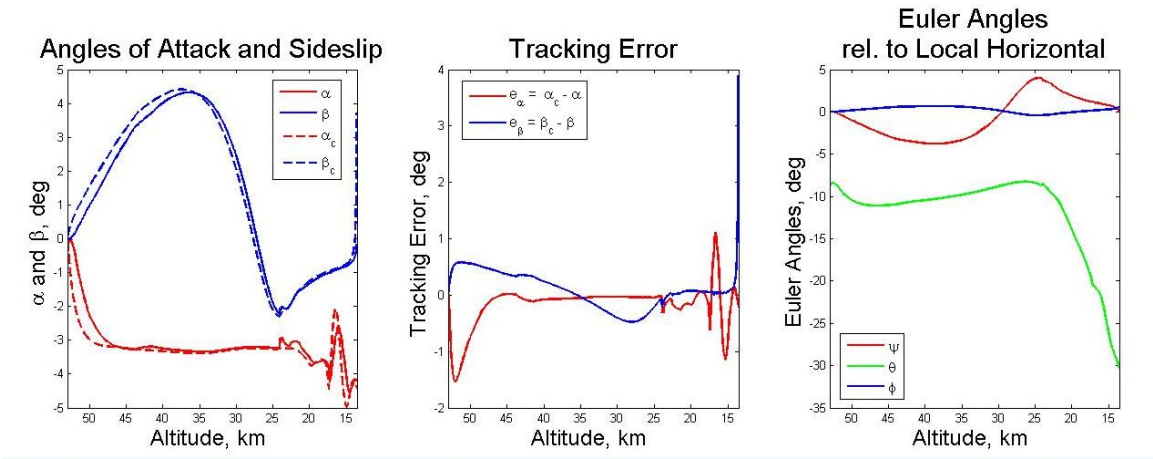

Figure 9.12: Guided trajectory G6, guidance commands and tracking performance

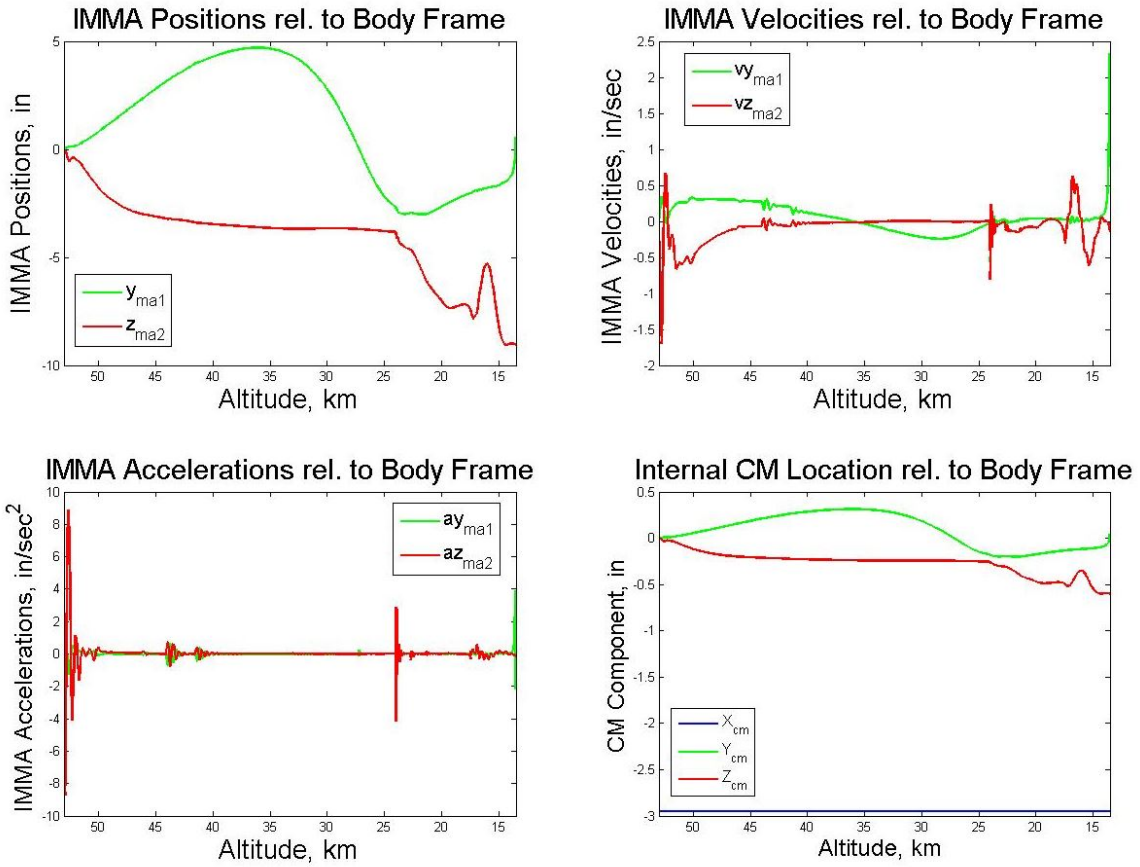

Figure 9.13: Guided trajectory G6, IMMA kinematics and CM internal location

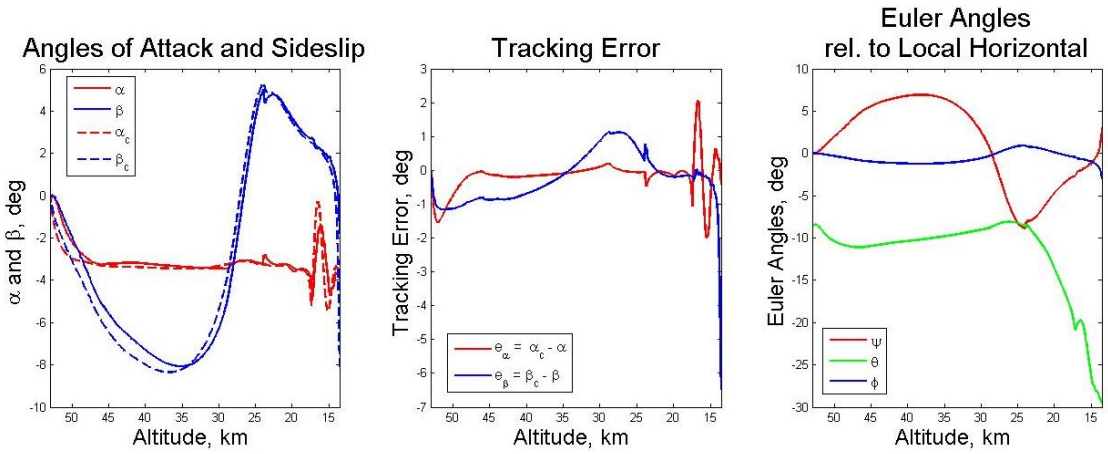

Figure 9.14: Guided trajectory G7, guidance commands and tracking performance

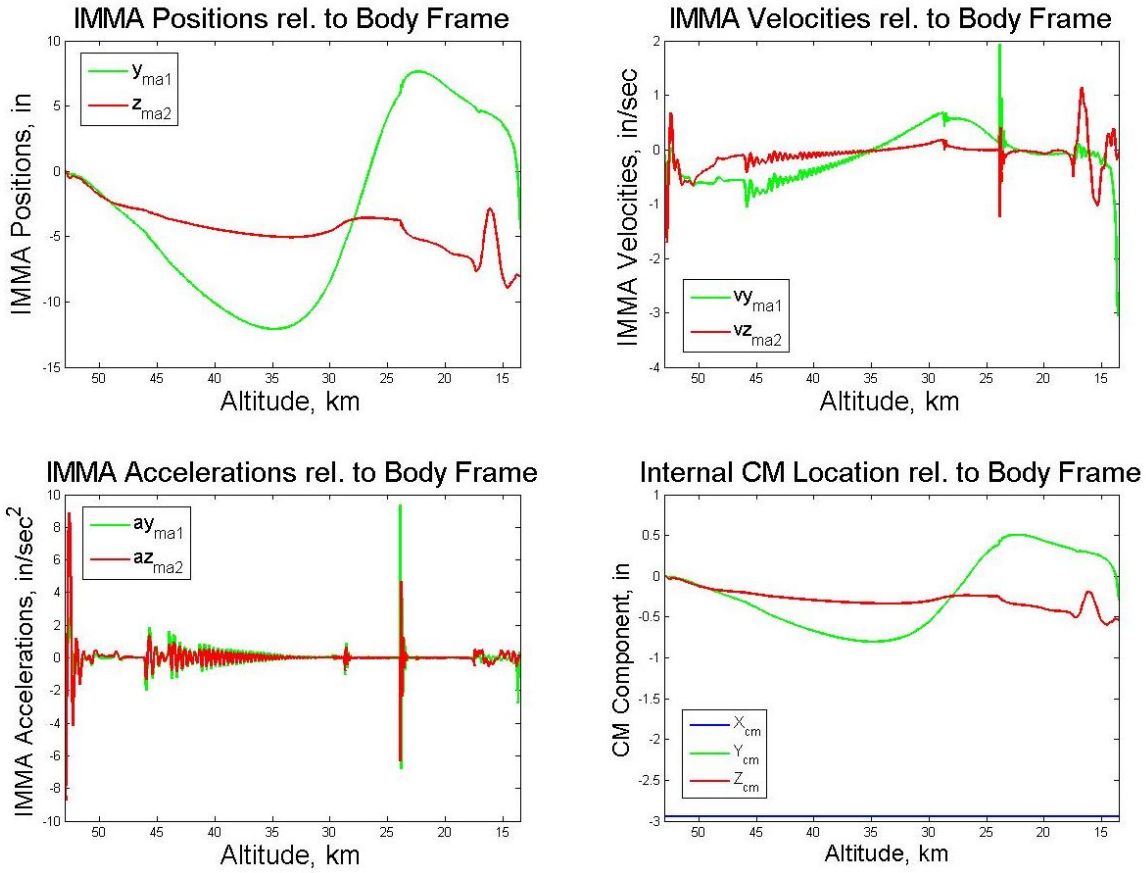

Figure 9.15: Guided trajectory G7, IMMA kinematics and CM internal location

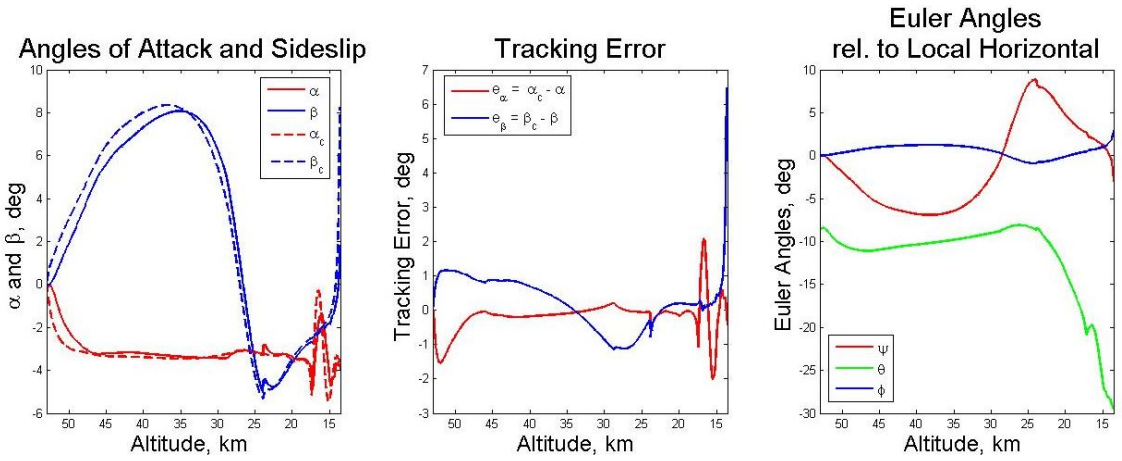

Figure 9.16: Guided trajectory G8, guidance commands and tracking performance

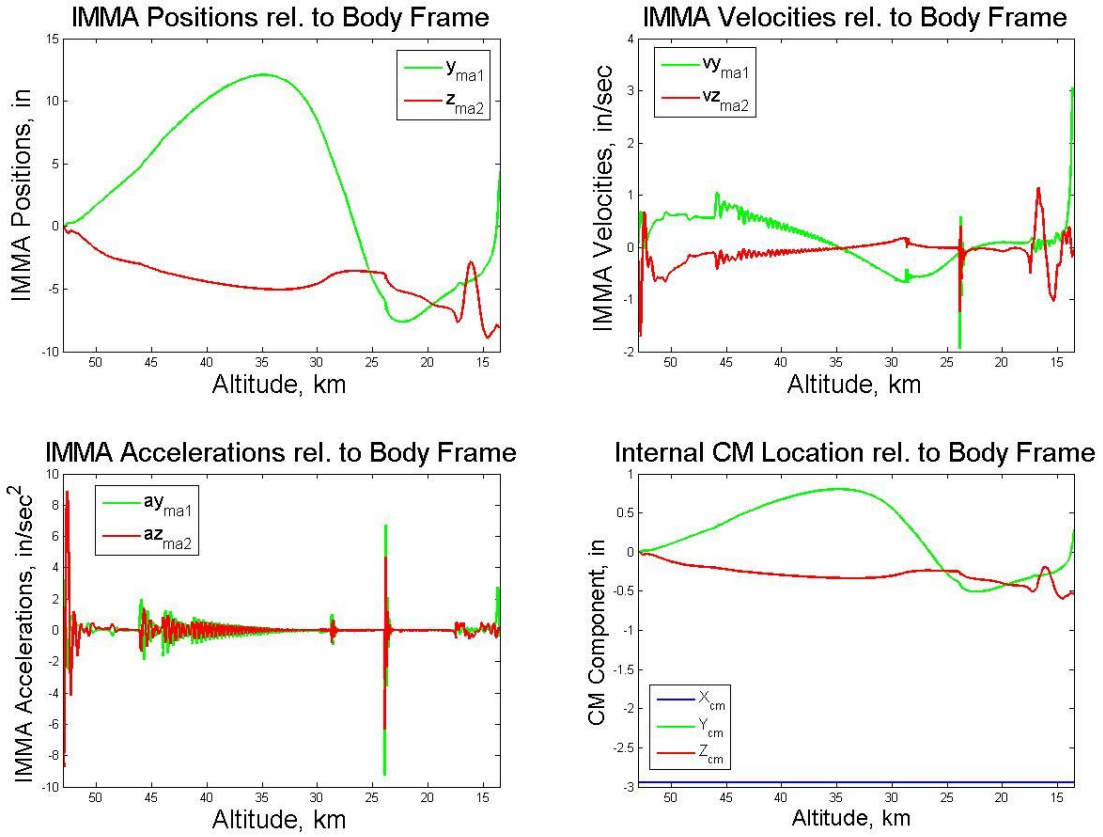

Figure 9.17: Guided trajectory G8, IMMA kinematics and CM internal location

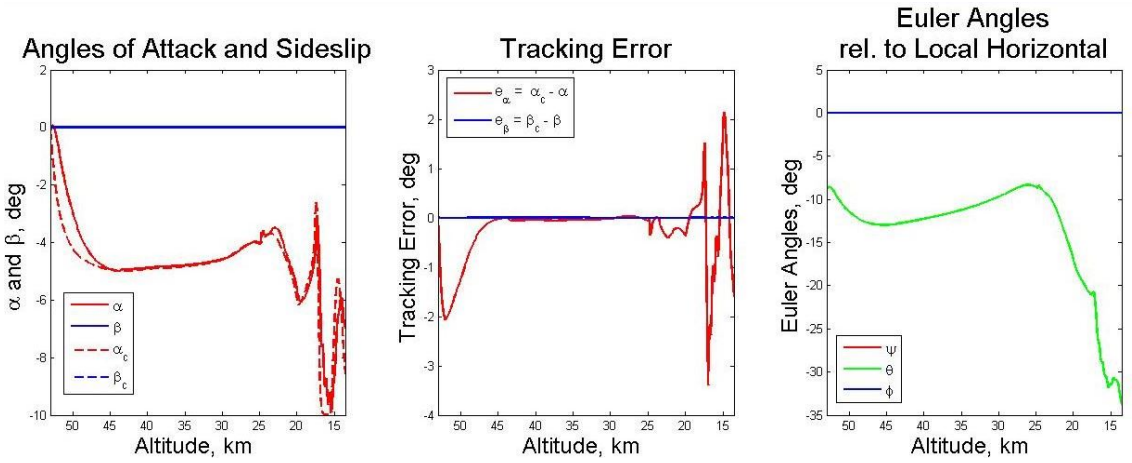

Figure 9.18: Guided trajectory G9, guidance commands and tracking performance

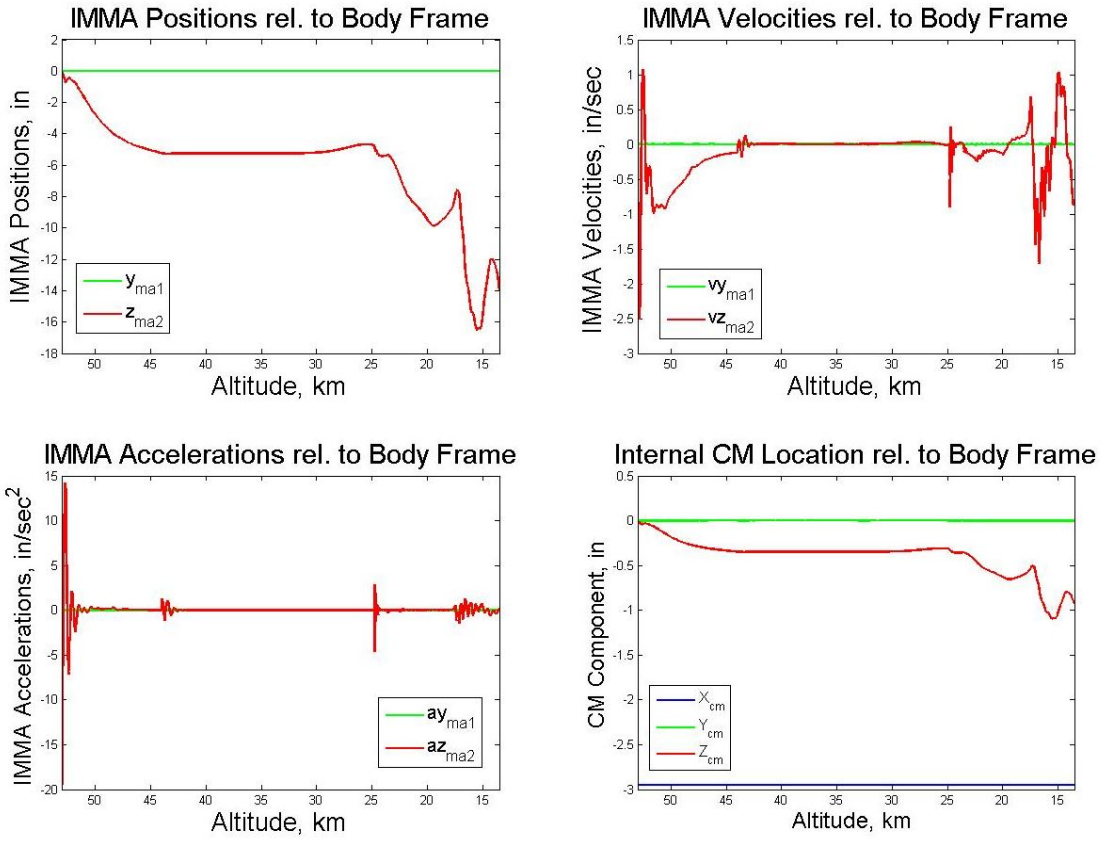

Figure 9.19: Guided trajectory G9, IMMA kinematics and CM internal location

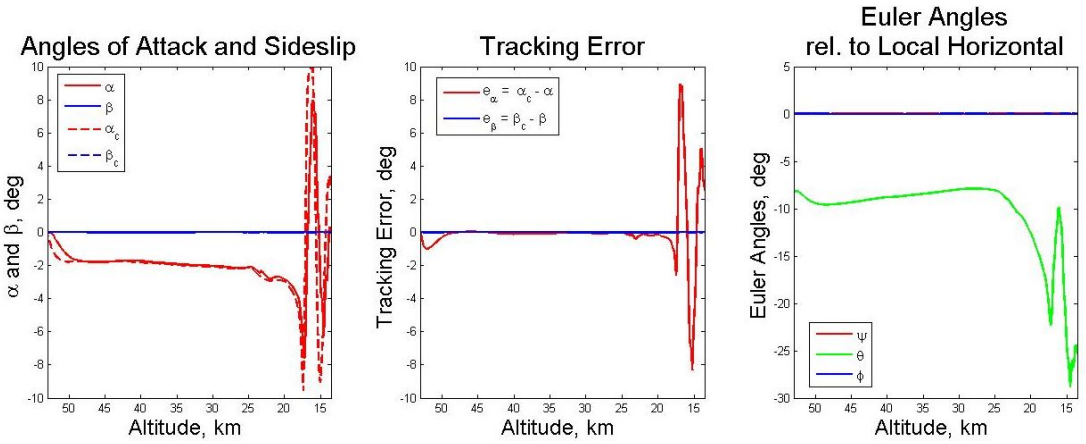

Figure 9.20: Guided trajectory G10, guidance commands and tracking performance

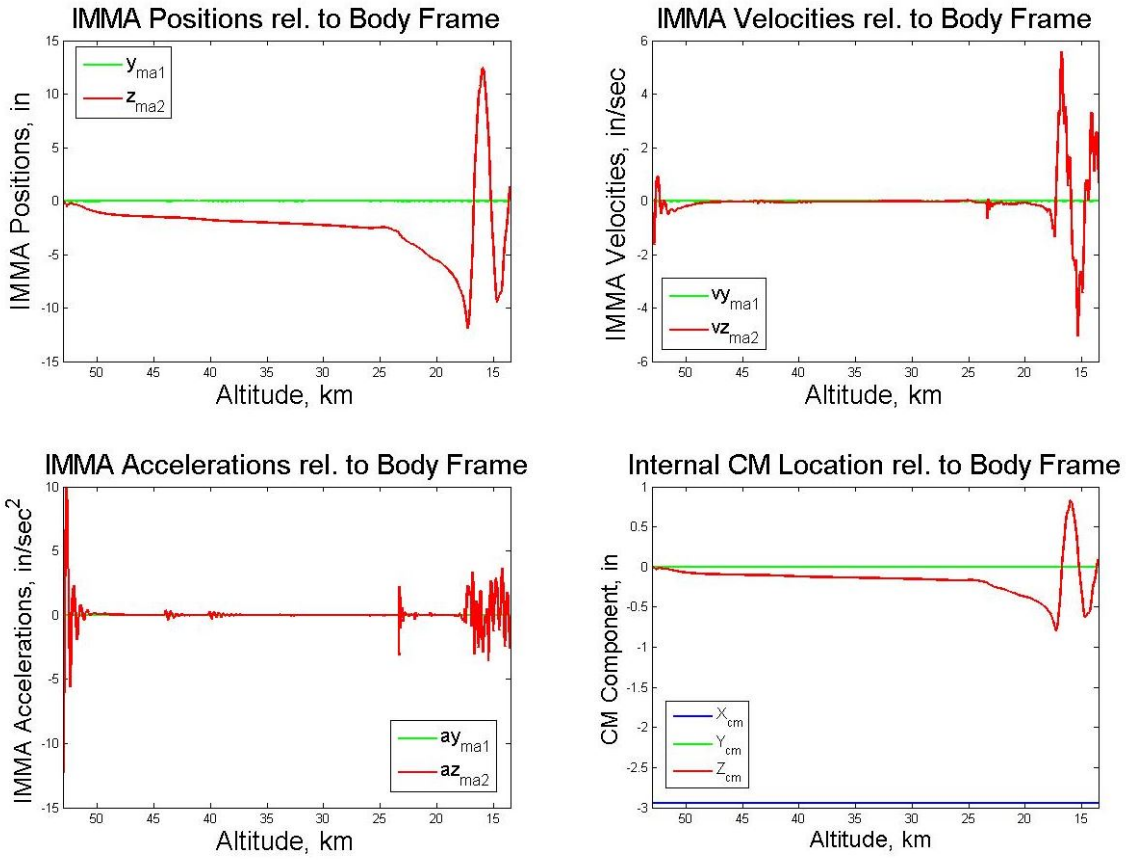

Figure 9.21: Guided trajectory G10, IMMA kinematics and CM internal location

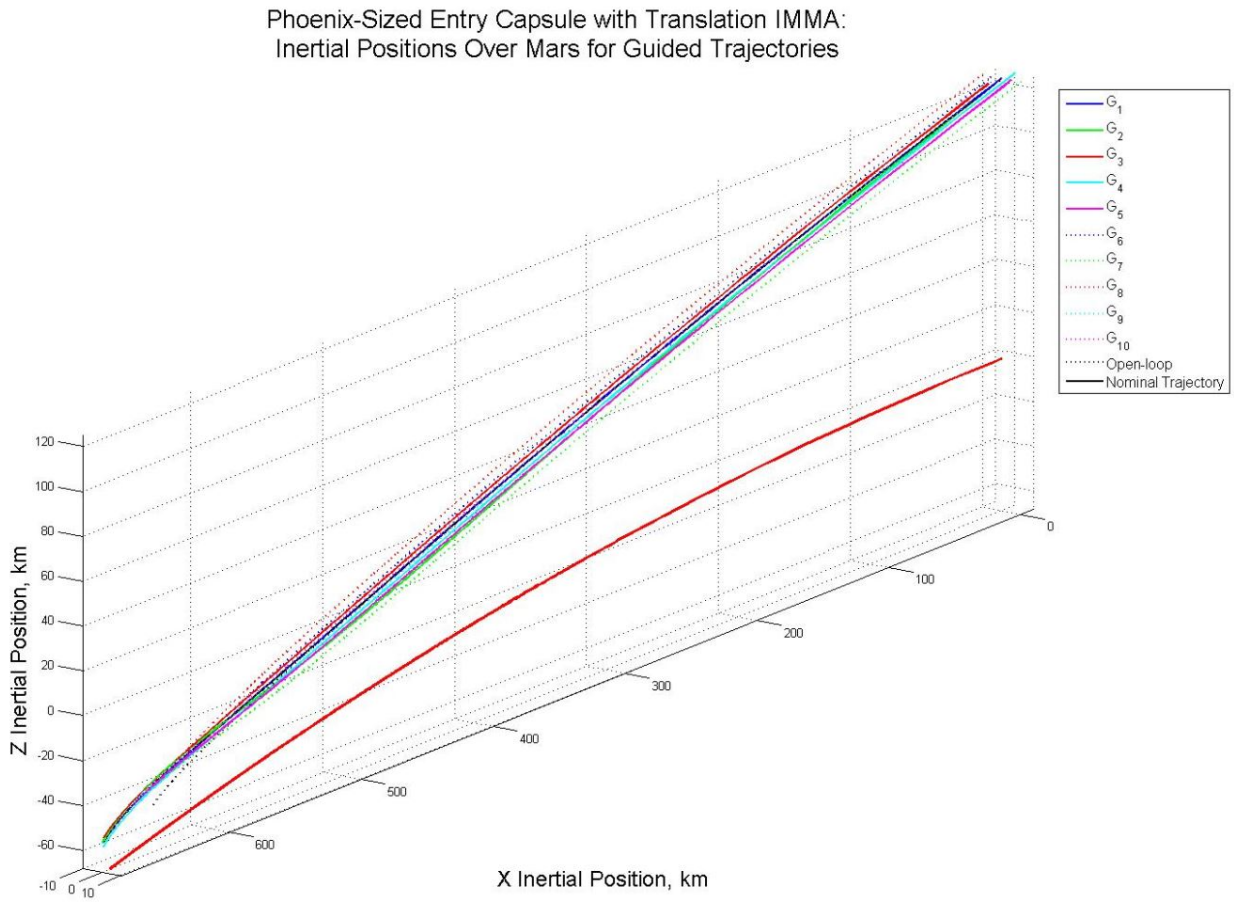

Figure 9.22: Guided trajectories over Mars with respect to the inertial frame

Chapter 10

HIAD Closed-loop Guidance Simulations

Nonlinear entry guidance simulations of the 8 DOF translation and rotation HIAD systems of Chapter 5 for feedback LQ integral guidance command tracking were implemented with MATLAB and Simulink. Roll attitude dynamics were included for both systems. The simulations use an ode45 solver with a relative tolerance of $1e-6$ to integrate the nonlinear equations of motion. The HIADS were assumed inflated to their nominal aeroshell diameter of 8.3 m and treated as fully rigid. No atmospheric winds were modeled. The feedback gains for each vehicle from Chapter 6 are implemented using linear interpolation between the design point altitudes along with the angle of attack and sideslip command laws developed in Chapter 7. Guidance angle of attack and sideslip commands were limited to a maximum of $\pm$ 10 degrees. No actuator constraints were imposed, but the IMMA stayed within the geometric envelope of the HIADs for all of the guidance simulations. The controllers operate between the same altitudes as the Phoenix-sized entry capsule translation IMMA system because the HIAD reference vehicle has the same ballistic coefficient. Chapter 10 differences from Chapter 9 include: the HIAD vehicle systems have greater mass and inertia than the rigid entry capsule system, guidance simulations include different off-nominal initial conditions, terminal targets include nonzero cross-range positions, and the HIAD IMMA parameters and configurations are different from the IMMA system of the rigid entry capsule. Recall, for the HIAD systems all vehicle parameters are the same with exception of the IMMA actuator paths, either translation or rotation relative to the rigid vehicle structure. The same vehicle parameters were chosen in order to compare guidance performance and mechanical power between the two IMMA systems.

All terminal targets are placed at the same down-range position of 695.5 km at parachute altitude 13.53 km. The nominal trajectory to reach this down-range target for zero terminal cross-range position was developed in Chapter 7. 11 guidance simulations were run for off-nominal initial entry conditions from this reference trajectory for each HIAD vehicle system.

The same respective initial entry conditions and same terminal targets for each of the 11 guided trajectories were implemented for both systems. Table 10.1 and Table 10.2 provide the initial conditions, terminal target locations, and terminal range and cross-range miss distances for both HIAD systems. Guided trajectory G0 corresponds to off-nominal initial angle of attack. Guided trajectories G1−G4 correspond to off-nominal initial angle of attack and terminal targets with nonzero cross-range positions. Guided trajectories G5, G6, G9, and G10 correspond to off-nominal initial angle of attack and initial range positions. G7 and G8 correspond to off-nominal initial angle of attack and initial flight path angle. Figure pairs for guidance command tracking and IMMA internal motion are shown for each guided trajectory for both IMMA systems. The first figure of each pair provides command guidance angles, error in tracking the guidance command angles, and Euler angles relative to the local horizontal versus altitude. The second figure contains IMMA internal motion and CM internal motion versus altitude. The figures are presented side by side for each IMMA system for clear comparison of command tracking performance and the IMMA internal motion between the two systems.

Note that the translation IMMA system does not shift the composite vehicle CM location in the $\underline{x}_c$ direction due to its planar orientation. However, the rotation IMMA configuration can induce CM shifts in the positive $\underline{x}_c$ direction, (less than 1.5 inches) shown in the internal CM location plots below. A shift of the CM in the positive $\underline{x}_c$ direction provides a slight increase in pitch and yaw stability due to a reduced moment arm between the CM and aerodynamic center of pressure. The translation IMMA system was tuned with longer rise times than the rotation IMMA system, shown in the step response plots in control tuning of Chapter 6. Difficulty arose in tuning the translation controllers for IMMA velocities greater than 2 in/s which ultimately led to the sluggish tracking performance per altitude compared with the rotation IMMA system. However, the translation IMMA velocity limits are consistent with internal CM motion limits from the 6 DOF HIAD CM control study in Reference [20]. Although the translation IMMA HIAD system is sluggish compared to the rotation system, it is quite quite capable of significant down-range and cross-range guidance. Down-range and cross-range guidance for each trajectory is shown for the translation system in Figure 10.1 and for the rotation system in Figure 10.2. These trajectories are shown with respect to the inertial frame over the surface of Mars for both vehicles in Figure 10.47 and Figure 10.48.

The initial roll attitude for all guided trajectories was zero degrees. Only guided trajectories G1−G4 required cross-range and down-range guidance. Guided trajectories G0 and G5−G10 involved down-range guidance only requiring only pitch control to meet angle of attack commands. Only G1−G4 had simultaneous pitch and yaw control to meet respective guidance sideslip angle and angle of attack commands. Simultaneous pitch and yaw attitude changes induced small vehicle roll angles for these trajectories. However, the total vehicle roll angle for all guided trajectories for both systems remained below ±5 degrees. G1−G2 corresponded to guidance to down-range targets with ∓5 km cross-range offsets from entry. G3−G4 corresponded to maximum cross-range guidance to targets at ∓ 10 km cross-range offsets from entry. The uncontrolled roll angle remaining below ±5 degrees is

clearly shown in Euler angle plots versus altitude. These plots for G1,G2,G3 and G4 for the translation system and rotation system are shown side by side in Figures 10.7−10.8, Figures 10.11−10.12, Figures 10.15−10.16, and Figures 10.19−10.20 respectively. Angle of attack and sideslip tracking included in these figures show the rotation IMMA system has quicker angle of attack and sideslip tracking response time and smaller guidance command tracking errors.

The superior sideslip command tacking for the rotation IMMA system led to smaller cross-range target misses by 470 m for G1 and G2, and 159 m for G3 and G4. The HIAD with rotation IMMA also had higher altitude convergence to the cross-range targets, see Figure 10.2 for the rotation system compared to the translation IMMA HIAD system in Figure 10.1. The higher altitude convergence can also be seen by examining altitudes for the initial peak sideslip angle for both systems for G1 and G3. G1 and G3 are guidance to cross-range targets at 5 km and 10 km offset from entry where G2 and G4 are respective guidance to the same cross-range distances, but in the opposite direction. The initial peak sideslip angle for the translation IMMA system for G1 and G3 occurs at 30 km and 27.5 km altitude respectively, see Figure 10.7 and Figure 10.15. For the rotation IMMA system for G1 and G3, the initial peak sideslip angle occurs at 37.5 km and 40 km altitudes respectively, see Figure 10.8 and Figure 10.16. The initial peak sideslip angle for both systems corresponds to the vehicle reaching the desired cross-range target, after which sidelisp reversals are made for both systems to correct for cross-range overshoots. Notice that the peak IMMA displacements effectively doubles for both systems at the initial peak cross-range angle altitudes for guidance trajectories G3 compared to G1 for both systems. This indicates there is sufficient IMMA control authority to raise cross-range convergence altitude for both systems for G1 and G2.

The doubling of IMMA displacements at the initial peak sidelsip angle altitude for the translation system for G1 and G3 can be seen in comparison of Figure 10.9 to Figure 10.17. The doubling of IMMA displacements at the initial peak sidelsip angle altitude for the rotation system for G1 and G3 can be seen in comparison of Figure 10.10 to Figure 10.18. Adding an over-control gain similar to the angle of attack command law to increase commanded sidelsip angle and also increasing the maximum sideslip angle limits would lead to higher cross-range convergence for both systems. This would reduce cross-range miss for the more sluggish translation system and permit greater distance for cross-range targets for both systems. It would also reduce control effort at lower altitudes for both systems, especially the translation system. Reducing IMMA motion is fundamental to keeping power requirements low, see the mechanical power discussion in the next chapter. The IMMA mass for the translation system could also be increased for greater CM control authority to enable higher altitude cross-range convergence. For the rotation system either the actuator lever arm to the IMMA CM from the fixed vehicle rotation point could be increased or the IMMA mass could be increased for higher altitude cross-range convergence.

For the translations system one or more design points could be added combined with control tuning to quicken command tracking response. This could also aid in guided trajectories

where the translation had oscillatory IMMA motion. Figures 10.17 and 10.21 show small IMMA oscillation (< 0.5 in/s) exists for the translation systems for guidance trajectories G3 and G4 starting around 37 km and nulling out close to 25 km. The altitude of initial oscillation at 37 km is between two of the design point altitudes used in control tuning, 44km and 33 km. At 37 km altitude the feedback gain is linearly interpolated between these two altitudes. Adding an extra design point altitude for control tuning between these altitude could aid in reducing IMMA oscillation. An additional step to reduce IMMA oscillation would be to increase penalties on actuator displacement and velocity states in the state and control weighting matrices. Note that for the less taxing guided trajectory for G0 involving down-range guidance only for an off-nominal initial angle of attack, IMMA oscillations between 35km and 22.5 km altitude are negligible, see Figure 10.5. In some instances the IMMA translation system even had slightly smaller range misses than the rotation IMMA system.

The IMMA translation system had slightly smaller range misses than the rotation IMMA system of 4 m for G1 and G2 and 12 m for G3 and G4. However, the cross-range miss distances are much larger, 470 m and 159 m respectively. For down-range guidance only, guided trajectories G0 and G5−G10, the rotation IMMA system has smaller peak guidance command tracking error and quicker tracking response time. The superior rotation IMMA system tracking performances is evident in guidance trajectory G0. Figure 10.3 compared to Figure 10.4 shows the angle of attack tracking response time and tracking error is smaller for the rotation IMMA system. This led to smaller down-range miss of 10 m, though both systems were able to provide substantial guidance. A ballistic entry for the same initial conditions of G0 has a terminal miss of 37 km. Around 25 km both vehicles transition from the hypersonic flight regime to the super-sonic flight regime. This leads to a changing dynamic pitch moment coefficient from a previous constant negative value in the hypersonic flight regime to an increasing and positive value. The dynamic pitch moment coefficient transition is shown in the aerodynamic database listed in Chapter 8. This aerodynamic change contributes to inducing counteractive and excitation pitch moments. However, both systems are able to correct for this disturbance and continue angle of attack tracking below 25 km altitude.

The superior tracking performance of the rotation IMMA system is most evident for guided trajectory G7. G7 corresponded to an off-nominal flight path angle pitched further below the horizontal than the nominal flight path angle. This led to an initial range error greater than 40 km behind the nominal range at that initial 53 km control altitude. Both systems are able to converge towards the nominal trajectory and correct for the majority of this initial miss. However, the terminal range miss for the rotation IMMA system is smaller by more than 1 km than the translation system. In addition, the translation IMMA system had track oscillations at altitudes corresponding to large angle of attack command changes from full lift to reduced lift once the vehicle reached the nominal reference range. This initial large range miss required maximum angle of attack attitude for full lift to catch up to the nominal range. However, after catching up the nominal range reduced lift was required to

correct for range overshoots . Increasing the IMMA mass or additional design point control tuning could reduce IMMA oscillation for these large attitude changes. The rotation IMMA system also had IMMA oscillatory behavior, but at the tail end of the trajectory where the vehicle has the least amount of lift control authority for range control.

Increasing IMMA mass and adding an additional operation point or higher actuator velocity penalties for feedback control tuning could reduce these oscillations for both systems. However the guidance results for this G7 and all of 11 of the off-nominal initial entry conditions for both systems shows substantial guidance capability. An open-loop ballistic entry for G0 leads to a 37 km down-range miss, comapred to the 47 m and 37 m respective misses for the translation and rotation IMMA systems. For the same initial conditions as G7, an open loop ballistic trajectory would miss by 95 km compared to the terminal range miss of 1.28 km by the translation IMMA system and 130 m by the rotation system !

Overall the IMMA rotation system had superior guidance command tracking compared to the translation IMMA system. This consisted of: quicker response time, smaller tracking errors, smaller cross-range misses, and for the least and most taxing off-nominal down-range guidance trajectories G0 and G7 respectively, smallest terminal range misses. IMMA mechanical power requirements associated with both controllers are computed for each of the guidance trajectories using mechanical power models presented in the next chapter. Low mechanical power is shown for both systems, with smaller requirements for the rotation IMMA system. The low mechanical power combined with precision guidance capability for IMMA control support their application to future Mars Lander missions. The lower mechanical power for the rotation system combined with above guidance results indicate it is the preferable IMMA configuration.

Table 10.1: Simulation runs for HIAD with translation IMMA

Simulation	Initial Conditions				(Range,Cross-range) Target, km	Range Miss, km	Cross-range Miss, km
	γ, deg	(α, β), deg	V_∞, km/s	Inertial Position, km			
Open-loop	-12.25	(0,0)	5.6	(0, 0, -125)	(695.5, 0)	-37	0
Nominal	-12.25	(0, -3)	5.6	$(0, 0, -125)$	(695.5,0)	0	0
G0	-12.25	(0,0)	5.6	(0, 0, -125)	(695.5,0)	0.047	0
G1	-12.25	(0,0)	5.6	(0, 0, -125)	(695.5,-5)	0.004	-0.48
G2	-12.25	(0,0)	5.6	(0, 0, -125)	(695.5,5)	0.004	0.48
G3	-12.25	(0,0)	5.6	(0, 0, -125)	(695.5,-10)	-0.025	-0.16
G4	-12.25	(0,0)	5.6	(0, 0, -125)	(695.5,10)	-0.025	0.16
G5	-12.25	(0,0)	5.6	(-10, 0, -125)	(695.5,0)	0.33	0
G6	-12.25	(0,0)	5.6	(10, 0, -125)	(695.5,0)	-0.33	0
G7	-13	(0,0)	5.6	(0, 0, -125)	(695.5, 0)	-1.28	0
G8	-12	(0, 0)	5.6	(0, 0, -125)	(695.5, 0)	-0.63	0
G9	-12.25	(0, 0)	5.6	(-5, 0, -125)	(695.5,0)	0.22	0
G10	-12.25	(0, 0)	5.6	(5, 0, -125)	(695.5, 0)	- 0.10	0

Table 10.2: Simulation runs for HIAD with rotation IMMA

Simulation	Initial Conditions				(Range,Cross-range) Target, km	Range Miss, km	Cross-range Miss, km
	γ, deg	(α, β), deg	V_∞, km/s	Inertial Position, km			
Open-loop	-12.25	(0,0)	5.6	(0, 0, -125)	(695.5, 0)	-37	0
Nominal	-12.25	(0, -3)	5.6	$(0, 0, -125)$	(695.5,0)	0	0
G0	-12.25	(0,0)	5.6	(0, 0, -125)	(695.5,0)	0.037	0
G1	-12.25	(0,0)	5.6	(0, 0, -125)	(695.5,-5)	0.008	0.01
G2	-12.25	(0,0)	5.6	(0, 0, -125)	(695.5,5)	0.008	-0.01
G3	-12.25	(0,0)	5.6	(0, 0, -125)	(695.5,-10)	-0.037	-0.001
G4	-12.25	(0,0)	5.6	(0, 0, -125)	(695.5,10)	-0.037	0.001
G5	-12.25	(0,0)	5.6	(-10, 0, -125)	(695.5,0)	0.31	0
G6	-12.25	(0,0)	5.6	(10, 0, -125)	(695.5,0)	-0.42	0
G7	-13	(0,0)	5.6	(0, 0, -125)	(695.5, 0)	0.13	0
G8	-12	(0, 0)	5.6	(0, 0, -125)	(695.5, 0)	-0.88	0
G9	-12.25	(0, 0)	5.6	(-5, 0, -125)	(695.5,0)	0.21	0
G10	-12.25	(0, 0)	5.6	(5, 0, -125)	(695.5, 0)	- 0.16	0

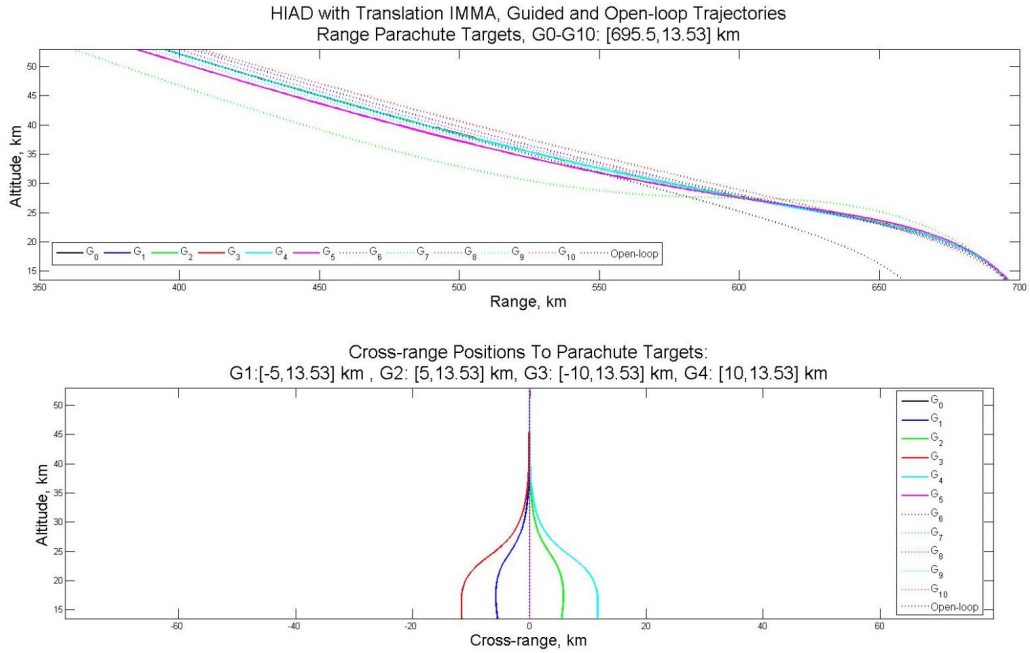

Figure 10.1: Translation IMMA HIAD: range and cross-range per altitude

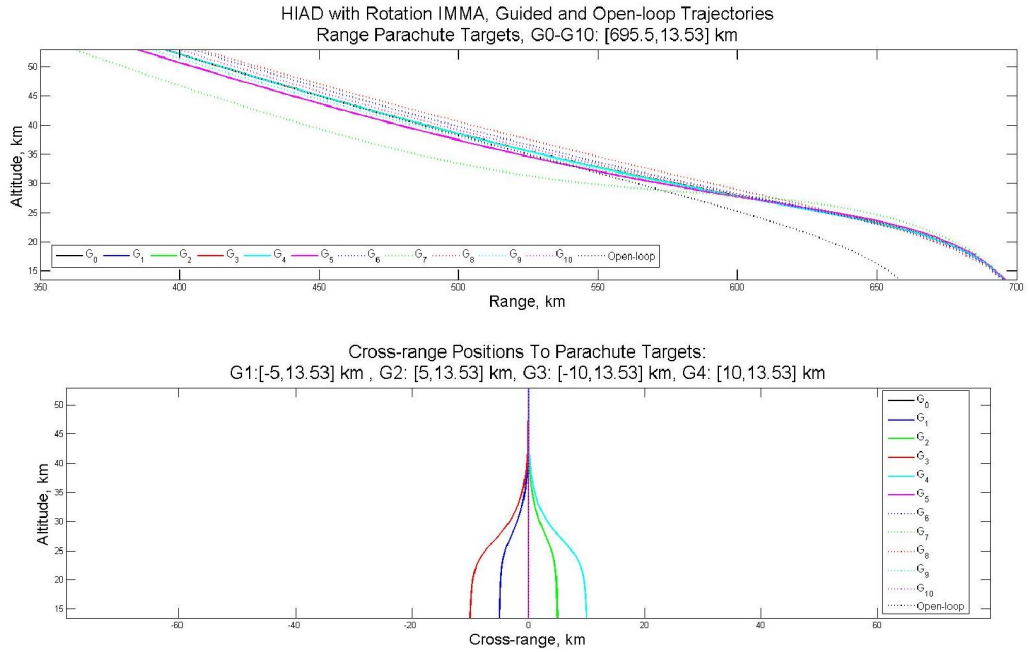

Figure 10.2: Rotation IMMA HIAD: range and cross range per altitude

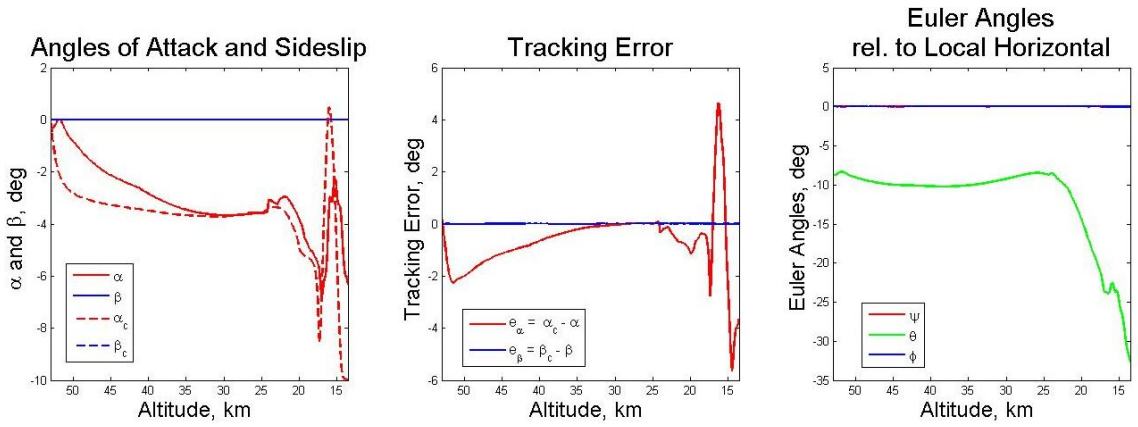

Figure 10.3: G0 Translation IMMA, guidance commands and tracking performance

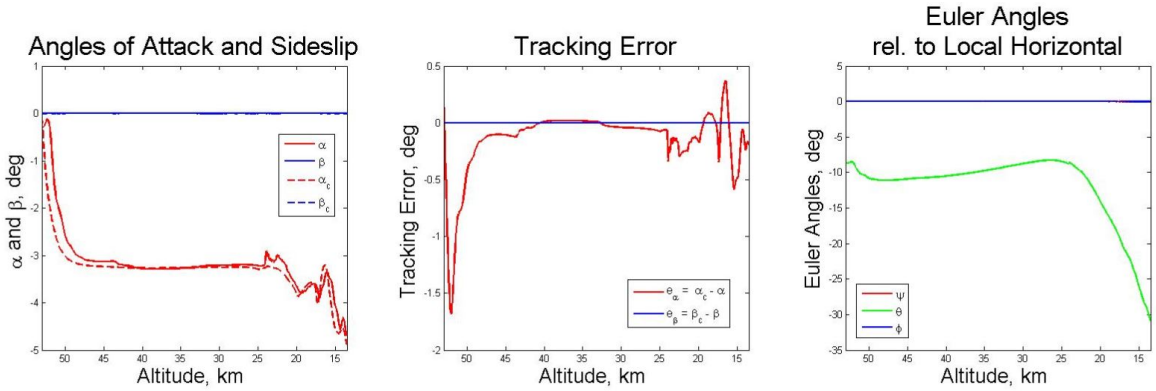

Figure 10.4: G0 Rotation IMMA, guidance commands and tracking performance

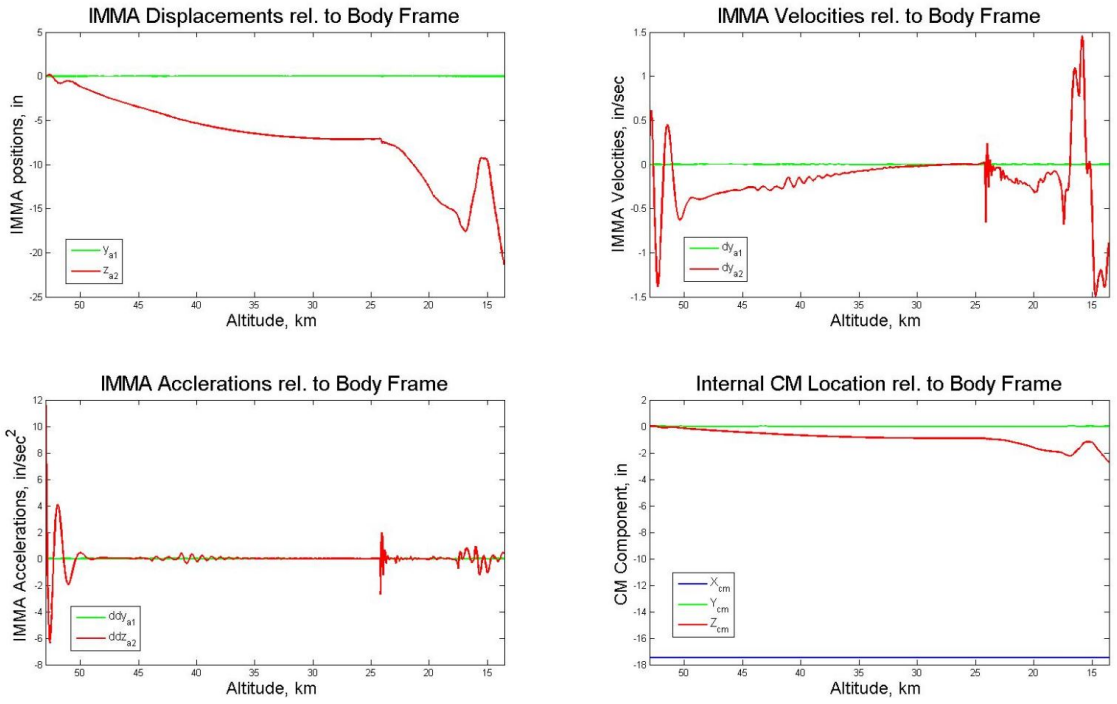

Figure 10.5: G0 Translation IMMA, IMMA kinematics and CM internal location

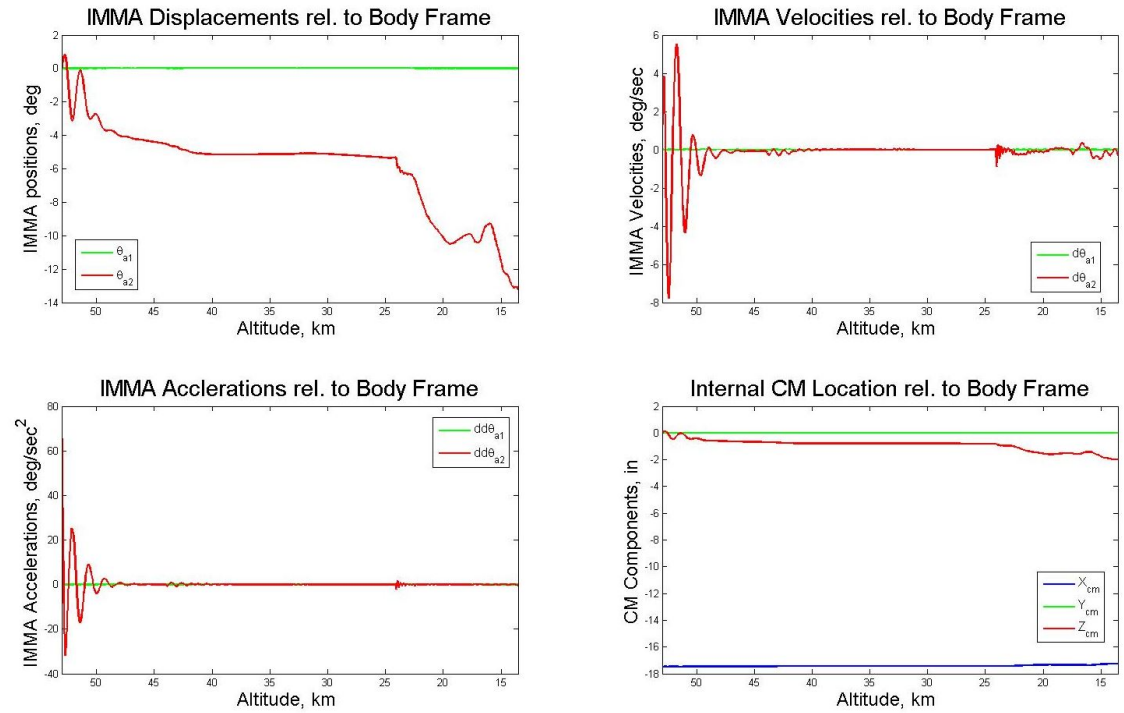

Figure 10.6: G0 Rotation IMMA, IMMA kinematics and CM internal location

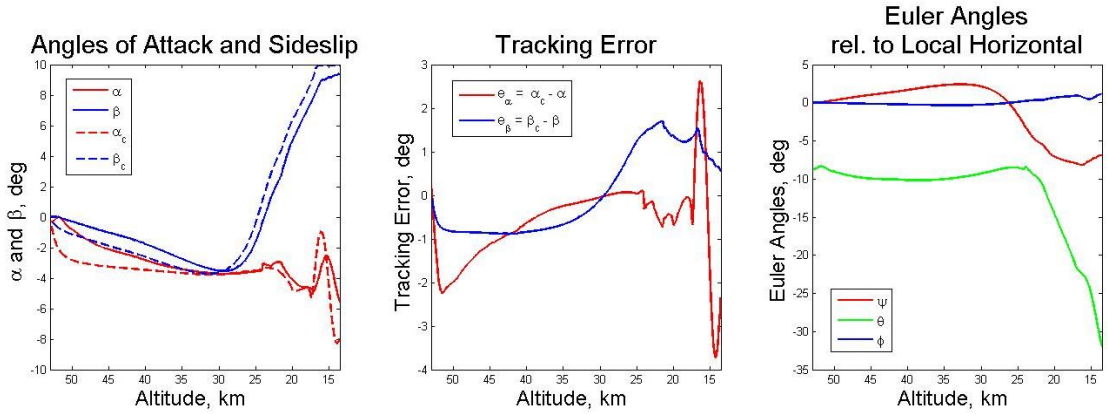

Figure 10.7: G1 Translation IMMA, guidance commands and tracking performance

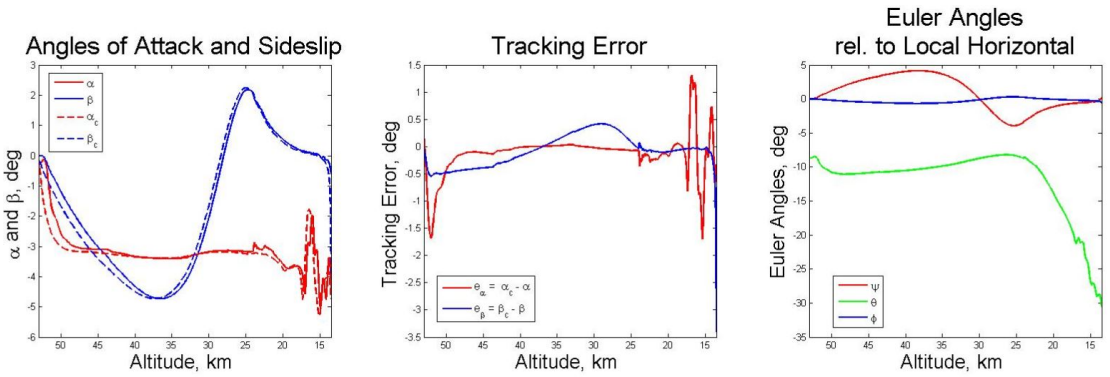

Figure 10.8: G1 Rotation IMMA, guidance commands and tracking performance

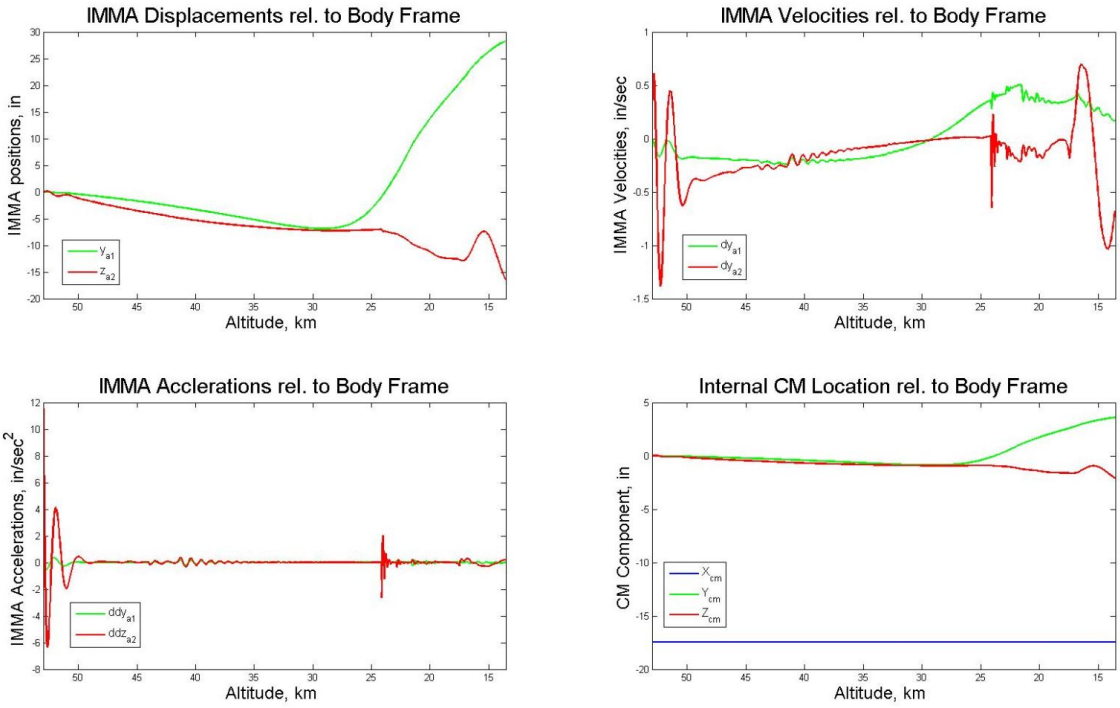

Figure 10.9: G1 Translation IMMA, IMMA kinematics and CM internal location

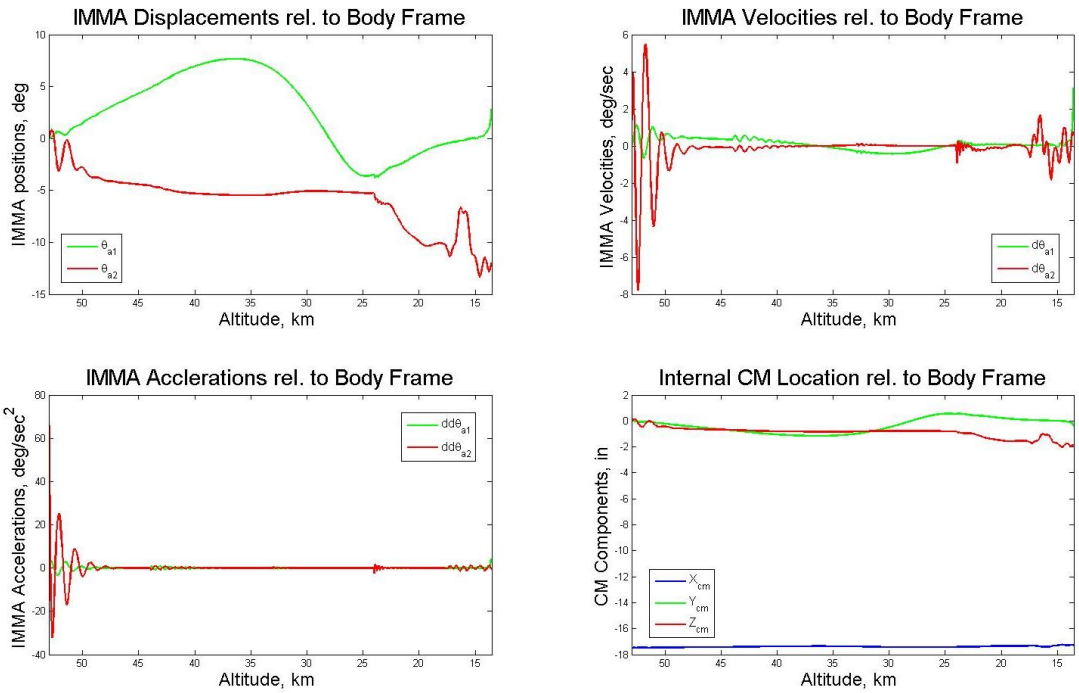

Figure 10.10: G1 Rotation IMMA, IMMA kinematics and CM internal location

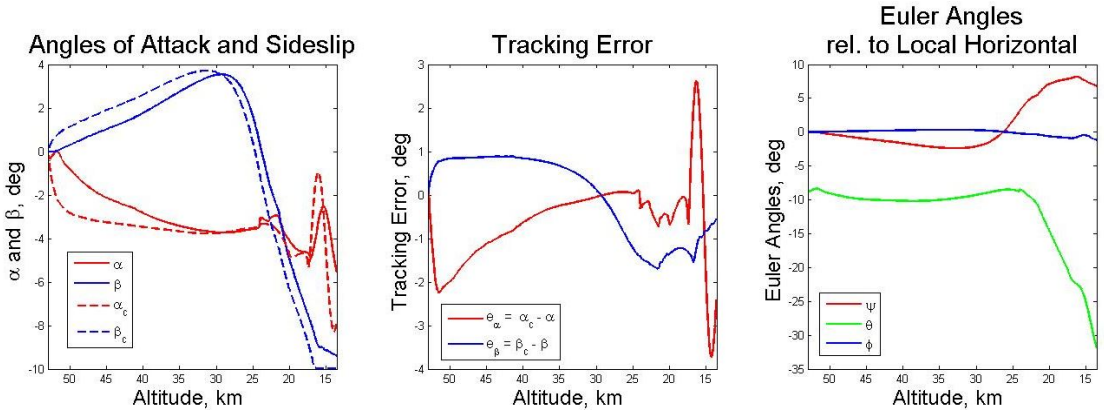

Figure 10.11: G2 Translation IMMA, guidance commands and tracking performance

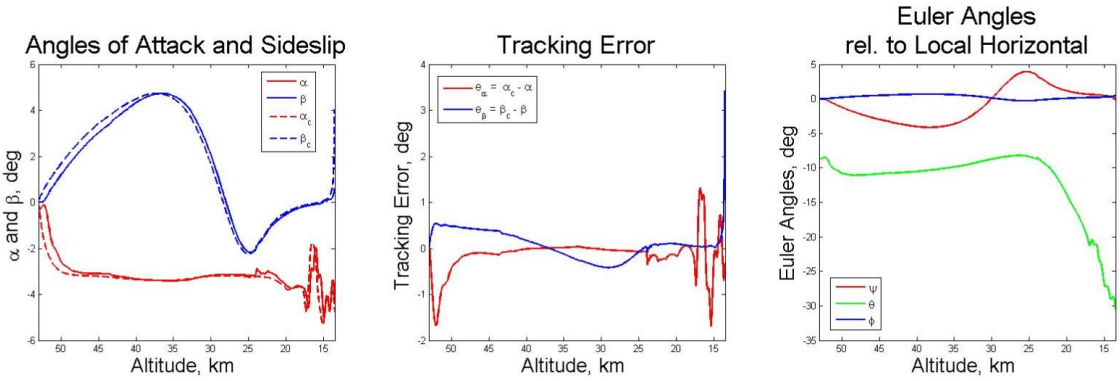

Figure 10.12: G2 Rotation IMMA, guidance commands and tracking performance

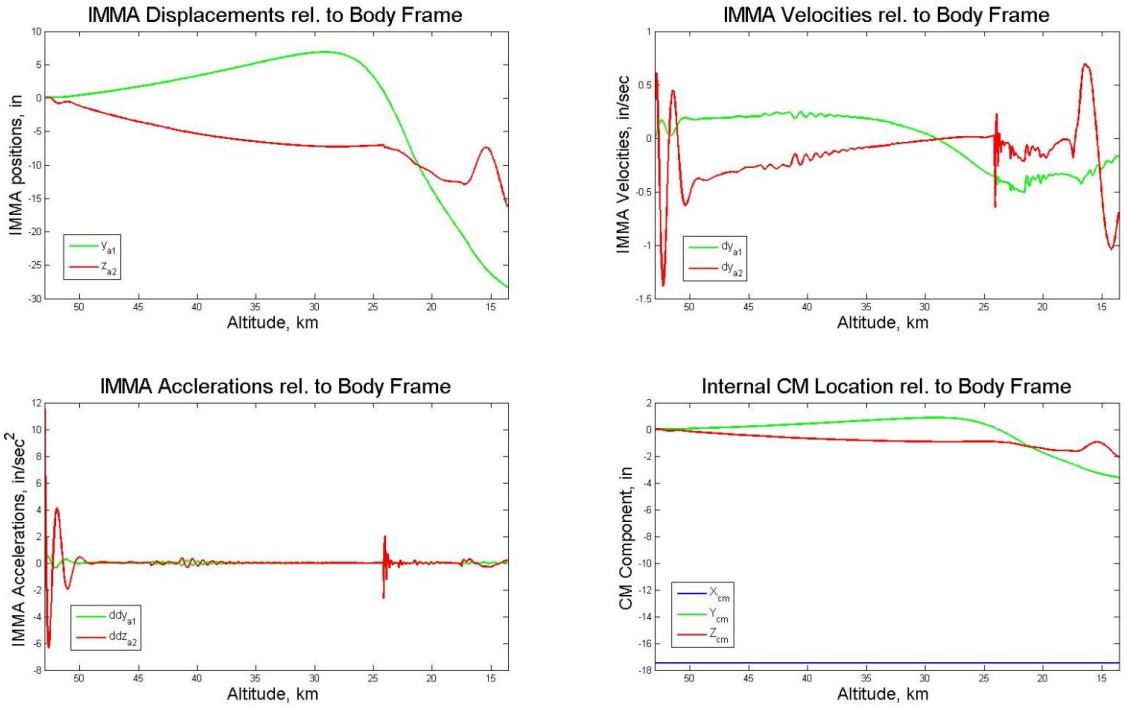

Figure 10.13: G2 Translation IMMA, IMMA kinematics and CM internal location

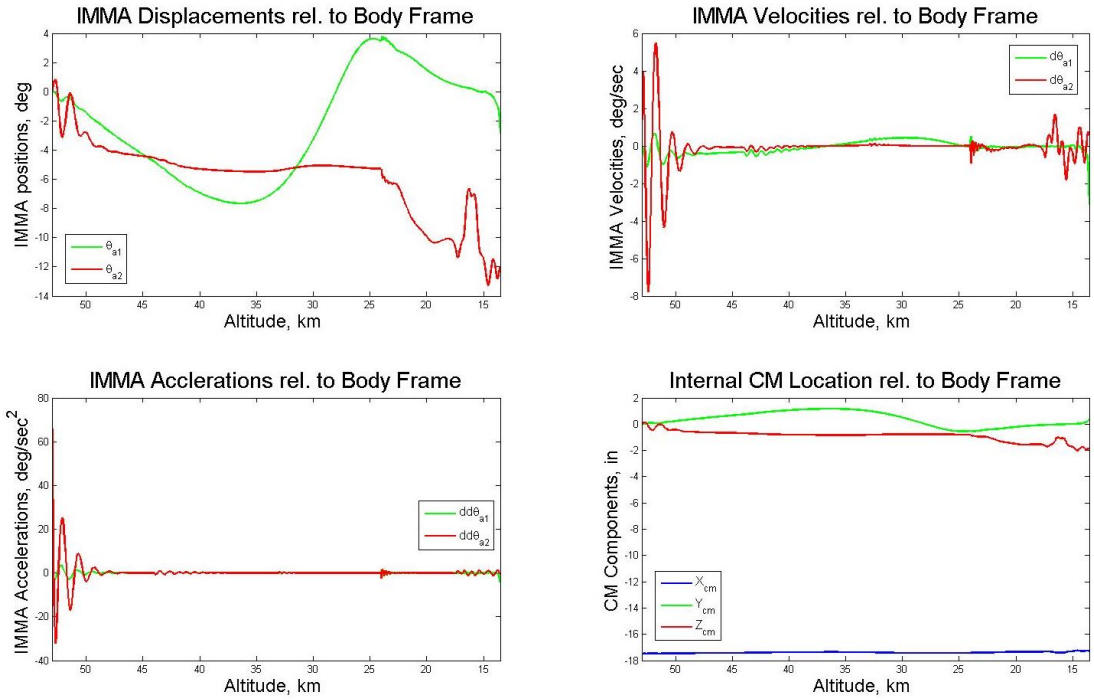

Figure 10.14: G2 Rotation IMMA, IMMA kinematics and CM internal location

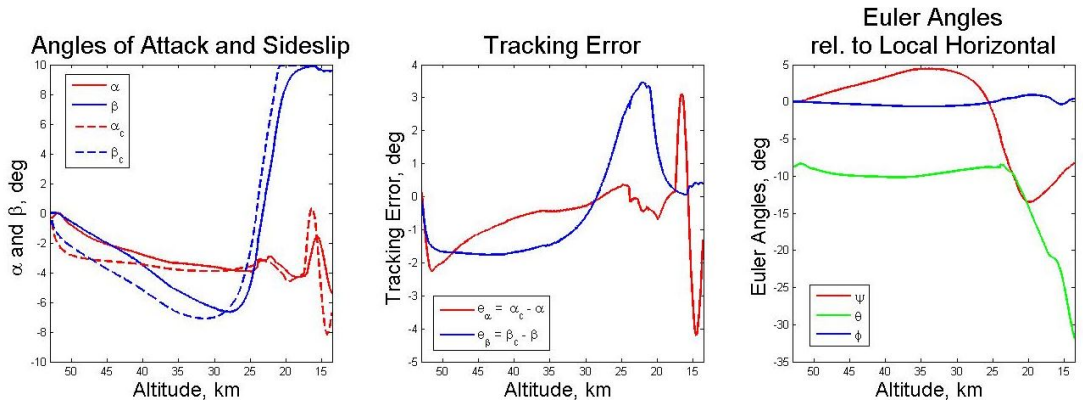

Figure 10.15: G3 Translation IMMA, guidance commands and tracking performance

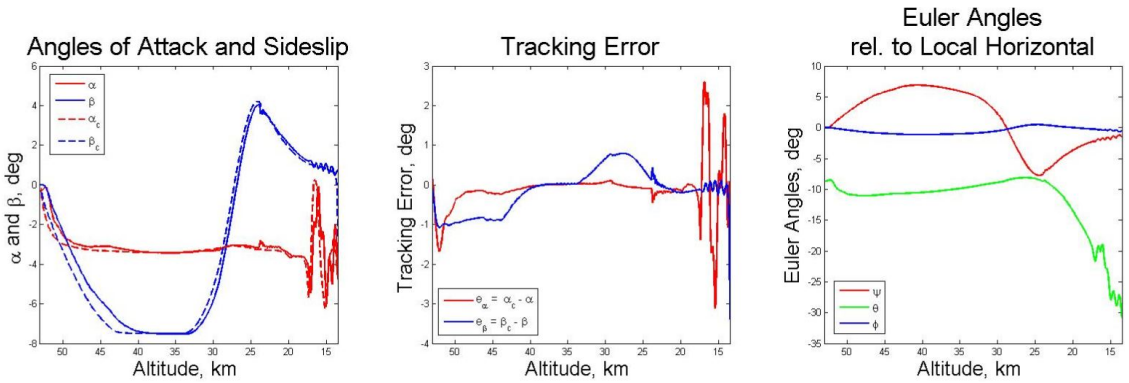

Figure 10.16: G3 Rotation IMMA, guidance commands and tracking performance

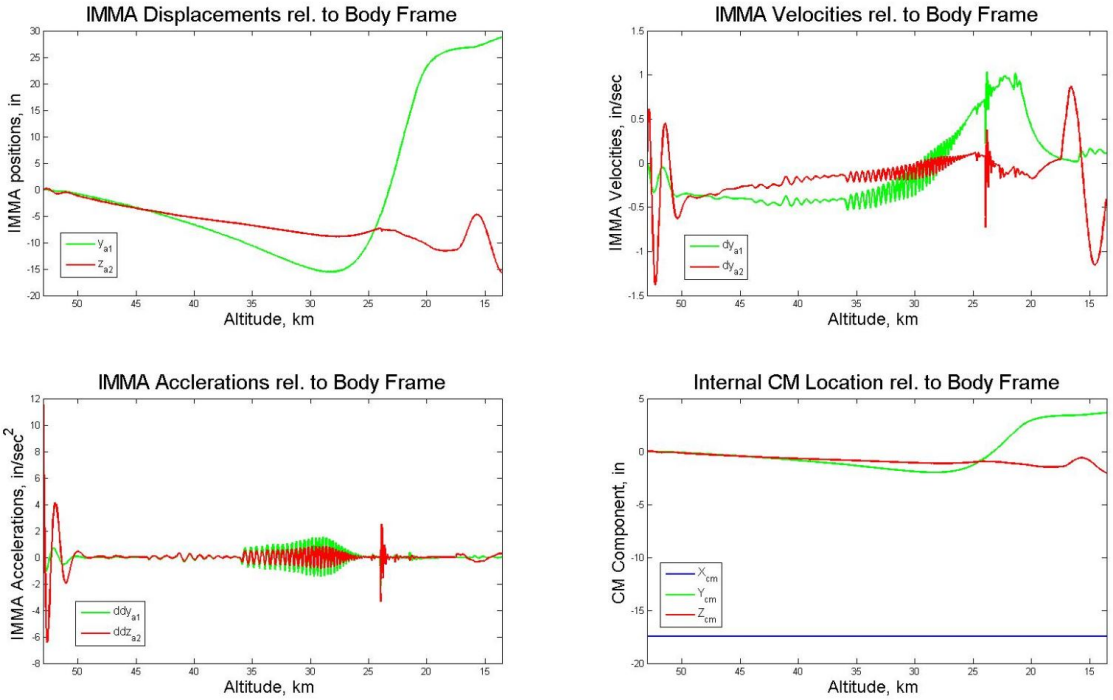

Figure 10.17: G3 Translation IMMA, IMMA kinematics and CM internal location

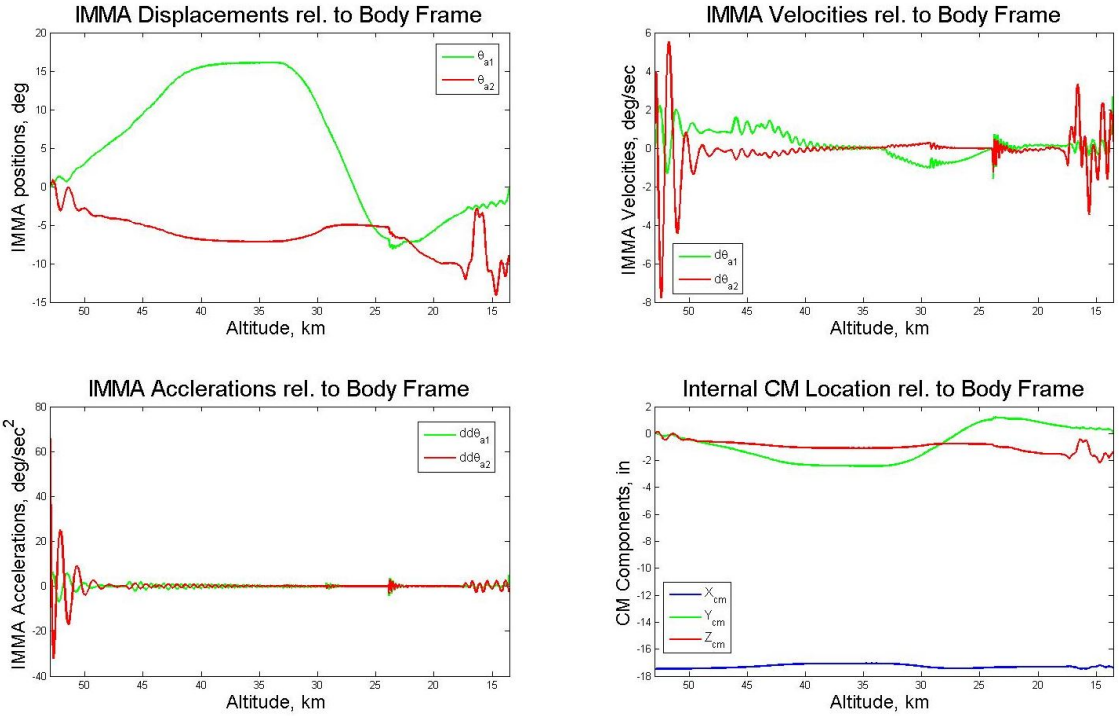

Figure 10.18: G3 Rotation IMMA, IMMA kinematics and CM internal location

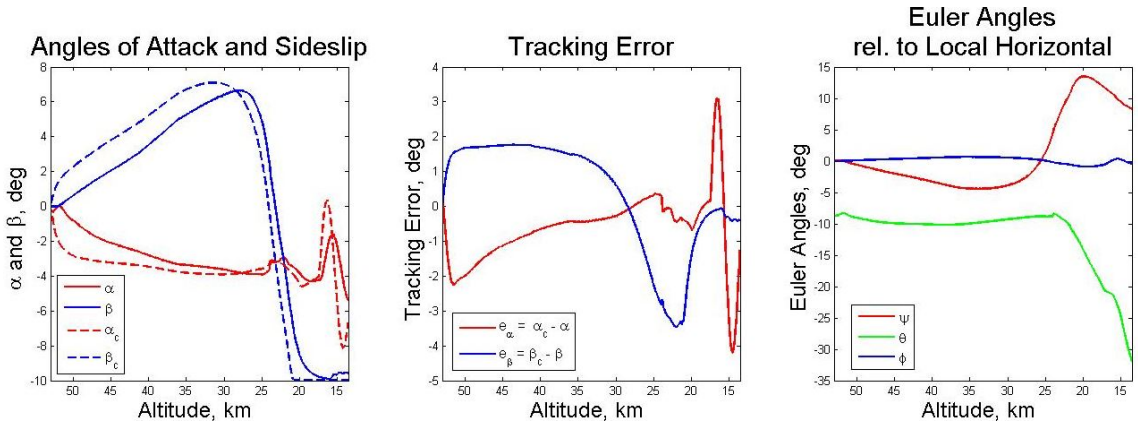

Figure 10.19: G4 Translation IMMA, guidance commands and tracking performance

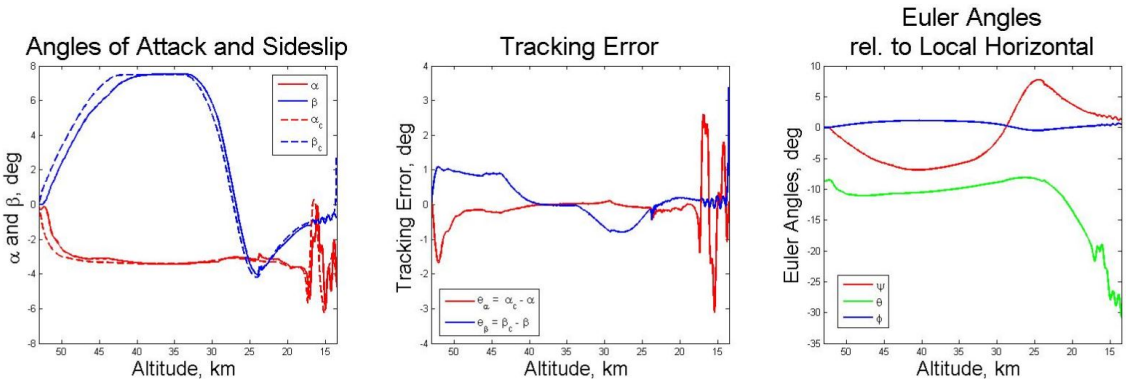

Figure 10.20: G4 Rotation IMMA, guidance commands and tracking performance

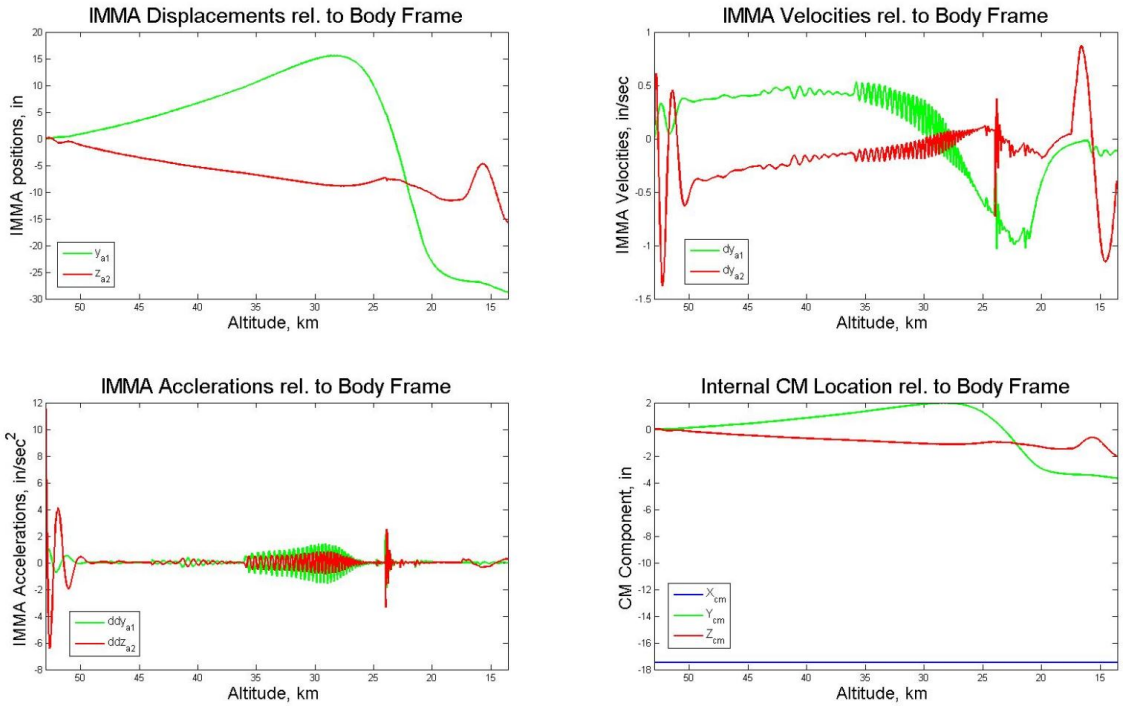

Figure 10.21: G4 Translation IMMA, IMMA kinematics and CM internal location

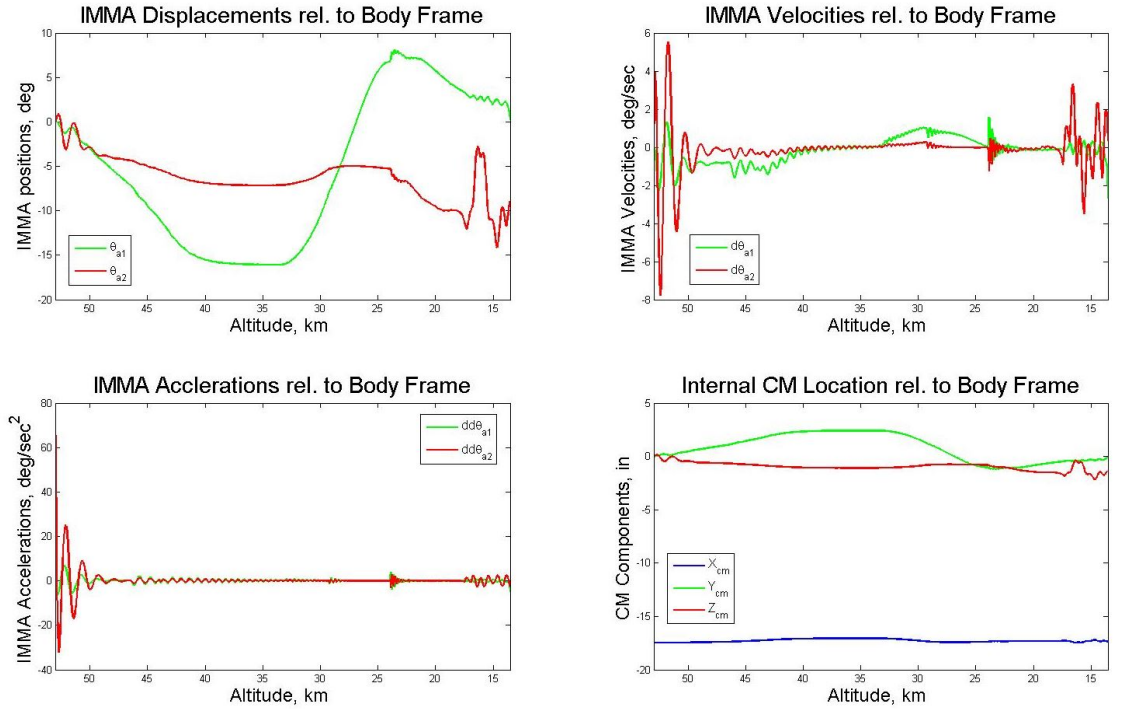

Figure 10.22: G4 Rotation IMMA, IMMA kinematics and CM internal location

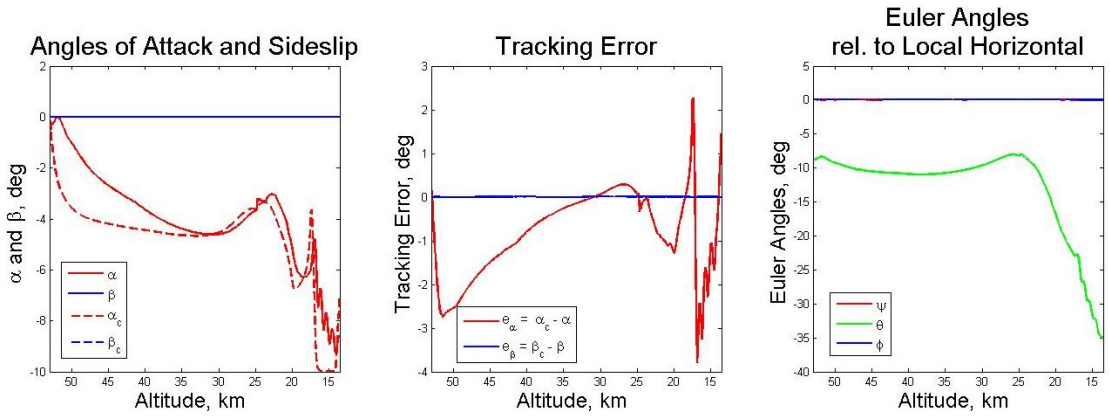

Figure 10.23: G5 Translation IMMA, guidance commands and tracking performance

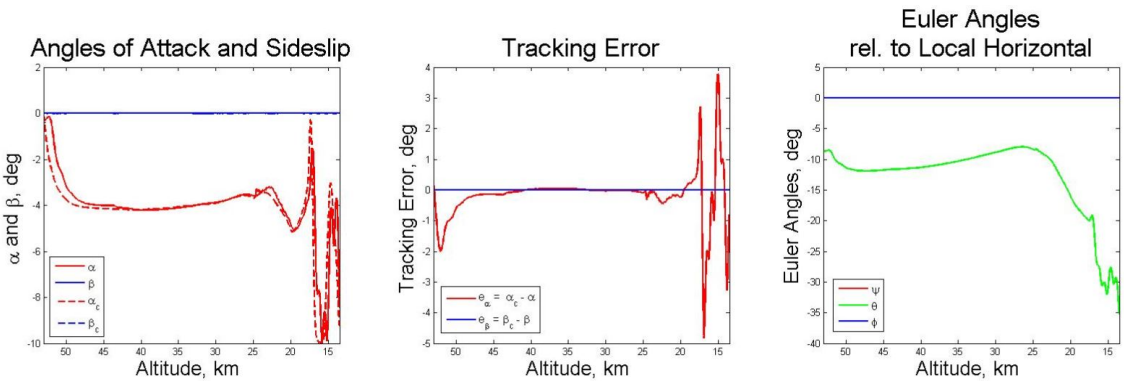

Figure 10.24: G5 Rotation IMMA, guidance commands and tracking performance

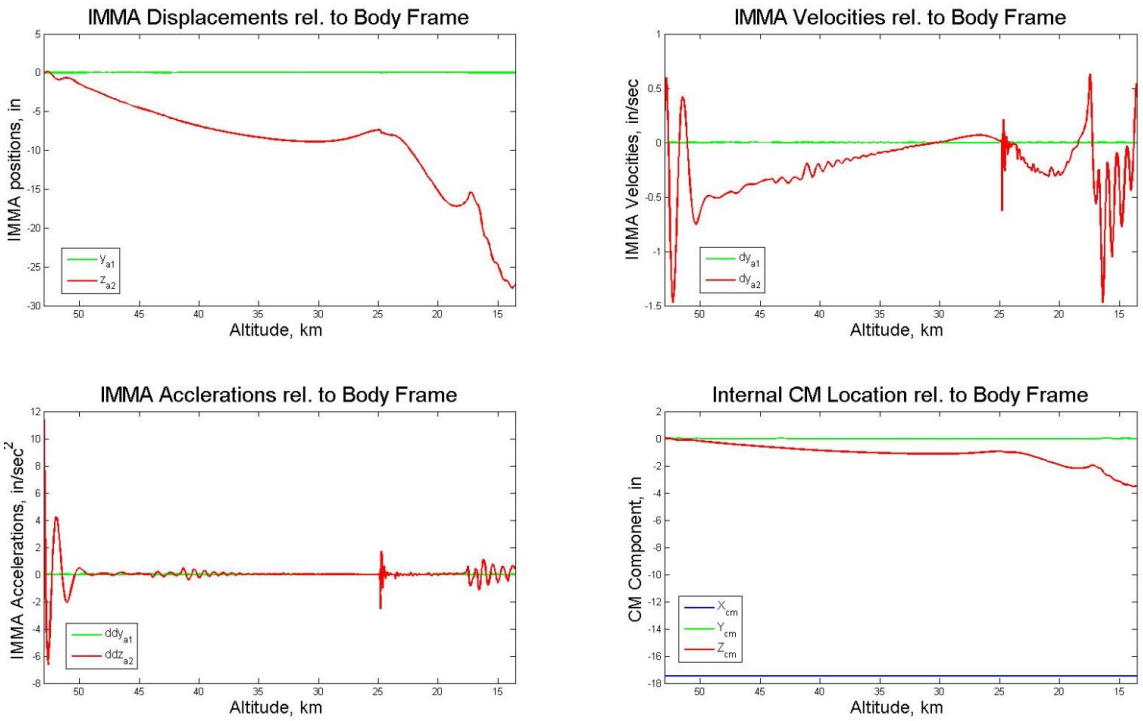

Figure 10.25: G5 Translation IMMA, IMMA kinematics and CM internal location

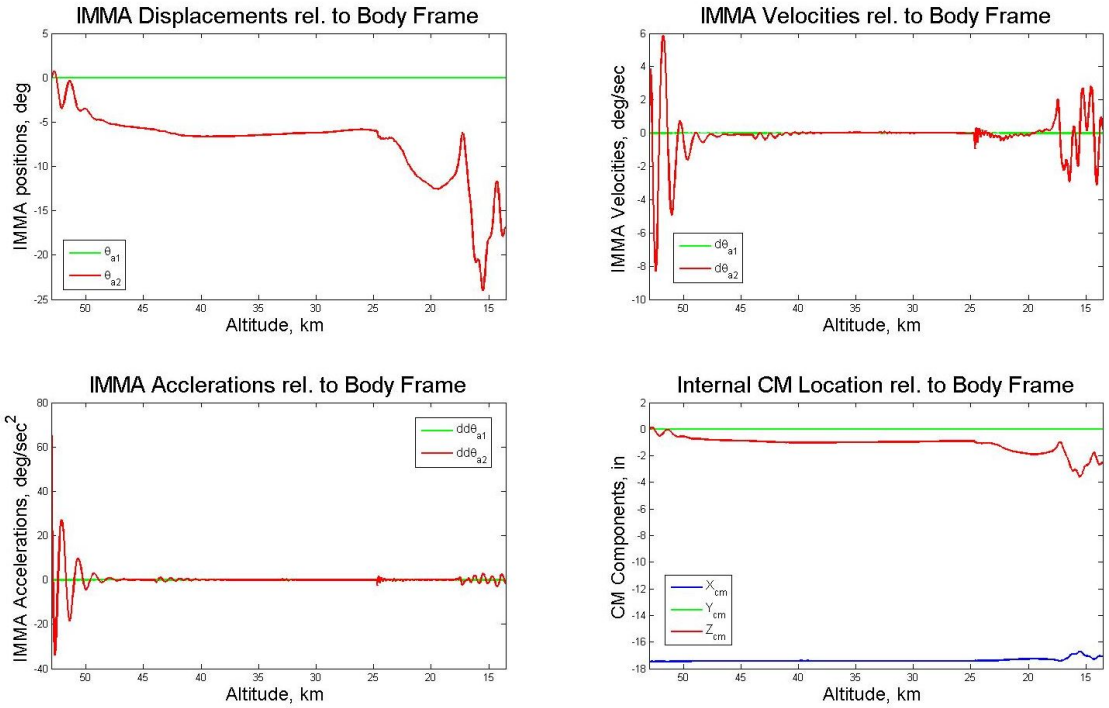

Figure 10.26: G5 Rotation IMMA, IMMA kinematics and CM internal location

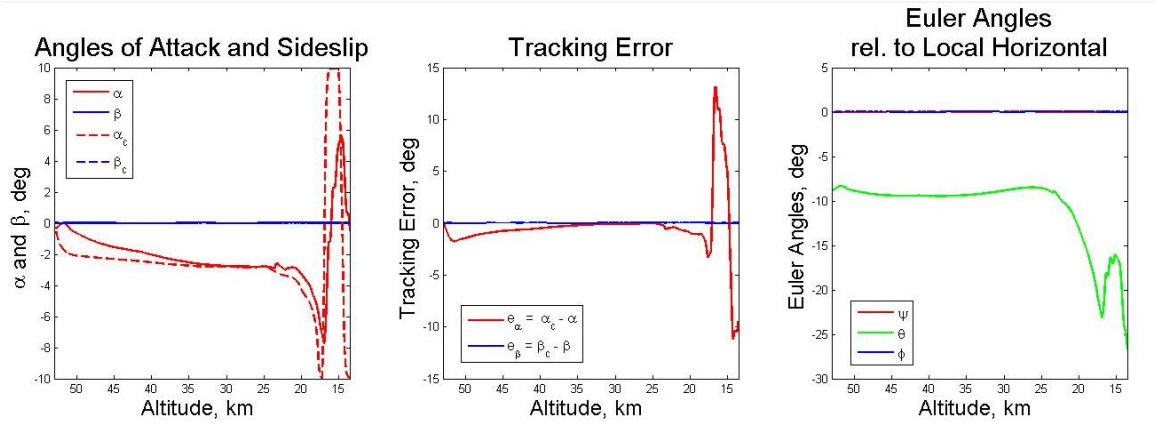

Figure 10.27: G6 Translation IMMA, guidance commands and tracking performance

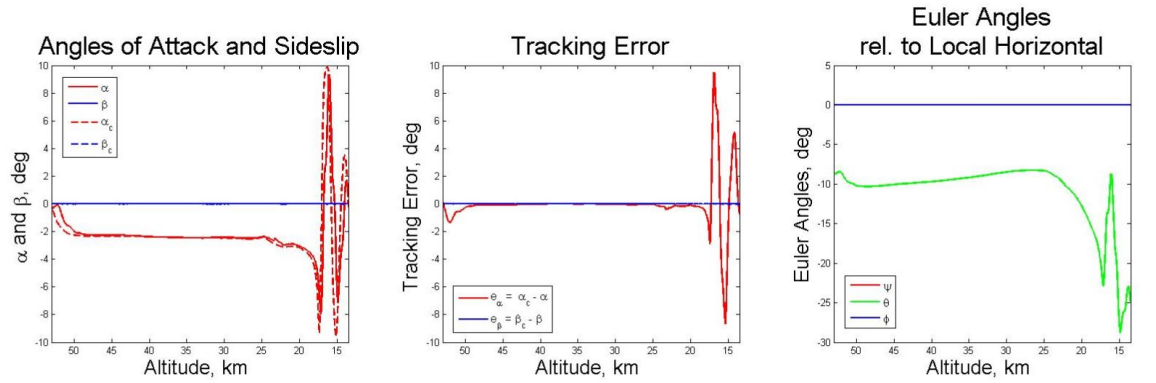

Figure 10.28: G6 Rotation IMMA, guidance commands and tracking performance

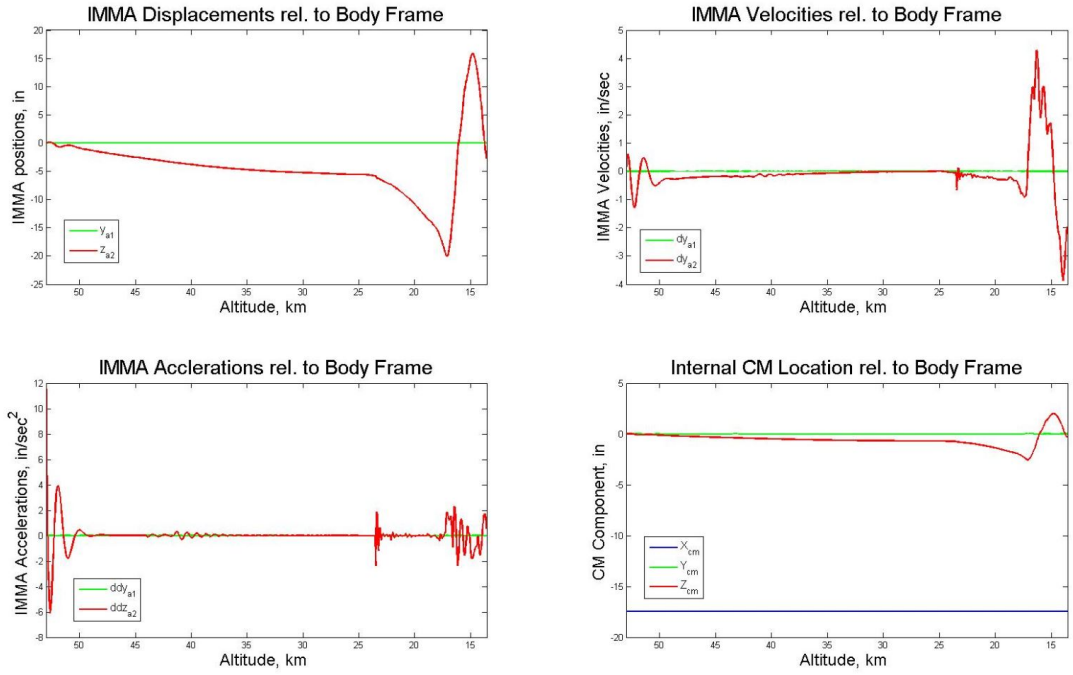

Figure 10.29: G6 Translation IMMA, IMMA kinematics and CM internal location

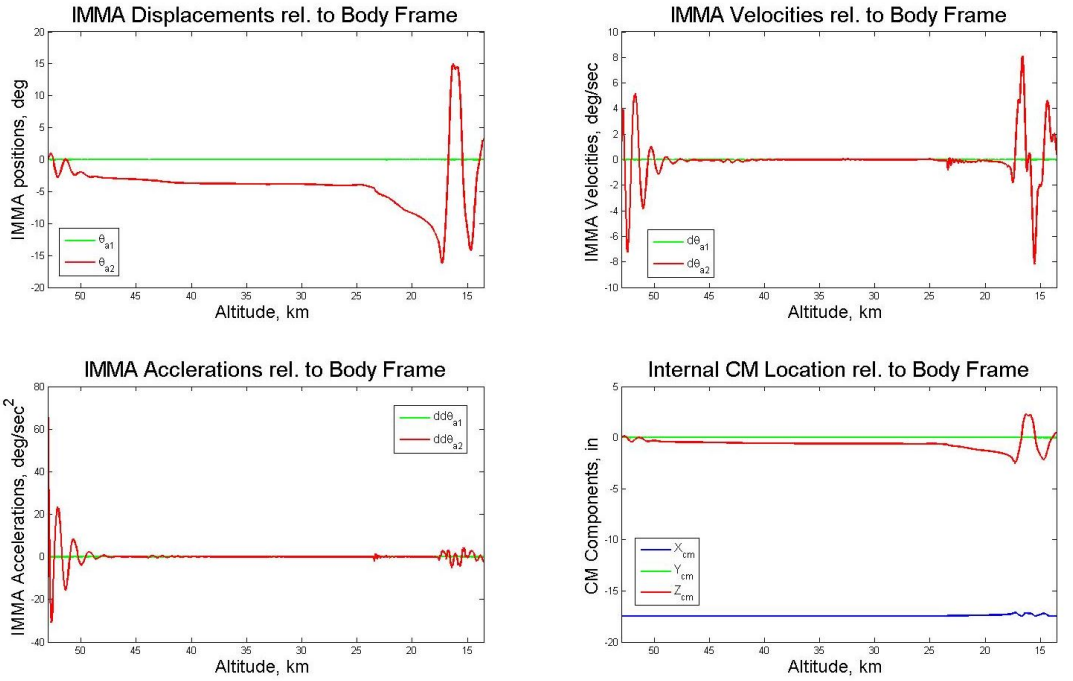

Figure 10.30: G6 Rotation IMMA, IMMA kinematics and CM internal location

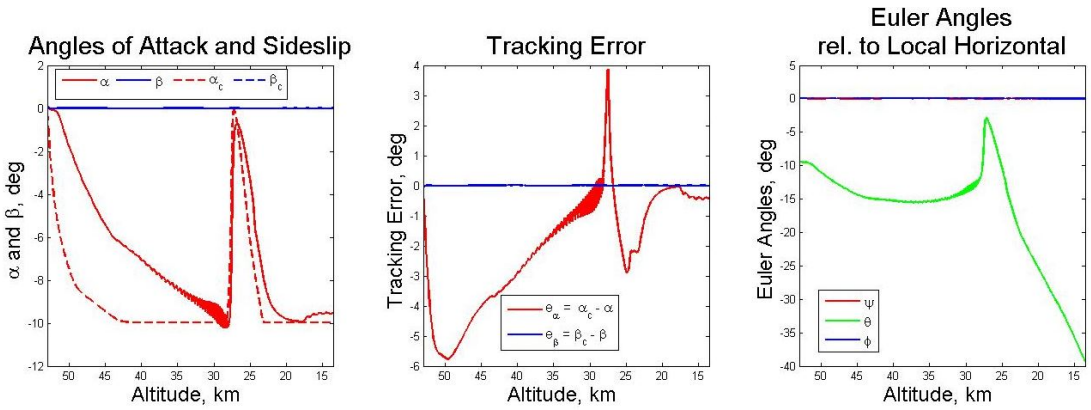

Figure 10.31: G7 Translation IMMA, guidance commands and tracking performance

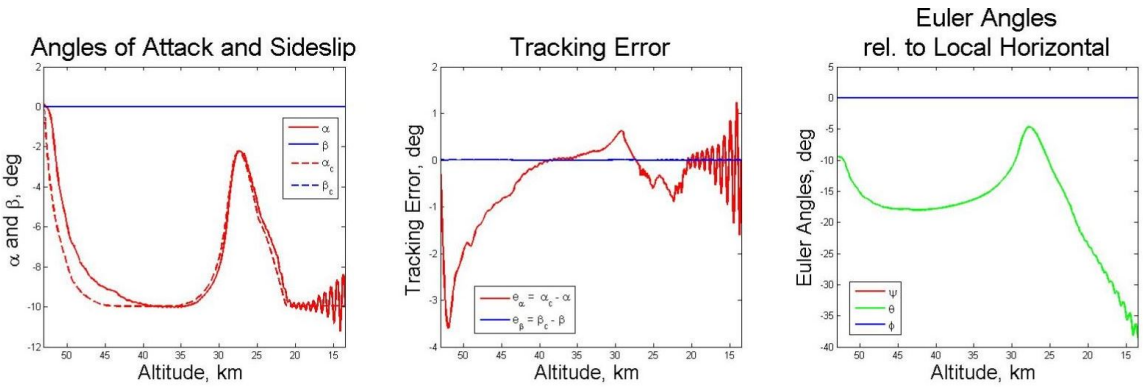

Figure 10.32: G7 Rotation IMMA, guidance commands and tracking performance

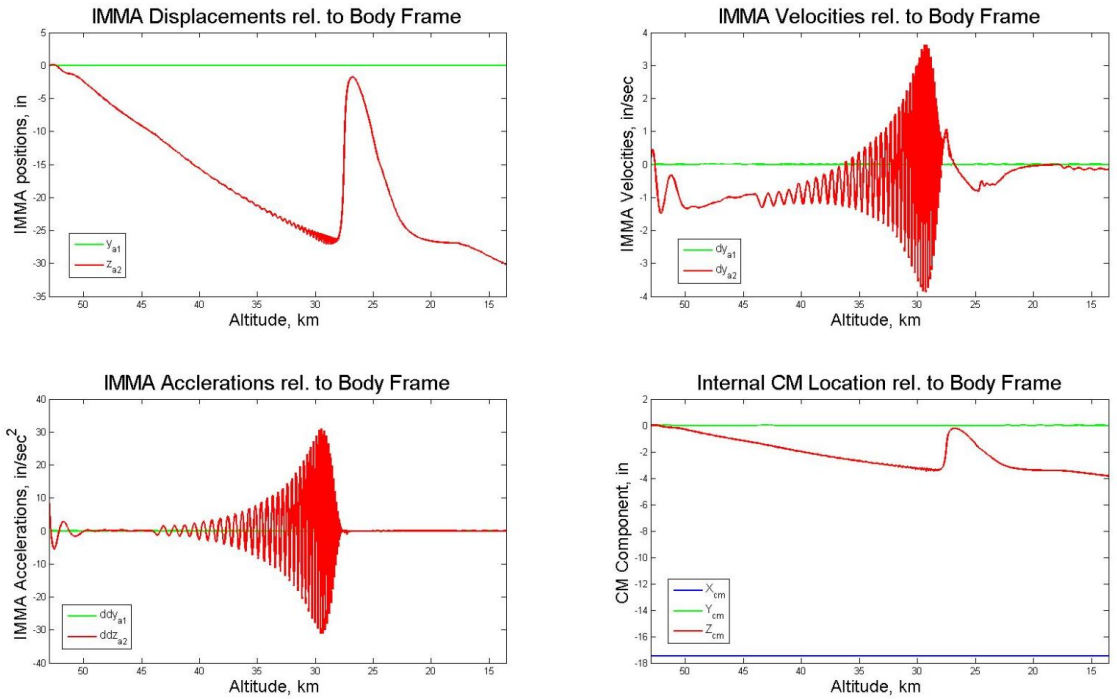

Figure 10.33: G7 Translation IMMA, IMMA kinematics and CM internal location

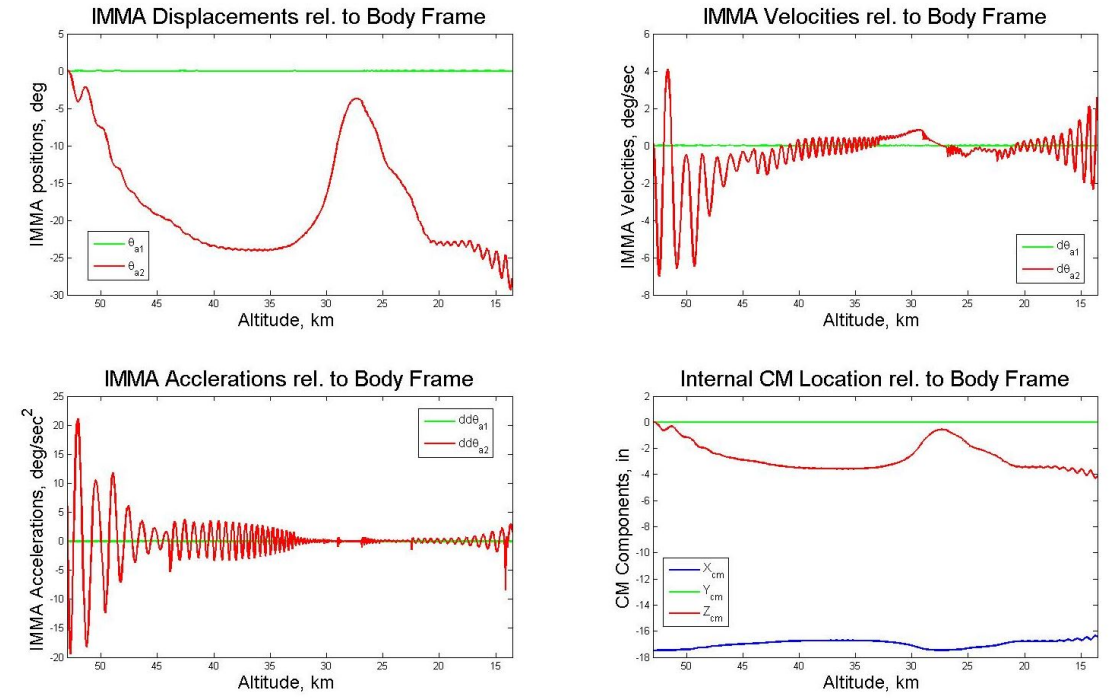

Figure 10.34: G7 Rotation IMMA, IMMA kinematics and CM internal location

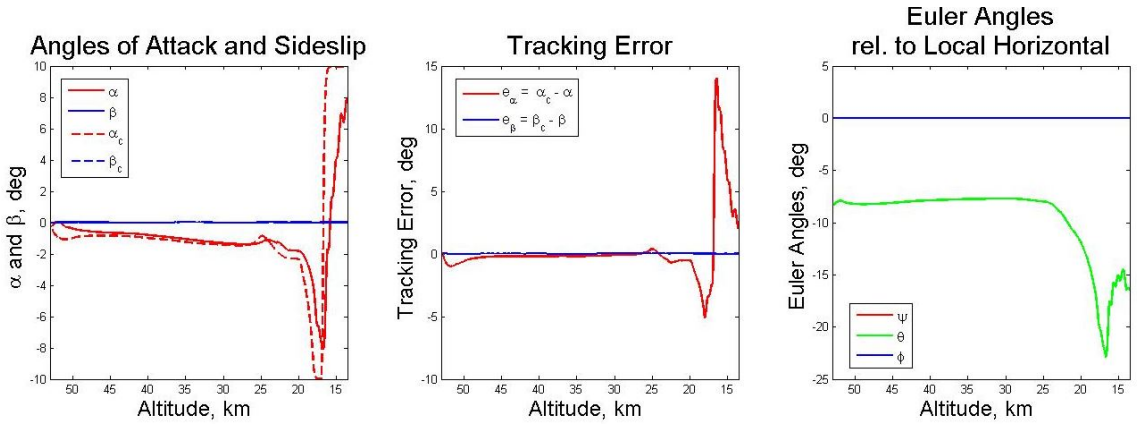

Figure 10.35: G8 Translation IMMA, guidance commands and tracking performance

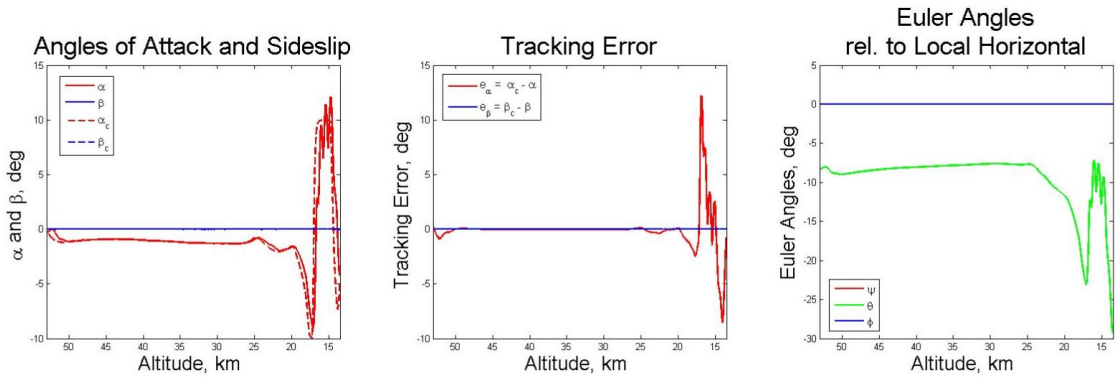

Figure 10.36: G8 Rotation IMMA, guidance commands and tracking performance

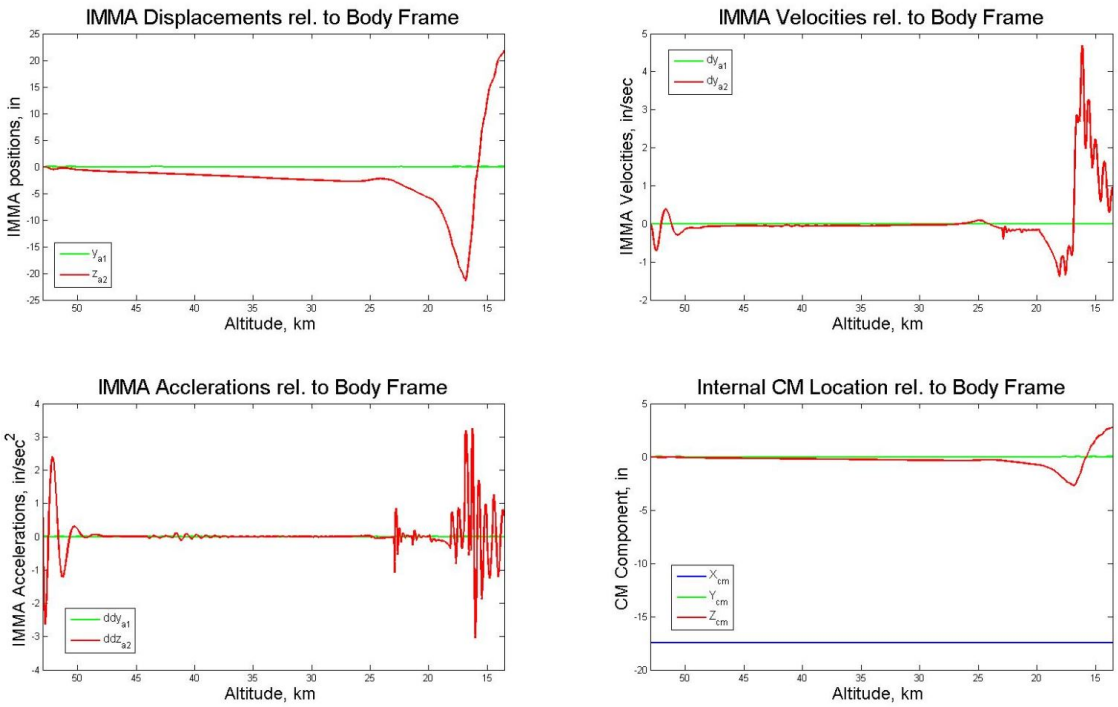

Figure 10.37: G8 Translation IMMA, IMMA kinematics and CM internal location

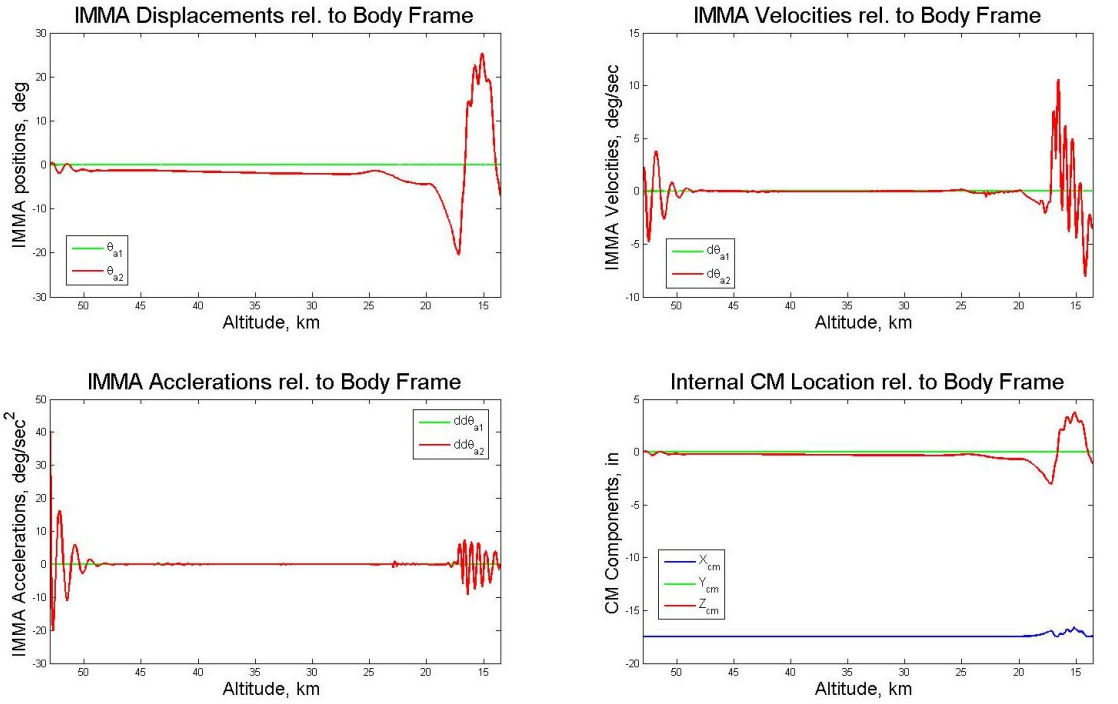

Figure 10.38: G8 Rotation IMMA, IMMA kinematics and CM internal location

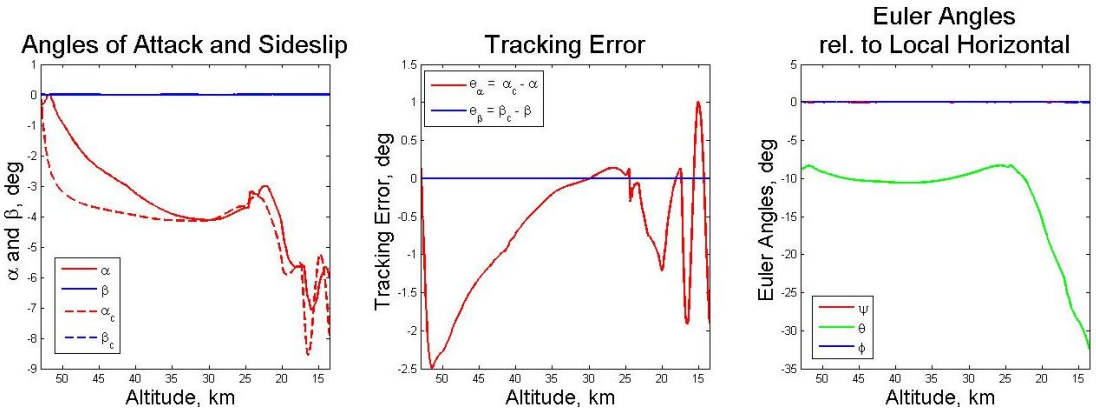

Figure 10.39: G9 Translation IMMA, guidance commands and tracking performance

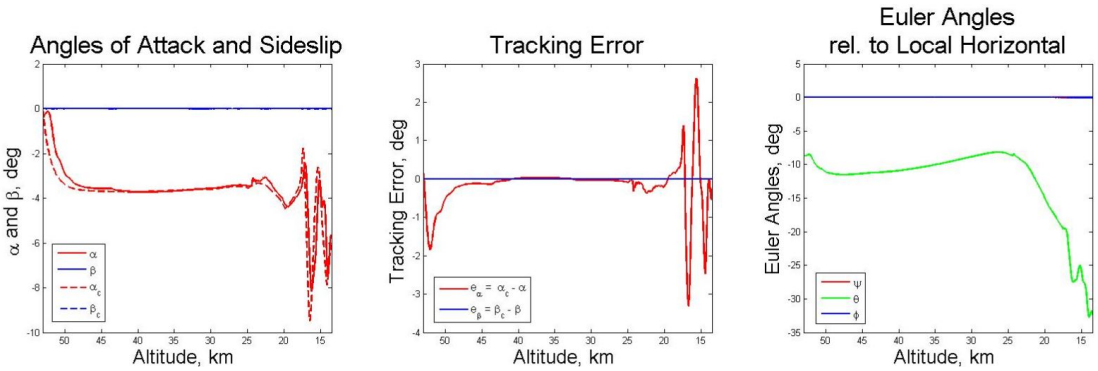

Figure 10.40: G9 Rotation IMMA, guidance commands and tracking performance

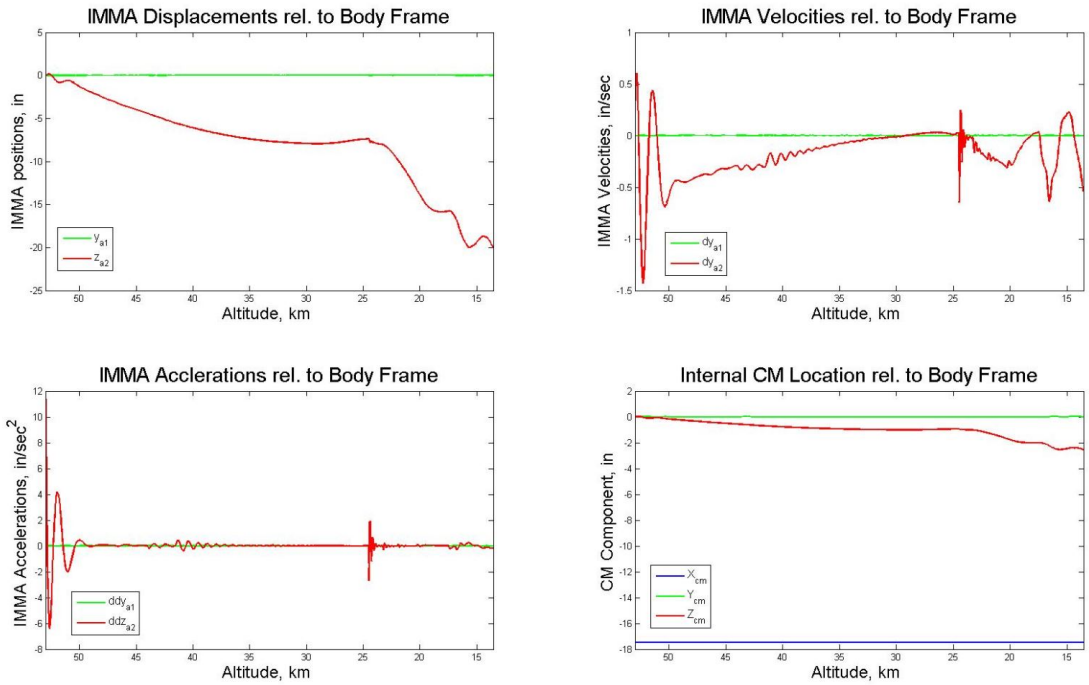

Figure 10.41: G9 Translation IMMA, IMMA kinematics and CM internal location

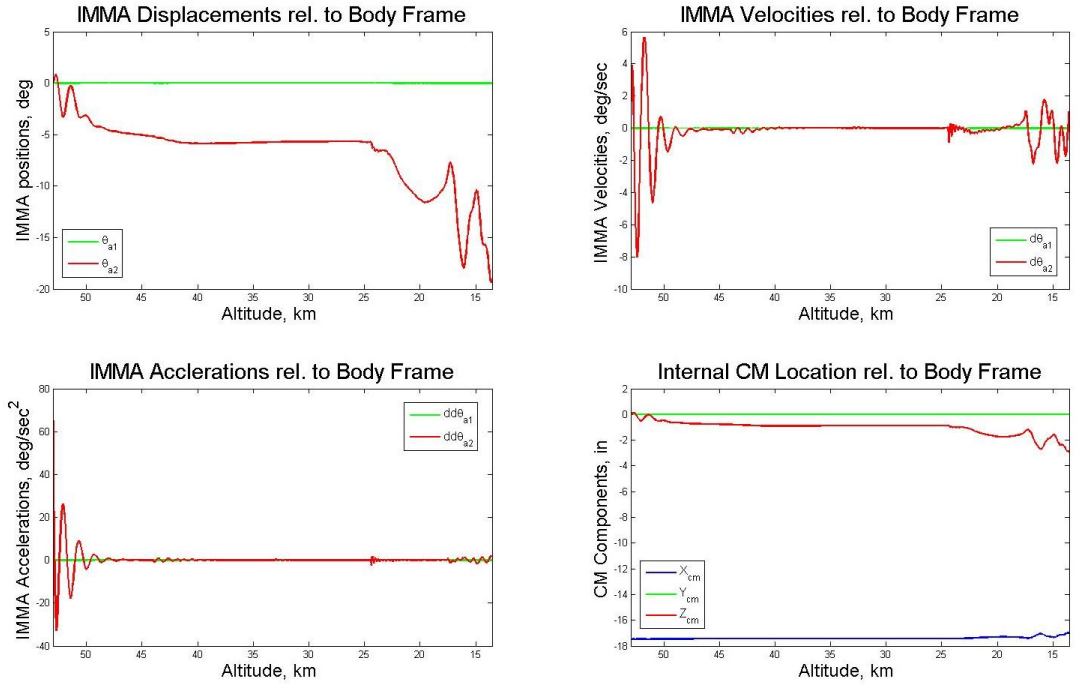

Figure 10.42: G9 Rotation IMMA, IMMA kinematics and CM internal location

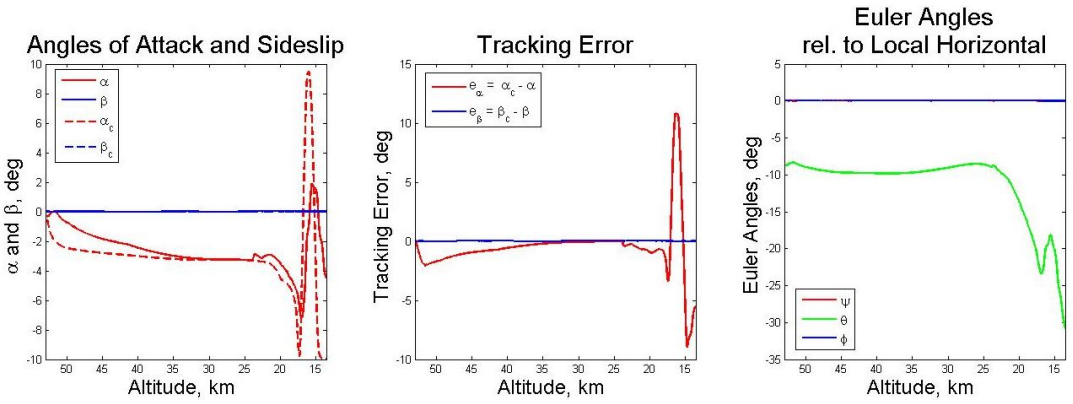

Figure 10.43: G10 Translation IMMA, guidance commands and tracking performance

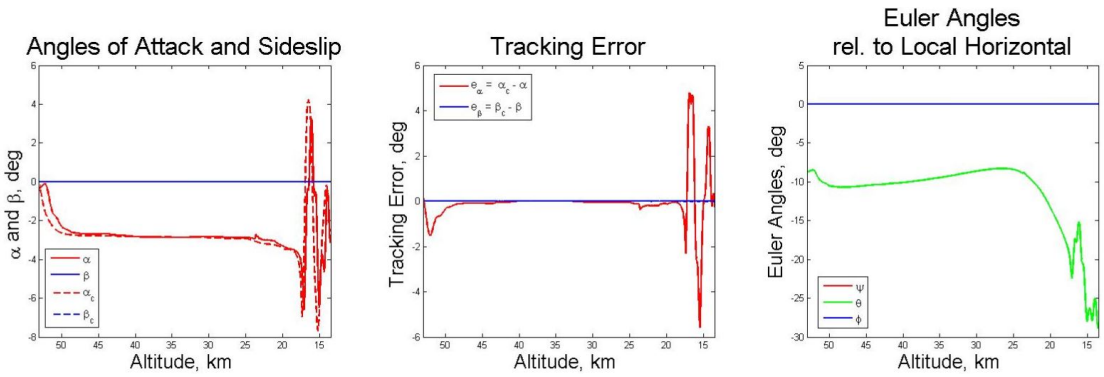

Figure 10.44: G10 Rotation IMMA, guidance commands and tracking performance

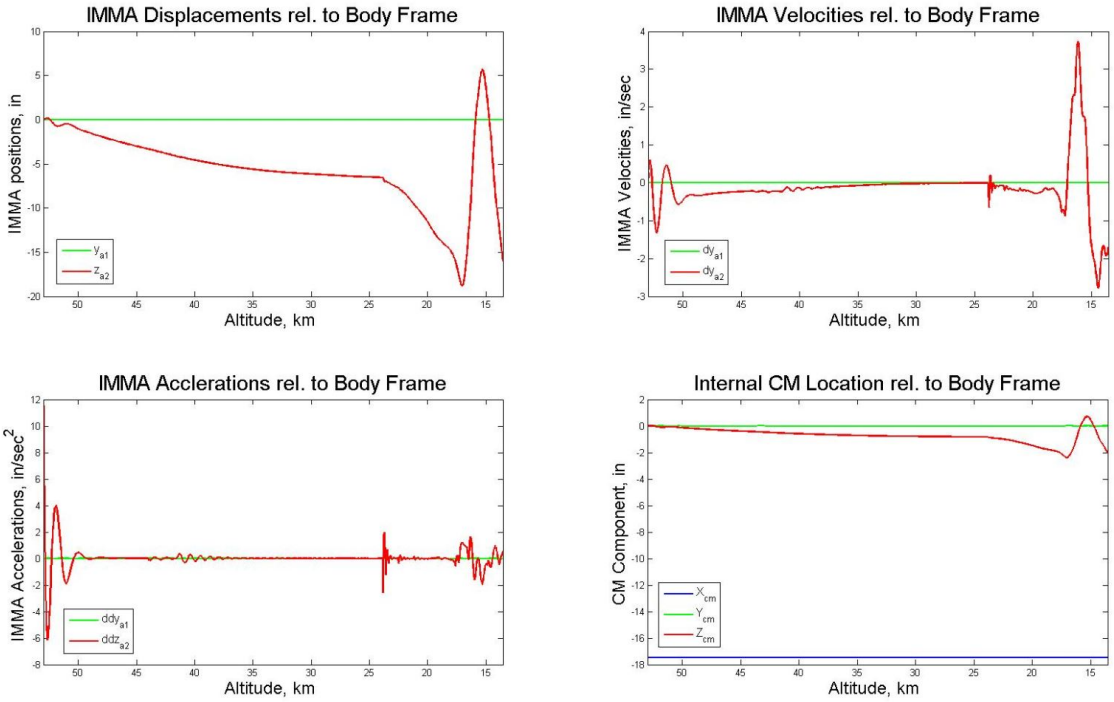

Figure 10.45: G10 Translation IMMA, IMMA kinematics and CM internal location

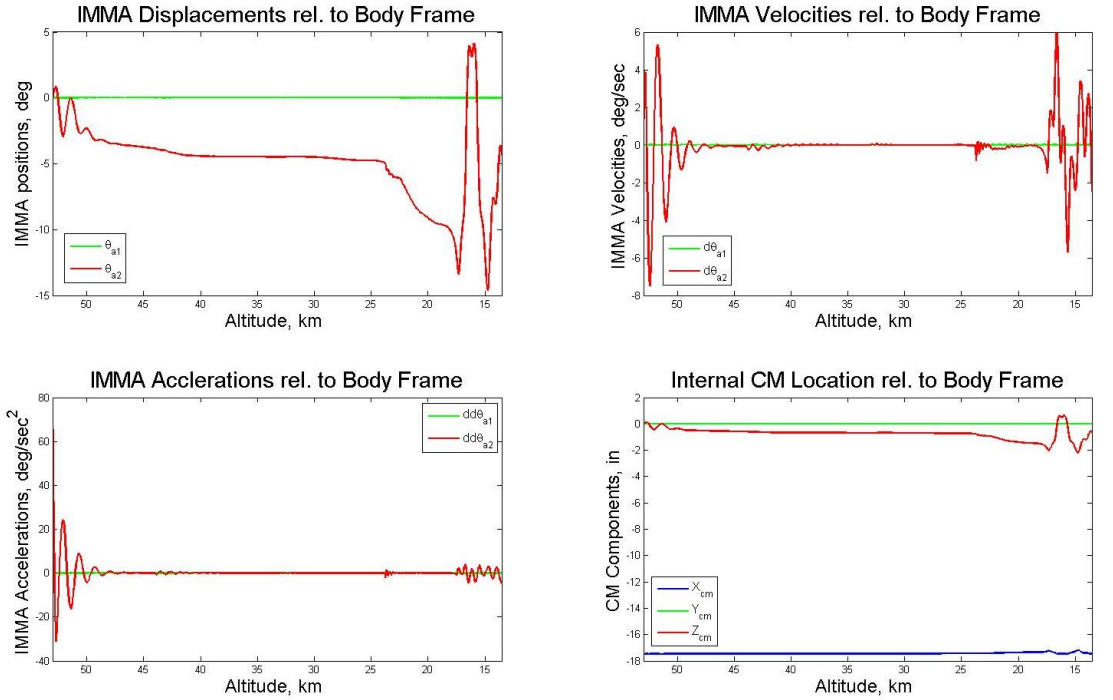

Figure 10.46: G10 Rotation IMMA, IMMA kinematics and CM internal location

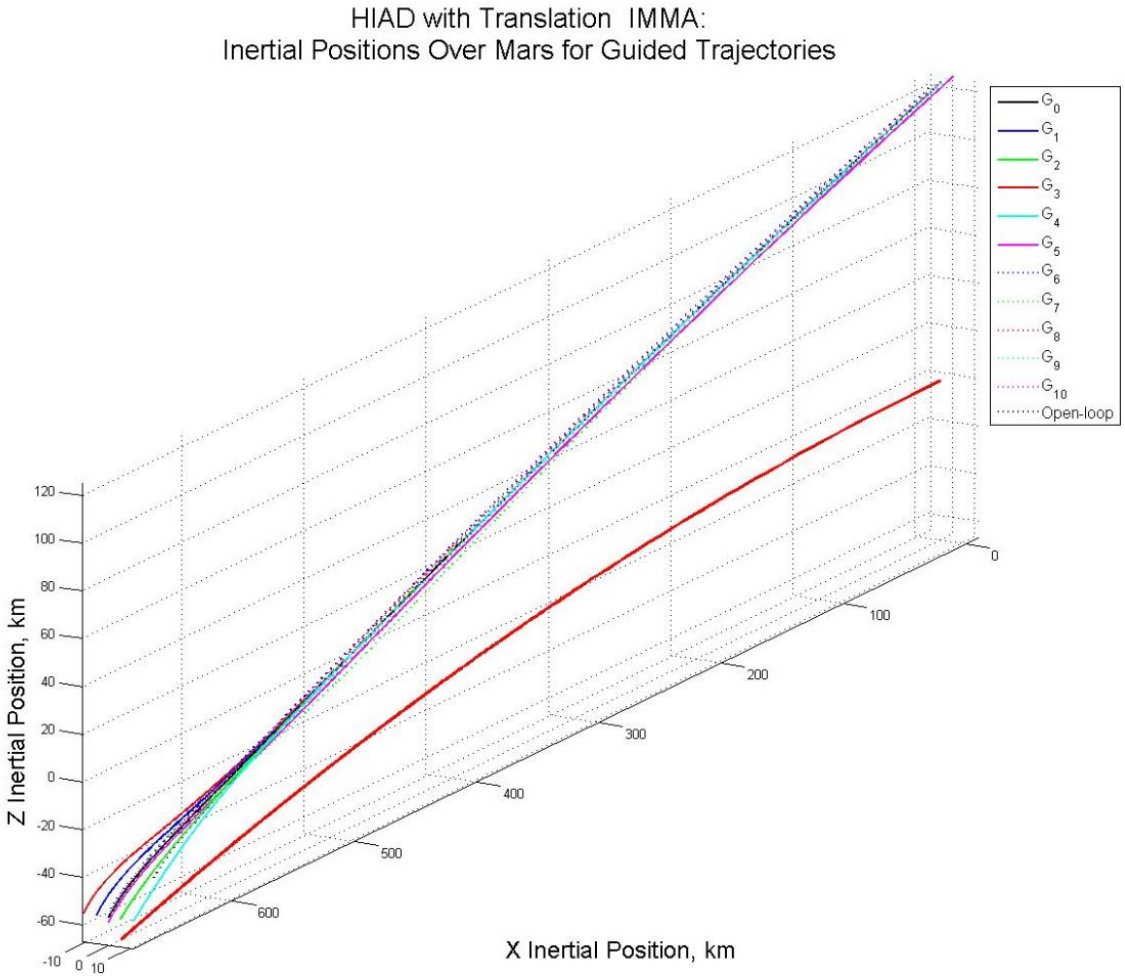

Figure 10.47: Translation IMMA HIAD, trajectories over Mars relative to inertial frame

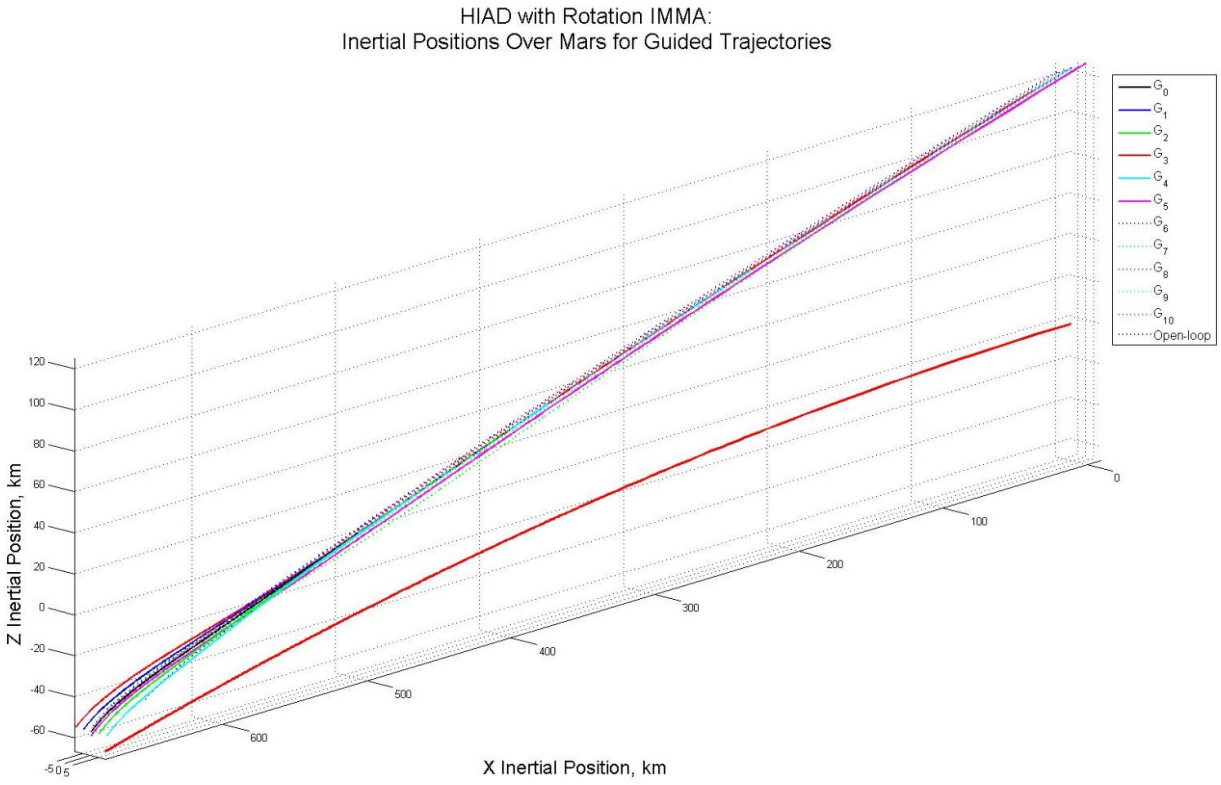

Figure 10.48: Rotation IMMA HIAD, trajectories over Mars relative to inertial frame

Chapter 11

Mechanical Power Studies

11.1 Translation and Rotation IMMA Mechanical Power Models

Mechanical power was computed for the translation and rotation IMMA systems for the guided trajectories in Chapter 10. Mechanical power is the power required for the IMMA motion assuming 100 percent actuator efficiency. In real application actuator efficiency will not be 100 percent. However, the mechanical power results below provide the general power requirements associated with IMMA based entry vehicle guidance and serve as starting point for development of actuators for implementation of IMMA control in future missions. Mechanical power also permits power comparison of the translation system driven by forces to the rotation system driven by torques. The mechanical power models are developed below followed by mechanical power results for each guided trajectory of Chapter 10.

The force acting on the translation IMMA system is the inertial force of the top structure mass:

$$\mathbf{F^c}_{i,ts} = m_{ts}\left[(\mathbf{a}_{i,c} + \tilde{\boldsymbol{\omega}}_{i,c}\mathbf{v}_{i,c}) + \mathbf{a}_{c,ts} + \tilde{\dot{\boldsymbol{\omega}}}_{i,c}\mathbf{r}_{c,ts} + 2\tilde{\boldsymbol{\omega}}_{i,ts}\mathbf{v}_{c,ts} + \tilde{\boldsymbol{\omega}}_{i,c}\tilde{\boldsymbol{\omega}}_{i,c}\mathbf{r}_{c,ts}\right]. \tag{11.1}$$

Equation Eq. (11.1) follows from application of Newton's Second Law and the Transport Theorem for taking inertial derivatives in a rotating reference frame [23]. The first two terms of Eq. (11.1) are due to the inertial acceleration of the vehicle CM frame. The last 4 terms arise from the prescribed relative motion of the top structure to the CM frame. Eq. (11.1) is a constraint force acting on the top structure translation IMMA system. The force parallel to the top structure motion is an opposing force which the mass must overcome to have the prescribed motion. Mechanical power associated with the prescribed relative IMMA motion is given by:

$$P_{\text{mech trans}} = -\mathbf{F^c}_{i,ts} \cdot \mathbf{v}^c_{c,ts} \tag{11.2}$$

The torque acting on the rotation IMMA system is the inertial torque of the top structure mass:

$$\begin{aligned} \boldsymbol{\tau}^c_{i,ts} &= \dot{\mathbf{h}}^c_{i,ts} + \boldsymbol{\omega}_{i,ts} \times \mathbf{h}_{i,ts} && (11.3)\\ &= \mathbf{I}^c_{ts}\dot{\boldsymbol{\omega}}_{i,ts} + \boldsymbol{\omega}_{i,ts} \times \mathbf{I}^c_{ts}\boldsymbol{\omega}_{i,ts} && (11.4)\\ &= \mathbf{I}^c_{ts}\left(\dot{\boldsymbol{\omega}}_{i,c} + \dot{\boldsymbol{\omega}}_{c,ts}\right) + \left(\boldsymbol{\omega}_{i,c} + \boldsymbol{\omega}_{c,ts}\right) \times \mathbf{I}^c_{ts}\left(\boldsymbol{\omega}_{i,c} + \boldsymbol{\omega}_{c,ts}\right) . && (11.5) \end{aligned}$$

Equation Eq. (11.5) follows from application of Euler's Rotational Equations of Motion [23] and separating inertial angular velocity of the top structure into respective angular velocity of the CM frame with respect to the inertial frame and the prescribed angular velocity of the top structure with respect to the CM frame. The angular acceleration has been similarly separated. Eq. (11.5) is the constraint toques acting on the IMMA, just like the constraint force for the IMMA translation system. Using the negative of the above equation and its dot product with the prescribed IMMA rotational motion with respect to the CM frame yields the IMMA mechanical torque equation:

$$P_{\text{mech rot}} = -\boldsymbol{\tau}^c_{i,ts} \cdot \boldsymbol{\omega}_{c,ts} \ . \tag{11.6}$$

Mechanical power model routines for Eqs. (11.2) and (11.6) were implemented in each of the MATLAB and Simulink nonlinear guidance simulations of Chapter 10. The mechanical power results presented for both systems are for the absolute value of Eq. (11.2) and Eq. (11.6) because IMMA track reversals can cause the mechanical power equations to become negative, but track reversal motion still requires positive mechanical power to make the direction changes. Both HIAD vehicles started from the same initial entry conditions for guidance to the same terminal targets. All system parameters with exception of the path of IMMA motion, translation versus rotation, were equivalent. The next section summarizes mechanical power requirements comparisons between the IMMA systems required for each of the guidance simulations.

11.2 Power Performance Comparison for HIAD Systems

Figures 11.1 − 11.3 are mechanical power versus altitude comparison plots for each of the guided trajectories of Chapter 10. Side by side comparison for the translation system, blue plots, and the rotation system, green plots, are shown for each of the 11 guidance trajectories. Figures 11.1−11.2 show mechanical power comparisons for entry trajectories where only range guidance was performed. Figure 11.3 shows mechanical power comparisons where both range and cross-range guidance was performed. At the initial control altitude of 53 km, the rotation IMMA systems exceed the translation IMMA system by 30 Watts or less. However, the IMMA systems had much swifter tracking response, less chattering,

and superior tracking performance for all of the guided trajectories shown side by side in Chapter 10. The more sluggish translation system required larger total mechanical power for all of the guided trajectories, shown in the power plots below. This included power differences exceeding 200 mechanical Watts. Low power requirements for IMMA systems depends upon effective tuning of the controller where in general less control actuation leads to less mechanical power demands.

Poor tracking performance though large tracking error ($>$ than 10 deg) or high IMMA induced CM internal motion ($>$ 2 in/s) can lead to mechanical power requirements in excess of 300 mechanical Watts. 300 mechanical Watts was the largest mechanical power demand of all the HIAD guided trajectories corresponding to trajectory G7 for the IMMA translation system of 300 Watts. The power results show that for the comparable IMMA systems that the rotation IMMA system requires less mechanical power and from Chapter 10 provides swifter and more accurate tracking response. Based on the guidance and power results of Chapters 10 and 11 rotation IMMA systems are recommend for future HIAD control missions. Collectively the low power demands and tracking performance of both systems indicate IMMA control systems are a viable guidance control system and an alternative to traditional RCS thruster systems and therefore merit further study for implementation into future missions.

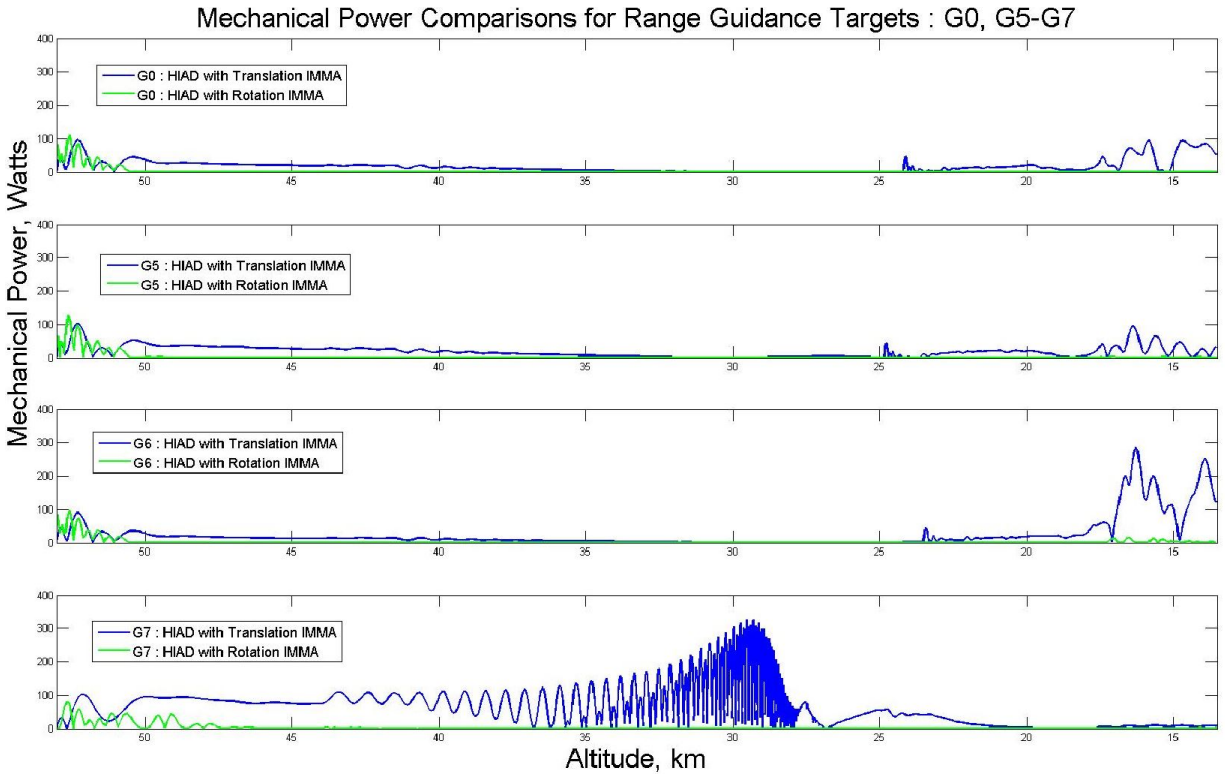

Figure 11.1: Mechanical power comparisons for G0, G5-G7 down-range guidance trajectories

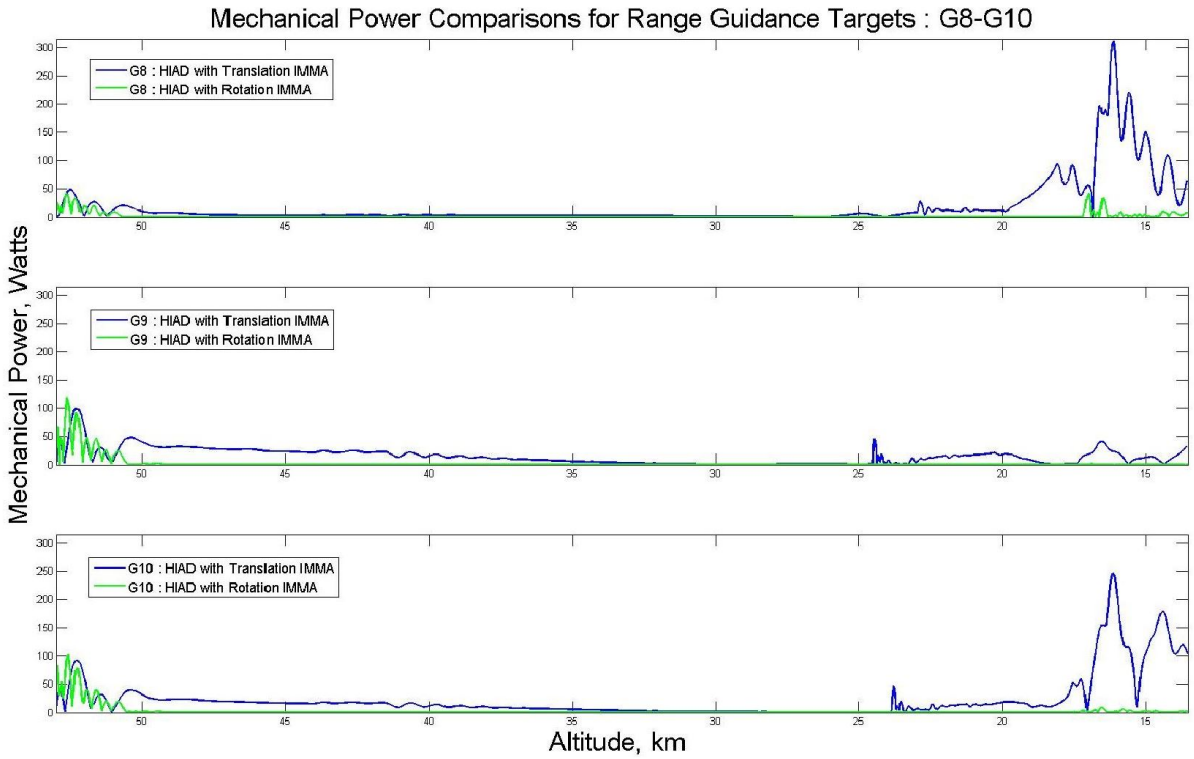

Figure 11.2: Mechanical power comparisons for G8-G10 down-range guidance trajectories

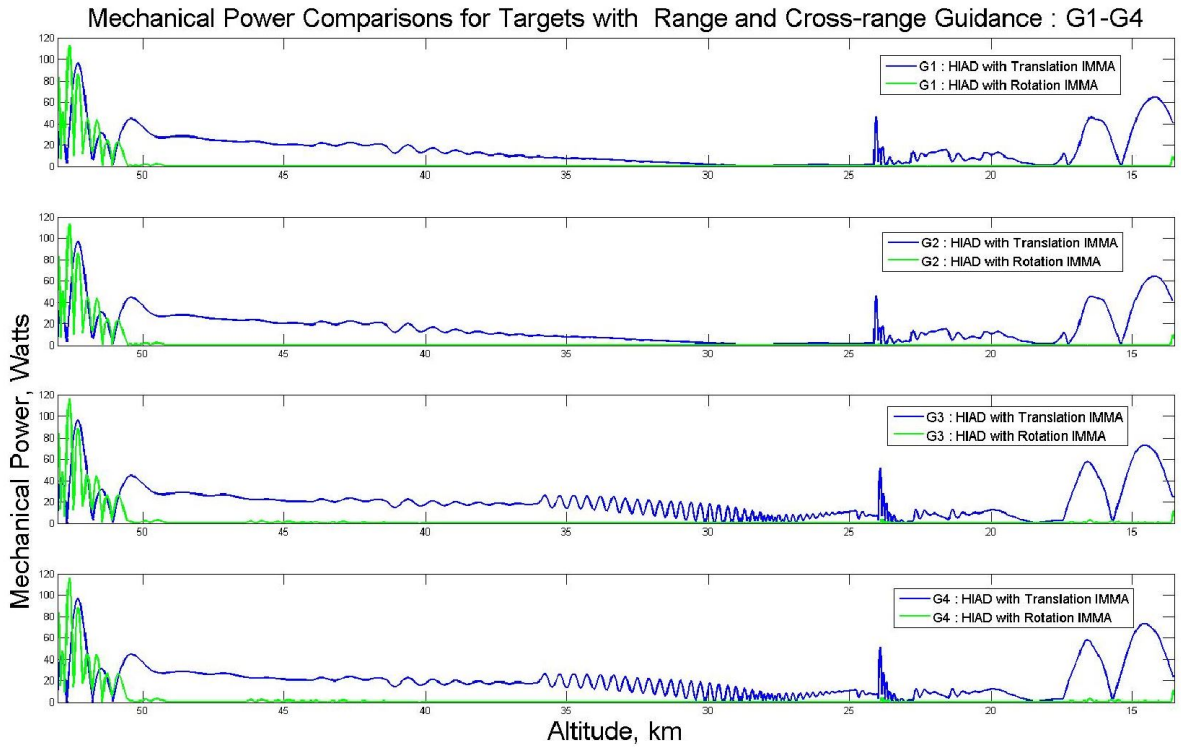

Figure 11.3: Mechanical power comparisons for G1-G4 range and cross-range guidance trajectories

Chapter 12

Summary and Recommendations for Future Work

12.1 Summary of Significant Research Contributions

The focus of this Dissertation was to demonstrate IMMA based control viability for precision guidance of Mars axisymmetric entry capsules and for precision guidance of the next generation of aeroshells, HIADS, for precision delivery of large payloads. Improving precision guidance and payload delivery is critical to accessing the largely unexplored Southern Hemisphere of Mars and meeting precision guidance demands for future human exploration missions. The proposed IMMA control systems avoid external flow field instability and aeorheating risks associated with traditional RCS thruster systems and aerodynamic flap systems. Multi-body attitude dynamics models for entry vehicles with rotation and translation IMMA were developed with respect to the vehicle instantaneous CM location. This was desirable for incorporation of the dynamics models into validated mission and simulation design software such as NASA's POST2. IMMA based guidance command tracking controllers using the dynamics models were developed for a blunt body entry capsule inspired by NASA's Mars Phoenix entry capsule and for a HIAD vehicle inspired by NASA's HEART vehicle. The IMMA configurations proposed offer flexibility for control system design for future missions and enabled guidance performance and mechanical power comparison between a translation IMMA versus a rotation IMMA configuration.

Angle of attack and sideslip command tracking was developed for decoupled range and cross-range control which can avoid drooping effects and terminal range errors associated with late bank angle reverses. A new variant of the Apollo Earth return terminal guidance algorithm was presented for angle of attack range control commands. The guidance algorithm is not specific to IMMA systems and is schematically similar to what was used for the 2012 Mars Science Laboratory Mission. A cross-range sideslip guidance law was also developed and

shown effective for steering out initial cross-range errors and to terminal parachute with nonzero cross-range offsets. Nonlinear closed-loop simulation was also shown for precision guidance of both rigid capsules and HIADs for correcting off-nominal range, flight path angle, attitude, and entry speed for guidance to desired terminal targets. This was for guidance over large dynamic pressure changes with a high fidelity aerodynamics model. The terminal targets chosen were located greater than 37 km downrange from an open-loop, unguided entry. Mechanical power studies for actuator configurations were developed demonstrating low mechanical power demands with nominal mechanical power below 150 Watts for rotation and translation IMMA. It was shown that the proposed rotation IMMA configuration had less total mechanical power requirements for all of the guided trajectories. Further, the IMMA rotation configuration was much easier to tune for quick response and greater tracking precision than the translation IMMA system. Accordingly, a rotation IMMA system like the 2 DOF configuration developed in this Dissertation is recommended over a translation IMMA system for future control system development.

Collectively, the low mechanical power requirements for the IMMA configurations and precision guidance results for both the entry capsule and HIADs show IMMAs are a viable candidate for future control systems and constitute a promising alternative control system to RCS thruster systems for the next generation of Mars lander missions.

12.2 Recommendations for Future Areas of Study

Some recommended areas of future study consist in the linearization of the equations of motion, development of the IMMA actuator equations, improving the gravity model, and exploring specific target locations for IMMA based guidance. In Chapter 7 the guidance range control law was chosen for a lifting trajectory associated with a constant negative angle of attack. In Chapter 6, parameters used in numeric plant and control influence matrices at design point altitudes and for density, flight path angle, and aerodynamic coefficients were taken from a reference zero angle of attack ballistic entry trajectory. This was done because the reference Phoenix entry capsule was flown for a ballistic entry and proved to have good inherent aerodynamic stability. Choosing a conservative design attitude ballistic entry for linearization in the event of IMMA is advisable for future missions to mitigate risks of catastrophic loss of vehicle. A recommended area for future IMMA guidance design is to explore linearizing the equations of motion around the nominal trajectory for investigating tracking performance versus linearization for ballistic entry. In Chapter 5 the equations of motion were arranged in standard form for nonlinear control techniques such as block backstepping. Future work to explore amenability of developing nonlinear tracking controllers using the dynamic models developed in Chapter 2 may prove fruitful for new control theory development.

Additional recommendations for future areas of study include determining more precise limits for IMMA displacement relative to the rigid payload frame for geometric constraint

considerations. Sufficient control authority through IMMA mass and location was made so that IMMA systems stayed within geometric constraints of the vehicles. Future studies will need to impose actuator limits and determine more optimal IMMA size for effective control. For HIADS where the IMMA are behind the aeroshell, but are not fully enclosed like IMMA in rigid entry capsules, aerodynamic analysis should be performed to determine maximum height of payload behind the aeroshell. This analysis should include influence of top structure IMMA actuation limits. For the capsule vehicle guidance simulations, track limits were imposed using the notional actuator models for maximum desired displacement. Important steps to successfully implement IMMA on actual missions will be to develop actuator models which incorporate constraint forces and track limits into control design. The constraint torques and forces are shown in the mechanical power models in Chapter 11.

Recommended future areas of study also include investigating guidance performance degradation when IMMA track limits and velocity limits are imposed. An additional recommend area of study is to improve upon the atmospheric model and gravity model. This should include accounting for atmospheric winds and improving upon the latitude restriction made for the rotation of the local horizontal frame which lead to representing entry trajectories as flight over a cylindrical planet. Trajectories were chosen such that the primary flight path was aligned with Mars prime Meridian for principal latitude variation. Cross-range motion was associated with longitudinal motion. It is recommended for future simulation development to model a spherical Mars with latitude and longitude local horizontal variation for more accurate modeling of the atmosphere and of the gravitational force. A final recommended area of future study is in selecting latitude and longitude specif targets for future missions and designing the nominal reference trajectory accordingly. This study kept the target location to a general terminal target with specific range and cross-range terminal position and altitude fixed at the surface of Mars Polar axis and aligned with the Mars Prime Meridian. Future IMMA control based mission design work will need to determine specific latitude and longitude terminal target locations.

Bibliography

[1] Braun, R. D. and Manning, R. M., "Mars Exploration Entry, Descent and Landing Challenges," *Journal of Spacecraft and Rockets*, Vol. 44:2, 2007, pp. 310–323.

[2] Smith, D. E., Zuber, M. T., Frey, H. V., Garvin, J. B., Head, J. W., Muhlemasn, D. O., Pettengill, G. H., hillips, R. J., Solomon, S. C., wally, H. J. Z., Banerdt, W. B., Duxbury, T. C., Golombek, M. P., Lemoine, F. G., Neumann, G. A., Rowlands, D. D., Aharonson, O., Forda, P. G., Iranovs, A. B., Johnson, C. L., McGovern, P. J., Abshire, J. B., Afzal, R. S., and Sun, X., "Mars Orbiter Laser Altimeter: Experiment Summary After the First Year of Global Mapping of Mars," *Journal of Geophysical Research*, Vol. 106, 201.

[3] Dyakonov, A. A., Glass, C. E., Edquist, K. T., Schoenenberger, M., Chwalowsk, P., Van-Norman, J., , Scallion, W. I., , Tang, C., Wright, M. J., Cheatwood, F. M., Hollis, B. R., Lessard, V. R., and Takashima, N., "Reaction Control system Design Considerations for Mars Entry Vehicles," *5th International Planetary Probe Workshop*, Bordeaux, France, 23-29, June 2007.

[4] Wright, H., Cutright, A., Corliss, J., Bruce, W., Trombetta, D., Mazaheri, A., Coleman, M., Olds, A., and Hancock, S., "HEART Flight Test Overview," *9th International Planetary Probe Workshop*, Toulouse, France, 2012.

[5] Edquist, K. T., Desai, P. N., and Schoenenberger, M., "Aerodynamics for Mars Phoenix Entry Capsule," *Journal of Spacecraft and Rockets*, Vol. 48. No. 5, 2011, pp. 713–726.

[6] Regan, F. J. and Anandakrishan, S. M., *Dynamics of Atmospheric Re-entry*, American Institute of Aeronautics and Astronautics Education Series, 1993.

[7] Dyakonov, A. A., Glassy, C. E., and Desaiz, P. N., "Analysis of Effectiveness of Phoenix Entry Reaction Control System," *Journal of Spacecraft and Rockets*, Vol. 48, issue 5, 2011, pp. 746–755.

[8] Dyakonov, A. A., Schoenenberger, M., Scallion, W. I., Norman, J. W. V., Novak, L. A., and Tang, C. Y., "Aerodynamic Interference Due to MSL Reaction Control System," *41st AIAA Thermophysics Conference*, San Antonio, Texas, 22-25 June 2009. AIAA Paper 2009-1030.

[9] Mendeck, G. and McGrew, L., "Post-Flight Entry Guidance Performance of the 2011 Mars Science Laboratory Mission," *23rd AIAA/AAS Space Flight Mechanics Meeting*, Kauai, Hawaii, February 2013, AAS Paper 13-419.

[10] Carman, G., Ives, D., and Geller, D., "Apollo-Derived Mars Precision Lander Guidance," *AIAA Atmospheric Flight Mechanics Conference*, August 10-12, 1998, Boston, MA, AIAA 98-4570.

[11] Rogers, J. and Costello, M., "A Variable Stability Projectile Using an Internal Moving Mass," *Journal of Aerospace Engineering*, Vol. 223 Part G, 2009.

[12] Petsopoulos, T., Regan, F. J., and Barlow, J., "Moving-Mass Roll Control for Fixed-Trim Re-Entry Vehicle," *Jorunal of Spacecraft and Rockets*, Vol. 33, 1996, pp. 54–60.

[13] Rogers, J. and Costello, M., "Cantilever Beam Design for Projectile Internal Moving Mass Systems," *Journal of Dynamic Systems, Measurement, and Control*, Vol. 131, 2009.

[14] Rogers, J. and Costello, M., "Control Authority of a Projectile Equipped with a Controllable Internal Translating Mass," *Journal of Guidance, Control, and Dynamics*, Vol. 31, No. 5, pp. 1323–1333.

[15] Menon, P., Sweriduk, G., Ohlmeyer, E., and Malyevac, D., "Integrated Guidance and Control of Moving Mass Actuated Kinetic Warheads," *Journal of Guidance, Control, and Dynamics*, Vol. 27 No. 1, 2004, pp. 118–127.

[16] Robinett, R. D., Sturgis, B. R., and Kerr, S. A., "Moving Mass Trim Control for Aerospace Vehicles," *Journal of Guidance, Control, and Dynamics*, Vol. 19, 1996.

[17] White, J. and Robinett, R. D., "Principal Axis Misalignment Control for Deconing of Spinning Spacecraft," *Journal of Guidance, Control, and Dynamics*, Vol. 17 No. 4, 1994.

[18] Murphy, C., "Influence of Moving Internal Parts on Angular Motion of Spinning Projectiles," *Journal of Guidance and Control*, Vol. 1 No. 2, 1978, pp. 117–122.

[19] Litton, D., Bose, D., Cheatwood, F., Hughes, S., Wright, H., Lindell, M., Derry, S., and Olds, A., "Inflatable Re-entry Vehicle Experiment (IRVE) - 4 Overview," *21st AIAA Aerodynamic Decelerator Systems Conference and Seminar*, 23 - 26 May 2011, Dublin , Ireland.

[20] Davis, J. L., Cianciolo, A. D., Powell, R. W., Shidner, J. D., and Garca-Llama, E., "Guidance and Control Algorithms for the Mars Entry, Descent, and Landing Systems Analysis," *AIAA Astrodynamics Specialist Conference*, Toronto, Canada, August 2010, AIAA-2010-7972.

[21] Atkins, B. M. and Queen, E. M., "Internal Moving Mass Actuator Control for Mars Entry Guidance," *Journal of Spacecraft and Rockets*, (In Peer Review), Sept. 2014.

[22] Petsopoulos, T., *Moving-mass Roll Control System for Fixed-trim Re-entry Vehicle*, Master's thesis, University of Maryland, College Park, 1993.

[23] Schaub, H. and Junkins, J. L., *Analytical Mechanics of Space Systems*, American Institute of Aeronautics and Astronautics, 1993.

[24] Cruz, J. R., "Equations of Motion for an Entry Vehicle, Version 7.0," Tech. rep., Atmospheric Flight and Entry Systems Branch , NASA Langley Research Center, January 23, 2011.

[25] Schoenenberger, M., Kutty, P., Queen, E., and Karlgaard, C., "The Aerodynamics of Axisymmetric Blunt Bodies Flying at Angle of Attack," *2014 IEEE Aerospace Conference*, Big Sky, MT, March 2014.

[26] Gazarik, M. J., Wright, M. J., Little, A., Cheatwood, F. M., Herath, J. A., Munk, M. M., and Novak, F. J., "Overview of the MEDLI Project," *2008 IEEE Aerospace Conference*, Big Sky, MT, March 2008.

[27] Schoenenberger, M., Norman, J. V., Karlgaard, C., Kutty, P., and Munk, M., "Reconstructed Aerodynamic Performance of the MSL Entry Vehicle Using Data from the MEADS and Experiment and Onboard Internal Measurements," *10th International Planetary Probe Workshop*, San Jose, CA June 17, 2013.

[28] Karlgaard, C. D., Beck, R. E., OKeefe, S. A., Siemers, P. M., White, B. A., Engelund, W. C., and Munk, M. M., "Mars Entry Atmospheric Data System Modelling and Algorithm Development," *41st AIAA Thermophysics Conference*, San Antonio, TX 2009.

[29] Kasich, D. C. and Cheng, P. Y., "Flush Port / lnertiallv Blended Air Data Estimator," *AIAA Aerospace Sciences Meeting*, AIAA Paper 1991-0670, 1991.

[30] Morelli, E. A., "Real-Time Aerodynamic Parameter Estimation without Air Flow Angle Measurements," *Atmospheric Flight Mechanics Conference*, Toronto, Canada, August 2010.

[31] Justus, C., James, B., Bougher, S., Bridger, A., Haberle, R., Murphy, J., and Engel, S., "Mars-Gram 2000: A Mars Atmospheric Model for Engineering Applications," *Advances in Space Research*, Vol. 29, No. 2,, 2002, pp. 193–202.

[32] Anderson, B. D. and Moore, J. B., *Linear Optimal Control*, Prentice Hall, 1971.

[33] Dutta, S., Clark, I. G., Russell, R. P., and Braun, R. D., "Statistical Entry, Descent and Landing Performance Reconstruction of the Mars Phoenix Lander," *8th International Planetary Probe Workshop*, Portsmouth, VA, 2011.